ELECTRONIC, ELECTRICAL AND MAGNETIC PROPERTIES OF GRAPHENE OXIDE FUNCTIONALIZED WITH GOLD AND IRON NANOPARTICLES

by

DAVID OMOEFE IDISI

submitted in accordance with the requirements for the degree of

DOCTOR OF PHILOSOPHY

in the subject

PHYSICS

at the

UNIVERSITY OF SOUTH AFRICA

SUPERVISORS:
Prof. S J MOLOI
Prof. S C RAY

2021

Abstract

In the current project, GO was synthesized and functionalized with gold and iron oxide nanoparticles. Several characterization techniques were performed to study the change in the microstructural, electronic, electrical and magnetic properties of rGO due to functionalization. The obtained results from the study showed weak ferromagnetic and superparamagnetic features for rGO:Au-NP and supermagnetism for rGO-ATA-Fe_2O_3 nanocomposites.

The source of the observed magnetic features were mainly attributed to defects induced into rGO by oxygen moieties, Au and Fe atoms bonding on the edge and basal planes of GO. The charge storage behavior and magnetic properties of rGO:Au-NP composite indicate that the material can be useful for applications in ferro-electric and memory devices. The rGO:Fe_2O_3 nanocomposite can find potential in magnetic resonance imaging contrast agent application due to the observed superparamagnetic properties.

Keywords: *Graphene oxide, reduced grapene oxide, gold nanoparticles, iron oxide nanoparticles,microstructural properties, electronic properties, density of state, electrical properties, magnetic properties, superparamagnetism*

What is important about graphene is the new physics it has delivered.

—

Andre Geim

Declaration

I declare that "**ELECTRONIC, ELECTRICAL AND MAGNETIC PROPERTIES OF GRAPHENE OXIDE FUNCTIONALIZED WITH GOLD AND IRON NANOPARTICLES**" is my own work and that all the sources that I have used or quoted have been indicated and acknowledged by means of complete references.

Idisi David Omoefe	Date
Student number: **6084-296-2**	

Dedication

This project is dedicated to my late wife Mrs Enoh Merry Idisi and my dad Late Engr. Moses Oruegwo. You both saw the dream but it's really painful you weren't part of it. I miss you both everyday.

Acknowledgements

This project will not be complete without the following people and organizations:

- My supervisors Prof Moloi for the financial support and pain staking time he took reviewing the thesis. Prof Ray for the tireless time he helped with the project design and reviewing the thesis.
- The financial assistance of the National Research Foundation (NRF) towards this research is hereby acknowledged. Opinions expressed and conclusions arrived at, are those of the author and are not necessarily to be attributed to the NRF.
- Prof Andre Strydom for SQUID magnetometry measurements, Prof Way F Pong for X-ray absorption near edge spectroscopy measurement and Prof Jana N. R., Indian Association for the Cultivation of Science, India for transmission electron microscopy measurement.
- My mum Mrs M O Oruegwo and my son Idisi Orevaogehene for their support and prayers.
- My big sister and friend who is also our departmental adminstrator "Mrs Bongi Hlela". Thanks for the morning hugs and chats.
- My buddies Dr. James Oke and Joe Bodunrin, you guys rock !!!!
- My friends Dr Amos Akande, Dr Uwaoma Chinonso and Dr Ezeokoli Obinna for their moral support.
- Dr Navneet Soin and Dr Mohammed Khenfouch for the input and suggestions.
- Lastly, colleagues and friends at the Department of Physics, it was nice meeting you guys.

Articles publication

Thesis related publication

- D.O. Idisi, H. Ali, J.A. Oke, S. Sarma, S.J. Moloi, S.C. Ray, H.T. Wang, N.R. Jana, W.F. Pong, A.M. Strydom. Appl. Surf. Sci. 483 (2019) 106–113
- D.O. Idisi, J.A. Oke, S. Sarma, S.J. Moloi, S.C. Ray, W.F. Pong, A.M. Strydom. J. Appl. Phys. 126 (2019) 35301.
- Idisi, D. O., Oke, J. A., Benecha, E. M., Moloi, S. J., & Ray, S. C. Materials Today: Proceedings 44 (2021), 5037.

Non-thesis related publication

- J.A. Oke, D.O. Idisi, S. Sarma, S.J. Moloi, S.C. Ray, K.H. Chen, A. Ghosh, A. Shelke, W.F. Pong, ACS Omega. 4 (2019) 14589–14598.
- J.A. Oke, D.O. Idisi, S. Sarma, S.J. Moloi, S.C. Ray, K.H. Chen, A. Ghosh, A. Shelke, S.-H. Hsieh, W.F. Pong. Diam. Relat. Mater. 100 (2019) 107570.
- Oke, J., Idisi, D., Moloi, S., Ray, S., Chen, K. H., Ghosh, A.,& Pong, W. F. (2020).Journal of Electron Spectroscopy and Related Phenomena, 147002.

Contents

List of Figures

List of Tables

Chapter 1

Introduction

The rapid growth of integrated circuits for electronic devices, microprocessors, data storage and logic device technology has led to the emergence of novel materials such as silicon and metal oxide semiconductors [1]. Since the emergence of silicon based integrated circuits, there has been exponential growth in electronic devices especially on-chip transistors and metal-oxide semiconductor field effect transistors (MOSFET) [2]. The on-chip and MOSFET semiconductor technology has led to production of microprocessors and memory chips for high performance computer to process and analyze big data [3].

The prediction of Gordon Moore [4] ~~suggest~~, the doubling of integrated circuits after consecutive 18 months due to technology advancement. His predictions suggested the miniaturization of transistor dimensions and increased operating frequency counts in electronic devices to improve efficiency and chips supply [1]. However, the steady increase in technology needs still pushes the limit of chip demands and supply [1].

Reflecting on the yearly advances in emerging technologies and electronic gadgets, the occurrence of the several decades long predictions of Gordon Moore ~~is~~ inevitable. The consequence of his prediction was recently reported when there was a short fall in global chip supply [5]. Hence, there is enormous need for introduction of other materials to complement the currently available materials ~~been~~ used for chip fabrication.

The current project seeks to offer a material that can be used for fabrication of electronic chips and memory related device applications. Here, graphene-oxide (GO) which acts as a substitute for graphene is used as starting material along-side gold nanopar-

ticles (Au-NP) and iron oxide (Fe_2O_3) nanoparticles as functionalizing agents with the aim of improving the properties of GO for electronic device applications.

Understanding the electronic, electrical and magnetic property of the rGO:Au-NP and rGO:Fe_2O_3 can help improve the properties of rGO. The improved properties of rGO can lead to improved performance of graphene based electronic devices. In the following sections, motivation of the study and brief overview of functionalizing agents are discussed.

1.1 Motivation of study

The need for improved technology in addressing the daily technological needs has led to increase in the number of transistor embedded in on-chip for processors and memory storage [1]. High performance computers for big data and processing analysis relies on increased clock speed of single-processor machines [6]. Furthermore, the fast growing interdisciplinary area of machine learning [7] is dependent on fast processing computers.

Meanwhile, silicon based transistor which is the bedrock of metal-oxide-semiconductor technology is fast approaching the fundamental limit. The limitations posed by the demand and supply will be unable to provide the projected increased density and performance required by most chip manufacturers [1]. Hence, there is an urgent need to offer other solutions to alleviate the looming crisis of processing and memory storage challenges.

In the race to alleviate the fundamental limit of modern semiconductor needs, a modification of the silicon based circuit was suggested which involves down-scaling of the components dimension [8]. The component down-scaling led to improved functionality and storage per unit area capacity [8]. However, the component down-scaling increases the resistance of the conductor and inter-metallic charge storage leading to reduction in chip performance [9].

Nickel silicides (NiSi) have been explored as modification to silicon [8]. The material showed bulk resistivity of approximately $10\,\mu\Omega\cdot$cm for single crystal nanowires with diameter of 58 nm [8]. Although, the different NiSi nanowires have shown promising results, the process of deposition of the desired phase of the composite is still ~~an ongoing~~ challenge and under ~~further~~ investigation [8] thereby making room for other materials. Ferroelectric (FE) materials have been topical in recent times owing to its potential in applications in nonvolatile memory, FETs and photovoltaics cells [10]. FEs are class of materials which exhibit electrically switch-able polarization. FEs are characterized by combination of reversible polarization by applied electric field and charge storage properties [11].

An advantage of the FEs is the miniaturization ability which enables easy electronic fabrication as in the case of Si based FETs [12]. The opportunities offered by FE based FET will offer advantages in-memory architecture by bridging the gap between memory and logic systems [13].

Graphene based FEs have been recently proposed owing to the outstanding properties of pristine graphene. Graphene is a single layer hexagonally arranged carbon based material which can be exfoliated from graphite [14]. Pristine graphene material is characterized by high electron mobility, high surface area and low resistivity [14]. Improving the electronic, electrical and magnetic properties of GO can lead to improved properties which can be useful for electronic devices for high end industrial and scientific productivity.

There have been attempts to improve the properties of graphene for electronic device applications for superior performances. For instance, Poh *et al.* [15] attempted the growth of In_2Se_3 Schottky diode junction by integrating graphene at the interface. Their results showed giant electroresistance ratio of 3.9×10^6 with a readout current density of $\approx 12\,\mathrm{A/cm^2}$. The result provides an avenue for fabrication of high performance devices that are based on 2D materials [14].

Among the draw-backs associated with pristine graphene, the difficulty of mass production of graphene sheets still looms since the structure can be easily altered/ distorted

by graphite exfoliation [16]. Another setback of pristine graphene is the absence of intrinsic magnetic spins which leads to nonmagnetism of the materials [17].

An easy route for producing graphene is through the chemical exfoliation of graphite powder using modified Hummers method. The process leads to formation of graphene oxide (GO) [18]. GO which is a derivative of graphene lacks intrinsic magnetic moment which makes them nonmagnetic. This study intends to alleviate the nonmagnetic issue by chemical functionalization.

It is worth mentioning that the current study does not intend to fabricate an electronic device. However, the study focuses on demonstrating the magnetic and charge storage properties of graphene oxide composite for possible application in ferroelectric electronic devices. The study entails functionalizing GO with gold and iron oxide nanoparticles with the intention on establishing their electronic, electrical and magnetic properties.

Moreover, GO sheets and Au-NPs which is one of the focus of the current study have been topical in recent researches [19–22]. Au-NPs possesses significant magnetic characteristics and when Au functionalizes other materials, it manifest interesting characteristics. For instance, iron oxide functionalized (covalent attachment of functional groups onto the basal planes or edges of 2D nanofillers through chemical reactions) with Au produces magnetic properties [20], which can be used for various applications. Most recently, reduced-GO (rGO) functionalized with Au was synthesized and used as catalytic system for electroreduction of oxygen in alkaline electrolytes [23].

The study of Wang *et al.* [24] synthesized rGO functionalized with Au nanoclusters. The synthesized nanocluster was used for drug delivery and cancer cell imaging applications. Furthermore, ~~another~~ recent study on GO functionalized with Au-NP was explored to determine electrochemical immunosensor of cortisol [25]. Their obtained results showed high response in terms of electrical conductivity and strong enhancement in the sensory performance [25].

In these recent findings, no significant attention has been given to the use of GO functionalized with Au-NPs with focus on its magnetic properties. The available literature

on the magnetic related composite involves magnetically reduced graphene oxide which focuses on aptasensors for cocaine detection [26].

On the ~~otherhand~~, the magnetic properties of GO:Fe composite have widely studied. However, the applications have been mostly focused on biomedicine, therapeutics,water purification and lithium ion batteries [27–30]. Fe_2O_3 have been used to functionalize carbon nanotubes and graphene for improved electrochemical performance of Li-ion batteries [30]. However, there have not been studies on electronic device applications such as ferroelectric memory devices.

The current study intends to bridge this gap by exploring the potential of GO functionalized with Au-NP for possible applications in electronic devices. Fe_2O_3-NPs were considered for this study based on its non-toxicity and ferromagnetic property; whereas Au-NPs are considered as a diluted magnetic material which can easily be decorated on graphene and GO sheets as described by Eustis and Muszynski [31, 32].

In this study, GO was synthesized using modified Hummers method [33] and reduced by hydrazine hydrate. The reduced GO were functionalized with Au-NP and Fe_2O_3-NP using covalent bonding technique. Various characterization techniques were carried out on the samples with the intention of establishing ferroelectric and ferromagnetic property of both materials. In the case of Au, it is envisaged that the magnetic properties of rGO:Au-NP would be enhanced and be useful material for soft magnet applications [34], whereas the suitability of the material for biomedical applications is expected when functionalized with Fe_2O_3-NP [35].

1.2 Brief overview of Gold (Au) and Iron (Fe) nanoparticles

The encouraging magnetic effects of Au nanoparticles (Au-NPs) functionalizing other materials have been widely studied by various researchers [20, 36–38]. Crespo *et al.*

[39] studied thiol-capped Au for magnetic properties. Paramagnetic and ferromagnetic behavior was observed at below and room temperature. Both magnetic behaviours were observed when Au-NP was coated with dodecane thiol. By virtue of the tunability of Au by ligand coating, there is a possibility of the material being used for inducing magnetism onto GO [39].

The non-toxicity and ferrous property of iron (Fe) has revolutionized interest into magnetism research and innovations. The magnetic properties of Fe is mostly attributed to the exchange interaction of the delocalized 3d band electrons as indicated in Fe electronic structure [40]. Fe can be easily manipulated with respect to its shape (squares, spheres e.t.c.) [41] and adsorbed to the surface of other materials [42]. These various shapes can tune the electronic property of Fe nanoparticle. Fe-NPs have created an avenue for electrical and magnetic applications. For instance, with the tunable coercivity (high or low magnetic intensity required to demagnetize a magnetic material), Fe-NP can easily be adapted to various applications such as recording media, transformer core materials, catalytic and biomedical applications etc [43].

Report indicates that gold nanoparticles could easily retain their bulk magnetization when used in functionalization of other materials. This magnetization retention in addition to bicompatibility accounts for its use in drug delivery applications [44]. Meanwhile, reduced graphene oxide/gold composite (rGO:Au) have been widely studied for different applications. Due to the inert/ bicompatibility property of gold in its bulk and nanoparticles form, it has been widely explored in biomedicine for drug delivery, electrochemistry and surface-enhanced raman scattering [45–47].

However, rGO:Au-NP composite have not been widely explored for potential in electronic device applications especially in the evolving area of ferroelectrics by exploring its charge storage property. Based on the outcome of the study where charge storage behavior and weak ferromagnetic/ superparagmetic features is expected, it is envisaged that the rGO:Au-NP composite will prove useful in the area of memory and other electronic device applications.

Graphene oxide/ iron oxide (GO:Fe_2O_3) have been widely explored in medicinal and

water purification technology due to its biocompatibility capabilities [48, 49]. However, GO:Fe_2O_3 composite have not been explored for ferroelectric properties by virtue of charge storage properties. The focus on current-voltage characteristics of the graphene oxide/ iron oxide nanocomposite in the current study by exploring its charge storage features can offer opportunities in the area of ferroelectric based electronic device applications.

1.3 Aim and objectives

The aim of this project is to study the electronic, electrical and magnetic properties of rGO composites for possible application in the fabrication of efficient electronic devices such as processors, memory, data storage using Au-NPs and Fe_2O_3 as functionalizers. The focus of the project will be based on synthesizing graphene oxide sheets, rGO:Au-NP and rGO:Fe_2O_3 nanocomposites after GO reduction. The microstructural, electronic, electrical and magnetic properties of the synthesized composites will be studied using different spectroscopic techniques, electrical characterization and magnetometry studies. Based on the obtained results, the properties of GO nanocomposites for the different application will be established with focus on the area of electronic device applications.

1.4 Structure of thesis

Chapter 1 deals with the introduction of the current trends in semiconductor electronic devices and the need for development of new materials with an overview of the importance of gold and iron oxide as functionalizing agent in the current study. The motivation of the current study is also presented in this chapter.

Chapter 2 discusses the properties of graphene and graphene oxide (GO). The elec-

tronic structure of graphene and its Fermi structure are presented in this chapter. The structure of GO and the previously proposed models regarding the arrangement of carbon atoms and oxygen functional groups are also presented in this chapter. The magnetic properties of solids as it relates to graphene are also presented here.

Chapter 3 entails the description of the characterization techniques that were used in this study. An overview of the theoretical background and schematic diagrams of the working principles of the experimental and characterization techniques are presented. The characterization techniques are categorized into structural, electronic, electrical and magnetic techniques.

Chapter 4 and 5 entails the experimental details that were used in the study, as well as the obtained results for the study. The study is in two parts, the first part which is presented in chapter 4 deals with rGO:Au-NP composites and the second part focuses on rGO:Fe_2O_3-NP composites which is presented in chapter 5. The synthesis, reduction, functionalization and silicon wafer deposition details are also presented in both chapters. The details of obtained results are discussed in both chapters with a brief summary at the end of both chapters.

Finally, the summary of all the obtained results are given in chapter 6 where the main highlights of the results of both rGO composites are compared. The conclusion of the study with potential recommendation is also presented in this chapter. Future research prospects with a brief overview is also presented in this chapter.

Bibliography

[1] Mark T Bohr. Nanotechnology goals and challenges for electronic applications. *IEEE Transactions on Nanotechnology*, 1(1):56–62, 2002.

[2] Robert G Arns. The other transistor: early history of the metal-oxide semiconductor field-effect transistor. *Engineering Science & Education Journal*, 7(5):233–240, 1998.

[3] Carl J Anderson, J Petrovick, JM Keaty, J Warnock, G Nussbaum, JM Tendier, C Carter, S Chu, J Clabes, J DiLullo, et al. Physical design of a fourth-generation power ghz microprocessor. In *2001 IEEE International Solid-State Circuits Conference. Digest of Technical Papers.*, ~~pages~~ 232–233. IEEE, 2001.

[4] Gordon Moore. Moore's law. *Electronics Magazine*, 38(8):114, 1965.

[5] Bradly J Condon. From ideas to action: Governance paths to net zero. *Journal of International Economic Law*, 00:1–6, 2021.

[6] Xue-Jun Yang, Yong Dou, and Qing-Feng Hu. Progress and challenges in high performance computer technology. *Journal of Computer Science and Technology*, 21(5):674–681, 2006.

[7] Michael I Jordan and Tom M Mitchell. Machine learning: Trends, perspectives, and prospects. *Science*, 349(6245):255–260, 2015.

[8] Anshul A Vyas, Changjian Zhou, and Cary Y Yang. On-chip interconnect conductor materials for end-of-roadmap technology nodes. *IEEE Transactions on Nanotechnology*, 17(1):4–10, 2016.

[9] SC Sun. Process technologies for advanced metallization and interconnect systems.

In *International Electron Devices Meeting. IEDM Technical Digest*, ~~pages~~ 765–768. IEEE, 1997.

[10] JF Scott. Applications of modern ferroelectrics. *Science*, 315(5814):954–959, 2007.

[11] Tengqiang Shao, Hongliang Du, Hua Ma, Shaobo Qu, Jun Wang, Jiafu Wang, Xiaoyong Wei, and Zhuo Xu. Potassium–sodium niobate based lead-free ceramics: novel electrical energy storage materials. *Journal of Materials Chemistry A*, 5(2):554–563, 2017.

[12] Hee Han, Yunseok Kim, Marin Alexe, Dietrich Hesse, and Woo Lee. Nanostructured ferroelectrics: fabrication and structure–property relations. *Advanced Materials*, 23(40):4599–4613, 2011.

[13] Asif Islam Khan, Ali Keshavarzi, and Suman Datta. The future of ferroelectric field-effect transistor technology. *Nature Electronics*, 3(10):588–597, 2020.

[14] Sergey Mikhailov. *Physics and Applications of Graphene: Experiments*. BoD–Books on Demand, 2011.

[15] Sock Mui Poh, Sherman Jun Rong Tan, Han Wang, Peng Song, Irfan H Abidi, Xiaoxu Zhao, Jiadong Dan, Jingsheng Chen, Zhengtang Luo, Stephen J Pennycook, et al. Molecular-beam epitaxy of two-dimensional in2se3 and its giant electroresistance switching in ferroresistive memory junction. *Nano Letters*, 18(10):6340–6346, 2018.

[16] J Jagiello, J Judek, M Zdrojek, M Aksienionek, and L Lipinska. Production of graphene composite by direct graphite exfoliation with chitosan. *Materials Chemistry and Physics*, 148(3):507–511, 2014.

[17] Hideki Kumazaki and Dai S. Hirashima. Nonmagnetic-defect-induced magnetism in graphene. *Journal of the Physical Society of Japan*, 76(6):064713, 2007.

[18] Leila Shahriary and Anjali A Athawale. Graphene oxide synthesized by using modified hummers approach. *Int. J. Renew. Energy Environ. Eng*, 2(01):58–63, 2014.

[19] Vaishali Gupta, Neeraj Sharma, Udai Singh, Mohd Arif, and Arun Singh. Higher oxidation level in graphene oxide. *Optik-International Journal For Light and Electron Optics*, 143:115–124, 2017.

[20] Everett E Carpenter, Amar Kumbhar, Joan A Wiemann, Hariharan Srikanth, Jason Wiggins, Weilie Zhou, and Charles J O'Connor. Synthesis and magnetic properties of gold–iron–gold nanocomposites. *Materials Science and Engineering: A*, 286(1):81–86, 2000.

[21] Louis Catherine and Pluchery Olivier. *Gold Nanoparticles for Physics, Chemistry and Biology*. World Scientific, 2017.

[22] Sweety Sarma, Sekhar C Ray, and André M Strydom. Electronic and magnetic properties of nitrogen functionalized graphene-oxide. *Diamond and Related Materials*, 79:1–6, 2017.

[23] Sylwia Zoladek, Iwona A Rutkowska, Magdalena Blicharska, Krzysztof Miecznikowski, Weronika Ozimek, Justyna Orlowska, Enrico Negro, Vito Di Noto, and Pawel J Kulesza. Evaluation of reduced-graphene-oxide-supported gold nanoparticles as catalytic system for electroreduction of oxygen in alkaline electrolyte. *Electrochemica Acta*, 233:113–122, 2017.

[24] Chensu Wang, Jingyuan Li, Christian Amatore, Yu Chen, Hui Jiang, and Xue-Mei Wang. Gold nanoclusters and graphene nanocomposites for drug delivery and imaging of cancer cells. *Angewandte Chemie International Edition*, 50(49):11644–11648, 2011.

[25] Bolu Sun, Yuqiang Gou, Yuling Ma, Xiaoping Zheng, Ruibin Bai, Ahmed Attia Ahmed Abdelmoaty, and Fangdi Hu. Investigate electrochemical immunosensor

of cortisol based on gold nanoparticles/magnetic functionalized reduced graphene oxide. *Biosensors and Bioelectronics*, 88:55–62, 2017.

[26] Pegah Hashemi, Hasan Bagheri, Abbas Afkhami, Yalda Hosseinzadeh Ardakani, and Tayyebeh Madrakian. Fabrication of a novel aptasensor based on three-dimensional reduced graphene oxide/polyaniline/gold nanoparticle composite as a novel platform for high sensitive and specific cocaine detection. *Analytica Ahimica Acta*, 996:10–19, 2017.

[27] Xin Yang, Changlun Chen, Jiaxing Li, Guixia Zhao, Xuemei Ren, and Xiangke Wang. Graphene oxide-iron oxide and reduced graphene oxide-iron oxide hybrid materials for the removal of organic and inorganic pollutants. *RSC Advances*, 2(23):8821–8826, 2012.

[28] Xinxing Ma, Huiquan Tao, Kai Yang, Liangzhu Feng, Liang Cheng, Xiaoze Shi, Yonggang Li, Liang Guo, and Zhuang Liu. A functionalized graphene oxide-iron oxide nanocomposite for magnetically targeted drug delivery, photothermal therapy, and magnetic resonance imaging. *Nano Research*, 5(3):199–212, 2012.

[29] Roberto Gonzalez-Rodriguez, Elizabeth Campbell, and Anton Naumov. Multi-functional graphene oxide/iron oxide nanoparticles for magnetic targeted drug delivery dual magnetic resonance/fluorescence imaging and cancer sensing. *PLoS One*, 14(6):e0217072, 2019.

[30] Lei Zhang, Hao Bin Wu, and Xiong Wen Lou. Iron-oxide-based advanced anode materials for lithium-ion batteries. *Advanced Energy Materials*, 4(4):1300958, 2014.

[31] Susie Eustis and Mostafa A El-Sayed. Why gold nanoparticles are more precious than pretty gold: noble metal surface plasmon resonance and its enhancement of the radiative and nonradiative properties of nanocrystals of different shapes. *Chemical Society Reviews*, 35(3):209–217, 2006.

[32] Ryan Muszynski, Brian Seger, and Prashant V Kamat. Decorating graphene sheets with gold nanoparticles. *The Journal of Physical Chemistry C*, 112(14):5263–5266, 2008.

[33] NI Zaaba, KL Foo, U Hashim, SJ Tan, Wei-Wen Liu, and CH Voon. Synthesis of graphene oxide using modified hummers method: solvent influence. *Procedia Engineering*, 184:469–477, 2017.

[34] JA Bas, JA Calero, and MJ Dougan. Sintered soft magnetic materials. properties and applications. *Journal of Magnetism and Magnetic Materials*, 254:391–398, 2003.

[35] David O Idisi, JA Oke, Sweety Sarma, SJ Moloi, Sekhar C Ray, WF Pong, and Andre M Strydom. Tuning of electronic and magnetic properties of multifunctional r-go-ata-fe2o3-composites for magnetic resonance imaging (mri) contrast agent. *Journal of Applied Physics*, 126(3):035301, 2019.

[36] Romain Gréget, Gareth L Nealon, Bertrand Vileno, Philippe Turek, Christian Mény, Frédéric Ott, Alain Derory, Emilie Voirin, Eric Rivière, Andrei Rogalev, et al. Magnetic properties of gold nanoparticles: A room-temperature quantum effect. *ChemPhysChem*, 13(13):3092–3097, 2012.

[37] L Creveling Jr and HL Luo. Magnetic properties of gold-rich gold-vanadium alloys. *Physical Review*, 176(2):614, 1968.

[38] Ivan H El-Sayed, Xiaohua Huang, and Mostafa A El-Sayed. Surface plasmon resonance scattering and absorption of anti-egfr antibody conjugated gold nanoparticles in cancer diagnostics: applications in oral cancer. *Nano Letters*, 5(5):829–834, 2005.

[39] P Crespo, Rojas Litrán, TC Rojas, M Multigner, JM De la Fuente, JC Sánchez-López, MA García, A Hernando, S Penadés, and A Fernández. Permanent mag-

netism, magnetic anisotropy, and hysteresis of thiol-capped gold nanoparticles. *Physical Review Letters*, 93(8):087204, 2004.

[40] Isabelle ML Billas, A Chatelain, and Walt A de Heer. Magnetism from the atom to the bulk in iron, cobalt, and nickel clusters. *Science*, 265(5179):1682–1684, 1994.

[41] Caroline De Montferrand, Ling Hu, Irena Milosevic, Vincent Russier, Dominique Bonnin, Laurence Motte, Arnaud Brioude, and Yoann Lalatonne. Iron oxide nanoparticles with sizes, shapes and compositions resulting in different magnetization signatures as potential labels for multiparametric detection. *Acta Biomaterialia*, 9(4):6150–6157, 2013.

[42] Baohua Gu, Juergen Schmitt, Zhihong Chen, Liyuan Liang, and John F McCarthy. Adsorption and desorption of natural organic matter on iron oxide: mechanisms and models. *Environmental Science & Technology*, 28(1):38–46, 1994.

[43] Dale L Huber. Synthesis, properties, and applications of iron nanoparticles. *Small*, 1(5):482–501, 2005.

[44] L León Félix, B Sanz, V Sebastián, TE Torres, Marcelo Henrique Sousa, JAH Coaquira, MR Ibarra, and Gerardo Fabian Goya. Gold-decorated magnetic nanoparticles design for hyperthermia applications and as a potential platform for their surface-functionalization. *Scientific Reports*, 9(1):1–11, 2019.

[45] Narges Elahi, Mehdi Kamali, and Mohammad Hadi Baghersad. Recent biomedical applications of gold nanoparticles: A review. *Talanta*, 184:537–556, 2018.

[46] Ibrahim Khalil, Nurhidayatullaili Muhd Julkapli, Wageeh A Yehye, Wan Jefrey Basirun, and Suresh K Bhargava. Graphene–gold nanoparticles hybrid—synthesis, functionalization, and application in a electrochemical and surface-enhanced raman scattering biosensor. *Materials*, 9(6):406, 2016.

[47] Jing-Liang Li, Bin Tang, Bing Yuan, Lu Sun, and Xun-Gai Wang. A review

of optical imaging and therapy using nanosized graphene and graphene oxide. *Biomaterials*, 34(37):9519–9534, 2013.

[48] Siaw Fui Kiew, Lik Voon Kiew, Hong Boon Lee, Toyoko Imae, and Lip Yong Chung. Assessing biocompatibility of graphene oxide-based nanocarriers: a review. *Journal of Controlled Release*, 226:217–228, 2016.

[49] Ayub Khan, Jian Wang, Jun Li, Xiangxue Wang, Zhongshan Chen, Ahmed Alsaedi, Tasawar Hayat, Yuantao Chen, and Xiangke Wang. The role of graphene oxide and graphene oxide-based nanomaterials in the removal of pharmaceuticals from aqueous media: a review. *Environmental Science and Pollution Research*, 24(9):7938–7958, 2017.

Chapter 2

Theoretical overview

2.1 Graphene and Graphene Oxide

Graphene is a thin layer of carbon with atoms arranged hexagonally in a lattice [1]. It is a class of material that has potential in various fields of science and technology. This is due to properties such as surface area of $2630\,\mathrm{m^2 g^{-1}}$, which makes it viable for adsorptive capabilities and high mobility due to its zero band gap semiconductor property [2]. The high mobility (approximately $200000\,\mathrm{cm^2 V^{-1} \cdot s^{-1}}$) enables the material being applicable to electronic devices [3]. The material possesses thermal conductivity of approximately $5000\,\mathrm{W \cdot m^{-1} \cdot K^{-1}}$, which indicates potential for heat flow applications [4]. Furthermore, graphene possesses optical transmittance of approximately 97.7% making the material useful for information transmission through optical processes [5]. Graphene is relatively expensive and difficult to produce and obtaining a single layer of graphene from the multilayers of pristine graphite is challenging. Graphene-oxide (GO) offers cost effective alternative for graphene-based materials as they can be produced by relatively cheap chemical techniques. GOs are single-atomic or few layered sheets of material with carbon, hydrogen and oxygen constituents which are formed by oxidation of graphite crystals [6]. GO can be described as a 2D material having similar carbon atomic arrangement as pristine graphene. The formation of GO derivative originates from the attachment of oxygenated groups at its edge and basal planes. The oxygen atoms bond covalently to the carbon atoms [1] resulting in an sp^3 hybridized

graphene based material [7]. The number of carbon-oxygen bonds ~~being~~ higher than that of pristine sp^2 hybridized carbon atoms, resulting in high density of defected sp^3 graphene material. The result of the population of sp^3 enables the differentiation of GO from pristine graphene [7].

Due to the introduction of oxygen, the electrical conductivity of graphene changes from a highly conducting semiconductor to an insulator. The presence of the oxygen functional groups (C−O, C−OH, C=O) improves the hydrophilicity and band gap tunability of graphene (widening of the zero band gap) [7]. The band gap tunability would result to the variation of the optical and electronic properties of graphene [7]. The main distinction between graphite oxide and GO is the interplanar spacing, which is approximately 0.335 nm for graphite oxide and 0.142 nm for GO between the individual atomic layers of compounds. This difference factor is attributed to water intercalation [6].

Attaining graphene-like sheets in GO is possible with a chemical reduction process (reduced graphene oxide (rGO)). The properties of rGO are similar to those of graphene with possible attachment of oxygenated groups on the edges of GO [6]. The carbon bonds, which form the components of pristine graphene are bonded together by σ hybridized bonds. Each carbon atom contributes to delocalized sets of electrons through its π orbital [8]. The hybridization enables the potential of GO for easy functionalization with other elements such as boron, nitrogen, silicon leading to properties of the material being useful for lithium-ion batteries, supercapacitors applications [9, 10].

Originally, a graphene sheet contains trigonal sp^2 bonded carbon, which is flat and becomes tetrahedral sp^3 carbon bonded atoms when modified into GO. The position of induced defects because of oxidation or functionalization can be displaced either above or below the graphene plane [6].

2.1.1 Hybridization in graphene

Graphene representing a single or few layers of carbon atoms possesses high mobility leading to high conductivity of the material [11]. The electronic properties can be attributed to the bonding structure of graphene. The graphene bond structure is a combination of carbon atoms in a molecular form. The carbon atom consists of six electrons surrounding a central nucleus. Four electrons in its inner shell and two electrons in its valence band. Considering its orbital configuration, carbon has two electrons in both $2s$ and $2p$ orbital shell and an electron can easily transit from $2s$ to $2p$ shell with little excitation [12]. The orbitals of graphene can easily hybridize in three modes as shown in Figure 2.1.1. The carbon atom produces two covalent sigma (σ) bonds with a bond angle of 180° and a diagonal symmetry. The remaining $2p_y$ and $2p_z$ out of the four $2p$ orbital results in π orbital lying perpendicular to the σ bond. The two $s-p$ hybridized carbon atoms are in contact, with the π orbitals being surrounded by a σ bond and form a triple bond [14]. The sp^2 cluster that accounts for the C=C bond are a consequence of the hybridization of the $2s$ and two $2p$ orbitals.

The hybridization process leads to the formation of three covalently σ bonded C atoms

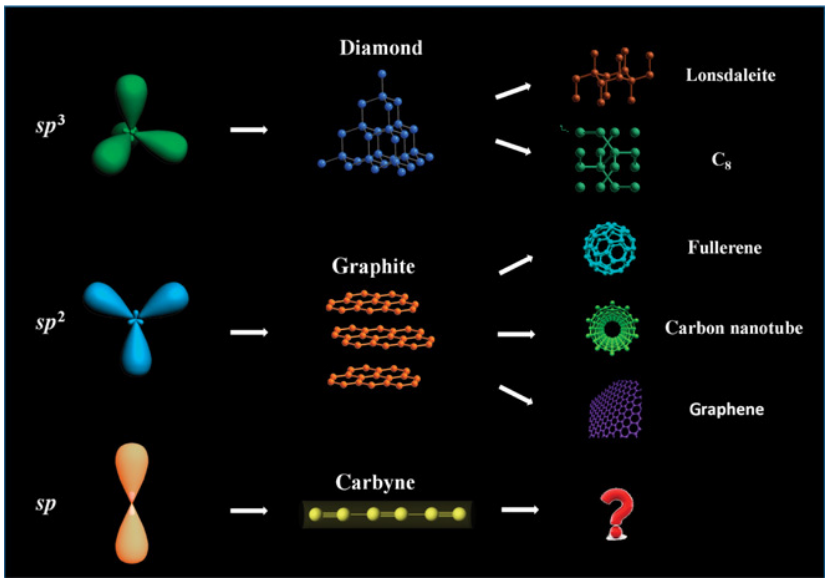

Figure 2.1.1: The hybridization state of graphene exhibiting sp, sp^2 and sp^3 states. Adapted from Pan et al. [13].

that are separated by a 120^0 angle and trigonal symmetry. Furthermore, delocalized π bond, which is independent of the former σ bonded C atoms produces an additional eight orbitals lying perpendicular to the three σ bonds. The free movement of the π electrons in carbon atoms accounts for the high electrical conductivity of graphene [12]. In sp^3 hybridization, the four orbitals hybridize to produce four equal tetrahedral orbitals with bond angle of 109.5°. The four σ covalent bonds are tightly bound together producing diamond material. The downside of the bonding property of diamond is that it makes the diamond a poor conductor where the antibody σ^* bond has high energy well above the σ bond, which prevents easy excitation of the electrons [12].

The action of hybridization of the carbon molecules results in the observed electrical properties of GO. The π electrons on the surface of graphene plane exhibit a massless fermion movement which plays a major role in the electron mobility in graphene. Meanwhile, considering GO, the π electrons produce a covalent bonding of carbon atoms and oxygenated groups, which destabilizes the sp^2 π electron network, thereby causing the insulator property exhibited by GO. However, with the variance of the degree of oxidation of GO (ratio of carbon to oxygen), the band gap of GO can be easily varied, hence varying the electrical conductivity of GO [15].

2.1.2 Electronic band structure of Graphene

Graphene comprises of carbon atoms layered in a hexagonal format as shown in Figure 2.1.2. As indicated in the Figure, the structure is visualized as a triangular lattice comprising two atoms per unit cell.

Mathematically, the lattice vectors can be expressed [16] as :

$$\mathbf{a_1} = \frac{a}{2}(3, \sqrt{3}) \qquad \text{and} \qquad \mathbf{a_2} = \frac{a}{2}(3, -\sqrt{3}), \tag{2.1}$$

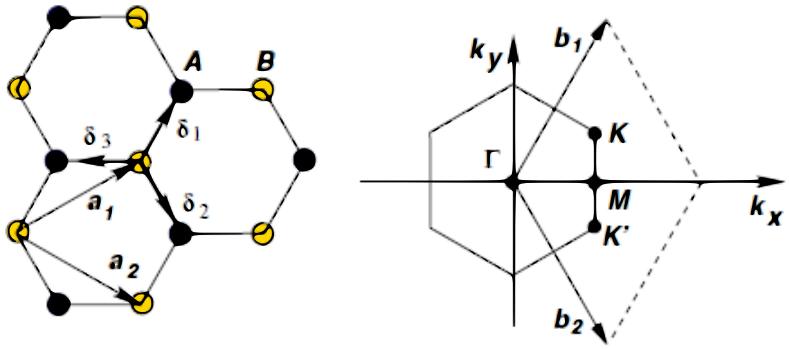

Figure 2.1.2: Electronic structure of graphene from tight bonding approach where left and right are real and reciprocal space. Image adapted from Neto et al. [16]

where $a \approx 1.42$ Å represents the distance carbon-carbon atoms and $|a_1| = |a_2| = 2.46$ Å. The reciprocal-lattice can also be expressed [16] as:

$$\mathbf{b_1} = \frac{2\pi}{3a}(1, \sqrt{3}) \qquad \text{and} \qquad \mathbf{b_2} = \frac{2\pi}{3a}(1, -\sqrt{3}). \tag{2.2}$$

Meanwhile, Γ and M are the dirac points which are located at the two centers and corner of the Brillouin zone edge. The K and K' are the two momentum positions at the corners and are given [16] as:

$$\mathbf{K} = \left(\frac{2\pi}{3a}, \frac{2\pi}{3\sqrt{3}a}\right) \qquad \text{and} \qquad \mathbf{K'} = \left(\frac{2\pi}{3a}, -\frac{2\pi}{3\sqrt{3}a}\right). \tag{2.3}$$

Using the tight binding model [17], the Hamiltonian can be solved by the analogy of nearest neighbor atomic system. The three nearest-neighbor vectors as indicated in Figure 2.1.2 and can be expressed [16] as:

$$\boldsymbol{\delta_1} = \frac{a}{2}(1, \sqrt{3}), \qquad \boldsymbol{\delta_2} = \frac{a}{2}(1, -\sqrt{3}) \text{ and } \boldsymbol{\delta_3} = -a(1, 0), \tag{2.4}$$

whereas the other six second-nearest neighbors are assigned to $\delta_1' = \pm\mathbf{a_1}$, $\delta_2' = \pm\mathbf{a_2}$ and $\delta_3' = \pm(\mathbf{a_1} - \mathbf{a_2})$.

The tight-binding theorem requires that the Hamilton for the electrons be able to hop

between both nearest and next neighbor atoms whereas the other six second-nearest neighbors are assigned to $\delta_1' = \pm\mathbf{a_1}$, $\delta_2' = \pm\mathbf{a_2}$ and $\delta_3' = \pm(\mathbf{a_1} - \mathbf{a_2})$

The tight-binding theorem requires that hopping of the Hamilton of the electrons between both nearest neighboring atoms. The simple Hamiltonian can be written [16] as:

$$E_{g2D}(k_x, k_y) = \pm t\left[+ 4\cos\left(\frac{3k_x a}{2}\right)\cos\left(\frac{k_y a}{2}\right) + 4\cos^2\left(\frac{k_y a}{2}\right)\right]^{1/2}, \qquad (2.5)$$

where $t \approx 2.8\,\mathrm{eV}$ is the nearest neighbor hopping energy. Figure 2.1.3 depicts the variation of the parameters in equation 2.5. For the case of pristine graphene, there are six points where the bands overlap with the exception of two points (K and K') shown in the zoomed region where the energy band is close to the dirac cone (not touching and not explicitly equal to zero) [16]. The implication of the dirac cone sitting at the Fermi level accounts for the zero band semicondcutor property of pristine graphene [18].

The $\pm$ in the equation 2.5 are associated with bonding and anti-bonding π energy bands. The derived energy bands associated with the Hamiltonian can be expressed

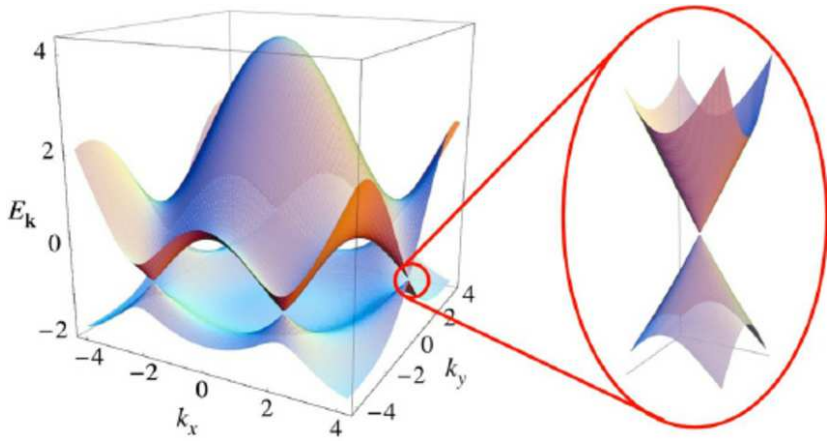

Figure 2.1.3: Electronic dispersion curve representing Graphene energy dispersion bands showing the Brillouin zones. Adapted from Recher and Trauzettel [19].

[16] as:

$$E_{\pm}(\mathbf{K}) = \pm t\sqrt{3 + f(\mathbf{K})} - t'f(\mathbf{K}), \tag{2.6}$$

where, $t'f(\mathbf{K})$ is the next nearest-neighbor hopping energy [16]. With further manipulation of equation 2.5, the equation can be rewritten as

$$E_{lin}^{\pm} = \pm h v_F |k|, \tag{2.7}$$

where $v_F \approx 10^6\,\mathrm{ms}^{-1}$ represents the Fermi electron velocity for graphene. It is the electron mobility behaviour (high electrical conductivity) that accounts for the zero band gap semiconductor property of graphene [20]. Supposing the value of the electron mass is substituted as zero and $v_F = c$ then equation 2.7 reduces to the Dirac equation. The Dirac equation reduction is the rationale behind the massless Dirac particle nature of graphene [16]. The Dirac equations can be used in clarifying the principle behind the Raman scattering modes of graphene. The phonon modes interactions that are close to K are quite significant as they are responsible for the D and G band observed in Raman spectroscopy studies of graphene.

2.1.3 Density of states

The density of state (DOS) is the population of energy eigenstates that are present in a unit energy interval. Equation 2.6 can be written and used to evaluate the DOS [21] as:

$$g(E)dE = 2g_z \frac{dA}{(2\pi)^2/\Omega}, \tag{2.8}$$

where g_z depicts the zone degeneracy (six **K** points). Each of the **K** points is distributed to three atoms with $g_z = 2$. Ω represents the area of the reciprocal lattice whereas dA represents the infinitesimal area in terms of k-space. The magnitude of dA can be evaluated using $2\pi k$ and is expressed as

$$dA = 2\pi k dk.$$

Considering the normalization of $g(E)$ over the total area Ω, the energy of the degenerate **K** points can be evaluated as:

$$g(E) = \frac{2}{\pi}\left|\frac{kdk}{dE}\right| = \frac{2}{\pi}\left|k\left(\frac{dE}{dk}\right)^{-1}\right|. \tag{2.9}$$

Substituting for the value of E from equation 2.7, $g(E)$ can be written as:

$$g(E) = \frac{2}{\pi(\hbar v_F)^2}|E| = \beta|E|. \tag{2.10}$$

The relationship between $g(E)$ and DOS is shown in Figure 2.1.4 [16, 20]. The constant parameters in equation 2.10 can be represented as a new quantity $\beta \approx 1.5 \times 10^{14}\,\mathrm{eV}^{-2}\mathrm{cm}^{-2}$ [21].

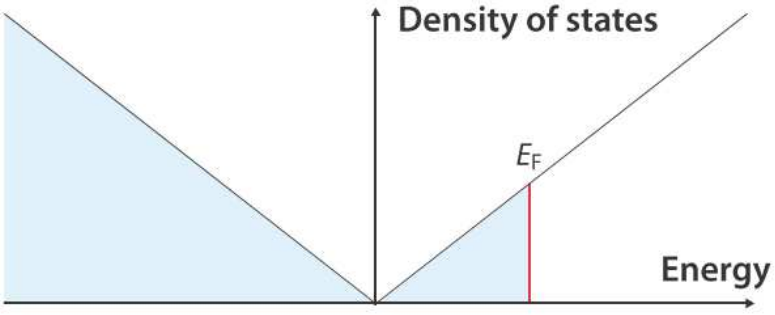

Figure 2.1.4: The plot of the linear relationship between energy and density of state emphasizing nearness to the Fermi level E_F. Adapted from Sepioni [21].

2.1.4 Structure of Graphene Oxide

The structure of GO gives an insight into the behavior of the material when functionalized with other materials. The precise chemical structure of GO has not been fully understood since GO is considered a non-stoichiometric compound; hence, the relative number of atoms is not integer-ratio-based [22]. Complexities associated with GO structure can be understood by chemical models. The models described herein are some of the recent propositions on the structure of GO compiled from literature. As shown in Figure 2.1.5, Hofmann structural model showed an epoxy functional group consisting of an oxygen atom joined by single bonds to two adjacent carbon atoms spread across the basal planes of graphite having a net chemical formula of C_2O [23]. The suggestion of the Ruess model made some changes to the structure of GO as formerly proposed by Hoffmann. In the Ruess model, there is a variation of hydroxyl-functional group incorporation into the basal plane structure. The hydroxyl incorporation accounts for the presence of hydrogen constituents in GO. The Ruess model changed the basal structure from sp^2 to an sp^3 hybridized system where lattice repetition occurs. The model suggests the substitution of the 1st and 4th positions of the cyclohexane with epoxides in the 1st and 3rd positions whereas hydroxyl is kept in the 4th position [23].

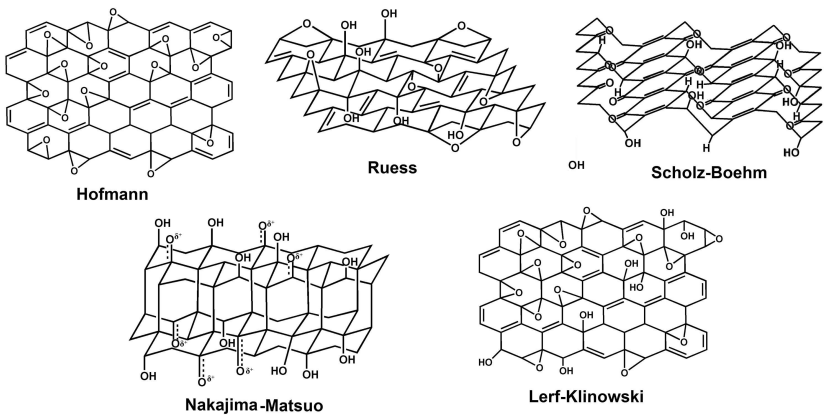

Figure 2.1.5: Various proposed models describing the chemical structure of GO. The models considered are based on the propositions of Hofmann, Ruess, Scholz-Boehm, Nakjima-Matsuo and Lerf-Klinowski. Adapted from Dreyer et al. [1].

Scholz and Boehm proposed removal of the epoxide and ether functional groups with a replacement of the hydroxyl group at the 4th position of 1,2-oxidized cyclohexane rings. The structure was modified into a corrugated carbon layer, which contains linked ribbons of quinoidal structure and opened cyclohexane rings [24].

A a more reliable model was proposed by Lerf and Klinowski which suggested the scrapping of the lattice-related model and substituted with a non-stoichiometric amorphous system [25]. In the study of Lerf and Klinowski, a solid-state nuclear magnetic resonance technique was used for GO structural characterization. Their experimental procedures are briefly described by Dreyer *et al.* and Gao [23, 24]. The results by Dreyer *et al.* [1] showed significant interplatelet hydrogen bonding through the epoxide and alcohol functional groups which accounts for the tightly packed structure of GO. Further studies of Lerf *et al* [25] indicated that the double bond was either aromatic or conjugated.

Szabo-Dekany (not shown in Figure) [1] proposed a two-domain model comprising trans-linked cyclohexyl species interspersed with tertiary alcohols and 1,3-ethers. The other domain contains a corrugated connection of keto/ quinoidal species with absence of carboxylic acid. The model further suggests a destruction of the alkenes contained in the quinones when additional oxidation is introduced. This occurs through the formation of 1,2-ethers and any aromatic pocket that may be present in the initial oxidation process during the synthesis of the GO compound [23].

Generally, GO is considered amorphous with strong dependence on the synthesis technique used and the degree of oxidation which is not limited to oxygen alone but includes other functional groups [26].

2.1.5 Exchange interaction and magnetism in graphene

Magnetism in materials is mainly due to interactions of electrons from the atoms in the material. The motions exhibited by the electrons generate magnetic moments. The magnetic moments couple with each other within the material cluster, thereby producing magnetic ordering. The quantum mechanical coupling of the moments is termed exchange interaction [27]. The interaction is simply an overlaps of electrons within the confines of Pauli's exclusion theory.

The exchange interaction can be either direct, indirect or superexchange. Direct exchange involves moments in close proximity to each other such that their wave functions overlap to produce a short-lived strong coupling, which decays with increased ion separation [28]. Given two atomic systems with electrons in close proximity, the electrons experience a weak Coulomb force. Consequently, the small distance between the electrons gives opposite spins due to the Pauli exclusion theory. The opposite spin leads to antiparallel alignment, which produces a negative exchange interaction, i.e., antiferromagnetic ordering. Meanwhile, when the distance between the atoms is slightly increased, there is a reduction in the electron-electron repulsion, leading to a parallel alignment or positive exchange interaction, i.e. ferromagnetic ordering [27].

The indirect exchange interaction involves atoms having relatively (arbitrary) long distance between the electrons. Depending on the relative distance between the electrons, the observed magnetic ordering can either be ferromagnetic or antiferromagnetic. Super-exchange interactions involve ions with extreme long distances and can easily interact through a nonmagnetic material. An instance is the case of coupled metal cations separated by diatomic anions [29]. In general terms, the electron undergoes two types of motion when rotating around the nucleus of an atom, which includes orbital and spin moments. Circulating current is associated with orbital motion and the magnetic

moment which can be expressed [29] as:

$$|\mu_{orbit}| = \pi r^2 \frac{ev}{2\pi rc} = \frac{evr}{2c}, \tag{2.11}$$

where $\frac{e}{c}$ (emu) is the electron charge, v and r represents the Bohr atomic radius and electron velocity, respectively. Assuming the orbital momentum is in a quantized state, the equation can be rewritten as:

$$\mu_{orbit} = \frac{ehn}{4\pi cm}. \tag{2.12}$$

Here, h is the Planck's constant, n which is an integer represents the level of quantization and m is the mass of the electron. Considering the spin of the electron, the Bohr magneton, μ_B, can be evaluated [30] as:

$$\mu_{spin} = \mu_B = \frac{eh}{4\pi cm} = 0.927 \times 10^{-20}\,\text{emu}. \tag{2.13}$$

Two important parameters that are worth mentioning are magnetization and susceptibility. Magnetization is the ratio of magnetic moment (μ) to volume (V) and can be expressed [30] as:

$$M = \frac{\mu}{V}. \tag{2.14}$$

Susceptibility of a material can be expressed as the ratio of its magnetization to the applied magnetic field. Susceptibility measures the degree of response of a material to magnetization when a field is applied [30] and it can be expressed as:

$$\chi = \frac{dM}{dH} \approxeq \frac{M}{H}. \tag{2.15}$$

Since density is the ratio of mass to volume, susceptibility can be rewritten in terms of mass susceptibility such that:

$$\chi_m = \frac{\chi}{\rho}. \tag{2.16}$$

Depending on the obtained value of susceptibility for various materials, the category of magnetization can classified. For instance, a negative susceptibility indicates a diamagnetic material. A positive susceptibility in the order of $\chi \geq 10^{-3}(\text{emu/cm}^3\text{Oe})$ indicates a paramagnetic material and a positive susceptibilty of the order $\approx 10^5$ indicates a ferromagnetic material [30].

2.1.6 Magnetic mechanism and theoretical formalism

The magnetic behaviour of materials occurs through magnetic torques exerted on the magnetic moment vectors from the electron spins. These spins stem from magnetic moments of the individual charged particles. The following Section describes the categories of magnetism and brief theoretical overviews.

Diamagnetism With the introduction of an external field to a material of diamagnetic nature, the orbital motion of the electrons are altered. The effect of the applied field reduces the effective current of the electron orbit. The reduced effective current leads to an opposition between the magnetic moment and the applied field, thereby producing a net magnetic moment [30].

Considering the case of an electric circuit being by a magnetic flux, there is a flow of current in the opposite direction to oppose the change of flux. These assumptions are based on the theory of Langevin [31].

From the Langevin theorem, it is assumed that each atom in the material possesses the precession motion around the applied field with equal current loop. At any point

in the loop, the current can be expressed as:

$$I = \frac{q}{T} = \frac{-e}{T} = \frac{-ew}{2\pi}, \tag{2.17}$$

where $w = \dfrac{2\pi}{Y}$ is Larmor frequency and Y the intensity of the magnetization. Assuming the population of atomic interactions is represented by N then the intensity (Y) of the magnetization can be evaluated as:

$$Y = N\mu_m = \frac{-Ne^2B}{6m} \left\langle r_0^2 \right\rangle, \tag{2.18}$$

where r_0 is the radial distance, N is the number of atomic interactions, m is the mass of the atoms and e is the atomic charge. Substituting the value of $B = \mu_0 H$ and $\alpha = 1/H$, then the moment can be written as:

$$\alpha = \frac{-Ne^2\mu_0}{6m}. \tag{2.19}$$

The implication of equation 2.19 is the reason behind the negativity of the magnetic susceptibilty. Based on the absence of the temperature parameter, the magnetization is temperature independent [30].

Paramagnetism The theoretical framework of paramagnetism can be seen from two perspective (classical and quantum aspects). The classical approach focuses on the Langevin theory. The energy of the magnetic moment when a magnetic field is applied is:

$$E = -\boldsymbol{\mu} \cdot \mathbf{H} = \mu H \cos\theta, \tag{2.20}$$

where θ depicts the angle between the magnetic moment and the applied field. Considering Boltzmann statistics, the probability of finding a magnetic moment at an angle θ can be resolved as:

$$e^{-E/k_BT} = e^{\mathbf{m}\cdot\mathbf{H}/k_BT} = e^{mH\cos\theta/k_BT}, \tag{2.21}$$

where $\mathbf{m}$, $\mathbf{H}$ and k_B is the magnetic moment, the applied magnetic field and Boltzmann constant, respectively [32]. The population of magnetic moments present between θ and $\theta + d\theta$ in terms of the applied field can be established. The number of magnetic moments indicates integral spin density of a magnetic material [32]. Consider the sphere shown in Figure 2.1.6 with a fractional surface area of $dA = 2\pi r^2 \sin\theta d\theta$, the probability $p_r(\theta)$ of the atomic moments can then be calculated as:

$$p_r(\theta) = \frac{e^{mH\cos\theta/k_BT}\sin\theta d\theta}{\int_0^\theta e^{mH\cos\theta/k_BT}\sin\theta d\theta}. \tag{2.22}$$

Here, the parameters under the integral represents the total population of the atomic magnetic moments and the $2\pi r^2$ terms becomes negligible as θ increases [32]. The Langevin function can be written as:

$$\mathbf{M} = Nm\mathbf{L}(\alpha), \tag{2.23}$$

where N is the number of atomic interactions, $\mathbf{L}(\alpha) = \coth(\alpha) - 1/\alpha$ and $\alpha = mH/k_BT$ represents the Langevin function [32]. For a large value of α, which is due to large applied field or low temperature tending toward 0 K, $\mathbf{M}$ tends to Nm and the magnetic spins will completely align in the direction of the field [32].

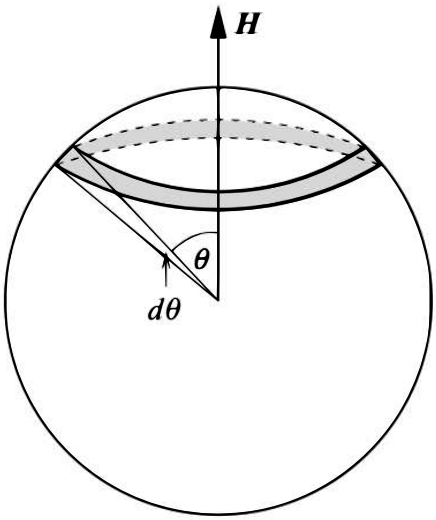

Figure 2.1.6: The sphere showing the fraction of magnetic moments between angle θ and $\theta + d\theta$. Image adapted from Nicola [32].

If the Langevin function is expanded by Taylor series such that

$$L(\alpha) = \frac{\alpha}{3} - \frac{\alpha^3}{45} + \frac{2\alpha^5}{945} - ...., \tag{2.24}$$

higher terms becomes negligible due to practical fields and $\mathbf{M}$ can be rewritten as:

$$\mathbf{M} = \frac{Nm\alpha}{3} = \frac{Nm^2}{3k_B}\frac{\mathbf{H}}{T}. \tag{2.25}$$

Equation 2.25 implies the direct relationship of the magnetization and the applied field but inversely related to temperature [32].

Considering quantum approach, the total magnetization can be expressed as:

$$M = NgJ\mu_B\left[\frac{2J+1}{2J}\coth\left(\frac{2J+1}{2J}\alpha\right) - \frac{1}{2J}\coth\left(\frac{\alpha}{2J}\right)\right] = NgJ\mu_B B_J(\alpha). \tag{2.26}$$

Here, B_J depicts the Brillouin function which is related to the Langevin with the constraint that $J \to \infty$ [30, 32].

If the Brillouin function is expanded in terms of Taylor series i.e

$$B_J(\alpha) = \frac{J+1}{3J}\alpha - \frac{[(J+1)^2 + J^2](J+1)}{90J^3}\alpha^3 + ..., \tag{2.27}$$

where $\alpha = Jg\mu_B H/k_B T$ and J is the quantum number. For simplicity, higher terms can be ignored so that the quantum mechanical approach in terms of susceptibility becomes:

$$\chi = \frac{Ng^2 J(J+1)\mu_B^2}{3k_B T} = \frac{C}{T}. \tag{2.28}$$

Equation 2.28 is called Curie law, where g and C are the Lande g-factor and the Curie constant, respectively. The Curie equation is given as:

$$C = \frac{Ng^2 J(J+1)\mu_B^2}{k_B}. \tag{2.29}$$

Equation 2.28 was later modified by Weiss in 1907 where intrinsic magnetic field parameter was included. The magnetic field accounts for fields that is generated from the material. The field H_m is given as:

$$H_m = \gamma M, \tag{2.30}$$

where γ represents proportionality constant because of the direct relationship between the molecular field and the magnetic field M [30]. If $H = H_{Total} - \gamma M$ is included in the susceptibility equation. The modified expression (Curie-Weiss) can then be rewritten as:

$$\chi = \frac{C}{T - T_C}. \tag{2.31}$$

Here T_C is the critical temperature which is the boundary between paramagnetic and ferromagnetic system.

Ferromagnetism The Weiss theory proposed that ferromagnetism was attributed to the intrinsic force interaction with the material, however, attention was not given to the origin of the intrinsic field. In reality, spontaneous magnetization occurs below and above the critical temperature where the applied field is required to maintain magnetization [30, 32].

The details of the origin of the molecular field were later put forward by Heisenberg in 1928. In his theory, there is an interaction of the electrons from two protons by Coulomb electrostatic forces [33, 34]. Considering the Pauli exclusion principle acting on the electrons, an exchange integral can be used to describe the interaction process. For the two electrons, the exchange integral can be written [32] as:

$$J_{12} = \int \phi_a^*(1)\phi_b^*(2)H_{12}\phi_a(2)\phi_b(1)d\tau_1 d\tau_2, \tag{2.32}$$

where, $\phi(1)$ and $\phi(2)$ are the wave functions describing electrons 1 and 2 that are centered around the two nuclei a and b. H_{12} is the Hamiltonian for Coulomb interactions of the electrons. Considering the Heisenberg rigid model [35], there is the possibility of interaction of neighboring spins given by $\mathbf{S_1}$ and $\mathbf{S_2}$. The spins are assumed to be localized within close proximity, which allows for direct exchange interactions. The exchange energy responsible for the interactions can be evaluated as:

$$E_{int} = -J_{12}\mathbf{S_1} \cdot \mathbf{S_2}. \tag{2.33}$$

In accordance with theory, when $J > 0$, the lowest energy state can be attained with the spins aligned in parallel position and a ferromagnetic state is obtained, whereas when $J < 0$, an antiparallel alignment is obtained, which corresponds to antiferromagnetic

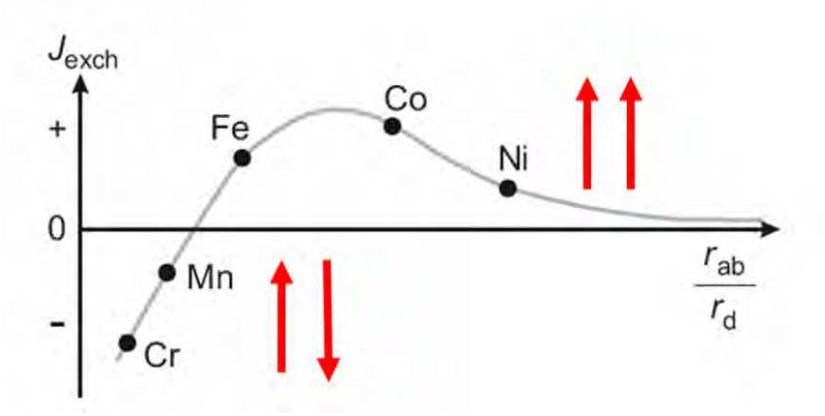

Figure 2.1.7: The Bethe-Slature curve showing the relationship between the exchange integral J and varying inter-atomic spacing. The resulting position for different magnetic materials are shown. Adapted from Moran et al. [36].

state [21, 30, 32].

The Bethe-Slater curve shown in Figure 2.1.7 depicts the relationship between inter-exchange energy with varying inter-atomic spacing [36]. Popular magnetic materials are also shown in the curve as examples of ferromagnetic or antiferromagnetic materials. The Stoner and Slater models imply that mobile electrons from the partially filled bands interact and eventually leads to a collective ferromagnetic behaviour [37]. As discussed earlier in Section 2.1, the oxidation of graphite to produce graphene oxide, which is a proxy of graphene leads to nonmagnetism. Magnetism in graphene oxide, which is the material of interest in the current study mainly arises due to certain factors. The factors include the introduction of edges and point defects, chemical reduction of GO and functionalization of GO with surfactants (metals, polymers) that can induce magnetism etc.

Of particular interest to this study is the chemical functionalization of GO with the intention of inducing magnetism. The next Section describes the techniques used in the synthesis and functionalization of GO.

2.1.7 Synthesis and functionalization of Graphene Oxide

The synthesis of GO is done through the exfoliation of graphite crystals. Graphite comprises carbon atoms in 3-dimension with multiple layers of graphene sheets. The graphite material can be oxidized with relevant oxidizing agent to form graphite oxide [22]. The use of oxygenated group materials for oxidizing graphite leads to the attachment of oxygenated related bonds in the edge of the graphite structure [6]. The oxidation process causes an expansion in the layer separation, thereby making graphite oxide hydrophilic [6].

The hydrophilic property of graphite oxide enables easy exfoliation in water using sonification technique [38]. The result of the exfoliation gives single-layer or few layers of graphene with the oxygen functional groups at the edge and basal planes (GO). The first method for synthesizing graphite oxide was proposed by Brodie [39]. The procedure in Brodie's method mixing 1 : 3 proportion of graphite and potassium chlorate ($KClO_3$) and reacting with fuming nitric acid (HNO_3) for about 4 days at 60°C. Brodie's method was improved in 1938 by Staundenmaier, where the fuming nitric acid was replaced by sulfuric acid [40]. The procedure was performed using multiple aliquots of $KClO_3$. The reaction was considered hazardous since it resulted in explosions. Staudenmaier later invented a new technique that was less hazardous and easier to implement. However, it became obsolete as new techniques became available [41].

Hummer and Offeman [41] introduced a technique, which involves oxidizing graphite by using potassium permanganate in presence of sulfuric acid. In the Hummers method, 100 g of graphite powder, 2.3 liters, 50 g of sodium nitrate ($NaNO_3$) and 300 g of potassium permanganate $KMnO_4$ were used for the synthesis procedure of GO. Hummer's method is a modified Staundenmaier where $KMnO_4$ was used as a substitute to $KClO_3$ to eradicate the explosive tendencies of the chemical reaction [40]. Furthermore, $KClO_3$ was used to substitute the fuming HNO_3 to eradicate the foggy acidic fumes that were generated after the reaction. The entire reaction procedure lapsed a couple of hours

and superior grade of GO was produced.

Hummer's method is, however, limited due to issues of toxicity. Toxic gases such as NO_2 and N_2O_4 were produced after the reaction and therefore not conducive for health safety. Furthermore, the reaction led to the production of more oxygen content compared with Brodie's method [40, 42] , which makes the method less favourable for GO synthesis. Scientific advancements have led to modification of the Hummers method, which is less toxic [43]. The modified Hummers method has been adopted in the current study. The experimental details are described in the later Section of 4.2.1.

In situations where large amounts of graphene are required especially for industrial purposes, GO can prove to be an adequate alternative. Various methods for GO reduction have been employed such as chemical and heating methods. Some methods include [6] :

- Treatment of GO with hydrazine hydrate whilst maintaining the reduced solution for $\approx$ 24 hours at 100°C.
- Exposition of GO residue to hydrogen plasma for a couple of seconds.
- Annealing of GO in distilled water at desired temperature and heating duration.
- Direct furnace heating of GO residue to extreme temperatures.
- The use of linear sweep voltametry can also enable GO reduction.

In the above-mentioned methods, the hydrazine hydrate reduction method was employed in the current study.

After the reduction of GO has been completed, the resulting mixture can be functionalized to optimize the properties of GO for several application potential. Functionalization can either be covalent or noncovalent [44]. In the case of covalent functionalization, oxygenated group is attached to the surface of GO. The oxygenated group includes the carboxylic group which is attached at the edges and epoxy at the basal plane.

Noncovalent functionalization involves the introduction of noncovalent intermolecular interactions i.e functionalizing GO with organic compounds and polymers [44].
Several attempts have been performed to functionalize GO using the noncovalent approach. One of which is to treat GO with isocyanates [45, 46]. The isocyanates treatment approach reduces the hydrophilic property of GO, thereby leading to an amine and carbamate ester formation. The origin of the ester formation is mainly from the carboxyl and epoxyl functional groups [6]. An advantage of the isocyanate treatment of GO is the formation of stable dispersion in polar aprotic solvents, which can be easily exfoliated to produce single layer graphene sheets. Furthermore, the dispersion can produce a homogeneous mixture of GO with the polymer matrix, which eventually gives high-quality graphene-polymer composites [6].

Bibliography

[1] Daniel R Dreyer, Sungjin Park, Christopher W Bielawski, and Rodney S Ruoff. The chemistry of graphene oxide. *Chemical Society Reviews*, 39(1):228–240, 2010.

[2] Sibel Korkut, Joseph D Roy-Mayhew, Daniel M Dabbs, David L Milius, and Ilhan A Aksay. High surface area tapes produced with functionalized graphene. *ACS Nano*, 5(6):5214–5222, 2011.

[3] Shuai Wang, Priscilla Kailian Ang, Ziqian Wang, Ai Ling Lena Tang, John TL Thong, and Kian Ping Loh. High mobility, printable, and solution-processed graphene electronics. *Nano Letters*, 10(1):92–98, 2009.

[4] Alexander A Balandin, Suchismita Ghosh, Wenzhong Bao, Irene Calizo, Desalegne Teweldebrhan, Feng Miao, and Chun Ning Lau. Superior thermal conductivity of single-layer graphene. *Nano Letters*, 8(3):902–907, 2008.

[5] LA Falkovsky. Optical properties of graphene. In *Journal of Physics: Conference Series*, volume 129, page 012004. IOP Publishing, 2008.

[6] Sekhar Ray. *Applications of Graphene and Graphene-Oxide Based Nanomaterials*. William Andrew, 2015.

[7] Jijun Zhao, Lizhao Liu, and Fen Li. *Graphene Oxide: Physics and Applications*. Springer, 2015.

[8] Yanwu Zhu, Shanthi Murali, Weiwei Cai, Xuesong Li, Ji Won Suk, Jeffrey R Potts, and Rodney S Ruoff. Graphene and graphene oxide: synthesis, properties, and applications. *Advanced Materials*, 22(35):3906–3924, 2010.

[9] K Gopalakrishnan, A Govindaraj, and CNR Rao. Extraordinary supercapacitor

performance of heavily nitrogenated graphene oxide obtained by microwave synthesis. *Journal of Materials Chemistry A*, 1(26):7563–7565, 2013.

[10] H Tang, J Zhang, YJ Zhang, QQ Xiong, YY Tong, Y Li, XL Wang, CD Gu, and JP Tu. Porous reduced graphene oxide sheet wrapped silicon composite fabricated by steam etching for lithium-ion battery application. *Journal of Power Sources*, 286:431–437, 2015.

[11] Kirill I Bolotin, KJ Sikes, Zd Jiang, M Klima, G Fudenberg, J Hone, Ph Kim, and HL Stormer. Ultrahigh electron mobility in suspended graphene. *Solid State Communications*, 146(9-10):351–355, 2008.

[12] Samuel David Littlejohn. *Electrical Properties of Graphite Nanoparticles in Silicone: Flexible Oscillators and Electromechanical Sensing*, volume 1. Springer Science & Business Media, 2013.

[13] Bitao Pan, Jun Xiao, Jiling Li, Pu Liu, Chengxin Wang, and Guowei Yang. Carbyne with finite length: The one-dimensional sp carbon. *Science Advances*, 1(9):e1500857, 2015.

[14] Alexander Gruneis and Denis V Vyalikh. Tunable hybridization between electronic states of graphene and a metal surface. *Physical Review B*, 77(19):193401, 2008.

[15] Mahmood Aliofkhazraei, William I Milne, Cengiz S Ozkan, Stanislaw Mitura, Juana L Gervasoni, and Nasar Ali. *Graphene Science Handbook: Electrical and Optical Properties*, volume 1. CRC press, 2016.

[16] AH Castro Neto, Francisco Guinea, Nuno MR Peres, Kostya S Novoselov, and Andre K Geim. The electronic properties of graphene. *Reviews of Modern Physics*, 81(1):109, 2009.

[17] Bart Partoens and FM Peeters. From graphene to graphite: Electronic structure around the k point. *Physical Review B*, 74(7):075404, 2006.

[18] Sivabrata Sahu and GC Rout. Band gap opening in graphene: a short theoretical study. *International Nano Letters*, 7(2):81–89, 2017.

[19] Patrik Recher and Bjorn Trauzettel. A defect controls transport in graphene. *Physics*, 4:25, 2011.

[20] KS Novoselov, SV Morozov, TMG Mohinddin, LA Ponomarenko, DC Elias, R Yang, II Barbolina, P Blake, TJ Booth, D Jiang, et al. Electronic properties of graphene. *Physica Status Solidi (B)*, 244(11):4106–4111, 2007.

[21] Margherita Sepioni. *Magnetic Properties of Graphene*. PhD thesis, University of Manchester, 2013.

[22] Michio Inagaki and Feiyu Kang. *Materials Science and Engineering of Carbon: Fundamentals*. Butterworth-Heinemann, 2014.

[23] Daniel R Dreyer, Alexander D Todd, and Christopher W Bielawski. Harnessing the chemistry of graphene oxide. *Chemical Society Reviews*, 43(15):5288–5301, 2014.

[24] Wei Gao. The chemistry of graphene oxide. In *Graphene oxide*, pages 61–95. Springer, 2015.

[25] Anton Lerf, Heyong He, Michael Forster, and Jacek Klinowski. Structure of graphite oxide revisited. *The Journal of Physical Chemistry B*, 102(23):4477–4482, 1998.

[26] Vaishali Gupta, Neeraj Sharma, Udai Singh, Mohd Arif, and Arun Singh. Higher oxidation level in graphene oxide. *Optik-International Journal For Light and Electron Optics*, 143:115–124, 2017.

[27] Stephen Blundell. Magnetism in condensed matter, 2003.

[28] Philip W Anderson. Theory of magnetic exchange interactions:exchange in insulators and semiconductors. In *Solid State Physics*, volume 14, pages 99–214. Elsevier, 1963.

[29] Alessandro Bencini and Dante Gatteschi. Exchange and superexchange. In *Electron Paramagnetic Resonance of Exchange Coupled Systems*, pages 1–19. Springer, 1990.

[30] Bernard Dennis Cullity and Chad D Graham. *Introduction to Magnetic Materials*. John Wiley & Sons, 2011.

[31] JA Pople. Molecular-orbital theory of diamagnetism. ii. calculation of pascal constants for some noncyclic molecules. *The Journal of Chemical Physics*, 37(1):60–66, 1962.

[32] A Spaldin Nicola. Magnetic materials: Fundamentals and applications, 2003.

[33] John H Van Vleck. A survey of the theory of ferromagnetism. *Reviews of Modern Physics*, 17(1):27, 1945.

[34] Elliott Lieb and Daniel Mattis. Ttheory of ferromagnetism and the ordering of electronic energy levels. In *Inequalities*, pages 33–41. Springer, 2002.

[35] J Sak. Critical behavior of compressible magnets. *Physical Review B*, 10(9):3957, 1974.

[36] S Morán, C Ederer, and M Fähnle. Ab initio electron theory for magnetism in fe: Pressure dependence of spin-wave energies, exchange parameters, and curie temperature. *Physical Review B*, 67(1):012407, 2003.

[37] Edmund Clifton Stoner et al. Collective electron ferronmagnetism. *Proc. R. Soc. Lond. A*, 165(922):372–414, 1938.

[38] DDL Chung. Exfoliation of graphite. *Journal of materials science*, 22(12):4190–4198, 1987.

[39] Benjamin Collins Brodie. Xiii. on the atomic weight of graphite. *Philosophical Transactions of the Royal Society of London*, 149:249–259, 1859.

[40] NI Zaaba, KL Foo, U Hashim, SJ Tan, Wei-Wen Liu, and CH Voon. Synthesis of graphene oxide using modified hummers method: solvent influence. *Procedia Engineering*, 184:469–477, 2017.

[41] William S Hummers Jr and Richard E Offeman. Preparation of graphitic oxide. *Journal of the American Chemical Society*, 80(6):1339–1339, 1958.

[42] Ji Chen, Bowen Yao, Chun Li, and Gaoquan Shi. An improved hummers method for eco-friendly synthesis of graphene oxide. *Carbon*, 64:225–229, 2013.

[43] Leila Shahriary and Anjali A Athawale. Graphene oxide synthesized by using modified hummers approach. *Int. J. Renew. Energy Environ. Eng*, 2(01):58–63, 2014.

[44] Vasilios Georgakilas, Michal Otyepka, Athanasios B Bourlinos, Vimlesh Chandra, Namdong Kim, K Christian Kemp, Pavel Hobza, Radek Zboril, and Kwang S Kim. Functionalization of graphene: covalent and non-covalent approaches, derivatives and applications. *Chemical Reviews*, 112(11):6156–6214, 2012.

[45] Sasha Stankovich, Dmitriy A Dikin, Geoffrey HB Dommett, Kevin M Kohlhaas, Eric J Zimney, Eric A Stach, Richard D Piner, SonBinh T Nguyen, and Rodney S Ruoff. Graphene-based composite materials. *Nature*, 442(7100):282, 2006.

[46] Sasha Stankovich, Richard D Piner, SonBinh T Nguyen, and Rodney S Ruoff. Synthesis and exfoliation of isocyanate-treated graphene oxide nanoplatelets. *Carbon*, 44(15):3342–3347, 2006.

Chapter 3

Experimental techniques

The experimental techniques used in the characterization of the samples in this study are described in this chapter. X-ray diffraction (XRD), scanning electron microscopy (SEM) and transmission electron microscopy (TEM) are for structural and morphology properties. Fourier transform infrared (FTIR) spectroscopy, Raman spectroscopy, X-ray photoelectron spectroscopy (XPS), Ultra-violet photon electron spectroscopy (UPS) and X-ray absorption near edge spectroscopy (XANES) are for electronic characterization of the samples. Current-voltage (I-V) characteristics were used for electrical properties, whereas superconducting quantum interference device (SQUID) was used for (M-H) loop measurements.

3.1 X-ray Diffraction

X-ray diffraction (XRD) technique is based on Bragg's diffraction theory , which involves the bombardment of a target (sample) by X-ray beams. When the X-ray beam interacts with the sample, they are either absorbed or scattered. The result of the bombardment leads to release of electrons from the targeted sample [1].
The working principle of XRD technique is based on bombarding a sample with beams of X-rays , which leads to the emission of diffracted waves. When a set of X-ray bombards a sample, the X-rays are diffracted by set of reflective planes embedded in the atoms (see Figure 3.1.1).

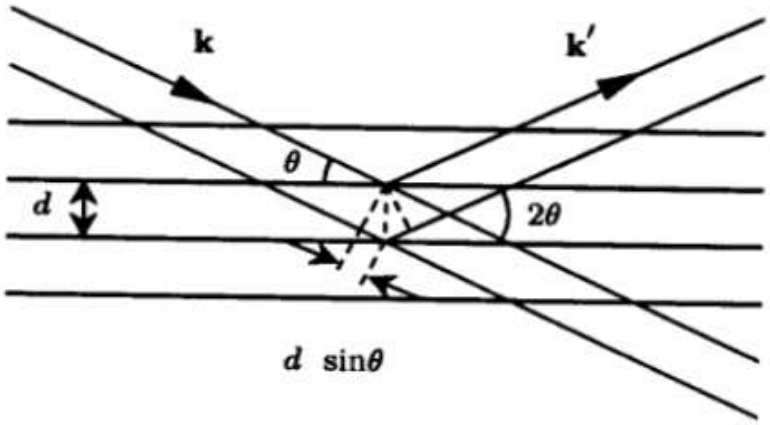

Figure 3.1.1: Bragg's diffraction principle. Only diffractive waves with constructive interferences forms reasonable planes. Adapted from Chalkin [2].

The intensity of the diffracted waves are modulated by constructive or destructive interferences [2]. Considering an infinite set of the reflective plane in a material with sets of atomic particles, only reflections of constructive interference that satisfy the Bragg's equation form a blueprint about a sample. The path difference between the reflected waves is adjacent to the incident X-rays, as indicated in equation 3.1. The adjacent planes are separated by distance d and are assumed to be a multiple of the wavelength of the X-rays [1]. The planar distance can be expressed in terms of the wavelength of the scattered X-ray waves as:

$$2d \sin\theta = m\lambda, \tag{3.1}$$

where m is a positive integer representing the number of planes, λ is the wavelength of the scattered X-rays and θ is the angle between the incident and scattered X-rays [2]. The structural properties of each material are uniquely based on their reflection planes. The reflection planes are represented by Miller indices (hkl), which can be calculated [3] as

$$\sin^2\theta = \frac{\lambda^2}{4a^2}(hkl). \tag{3.2}$$

The parameters in the equation 3.2 are related to equation 3.1 where θ is the diffracting angle from the scattered X-ray waves (angle between the reflected waves), λ is the wavelength of the X-ray source originating from the scattered X-ray waves and a is the lattice parameter associated with the crystal structure of the material.
Amorphous materials or non-stoichiometric material such as GO and glass does not display periodic array with long-range order of reflections [4]. The non-stoichiometric property is the main reason why there are humps for GO materials and related composites [4].

3.2 Scanning electron microscopy

Scanning electron microscopy (SEM) technique generates images and analyzes the sample for morphological arrangement of the particles. The sample can be easily observed, i.e. flakes, nanotubes or nanowires, etc. The principle behind the SEM imaging follows from the interaction of the sample with beams of electrons [5].
The main part of SEM includes electron source, travel medium for electrons, electron detector, the sample chamber and computer display. The complete technical detail description of the components of the SEM equipment can be found in the literature [6, 7]. The components consist of an electron gun, condenser lens, objective lens, deflection coil and detectors, as shown in Figure 3.2.1. In principle, the tungsten filament or field emission gun generates the beam of electrons . The electron beams are accelerated through high voltage where the beam scans the surface of the sample. The working principle schematics is shown in figure 3.2.2. Electrons that are generated at the top of the column travel down the column and pass through different combinations of lenses and aperture to generate a collimated beam of electrons, which targets the surface of a sample. The interaction between the sample and the electron beam is easily controlled by scan coils (shown in Figure 3.2.1) that are above the objective lens. The coils scans the surface of the sample and the signals are generated from the electron-sample inter-

action and captured by a detector [7].

Images are generated when a sample is scanned with electron beams possessing high energy. As the sample interacts with the electrons, three signals are generated, such

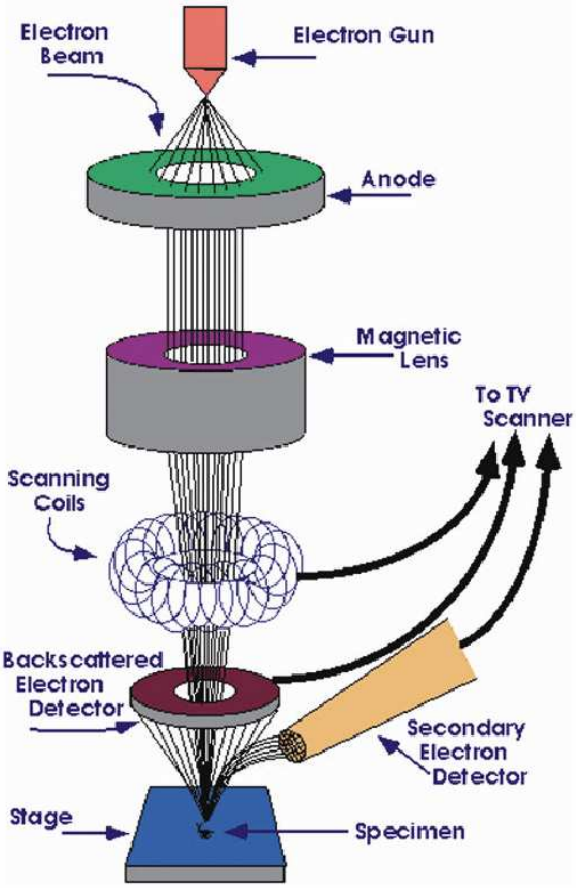

Figure 3.2.1: Schematics showing the component of scanning electron microscope. Image adapted from [6].

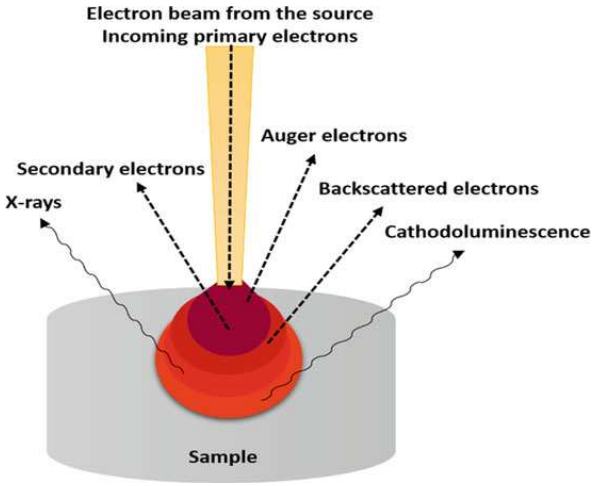

Figure 3.2.2: The working principle of the scanning electron microscope. Image adapted from Sharma [8].

as secondary electrons, back-scattered electrons, and characteristic X-rays. The sets of signals are recorded by the detectors and displayed in the computer aided monitor. Depending on the accelerating voltage and density of the sample, the electron beams penetrate the sample within some few microns. The quality of the generated image depends on the electron spot size and the volume of the interaction of the sample with the electron beam [7].

3.3 Transmission electron microscopy technique

Transmission electron microscopy (TEM) is a versatile technique for probing the internal structure of thin samples. In this technique, an electron gun is used for generating electron beams. When the collimated electron beam hits a targeted sample, it is diffracted according to Bragg's second law [9]. The Fourier transform of the electron wave function and image plane of the TEM setup acts in accordance with Bragg's law [9]. Assuming, a sample is oriented at an exact Bragg reflection with respect to the incident electrons, then the recorded images gives appropriate magnifications [9].
The components of the TEM equipment are shown in Figure 3.3.1. The electron gun generates collimated electron and focuses the electrons on the sample with the aid of a condenser lens. The direct focus of the electron beams is enhanced by magnetic lenses. The column tube of the condenser lens also facilitates the generation of high resolution images by harnessing the vacuum chamber, thereby minimizing the impact of air molecule deflections. Figure 3.3.2 is a block diagram describing the working principle of the TEM technique. When the beam reaches the sample, the electrons are scattered and refocused by aid of the magnetic lens/projector leading to the formation of an image. The image is channeled through a fluorescent screen where a polychromatic image is generated. The scattered electrons depend on the density (thickness of the sample layer) of the sample [10]. For dense samples, fewer electrons reach the screen leading to darker images. The detector produces brighter images when the sample is

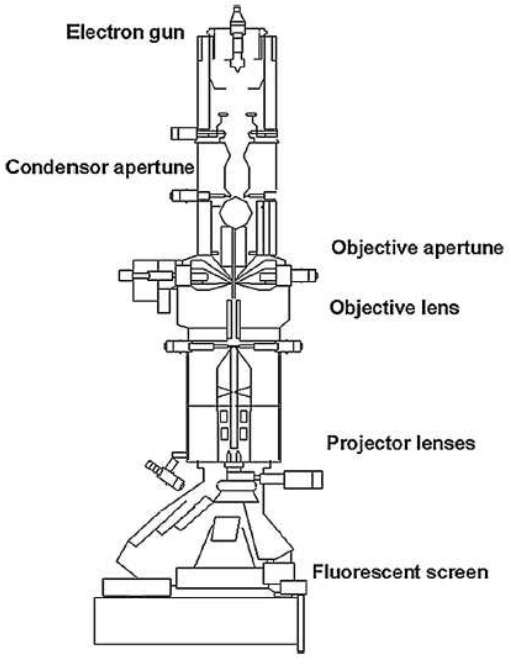

Figure 3.3.1: The component of a typical transmission electron microscopy equipment. Image adapted from Alqaheem and Alomair [10].

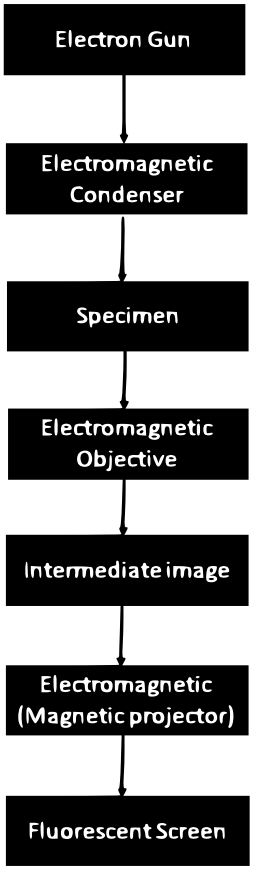

Figure 3.3.2: Block diagram showing the working principle of transmission electron microscopy.

less dense (thinner sample layer) [10].

3.4 Raman spectroscopy

Raman spectroscopy is an invaluable technique that is used in the characterization of the electronic properties of materials [11–13]. A variation in the concentration of an element in a sample can be evaluated using the Raman technique. The analysis and Raman shift in Raman spectra represent a change in concentration, which in some cases depicts the quality of the sample being analyzed. The quality of the sample in some instance can lead to prominent peaks with negligible appearance of background noise in the Raman spectra.

The details of the Raman spectroscopy equipment are shown in Figure 3.4.1 where the main component comprises of a laser, plasma filter, lenses, detectors and a computer processing unit [14]. The working principle of Raman spectroscopy system is shown in figure 3.4.2. The Raman spectroscopy technique involves the scattering of light when

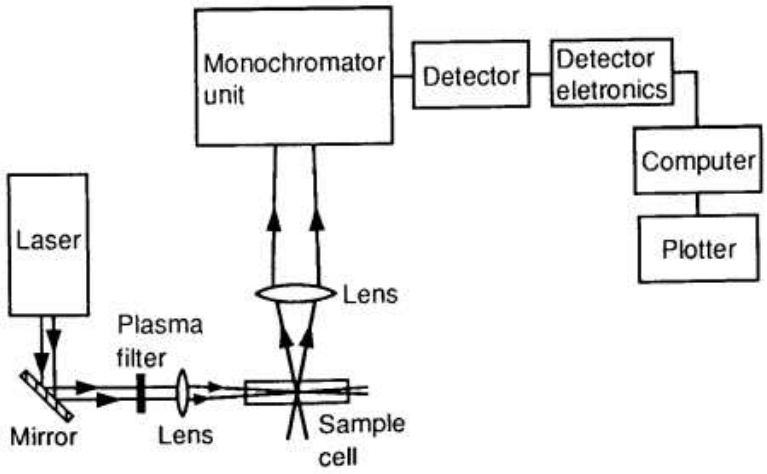

Figure 3.4.1: The schematics of the component of a typical raman spectroscopy. Image adapted from Lewis [14].

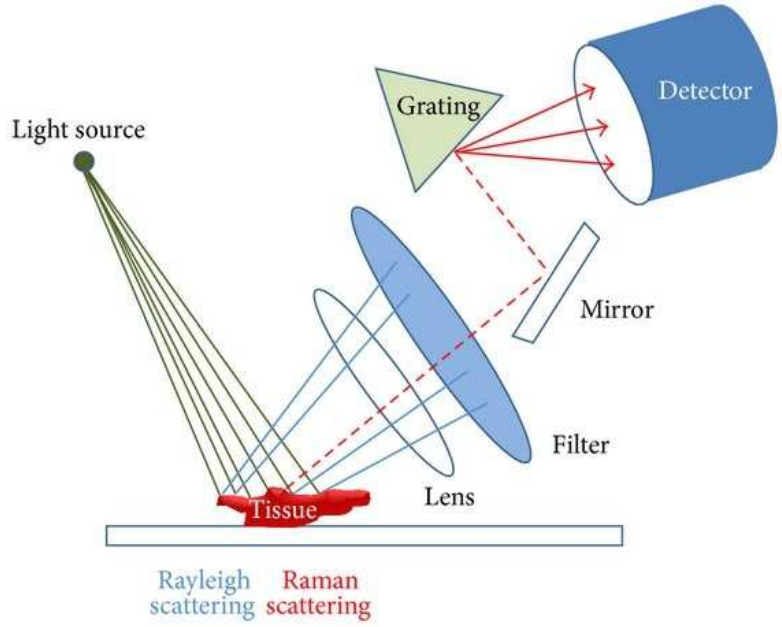

Figure 3.4.2: The schematic showing the working principle of Raman spectroscopy system. Image redrawn from Kim [15].

a sample is illuminated with a high intensity laser light. When a sample is illuminated with a laser of specific wavelength, most of the light is scattered [14]. The scattered light having a wavelength equal to that of the incident laser source is not recorded as they do not give useful information about the sample [14]. This type of scattered light is referred to as Rayleigh scatter. However, the small amount of scattered light waves with wavelengths different from that of the laser source (usually $\approx 0.0000001\%$) are detected and recorded by the detector. These few scattered light are representative of the chemical structure of the sample. These sets of scattering are referred to as Raman scatter [14].

The Raman spectrum consists of peaks indicating the intensity and wavelength positions of the Raman scattered light. Each peak depicts molecular bonding vibrations of the material [16]. Concerning carbon materials, Raman spectra indicate two signature peaks at approximately $1580\,\mathrm{cm}^{-1}$ and approximately $2700\,\mathrm{cm}^{-1}$, which represent G band and 2D bands, respectively [11].

In terms of GO, the Raman spectroscopy technique detects the phonon vibrational behavior, which is influenced by the lattice, the structure of the GO material. The

atomic mass vibration frequency depends on the bond strength of the atoms, which can be high or low [11]. For simplicity, the analogy of two atomic systems (A and B) is used for the description shown in Figure 3.4.3. Based on the lattice structure, electron interactions lead to the formation of different vibrational modes [11]. Considering the electronic structure of graphene shown in Figure 3.4.3 and assuming a two carbon atomic systems in a monolayer graphene structure with unit cell distribution, six unit cells can be observed leading to six phonon dispersion bands. The six phonon dispersion bands can be classified as optic (O) and acoustic (A) phonons [18]. The combination of one optic and acoustic phonon (OA) branch produces an atomic vibration that is perpendicular to the plane of graphene. Atomically perpendicular vibration is assigned to out-of-plane phonon modes, whereas the other four vibration phonon modes (two acoustic and two optic) are assigned to the in-plane mode [18].

The modes can be categorized into longitudinal (L) or transverse (T) based on either parallel or perpendicular alignment with respect to the A-B carbon atomic directions [18]. Figure 3.4.4 shows the six vibrational phonons where the phonons can be classified as longitudinal optic (LO), in-plane transverse optics (iTO), out-of-phase transverse optic (oTO), longitudinal acoustic (LA), in-phase transverse acoustic (iTA) and out-of-phase transverse acoustic (oTA) [18].

The planar modes iTO and LO close to the Γ centre correlate with the vibrations

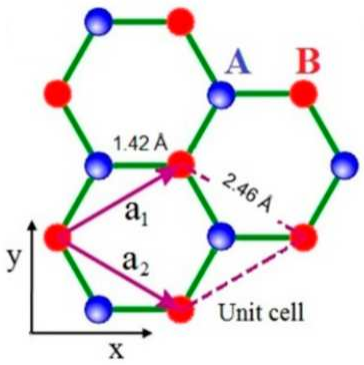

Figure 3.4.3: The electronic structure of graphene showing the six units cells. Image adapted from Yazdi et al. [17].

of the sublattice A interacting with sublattice B. These modes are degenerate and are categorized as two-dimensional E_{2g} phonon class displaying Raman active modes [12, 18]. The assignment of the Raman vibration values in graphene is described in the work of Tuinstra and Koenig [19]. The Raman vibration value assignment of graphene shares similarity with other aromatic hydrocarbons [20].

The higher frequency vibration in the Raman spectra occurs because of sp^2 bond-stretching pairs where the stretching occurs in both rings and chains. Lower frequency vibrations in the Raman spectra are mainly due to sp^2 breathing modes. The main distinction between high and low frequency vibrations is the presence/absence of rings. For instance, the absence of ring gives higher Raman spectra frequency vibrations and vice-versa [20, 21]. Hence, modes at $\approx 1580\,\mathrm{cm}^{-1}$ are ascribed to high mode vibrations E_{2g} Raman phonons (G peak) whereas peak at approximately $1350\,\mathrm{cm}^{-1}$ (D peak) is ascribed to A_{1g} breathing mode [19].

The work of Tuinstra and Koenig [19] on Raman analysis of graphene cannot explicitly explain the other peaks that are observed outside the range of $\approx 1580\,\mathrm{cm}^{-1}$ and $\approx 2700\,\mathrm{cm}^{-1}$. Vidano and Fischbach [22] proposed G' for G peak and D' for D peak. Other peaks were also found by Nemanich and Solin [23] around $\approx 3250\,\mathrm{cm}^{-1}$ and $\approx 2450\,\mathrm{cm}^{-1}$ in pristine graphene and $\approx 2950\,\mathrm{cm}^{-1}$ for defective graphene.

These peaks were ascribed by Vidano and Fischbach as D'' peaks [21–23]. All other peaks appearing between $\approx 2300\,\mathrm{cm}^{-1}$ and $\approx 3250\,\mathrm{cm}^{-1}$ were considered as overtones.

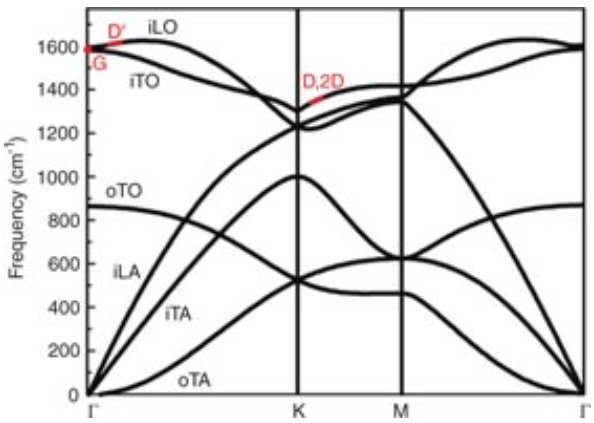

Figure 3.4.4: Phonon dispersion relation of graphene. Image adapted from Lazzeri et al. [18].

.

The peaks around $\approx 2950\,\mathrm{cm}^{-1}$ were regarded as $D + D'$. Situations also arise where small $2D$ peak is visible around $2680\,\mathrm{cm}^{-1}$, which represents an overtone of D peak. The $2D$ peak occurs due to the second-order process from two iTO phonon vibrations from the K point [18].

3.5 Fourier transform infrared spectroscopy

Fourier transform infrared (FTIR) spectroscopy is a versatile technique for analyzing materials. The infrared spectrum serves as a blueprint for different materials due to the uniqueness of the spectra [24]. The absorption peaks which are associated with the vibration frequencies of atomic bonds are related to the constituents of the material [24]. Each material has unique combination of atoms and it is impossible to have two compounds with the same infrared spectrum. Thus, FTIR spectroscopy technique can be used to identity a material when it is cross-checked with a database [24]. FTIR spectroscopy is based on infrared absorption when there is an interaction of infrared radiation with a molecule undergoing dipole change. The absorption occurs at certain wavelengths where infrared photons possess a threshold energy [24].

The threshold energy causes the transitions of energy from low to higher states. The

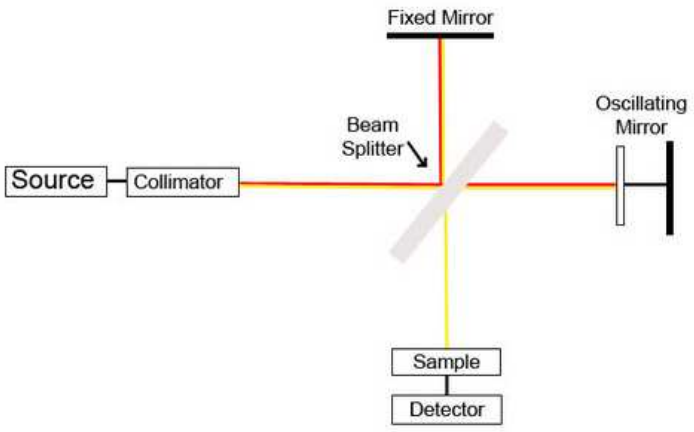

Figure 3.5.1: The schematics of FTIR system showing the working principle. Image adapted from Sharma [8].

energy transition enables the transition of energy levels from the ground state to higher excitation state [24]. The spectrum generated during the transition can be analyzed for structural information which is related to the sample. The structural information is based on a change of dipole moments and energy-level transition. This dipole change and energy transition lead to absorption peaks [24].

The number of peaks recorded is mainly due to the amount of vibrational freedom of the molecules in the sample [16, 24]. For graphene related material such as GO, the peak at the range $3320 - 3430\,\mathrm{cm}^{-1}$ are allocated to hydroxyl group (C-OH), $\approx 1620\,\mathrm{cm}^{-1}$ - sp^2 C=C bond vibrations and $1050\,\mathrm{cm}^{-1}$ is ascribed to alkoxy C−O vibrations [25, 26].

3.6 X-ray photoelectron spectroscopy

The process of XPS follows from the concept of photoelectric effect which involves illuminating the surface of a sample with photons of precise energy as shown in Figure 3.6.1. XPS is a quantity-based technique that relies on the number of emitted electrons from the surface of the sample [27, 28]. The recorded data are represented in the form of spectra having varied binding energies.

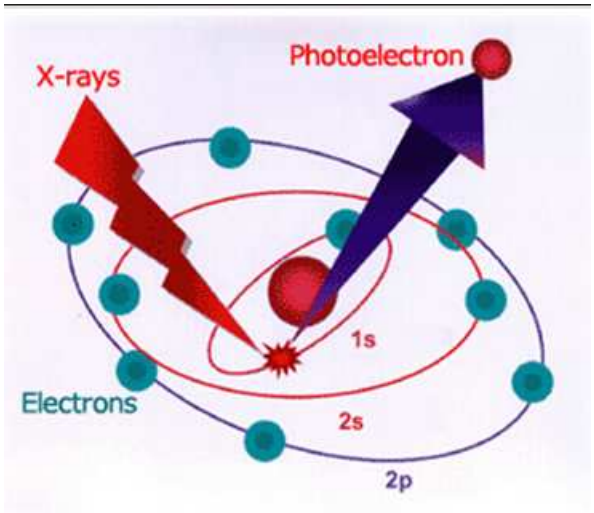

Figure 3.6.1: Schematic representing the basic principle of XPS characterization where an electron is emitted when irradiated with a photon source. Image adapted from Sharma [8].

Attention is drawn to the fact that the totality of peaks emanating from XPS data does not result from direct photon-electron interaction. Some of the observed peaks are attributed to the Auger effect, which are due to the decay of electrons possessing more energy. The electrons tend to fill the hole vacancy created by the X-ray photons because of the emission of the electrons [29, 30]. Other sources of recorded peaks may be due to the background signal originating from resonant scattering of electrons from the sample surface [31].

The quantification of concentrations of elements in a sample relies on the electron counts that are emitted from a sample surface when irradiated by X-rays. The recorded spectrum with varied energies consists of contributions from background (sample and substrate) and resonant peak characteristics of the bound states on the electrons in the atom surface [28]. The XPS recorded peak intensities depict the amount of material (concentrations) deposited on the surface, whereas the peak position describes the elemental and chemical composition of the material [28]. Furthermore, changes in the number of chemical bonds are indicated by the peak shape (peak splitting and broadening) [28].

A drawback of the XPS technique is the inability of the detector to capture all the ejected electrons since the emitted electrons depend on the kinetic energy, which invariably depends on the accelerating voltage of the photon source. However, the reliable technique of comparing samples is by atomic percentage quantification, which is depicted by the ratio of the electron intensity to the total intensity of the entire system [28].

Each element is analyzed based on its electronic state that is available for excitation by the X-ray photons. Figure 3.6.2 shows the energy difference between the initial and final states of the core states. When both initial and final states are well defined, a single peak is observed in the spectrum. However, the peak is not observed when there is no distinction between the initial and final core states [28].

A conventional electronic state consists of electrons paired with orbital and spin angular momentum. The initial state for the electronic system for the electronic system

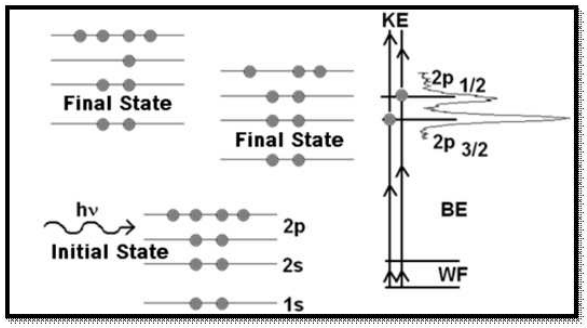

Figure 3.6.2: The electronic energy levels with change of energy states. Image adapted from Sharma [8].

creates a base energy level for a transition. When an electron is emitted from the initial state through the absorption of a photon, the electron emerges with kinetic energy of the final state. The final state includes electronic subshell with unpaired electrons [28]. The electronic state levels in XPS depend on the nlj nomenclature, where n is the principal quantum number, l is the angular momentum quantum number and j represents the combined spin (s) and orbital angular momentum ($j = l + s$). Except for s level orbitals, other orbital levels show spin orbit (SO) splitting tendencies. SO splitting refers to the orbital levels producing doublets of different binding energies [32]. Doublet peak intensities occur in the ratio $2j_1 + 1 : 2j_2 + 1$. Thus, p orbital doublet peaks are assigned j quantum numbers $\frac{1}{2}$ and $\frac{3}{2}$, which invariably give relative intensities of the ratio 1 : 2 [28]..

In summary, XPS is invaluable in probing the sp^2 and sp^3 components of the core state of a sample. The intensity of the binding energy bears a direct relationship to the sp^2, sp^3 clusters, and the ionization cross-section [33].

3.7 Ultraviolet photoelectron spectroscopy

Ultraviolet photoemission spectroscopy (UPS) technique shares a similar working principle with the XPS technique. It involves the emission of electrons from an occupied orbital when illuminated with a photon source. With reference to Koopmans' theory,

ionization potential, I_j, varies with orbital energy E_j [34] and is expressed as

$$I_i = -E_j. \tag{3.3}$$

Information about a change in the features of the molecular orbital energy with concentration can be related using equation 3.3. Additionally, the features indicate the type of band and molecular geometry dynamic due to the electron emitted from the occupied orbital. Molecular geometry dynamics provides information on the bonding properties, whether they are anti-bonding or non-bonding [34].

The UPS technique consists of two helium photon excitation energy sources, which include He I (21.2 eV) and He II (40.8 eV) whereas XPS consist of monochromatic Al Kα photon source with excitation energy of ≈ 1486 eV. These energies have huge importance in the penetration depth of the material. UPS technique provides information on the valence band, which is inaccessible by XPS technique [34].

Another significance of UPS is the resolution. XPS has a resolution ranging from 0.3 eV to 0.7 ev whereas UPS can probe up to 0.01 eV. The high resolution of UPS can reach compositions that cannot be accessed by XPS. The obtained spectra from UPS can be easily assigned based on the available orbital state in a material. For a typical graphene material, the orbital states are in the range of $3 - 15$ eV [35]. For instance, the ranges $3-4$ eV are assigned to $2p-\pi$, $5-7$ eV are assigned to $2p-(\sigma+\pi)$, $8-11$ eV are assigned to $2p-\sigma$ and $13-15$ eV are assigned to $2s-\sigma$ state [35].

3.8 X-ray absorption near edge spectroscopy

X-ray absorption near edge spectroscopy (XANES) technique is one of the most versatile techniques for characterizing materials. The information obtained from XANES measurements can give the degree of bond hybridization in a mixed sp^2/sp^3 bonded carbon configuration [36].

The XANES spectroscopy technology is based on the principle of Beer's law, which indicates the direct relationship between absorbance and the thickness or path length of a material [37]. The XANES technique measures the exponential decay of photon beams with specific energy sources. X-ray absorption depends on the photon energy source and can be increased arbitrarily. The increase in absorption of atoms after irradiation creates an edge, which is attributed to the atomic number of the absorbing atoms. The energy of the photon beam is measured as it passes through the sample [38].

Consider a material with a homogeneous-isotropic property, the intensity of the transmitted beam through the material can be written as:

$$I = I_0 e^{-\mu D}, \tag{3.4}$$

where I_0 represents the intensity of the incident photon. Equation 3.4 is analogous to the Beer-Lambert law given as:

$$\ln(\frac{I_0}{I}) = \mu D, \tag{3.5}$$

where μ and D are the total linear absorption coefficient and concentration of the components in the sample, respectively. The value of μ for a solid with crystalline symmetry has absorption cross-section σ_i, where σ_i is related to n elements and unit cell. The value of μ can be evaluated using:

$$\mu = \frac{1}{V} \sum_{i=1}^{n} \sigma_i, \tag{3.6}$$

where V is the volume of the unit cell. The magnitude of the absorption cross-section is in the order of $1\,\text{Mbarn} = 10^{-18}\,\text{cm}^2$ [38].

Graphene and graphene oxide (GO) related materials have a C K edge spectrum de-

picting different boundaries with precise resonance energies. GO has an additional O K edge spectrum that gives the bonding between carbon and oxygen functional groups present in GO configuration [39]. Depending on the functionalizing agent, other edge spectra can be observed.

The typical C K edge spectra comprises of π^* and σ^* resonance boundary, which is prominent at approximately $285 \pm 1\,\text{eV}$ and $291 \pm 1\,\text{eV}$ peak positions, respectively. These π^* and σ^* are ascribed to $1s \rightarrow \pi^*$ and $1s \rightarrow \sigma^*$ transitions as per graphitic carbon atomic system [39–41].

Another mathematical quantity that is significant to the analysis of XANES spectra is the Gaussian distribution function. The Gaussian distribution function is an invaluable tool that is used to extrapolate parameters of interest from a given spectra. Due to the symmetric feature of the Gaussian function, it can be easily fitted with a curve to extrapolate relevant parameters [42].

The Gaussian function is given as:

$$f(x) = \frac{1}{\sigma\sqrt{2\pi}} e^{-\frac{1}{2}\left(\frac{x-\mu}{\sigma}\right)^2}, \tag{3.7}$$

where x is any arbitrary variable, μ is the mean of the set of the variables and σ is the standard deviation. The Gaussian function can be rewritten as:

$$f(x) = a e^{-\frac{1}{2}\left[(x-b)/c\right]^2}, \tag{3.8}$$

where a determines the height of the peak, b represents the peak position and c determines the width of the peak [42].

3.9 Current-Voltage characterization

Current-Voltage (I-V) characterization technique is used to study the electrical conductivity of materials. The I-V measurement indicates the relationship between the applied voltage on a materials and the corresponding current. The corresponding I-V characteristics will be shown in the first and third quadrants, respectively (Figure 3.9.1). Therefore, the relationship between current and voltage is considered ohmic and linear with a constant slope of $1/R$ (not for all materials/devices) [43].

The relationship is nonlinear in the case of semiconductor materials as shown in Figure 3.9.2. When a semiconductor is forward biased (the anode terminal is positive with respect to the cathode terminal), a positive current flows through the material as indicated in the right side of the quadrant of Figure 3.9.2. The current increases steadily till the forward voltage exceeds the internal barrier voltage of the material. The forward current increases steadily with respect to the voltage giving a non-linear

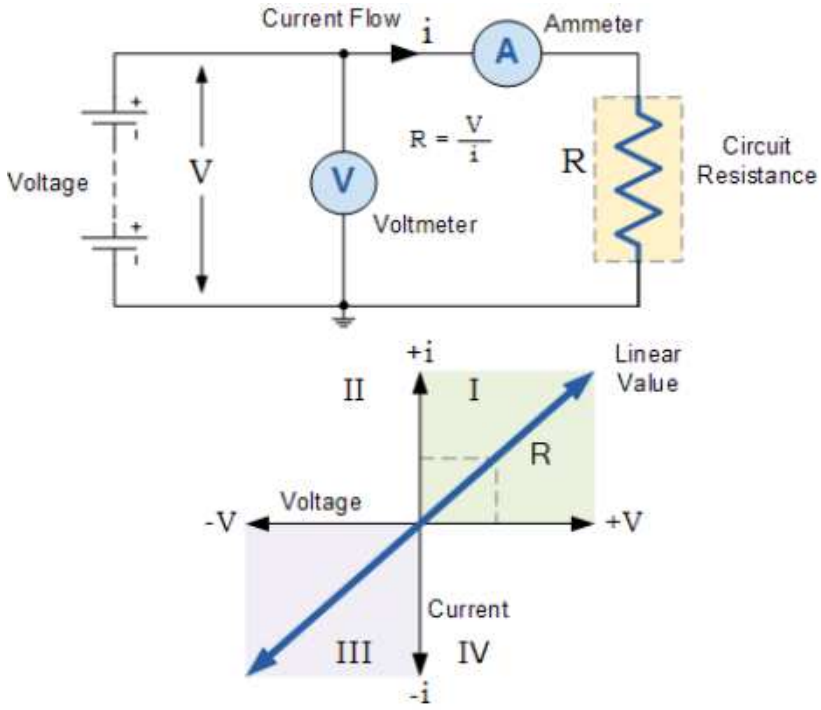

Figure 3.9.1: The I-V curve for an ideal conductor where the input voltage is arbitrary. Image adapted from Henderson [44].

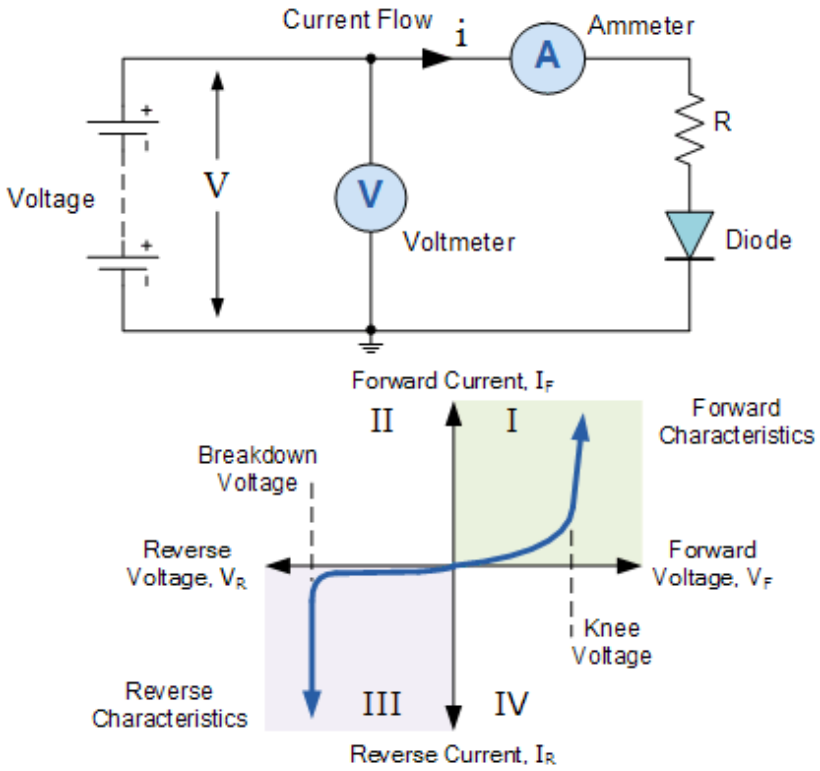

Figure 3.9.2: The I-V curve for a semiconductor related material. Image adapted from Henderson [44].

curve in the process. Meanwhile, with reverse bias (positive voltage at the cathode terminal with respect to the anode terminal), the material acts like a diode where a block current is generated due to leakage current [44]. The action of the diode block continues till the reverse voltage becomes greater than its breakdown voltage. The implication of the superposition of the diode voltage and the break down voltage gives an abrupt increase in the production of reverse current. The effect is observed as a straight downward line as indicated in Figure 3.9.2 [44].

Furthermore, I-V characteristics can be used to study charge storage properties of a material. Charge storage properties occur when electronic polarization in a dielectric material shows a separation and alignment of the electric charges [45]. The separation and alignment of the charges occur when an electric is applied. The implication of the separation and alignment of the charges indicates capacitance enhancement in the material .

The charge storage property is associated with ionic polarization where there is ionic

vibration with the material [46]. With the introduction of electric field due to the flow of current, there occurs an opposition displacement of positive and negative ions.The ionic displacement continues until the formation of ionic bonding between the elemental components of the material [46]. The ionic bonding formation leads to formation of dipole moment and dielectric constant. the charge storage property is consistent with inorganic crystals and ceramics [45].

3.10 Superconducting quantum interference device magnetometry

The superconducting quantum interference device magnetometry (SQUID) is a technique that enables the measurement of magnetic response of materials. The SQUID is sensitive and can measure insignificant magnetic responses. The working principle of a SQUID is based on mathematical formalism of Josephson and was implemented experimentally in 1963 [47].

The working principle of SQUID is due to the effect of flux quantization in superconducting rings and the Josephson effect. Josephson's theory proposes the sustenance of superconducting current in the loop in spite of interference by insulating barrier or conducting metals [48].

As shown in Figure 3.10.1(a), there are weak links at W and X points with critical current (i_c) , which is smaller than the main ring critical current. The difference in the critical current generates a low current density , which enables low magnitude of the electron pair. The low electron pair magnitude invariably gives a long wavelength of the electron pair and small phase difference in the ring [49]. Suppose an external field Ba is perpendicularly applied to the plane of the ring, a phase difference is generated in the electron pair wave in the XYW and WZX paths. Moreover, the magnetic flux passing through the loop is a combination of the magnetic field and area of the loop.

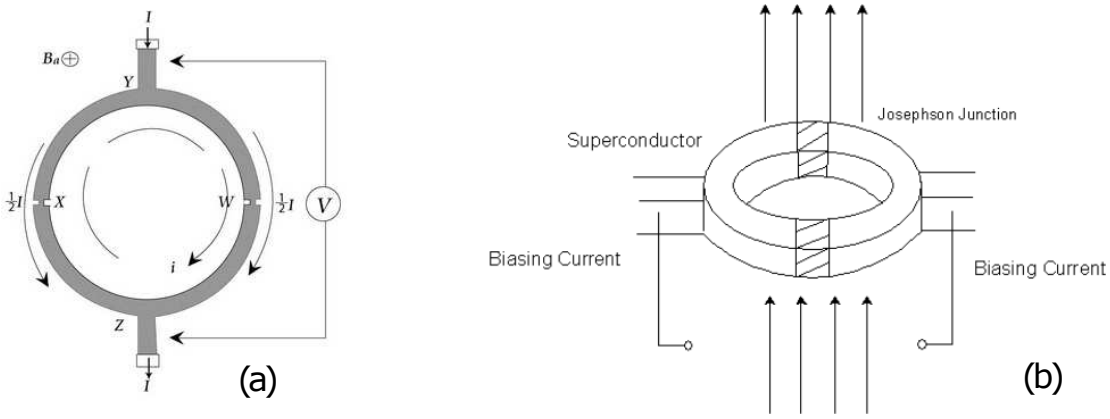

Figure 3.10.1: The schematic representation of the SQUID describing the principle behind its functionality.Image adapted from Maron and Ostanina [50].

The combination allows for quantization, which can be represented as:

$$\Phi_0 = \frac{h}{2e}, \tag{3.9}$$

where h is the Planck constant and $2e$ represents the charge of the pair of electrons. The magnitude of Φ_0 is approximately $2 \times 10^{-15}\,\text{Tesla} \cdot \text{m}^2$. Assuming an ideal loop with no obstacles, the superconducting current can account for the generated arbitrary magnetic field. The additional compensated field can allow for the total flux passing through the loop to be a multiple of Φ_0 [47, 49]. Based on Josephson's theory, the SQUID system comprises two junctions. Both junctions produce the same phase difference when the magnetic flux through the loop equals zero i.e. $\Phi_0 = 2\Phi_0$ and leads to a constructive interference [51]. When the phase difference becomes $\Phi_0/2$ and $2\Phi_0/2$, then destructive interference occurs, and causes the varying value of the critical current density (maximum current allowed for the device with dissipation). The voltage drop across the junctions of the total current can be used to obtain the critical current. Furthermore, when an external field is introduced in the loop, a phase change around the ring is generated such that:

$$\Delta\Phi(B) = 2\pi\frac{\Phi_a}{\Phi_0}, \tag{3.10}$$

where Φ_a is the flux generated in the ring due to the external field. Meanwhile, the value of the critical current is related to the critical current of the weak link and the phase change around the ring. Furthermore, the ring is assumed to be multiple of 2π. In order to fulfill the condition of superconductance of the ring, it is expected that:

$$\alpha + \beta + 2\pi\frac{\Phi_a}{\Phi_0} = n \cdot 2\pi, \tag{3.11}$$

where α and β represents the change in phase due to the current flowing across the weak links and $2\pi\frac{\Phi_a}{\Phi_0}$. With the application of varying current to α and β, the phase change becomes:

$$\alpha = \pi\big[n - \frac{\Phi_a}{\Phi_0}\big] - \delta\beta = \pi\big[n - \frac{\Phi_a}{\Phi_0}\big] + \delta, \tag{3.12}$$

where δ represents an arbitrary parameter that is dependent on the current I. The current can be evaluated using:

$$I_c = 2i_c\Big|\cos\pi\frac{\Phi_a}{\Phi_0}.\sin\delta\Big|. \tag{3.13}$$

Assuming $\sin\delta$ is small, then the current I_c can be rewritten as:

$$I_c = 2i_c\Big|\cos\pi\frac{\Phi_a}{\Phi_0}\Big|. \tag{3.14}$$

The implication of equation ref cur is the periodic relationship between the applied field and the critical current. Here, the maximum period gives an integer number of fluxons, whereas minimum period leads to half integer magnitude. It critical current principle is responsible for the sensitivity of the SQUID technique to low magnetic field. [49, 51].

Summary

In this chapter, the characterization techniques used in the current study were discussed. The chapter was focused on the working principle of the systems. The scope of the chapter did not focus on the mathematical framework on the techniques due to the experimental nature of the current project, except in the case of SQUID magnetometry. The mathematical framework for the other techniques can be found elsewhere in literatures.

Bibliography

[1] B Warren. X-ray diffraction. *Massachusetts: Addison-Wesley*, 46, 1969.

[2] Paul M Chaikin, Tom C Lubensky, and Thomas A Witten. *Principles of condensed matter physics*, volume 1. Cambridge university press Cambridge, 1995.

[3] Christopher Hammond. *The basics of cristallography and diffraction*, volume 214. Oxford, 2001.

[4] Ashish Chauhan and Priyanka Chauhan. Powder xrd technique and its applications in science and technology. *J Anal Bioanal Tech*, 5(5):1–5, 2014.

[5] Agnes Bogner, P-H Jouneau, Gilbert Thollet, D Basset, and Catherine Gauthier. A history of scanning electron microscopy developments: Towards "wet-stem" imaging. *Micron*, 38(4):390–401, 2007.

[6] Anwar Ul-Hamid. *A Beginners' guide to scanning electron microscopy*, volume 1. Springer, 2018.

[7] John Humphreys, Richard Beanland, and Peter J Goodhew. *Electron microscopy and analysis*. CRC Press, 2014.

[8] Surender Kumar Sharma, Dalip Singh Verma, Latif Ullah Khan, Shalendra Kumar, and Sher Bahadar Khan. *Handbook of Materials Characterization*. Springer, 2018.

[9] CJ Humphreys. The significance of bragg's law in electron diffraction and microscopy, and bragg's second law. *Acta Crystallographica Section A: Foundations of Crystallography*, 69(1):45–50, 2013.

[10] Yousef Alqaheem and Abdulaziz A Alomair. Microscopy and spectroscopy techniques for characterization of polymeric membranes. *Membranes*, 10(2):33, 2020.

[11] JR Dennison, Mark Holtz, and Greg Swain. Raman spectroscopy of carbon materials. *Spectroscopy*, 11(8), 1996.

[12] Yan Wang, Daniel C Alsmeyer, and Richard L McCreery. Raman spectroscopy of carbon materials: structural basis of observed spectra. *Chemistry of Materials*, 2(5):557–563, 1990.

[13] Mildred S Dresselhaus, G Dresselhaus, R Saito, and A Jorio. Raman spectroscopy of carbon nanotubes. *Physics Reports*, 409(2):47–99, 2005.

[14] Ian R Lewis and Howell Edwards. *Handbook of Raman spectroscopy: from the research laboratory to the process line*. CRC press, 2001.

[15] Hyung Hun Kim. Endoscopic raman spectroscopy for molecular fingerprinting of gastric cancer: principle to implementation. *BioMed Research International*, 2015(2), 2015.

[16] Stephen Y Lin and Carlton W Dence. *Methods in Lignin Chemistry*. Springer Science & Business Media, 2012.

[17] Gholam Reza Yazdi, Tihomir Iakimov, and Rositsa Yakimova. Epitaxial graphene on sic: A review of growth and characterization. *Crystals*, 6(5):53, 2016.

[18] Michele Lazzeri, Claudio Attaccalite, Ludger Wirtz, and Francesco Mauri. Impact of the electron-electron correlation on phonon dispersion: Failure of lda and gga dft functionals in graphene and graphite. *Physical Review B*, 78(8):081406, 2008.

[19] F Tuinstra and J Lo Koenig. Raman spectrum of graphite. *The Journal of Chemical Physics*, 53(3):1126–1130, 1970.

[20] Rasmita Sahoo and Rashmi Ranjan Mishra. Phonon dispersion for armchair and zigzag carbon nanotubes. *Graphene*, 3(02):14, 2014.

[21] Andrea C Ferrari and Denis M Basko. Raman spectroscopy as a versatile tool for studying the properties of graphene. *Nature Nanotechnology*, 8(4):235, 2013.

[22] R Vidano and David B Fischbach. New lines in the raman spectra of carbons and graphite. *Journal of the American Ceramic Society*, 61(1-2):13–17, 1978.

[23] Robert John Nemanich and SA Solin. First-and second-order raman scattering from finite-size crystals of graphite. *Physical Review B*, 20(2):392, 1979.

[24] Peter R Griffiths and James A De Haseth. *Fourier transform infrared spectrometry*, volume 171. John Wiley & Sons, 2007.

[25] C Hontoria-Lucas, AJ López-Peinado, J de D López-González, ML Rojas-Cervantes, and RM Martin-Aranda. Study of oxygen-containing groups in a series of graphite oxides: physical and chemical characterization. *Carbon*, 33(11):1585–1592, 1995.

[26] Sabina Drewniak, Roksana Muzyka, Agnieszka Stolarczyk, Tadeusz Pustelny, Michalina Kotyczka-Morańska, and Maciej Setkiewicz. Studies of reduced graphene oxide and graphite oxide in the aspect of their possible application in gas sensors. *Sensors*, 16(1):103, 2016.

[27] C Defosse and PG Rouxhet. Introduction to x-ray photoelectron spectroscopy. In *Advanced chemical methods for soil and clay minerals research*, pages 169–203. Springer, 1980.

[28] John F Watts. X-ray photoelectron spectroscopy. *Surface science techniques*, 45:5–23, 1994.

[29] Thomas Carlson. *Photoelectron and Auger spectroscopy*, volume 1. Springer Science & Business Media, 2013.

[30] Marc Simon, Ralph Puttner, Tatiana Marchenko, Renaud Guillemin, Rajesh K Kushawaha, Loc Journel, Gildas Goldsztejn, Maria Novella Piancastelli, James M Ablett, Jean-Pascal Rueff, et al. Atomic auger doppler effects upon emission of fast photoelectrons. *Nature Communications*, 5:4069, 2014.

[31] Jorg Fink, E Schierle, E Weschke, and J Geck. Resonant elastic soft x-ray scattering. *Reports on Progress in Physics*, 76(5):056502, 2013.

[32] L Ley, RA Pollak, FR McFeely, Sa P Kowalczyk, and DA Shirley. Total valence-band densities of states of iii-v and ii-vi compounds from x-ray photoemission spectroscopy. *Physical Review B*, 9(2):600, 1974.

[33] Paul K Chu and Liuhe Li. Characterization of amorphous and nanocrystalline carbon films. *Materials Chemistry and Physics*, 96(2-3):253–277, 2006.

[34] Rolf Manne and T AAberg. Koopmans' theorem for inner-shell ionization. *Chemical Physics Letters*, 7(2):282–284, 1970.

[35] Wei-Hsiang Lin, Ting-Hui Chen, Jan-Kai Chang, Jieh-I Taur, Yuan-Yen Lo, Wei-Li Lee, Chia-Seng Chang, Wei-Bin Su, and Chih-I Wu. A direct and polymer-free method for transferring graphene grown by chemical vapor deposition to any substrate. *ACS Nano*, 8(2):1784–1791, 2014.

[36] Cheng-Hao Chuang, Sekhar C Ray, Debarati Mazumder, Surbhi Sharma, Abhijit Ganguly, Pagona Papakonstantinou, Jau-Wern Chiou, Huang-Ming Tsai, Hung-Wei Shiu, Chia-Hao Chen, et al. Chemical modification of graphene oxide by nitrogenation: An x-ray absorption and emission spectroscopy study. *Scientific Reports*, 7:42235, 2017.

[37] August Beer. Bestimmung der absorption des rothen lichts in farbigen flussigkeiten. *Ann. Physik*, 162:78–88, 1852.

[38] Jeroen A Van Bokhoven and Carlo Lamberti. *XX-Ray Absorption and X-Ray Emission Spectroscopy: Theory and Applications*, volume 1. John Wiley & Sons, 2016.

[39] Jijun Zhao, Lizhao Liu, and Fen Li. *Graphene Oxide: Physics and Applications*. Springer, 2015.

[40] SC Ray, CW Pao, HM Tsai, B Bose, JW Chiou, WF Pong, and D DasGupta. Orientation of graphitic planes during annealing of "dip deposited" amorphous carbon film: A carbon k-edge x-ray absorption near-edge study. *Carbon*, 44(10):1982–1985, 2006.

[41] Sekhar C Ray, Navneet Soin, Way-Faung Pong, Susanta S Roy, Andre M Strydom, James A McLaughlin, and Pagona Papakonstantinou. Plasma modification of the electronic and magnetic properties of vertically aligned bi-/tri-layered graphene nanoflakes. *RSC Advances*, 6(75):70913–70924, 2016.

[42] David JC MacKay. Introduction to gaussian processes. *NATO ASI Series F Computer and Systems Sciences*, 168:133–166, 1998.

[43] Simon M Sze and Kwok K Ng. *Physics of Semiconductor Devices*. John wiley & sons, 2006.

[44] John Henderson. *Electronic devices: Concepts and applications*. Prentice Hall, 1992.

[45] K Deshmukh, M Basheer Ahamed, RR Deshmukh, SK Khadheer Pasha, PR Bhagat, and K Chidambaram. Biopolymer composites with high dielectric performance: interface engineering. In *Biopolymer composites in electronics*, pages 27–128. Elsevier, 2017.

[46] Ji Eun Lee, Seon Joo Park, Oh Seok Kwon, Hyeon Woo Shim, Jyongsik Jang, and Hyeonseok Yoon. Systematic investigation on charge storage behaviour of multidimensional poly (3, 4-ethylenedioxythiophene) nanostructures. *RSC Advances*, 4(71):37529–37535, 2014.

[47] John Clarke and Alex I Braginski. *The SQUID Handbook: Applications of SQUIDs and SQUID Systems*. John Wiley & Sons, 2006.

[48] Yukio Tanaka and Satoshi Kashiwaya. Theory of josephson effects in anisotropic superconductors. *Physical Review B*, 56(2):892, 1997.

[49] John Bland. A mossbauer spectroscopy and magnetometry study of magnetic multilayers and oxides, 2002.

[50] P Marcon and K Ostanina. Overview of methods for magnetic susceptibility measurement. In *PIERS Proceedings*, 2012.

[51] RL Fagaly. Superconducting quantum interference device instruments and applications. *Review of Scientific Instruments*, 77(10):101101, 2006.

Chapter 4

Graphene oxide functionalized with gold nanoparticles

Graphene is a 2D carbon material which has been topical in the last decade owing to its potential in various spheres of science and technology. It has found application in energy storage, biomedical, electrochemical, electronic applications etc [1, 2]. The underlying potential of graphene and its derivative can be harvested by exploring the electronic, electrical and magnetic properties of graphene. Previous literature has suggested one of the alternative routes to synthesizing graphene related materials as graphene oxide (GO) sheets [3, 4].

The electronic properties of GO is based on the conjugated network of sp^2 hybridization and the electronic structure of carbon. The study of the electronic properties of GO creates an avenue for understanding the transport behaviour of GO. For instance, GO is considered as an insulator due to the effect of oxidation of the carbon atoms [1, 5]. However, the possibility of tuning the degree of oxidation by complete removal of the C−O bonds can give a zero-band gap graphene property [6]. Another intriguing property of GO is the large surface area that enables the attachment of surfactant or adatoms [7]. The large surface property is due to the hexagonal arrangement of the sp^2 carbon network. These adatoms are different from the usual oxygenated groups that are found at the basal planes and edges of GO (see Figure 4.0.1). The effect of adatoms or surfactants on graphene oxide can affect other properties of the material. As indicated in Figure 4.0.1, the hydrophilic property of GO is mostly associated with

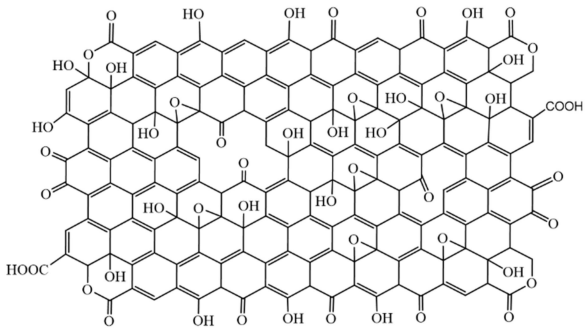

Figure 4.0.1: The structure of graphene oxide shown the oxygen functional groups. Image adapted from Dreyer et al. [8]

.

the −COOH group at the edges and the basal plane which comprises mainly of −OH groups. The GO structure becomes more complex and can be considered as amphiphile with large hydrophobic basal planes and hydrophilic edges [7].

Attempts have been made to understand the electronic structure and bonding structure of GO by various researchers [9–11]. GO has been reported to be in the form of rough sheets with average surface roughness of $\approx 0.6\,\text{nm}$ [6]. At the same time, GO was considered amorphous with the amorphicity resulting from the −OH and $-O^-$ [12]. GO is experimentally reported by Kim *et al.* [7] to be amphiphilic and can be adsorbed onto interfaces. Their report proposed that the adsorption of GO can be varied by manipulating the pH of the interface. This implied the possibility of attaching of GO to adatoms and the attachment of the adatoms can lead to formation of other bonds, which can improve the properties of GO.

Graphene is characterized as having high electron mobility among other properties [13]. However, the production of graphene derivative (GO) from graphite sheets exfoliation leads to decreased electron mobility and poor electrical conductivity [14]. The improvement of the electrical conductivity of GO for different applications has received attention from researchers in recent times [15, 16]. Some of the techniques used to improve the electrical conductivity are through graphene-polymer composite [17], chemical reduction [18], nanostructural sheet deformation [19] etc. Chemical reduction which was suggested by Pei and Cheng [18] is a relatively efficient method in enhancing the properties of GO. Meanwhile, an advantage of improving the properties of GO is the

spin-orbit coupling with long spin diffusion that can be useful for ferro-electric related applications [20]. Long spin diffusion length is a property, which is one of the pre-requisite for resistance switching [20]. Coupled with the high electron mobility and the diffusion length, graphene can be a good candidate for ferroelectric electronic applications. However, the absence of intrinsic magnetic moment in pristine graphene poses a challenge in the realization of a graphene as a soft magnetic material. The nonmagnetic challenge of graphene has created an avenue for rigorous studies into inducing magnetism into graphene. Some previous attempts for inducing magnetization on to graphene include irradiation of vacancies to increase unpaired electrons [23], introduction of adatoms [24–26] and inducing of zigzag edges on the structure of graphene [27]. The magnetizaton of GO is $1\,\mu_{\mathrm{B}}$ which is mainly due to the hydroxyl group [26] and possibility of ferrommagnetism from epoxy group [28]. Since GO atomic dynamics is non-stoichoimetric in nature, magnetism in GO becomes variable based on the synthesis technique. The non-stoichiometric nature of GO becomes advantageous such that the magnetization can be easily tuned by adatoms.

Considering the possibilities that can be harvested by exploring the electronic, structure, electrical and magnetic properties of GO, this study attempts to explore these properties.

4.1 Experimental details

In this study, graphene oxide (GO) having similar characteristics (in the form of reduced graphene oxide) as graphene was functionalized with gold (Au) nanoparticles (NP) with concentrations ranging 0.08, 0.11, 0.22 and 4.88 (at. %) as emphasized in Section 4.2.3. The synthesis comprises the preparation of graphene oxide from graphite crystals and the reduction of graphene oxide to reduced graphene oxide with hydrazine. Both procedures are described in the following sections.

4.2 Sample preparation

Graphite powder, sodium nitrate ($NaNO_3$) 99.99 %, hydrogen sulphide (H_2SO_4) 99.99 %, potassium permanganate ($KMnO_4$) 99.99 % and silica coated gold nanoparticles were procured from Sigma Aldrich. The chemicals were used without further purification. All colloidal samples from the precursor chemicals were obtained at room temperature and not pre-heated. The sample preparation procedures are described in the sections below.

4.2.1 Graphene oxide

Graphene oxide in colloidal form was synthesized using modified Hummer's method as previously reported [29]. 300 mg of graphite powder, 100 mg of sodium nitrate and 5 ml of concentrated hydrogen sulphide (H_2SO_4) were used in the synthesis process. Both powders (graphite and sodium nitrate) and the H_2SO_4 solution were mixed and cooled from ambient temperature to 0 °C. The mixture was stirred for homogeneity with stepwise addition of $KMnO_4$. The solution temperature was maintained at approximately 20 °C. The temperature of the solution was further raised and kept at 35 °C for approximately 40 min. The solution turned brownish-grey colour in a slurry form. The temperature of the solution was further increased to 90 °C after addition of water. 28 ml of water and 300 μl of 3% H_2O_2 were mixed with the solution. The 300 μl of 3% H_2O_2 component enables the reduction of the residual $KMnO_4$. The solution formed light yellow particles after the treatment. The obtained solution was washed and centrifuged with water several times. The obtained solid particles were thereafter air-dried and dissolved in 20 ml of distilled water. The solution was thereafter centrifuged at 3000 rpm for 30 min and collected in a supernatant form as GO.

4.2.2 Reduced graphene oxide

The reduction of GO to rGO was performed using hydrazine hydrate. 10 mL of the supernatant GO was collected in a glass vial. 1 mL hydrazine hydrate was mixed with the GO solution. The mixed solution was heated with stepwise stirring at 70 °C for approximately 30 min. A black colored solution slowly appeared which eventually precipitated.

4.2.3 Reduced graphene oxide - gold nanoparticles nanocomposites

5 ml of concentrated GO prepared as per Section 4.2.1 was collected in a beaker. 5 ml of colloidal silica coated Au nanoparticles was added in drop-wise manner whilst stirring the solution. 50 μL of hydrazine hydrate solution was thereafter added to the colloidal mixture and heated to about 80 °C for 30 mins. A blackish precipitate was obtained afterwards. The black precipitate was washed with distilled water and eventually collected as rGO:Au-NP. The process was repeated for the preparation of the various concentration of rGO:Au-NP (0.08 at. %, 0.11 at. %, 0.22 at. % and 4.88 at. %).
It is worth mentioning that the choice of Au-NP concentration was to study the impact of low and high concentration on the electronic, electrical and magnetic properties of rGO:Au-NP composite. Previous studies have shown that low concentration of Au is useful for biomedical applications as they are non-cytotoxic at low concentration [30]. However, considering electronic device applications, high concentration of Au may give interesting results. The concentration of Au-NP was initially increased as background study from 0.08 at. % to 0.32 at. % (not included in the samples) and there was no significant change in the properties. It was based on this observation that necessitated the abrupt increase of Au-NP concentration to 4.88 at. %

4.3 Sample characterization

The presentation of the results which encompasses the sample characterization techniques are divided into sections. The subsections covers the microstructural, morphological, electronic, electrical and magnetic properties of rGO-Au nanocomposites.

4.3.1 X-ray diffraction

The X-ray diffraction (XRD) spectra was obtained using Rigaku Smartlab X-rays diffractometer (0.154 nm Cu Kα line). The obtained XRD patterns of rGO and rGO:(Au-NP)x are shown in Figure 4.3.1. The XRD pattern indicates microstructural nature of the material as it gives a blueprint of the elemental component of the material. The XRD pattern shows the 2θ peak positions aligned at 26.95^0 with d spacing 0.33 nm and lattice plane index of C(002) for carbon atoms. The C(002) peak is also present in all the samples with the exceptions of rGO:Au-NP (0.22 at. %) where the prominence is insignificant.

A weak C(001) peak appears at approximately 19° for rGO:Au-NP(0.11 at.%), rGO:Au-NP(0.22 at.%) and rGO:Au-NP(4.88 at.%) signifying the presence of graphite [31] which is the precursor material used for the synthesis of the nanocomposites. The peak weakness may be due to inhomogeneous distribution and agglomeration of the composites on the films. Meanwhile, the peaks at 38.3° and 44.5° are assigned to C(111) and C(100), respectively [32, 33]. Other prominent peaks are aligned at 30.3°, 32.9°, 33.6°, 46.2°, 47.7° and 54.6°. These peaks correspond to Au(321), Au(111), Au(331), Au(420), Au(420) and Au(511), respectively [34]. The prominent peak labelled as # is attributed to possible interaction between Si and C (Si-C) atoms [35].
The shape and intensity of the peaks are attributed to the face centred cubic (fcc) na-

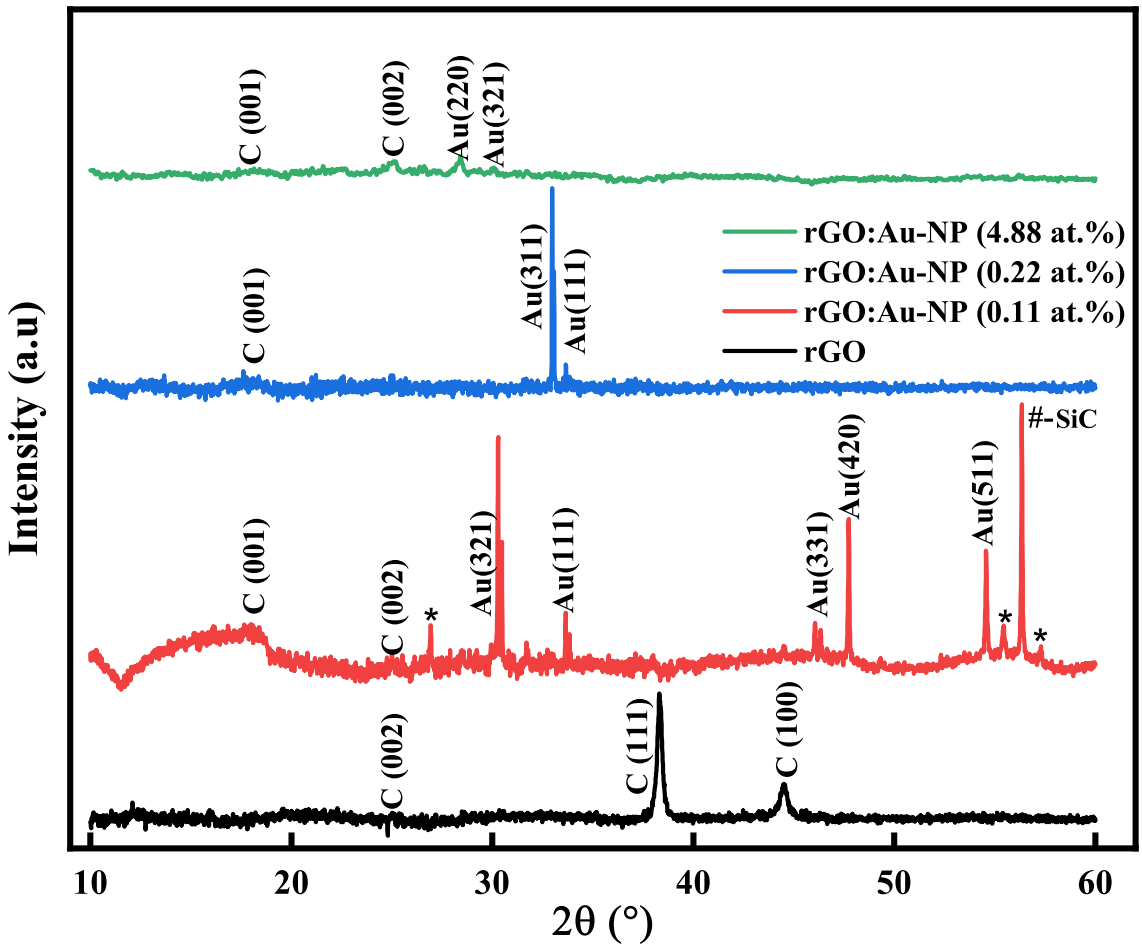

Figure 4.3.1: The obtained XRD pattern for rGO and rGO:(Au-NP)x (x=0.08 at.%, 0.11 at.%, 0.22 at.% and 4.88 at.%). The XRD plots for all the samples are stacked, hence, the intensities (y axis) can not be compared.

ture of Au nanoparticles. The special case of rGO:Au-NP(0.11 at.%) sample possessing most of the peak positions is an indication of the Au-NP decoration during synthesis process. The hump shape for both rGO:Au-NP(0.11 at. %) and rGO:Au-NP(0.22 at. %) which are indicated at $\approx 19^0$ confirms the presence of few layers of graphene in GO [36]. Furthermore, there are absence of other peaks of Au in rGO:Au-NP (4.88 at.%) which is an indication of the film used for the XRD analysis. Presumably, the deposited sample was not homogeneously spread over the substrate. XPS analysis of rGO:Au-NP(4.88 at.%) sample showed the presence of Au atoms. All the peaks represented in the spectra are in accordance with JCPDS data (JCPDS card 01-01172) [34]. Other peaks that are not indexed may be due to impurities/ trace elements (asterisked

peaks) that might have been introduced during synthesis and characterization process. Presumably, the impact of trace element does not explicitly impact the properties of material since the concentrations are very low.

The Debye-Scherrer equation, which can be used to estimate the crystallite size of the nanocomposite is given as:

$$2R = \frac{0.9\lambda}{\beta} \tag{4.1}$$

where $2R$ is the diameter of the composite, β is the full width of maximum (FWHM) of the peaks and λ is the wavelength of the X-ray source. Considering the C(002) 2θ reflection plane and using pseudovoigt function in Originlab software, the values of the extrapolation particles size were extrapolated, The extrapolated values are shown in Table 4.3.1 where the average particle size of the nanocomposite were estimated to be approximately 10-15 nm.

Table 4.3.1: The extrapolated estimated values of particle size of rGO and rGO:(Au-NP){x} from XRD spectra using C(002) reflection plane.

Samples	2θ (degree)	FWHM	Particle size (nm)
rGO	24.7	0.849±0.08	10.01
rGO:Au-NP(0.11 at.%)	25	0.611±0.08	13.9
rGO:Au-NP(4.88 at.%)	25	0.565±0.08	15.1

4.3.2 Scanning electron microscopy

The field emision scanning electron microscopic (FESEM) images were obtained using JSM-7800F FESEM from JEOL Ltd coupled with an ultradry EDS detector. The FE-SEM images of rGO for various magnification are shown in Figure 4.3.2. The images show the morphology (it is the property that describes the shape of the particles and how they are arranged in the material.) of rGO. The EDX spectrum shows the elemental composition of rGO where the constituents includes: carbon (C), oxygen (O) and

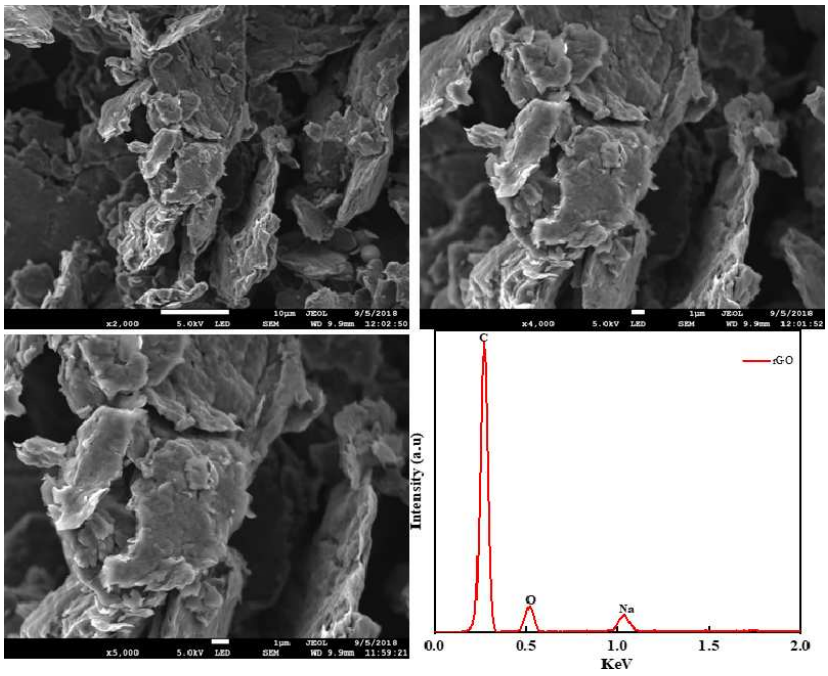

Figure 4.3.2: Field emission scanning electron microscopy (FESEM) images of rGO for various magnification. The bottom right column shows the EDX spectra indicating the element composition of rGO.

sodium (Na) impurity.

The appearance of carbon and oxygen peaks are expected from the exfoliation process of graphite sheets [37]. Sodium impurities on the other hand are from the hydrazine hydrate. Figures 4.3.4 - 4.3.6 are FESEM images for rGO:Au-NPx ($x = 0.88$, 0.11, 0.22 and 4.88 at. %)) for different magnifications. The appearance of nitrogen component is from the reduction process with hydrazine hydrate [38]. The peak for silicon (Si) is from the silicon wafer substrate on which rGO:Au-NP was deposited. As can be seen in the FESEM images, there is an observed change in the shape of the particles from flake to smaller granules contained in the nanocomposites as Au-NPx is increased.

The changes are mostly due to the reducing agent and the functionalizing agent [39]. For instance, there is a transition from huge flakes for rGO to granules in the case of rGO:(Au-NP)x ($x = 0.11$ and 0.22 at. %). The change in the concentration of Au-NP in rGO:Au-NP does not change the appearance of the granules. The FESEM images for rGO and rGO:(Au-NP)x also show continuous attachment between the flakes and particles. The attachment of the sheet signifies easy mobility of electrons between the

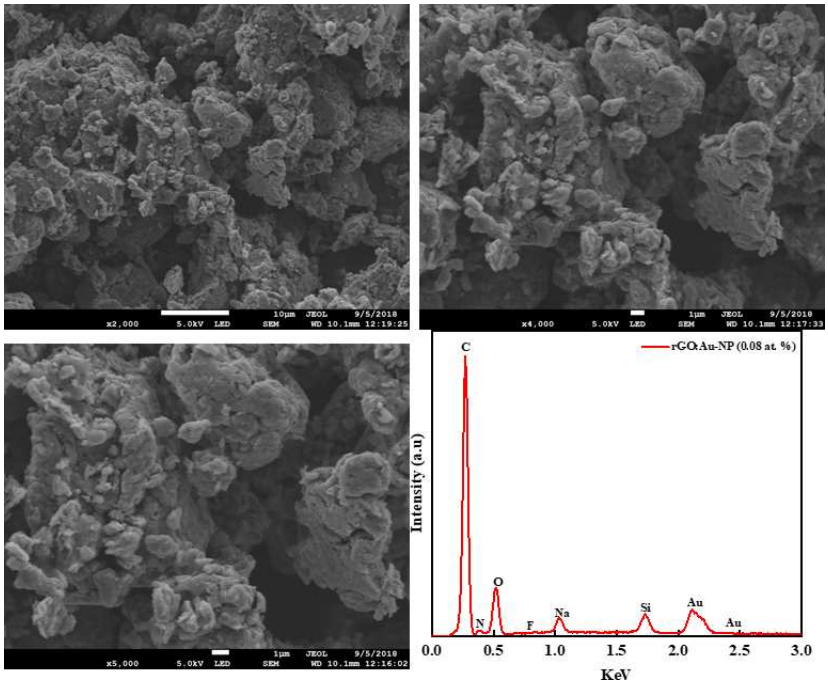

Figure 4.3.3: Field emission scanning electron microscopy (FESEM) images of rGO:Au-NP(0.08 at. %) for various magnification. The bottom right column shows the EDX spectra showing the element composition of rGO:Au-NP(0.08 at. %)

atoms and could impact the electrical conductivity of rGO and rGO:(Au-NP)x. The magnification of the images does not change the features of the particles, signifying the morphology of the nanocomposite are stable when rGO is functionalized with Au-NPx. Reports have indicated the relationship between grain boundary and charge transport [40]. The grain boundary can be easily probed by scanning tunnelling microscopy, however, it is beyond the scope of the current study. The grain boundary can reveal the single or poly crystallinity of any material. Single crystals allow easy electron transition between atoms which inevitably gives higher electrical conductivity whereas poly crystallinity favours electron hopping between atoms which hampers electrical conductivity [41].

Figure 4.3.7 shows the histogram distribution of the grain size boundary of rGO and rGO:Au-NPx using Image J software. As indicated, there is a decrease in the mean grain sizes with low Au-NP concentration in comparison with rGO. However, an increase is observed for high concentration of Au-NP (4.88 at. %) which show consistency when both images of rGO:Au-NP (0.22 at. %) and rGO:Au-NP (4.88 at. %) are com-

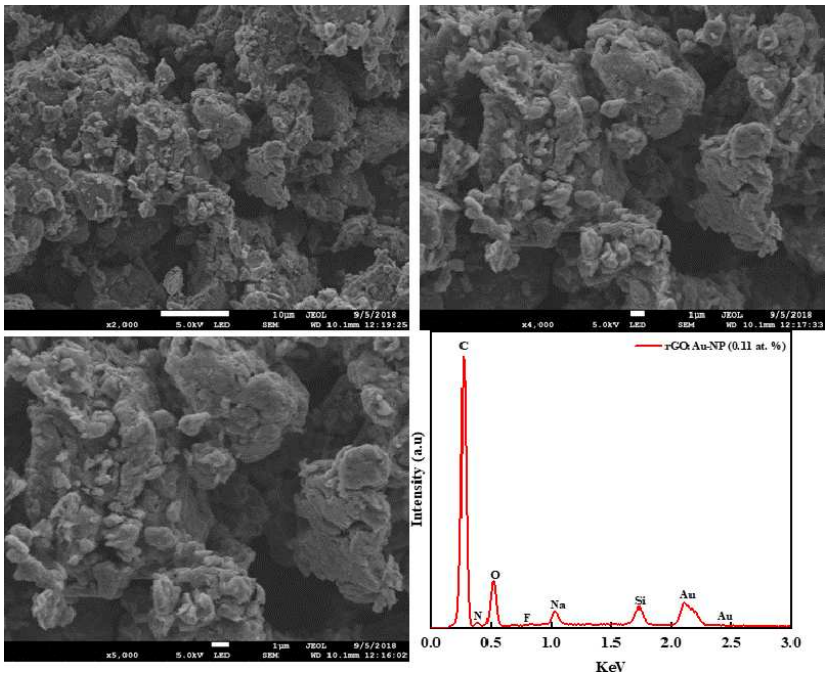

Figure 4.3.4: Field emission scanning electron microscopy (FESEM) images of rGO:Au-NP(0.11 at. %) for various magnification. The bottom right column shows the EDX spectra showing the element composition of rGO:Au-NP(0.11 at. %).

pared. A change in the morphology of particles indicates a change in the crystallinity of the grain boundaries. The change in the grain boundary from rGO → rGO:Au-NP(0.22 at. %) indicates the grain size tending towards single crystallinity. The observation can be seen in the higher electrical conductivity shown in the I-V features in later section of Figure 4.3.25. The SEM images of rGO:Au-NP(4.88 at. %) showing bigger grain size in comparison with rGo:Au-NP(0.22 at. %) signify polycrystallity.

4.3.3 Transmission electron microscopy

The transmission electron microscopy (TEM) images of the GO and rGO:Au-NP(4.88 at. %) are shown in Figure 4.3.8. As expected in the case of rGO, the flake-like sheet are represented in Figure 4.3.8 (right) as in the SEM images. The dark dots on the left-hand-side indicates the decoration of Au nanoparticles across rGO. The Au-NP are unevenly distributed and clustered around the rGO sheet. The uneven distribution can be attributed to weak agglomeration due to electrostatic interaction between rGO and

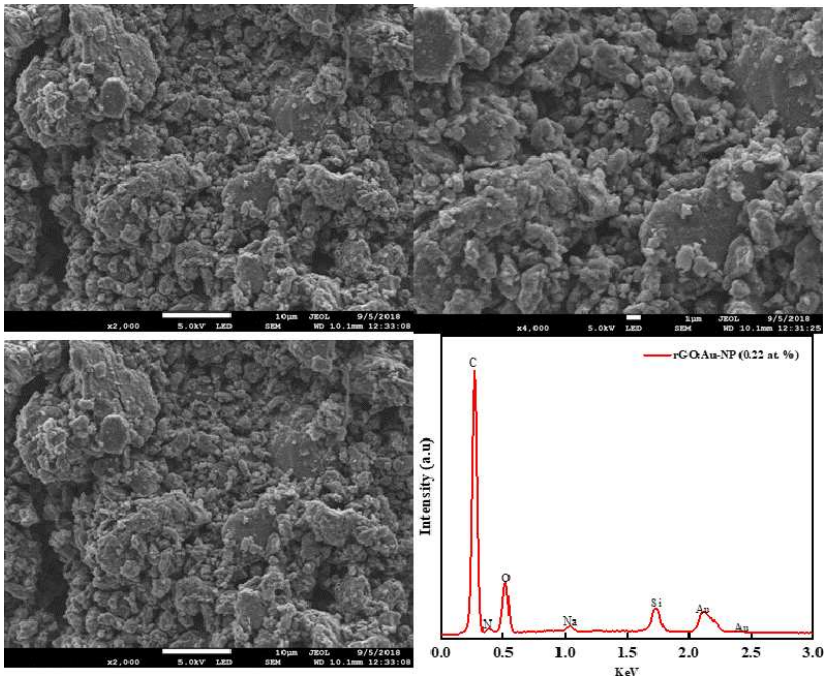

Figure 4.3.5: Field emission scanning electron microscopy (FESEM) images of rGO:Au-NP(0.22 at. %) at various magnification. The bottom right column shows the EDX spectra showing the element composition of rGO:Au-NP(0.22 at.%).

Au-NP [29]. Due to the magnification of the images, it is impossible to extrapolate the particle size of rGO and rGO:Au-NPx. Furthermore, there is an uneven distribution of the Au-NP on rGO. This implies attachment of Au atoms on the edge of rGO. The attachment of the Au nanoparticles can improve the mobility potentials of electrons between different atomic points in the material. As a result of the mobility, high electrical conductivity can be expected due to easy transition between the electrons. Although, the particle size distribution cannot be extrapolated, however, the estimate from XRD particle analysis using the Debye-Scherrer equation in Section 4.3.1 indicates nanosized particles for rGO and rGO-Au-NPx.

4.3.4 Raman spectroscopy

The Raman spectra for Au-NP, rGO and rGO:(Au-NP)x (x = 0.08 at. %, 0.11 at. %, 0.22 at. % and 4.88 at. %) were obtained using HORIBA scientific Xplora with wavelength and excitation power of the laser beam been 532 nm and 16 mW, respectively.

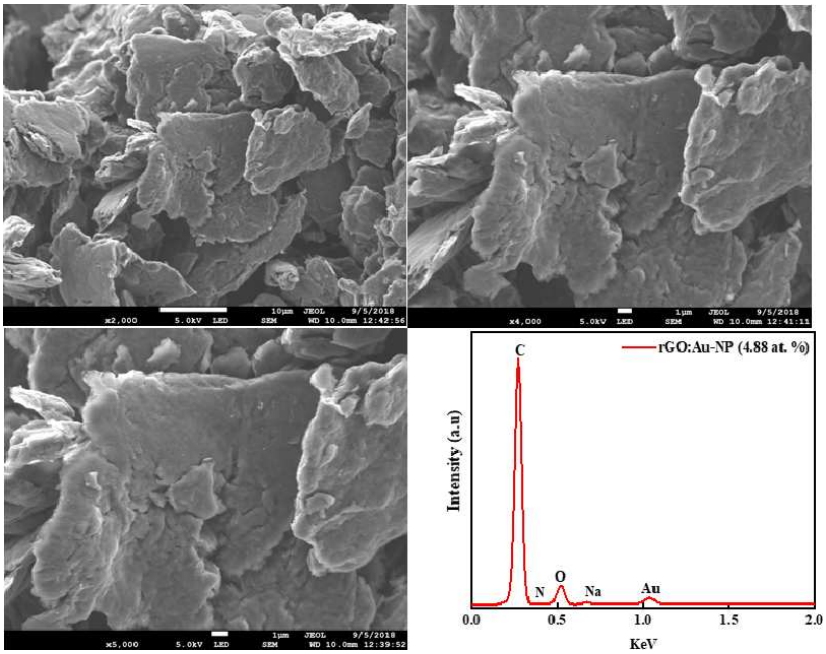

Figure 4.3.6: Field emission scanning electron microscopy (FESEM) images of rGO:Au-NP(4.88 at. %) for various magnification. The bottom right column shows the EDX spectra showing the element composition of rGO:Au-NP(4.88 at. %)

It is worth mentioning that the intensity of the Raman spectra depends on the image focusing and not necessary the sample. The important parameter involves the comparison between the D and G peaks of individual samples. The comparison between the peak intensity of different samples can be misleading since the image focusing of each sample is independent of one another.

The spectra of the Raman measurements are shown in Figure 4.3.9 and 4.3.10. The Raman spectra in Figure 4.3.9 were fitted with Gaussian function in Originlab software to obtain the values of D, G, 2D, D+G. Table 4.3.2 shows the various positions ($X_{D,G}$), width ($W_{D,G}$) and area under the peak ($A_{D,G}$) of rGO and rGO:Au-NPx. The peak I in the spectrum of Figure 4.3.9 (a) located at 985 cm^{-1} depicts the second order vibrations for silicon wafer substrate [42]. The silicon peak was present in all the samples with the exception of rGO:Au-NP (4.88 at. %). The intensity of Si peak is very high and it was removed to avoid peaks II and III suppression. The spectrum for Au nanoparticles (see Figure 4.3.9 (a)) does not show D or G peak, implying the absence of carbon atoms in the sample.

The phonon vibrations associated with Au can be observed around 1318 cm^{-1} and

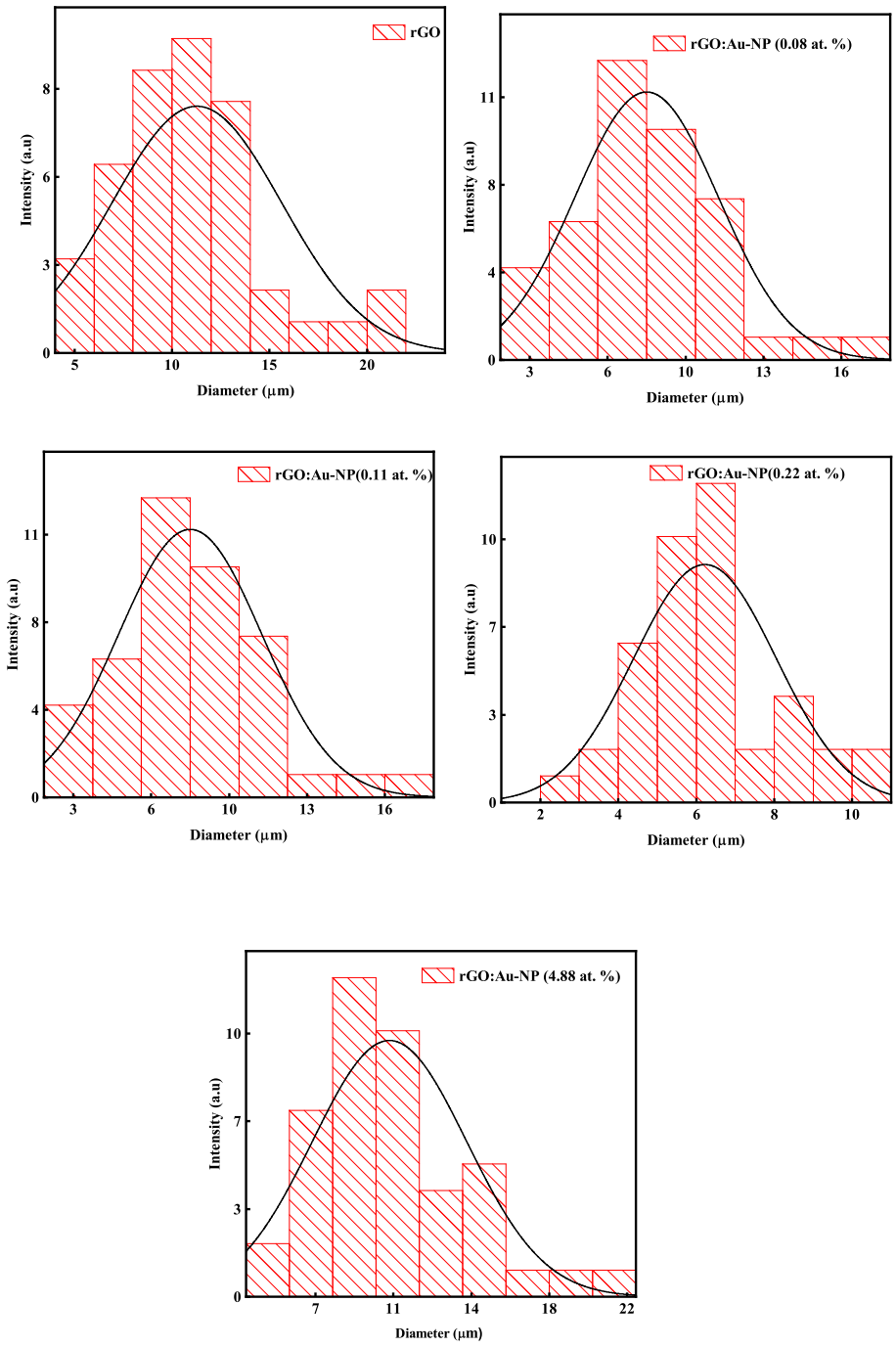

Figure 4.3.7: Histogram showing the grain size distribution of rGO and rGO:Au-NPx extrapolated from SEM images.

1462 cm^{-1} [43]. Sample labelled as (b) is rGO which has the usual D, G and 2D as expected for an unfunctionalized GO [44, 45]. The 2D depicts the presence of few layer of graphene [46], however, with Au functionalization, the possibility of extrapolating the number of layers may become challenging due to the interaction between the car-

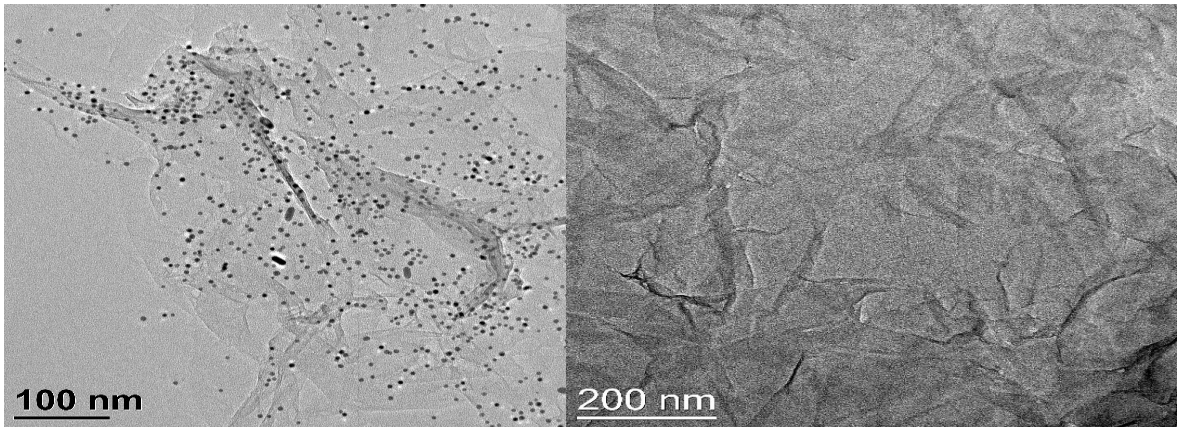

Figure 4.3.8: The TEM images of samples considered in the study. rGO:Au-NP (4.88 at. %) composite (left) and rGO (right).

bon and Au atoms.

The D peak for samples labelled (c)-(e) are in 1330 cm^{-1} to 1350 cm^{-1} range as previously reported by Gupta *et al.* [47]. D and G peaks are prominent in all of the samples, however, the signal for 2D is prominent for (b) and weak for samples (c) to (d).

A variation in the height of the D and G peaks as the concentration of Au increases as expected [48]. The variation is attributed to effect of atomic interaction of the Au with GO and may be caused by the sensitivity of the excited electron and hole scattering [48]. The excitation occurs with the assumption that the origin of the scattering is due to phonon emission and electron – electron collisions [48]. The shifts in the peaks can also be due to local strain as proposed by Zheng *et al.* [49]. Without the effect of Au-NP, the Fermi level in graphene is relatively close to the Dirac point (conical point) in its band structure [50]. The introduction of Au-NP causes a shift in the Fermi level [50, 51].

Impact of the Fermi level shift causes the mobility of charges from graphene to Au-NP which leads to an induction of graphene p-type doping. The result of the charge transfer is evident from difference in the work function of Au ($\approx 5.4\,\mathrm{eV}$) and graphene ($\approx 4.5\,\mathrm{eV}$) [50, 51]. There is also a possibility of electron transfer from Au to graphene due to hot electrons from the decomposition of the surface plasmon of Au-NP [50, 51]. The mobility of the electrons can be associated with the excitation of the atoms created

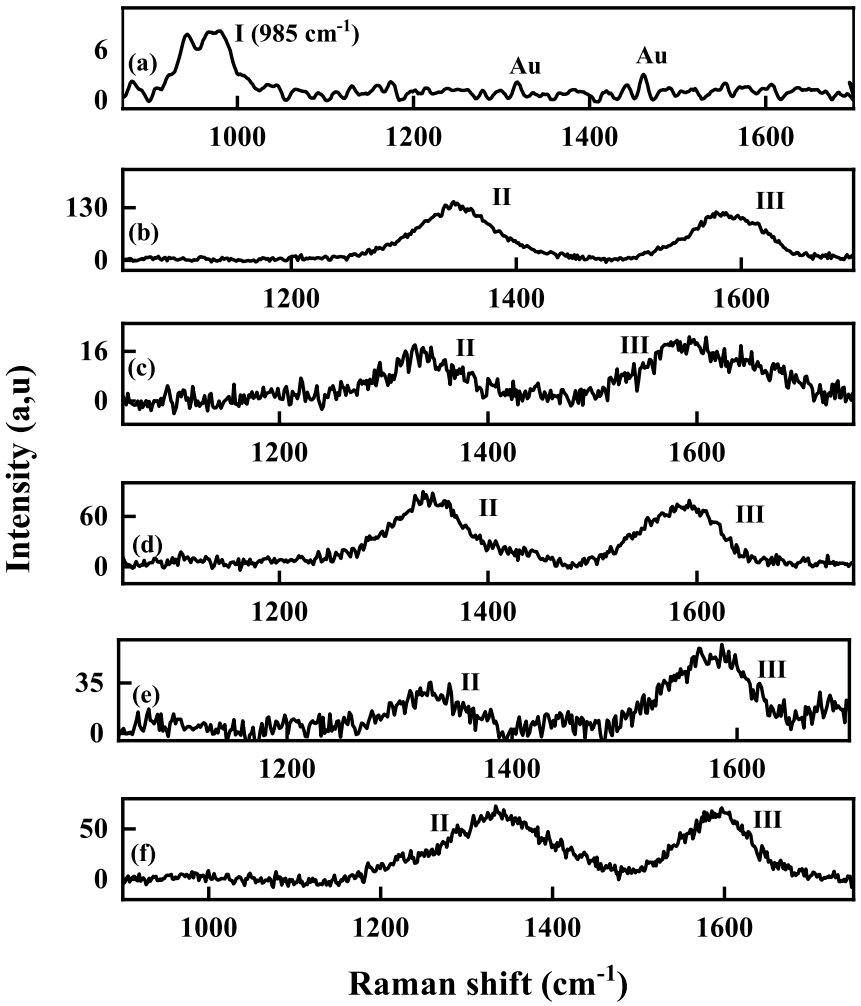

Figure 4.3.9: Raman spectra for Au-NP, rGO and rGO:Au-NP for various concentrations (a) Au-NP (b) rGO (c) rGO:Au-NP (0.08 at %), (d) rGO:Au-NP (0.11 at.%), (e) rGO:Au-NP (0.22 at.%) and (f) rGO:Au-NP (4.88 at.%). The numbering of the peaks are as follows: I – Si peak, II – D peak, III – G peak

.

by the 532 nm laser used in the Raman spectroscopy measurements [49].

An interesting observation is noted in the Raman spectra when Au-NP concentration was increased to 4.88 at.% as shown in Figure 4.3.9(f). A complete disappearance of the silicon wafer substrate peak at 985 cm^{-1} was observed in comparison with all other samples (Figure 4.3.9 (b)-(e)). The disappearance of the silicon peak is explained in the work of Yingying *et al.* [52]. They suggested that the increase of concentration of Au creates a strong resonance energy transference from Au to graphene. The strong resonance transference between graphene and Au can acts as a photoluminescent quencher

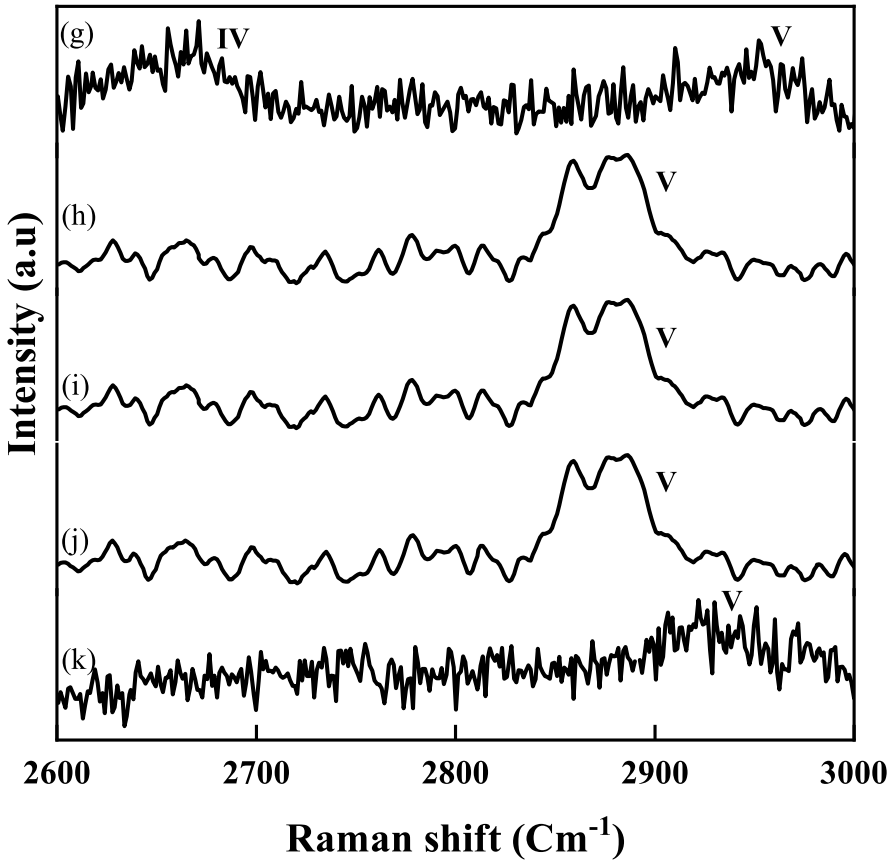

Figure 4.3.10: Raman spectra for rGO and rGO:Au-NP for various concentrations (g) rGO, (h) rGO:Au-NP (0.08 at %), (i) rGO:Au-NP (0.11 at.%), (j) rGO:Au-NP (0.22 at.%) and (k) rGO:Au-NP (4.88 at.%).The numbering of the peaks are as follows: IV – 2D peak, V – 2G peak. Peaks (h)-(k) has been magnified 10 × for rGO:Au-NP (0.08 at.%), rGO:Au-NP (0.11 at.%) and rGO:Au-NP (0.22 at.%) for clarity.

[52]. One can easily infer that the same action is responsible for the disappearance of the silicon second order peak since the thickness of the substrate was the same for all other samples. Since surface composition is an important factor in PL quenching, the high concentration of Au affect the composition of rGO leading to the disappearance of the Si peak [52].

Figure 4.3.11 is the Raman spectra for rGO:Au-NP(0.22 at. %) and is used to show some intriguing features of the composite. The appearance of the various peak position between $1400\,\mathrm{cm}^{-1}$ and $1500\,\mathrm{cm}^{-1}$ are consequence of local strains from the interactions between rGO and Au-NP [49]. The peaks labelled as D_1 ($1403\,\mathrm{cm}^{-1}$), D_2 ($1425\,\mathrm{cm}^{-1}$), D_3 ($1445\,\mathrm{cm}^{-1}$), D_4 ($1477\,\mathrm{cm}^{-1}$) and D_5 ($1496\,\mathrm{cm}^{-1}$) are defect modes.

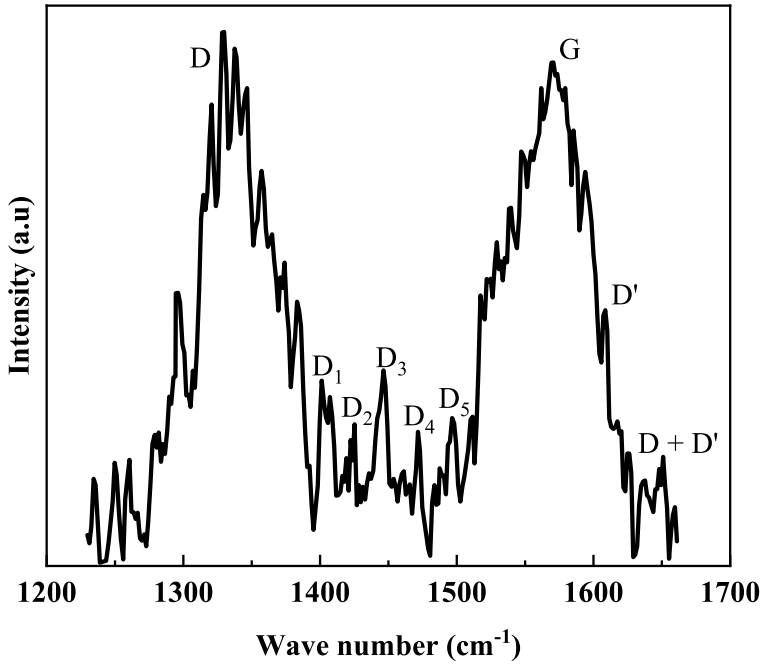

Figure 4.3.11: The Raman spectra for rGO/Au-NP(0.22 at. %) showing features of a highly defected rGO composite. D1 - D5 peaks are defect modes which are attributed to graphene atomic hybridization.

Vecera *et al.* [53] previously reported 1442 cm^{-1}, 1483 cm^{-1} and 1518 cm^{-1} peak positions. The peaks were attributed to vibrations from graphene lattice hybridization where the hybridization is consistent with hydrogenated carbon atoms [53]. The peak positions $D_1 - D_5$ in the current study are in promixity to the previously reported values of Vecera *et al.* and Liu [54], hence can be attributed to graphene related lattice hybridization. Moreover, there is also an appearance of a weak 2D peak at the position 2670 cm^{-1}. The weakness is due to strong dominance of the Au-NP in the bonding of the carbon atoms which shifts the Fermi level from the Dirac position [46].

Figure 4.3.12 shows the de-convolution of D and G peaks for all the samples considered after baseline subtraction using Gaussian function from Originlab software. Peak V and VI in the case of (c) and (d) are defect peaks originating from oxygen presence and crystallinity of the rGO-Au-NP nanocomposite [54]. Table 4.3.2 shows the position, width and area of the peaks that were extrapolated from the deconvoluted peaks of Figure 4.3.12. The I_D/I_G ratios were calculated from the peak height intensity of the D and G peaks. There is an initial decrease in the value of the ratio of rGO:Au-NP

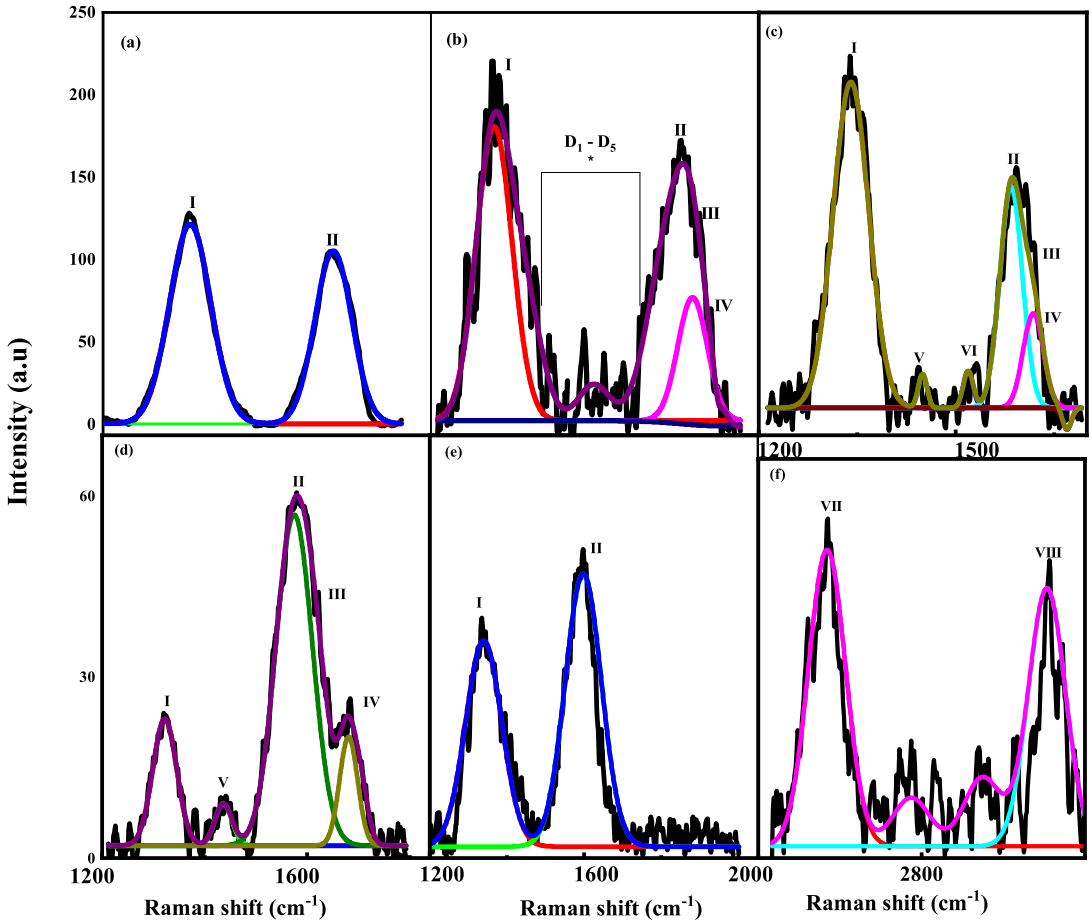

Figure 4.3.12: Raman spectrocopy plots of rGO:Au-NP showing first order deconvolution of D and G peak with a Gaussian fit for both rGO and (rGO:Au-NP)x. (a) rGO, (b)rGO:Au-NP, (0.08 at.%), (c) rGO:Au-NP(0.11 at.%), (d)rGO:Au-NP(0.22 at.%), (e) rGO:Au-NP(4.88 at.%), and (f) second order 2D peak for rGO. The deconvoluted peaks are as follows I -D Peak, II- G peak, III- D′ peak, IV- D″, V - VI are defect mode vibrations, VII - 2D peak and VIII-2G peak. The different colours represents the different peak positions.

(0.08 at.%) (1.20) in comparison with rGO (1.22) and this was followed by slight drop in the value of I_D/I_G with an increase in the concentration of Au (0.11 at.%) (1.18). A further drop in the I_D/I_G ratio (1.18 $\rightarrow$ 1.15) was observed with further increase in concentration of Au-NP (0.11 at.%) to (0.22 at.%).

The quality of graphene material has been suggested to impact the value of the D band [55]. Although all the samples considered in the study as discussed in Section 4.2.3 were prepared under the same condition, the samples were reduced and functionalized separately. The preparation procedure could significantly impact the quality of the sample [55]. This may be the reason for the low intensity of the D and G peaks in

Table 4.3.2: The various position, width and area of the peaks in the Raman spectra of all the samples studied where Position-$X_D(cm^{-1})$, X_G, Area-$A_D(a.u)$,A_G and Width-$W_{D,G}(a.u)$.

Samples	D peak			G peak		
	$X_D(cm^{-1})$	W_D	A_D	$X_G(cm^{-1})$	W_G	A_G
AuNP						
rGO	1347.1	0.7±0.1	9.9±0.1	1587.3	0.7±0.1	8±0.1
rGO:AuNP(0.08 at.%)	1343.6	1.1±0.1	1.6±0.1	1595.2	1.3±0.1	2.3±0.1
rGO:AuNP(0.11 at.%)	1338.9	0.9±0.1	7.2±0.1	1584.21	0.7±0.1	5.6±0.1
rGO:AuNP(0.22 at.%)	1326.7	0.6±0.1	1.9±0.1	1584.7	1.0±0.1	6.5±0.1
rGO:AuNP(4.88 at.%)	1337.2	2.5±0.1	4.0±0.1	1586.8	1.1±0.1	1.5±0.1

Table 4.3.3: Table showing the various position, width and area of the peaks in the Raman spectra of all the samples studied where Position-$X_{2G}\mathrm{cm}^{-1}$ Area-$A_{2D}(a.u)$ and Width-$W_{2G}(a.u)$

Samples	2D peak			2G peak			I_D/I_G
	X_{2D}	W_{2D}	A_{2D}	X_{2G}	W_{2G}	W_{2G}	
AuNP							
rGO	2678.2	0.5±0.1	4.1±0.1	2.9±0.1	0.4±0.1	4.5 ± 0.1	1.22
rGO:AuNP(0.08 at.%)	-	-	-	-	-	-	1.20
rGO:AuNP(0.11 at.%)	-	-	-	-	-	-	1.18
rGO:AuNP(0.22 at.%)	-	-	-	-	-	-	1.15
rGO:AuNP(4.88 at.%)	-	-	-	-	-	-	0.98

.

Raman spectra, which eventually affects the I_D/I_G. With further increase in concentration of Au (4.88 at.%), the value of the I_D/I_G decreases from 1.15 to 0.98 due to the stability of mobile electrons as the population of the atoms of Au increases [29]. A decrease in the I_D/I_G ratio can be attributed to the replacement of carbon atoms or formation of new bonds with Au atoms (C−Au) which can impacts the structure of GO [29].

4.3.5 X-ray photoelectron spectroscopy

The X-ray photoelectron spectroscopy (XPS) spectra of rGO and rGO:(Au-NP)x were obtained using Kratos-SUPRA spectrometer with monochromatic Al−Kα radiation. The excitation energy of the radiation source was set at $hv = 1486.6\,\mathrm{eV}$ with base pressure of $1.2 \times 10^{-8}\,\mathrm{Torr}$. The $Au - 4f_{3/2}$ line set at 83.87 eV was used as a baseline reference for internal energy for charging effect interference. All of the XPS measure-

ments were carried out at room temperature.

It is pertinent to note that the intensity of the XPS spectra depends on the accerating voltage and not necessarily on the sample composition. The comparison of the change in the properties of individual samples is on the peak positions and the associated peak shifts. Additionally, the chemical shift in XPS due to doping or functionalization of GO is insignificant ($\approx 0.5 - 1.5\,\mathrm{eV}$). This is the main reason for negligence of errors in the description of chemical shifts and tabulated values by most reported literatures [56–58]. This is the main reason why there are no indented peaks in the y axis of the spectra for all the samples.

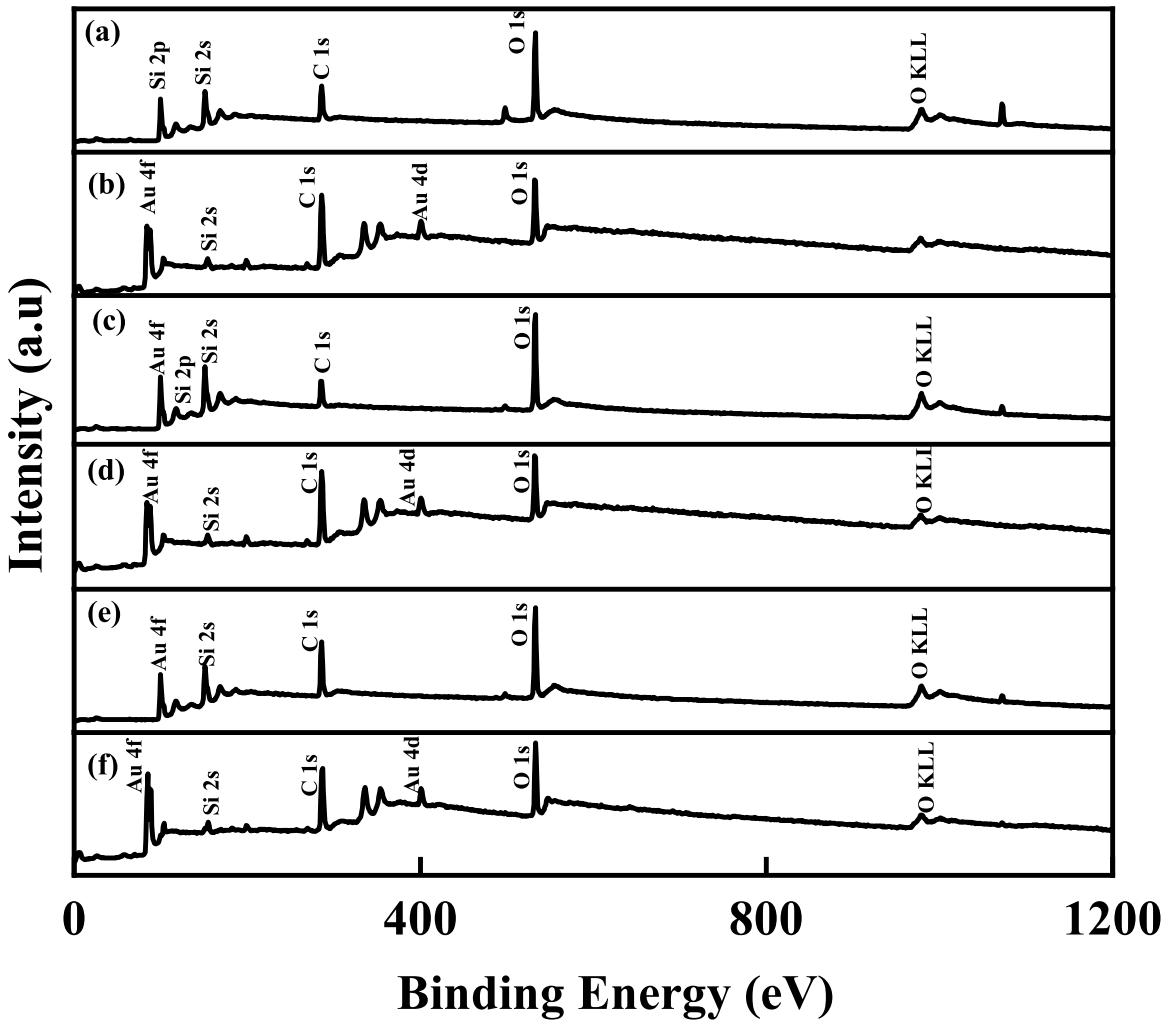

Figure 4.3.13: The XPS wide scan spectra for all the samples where (a) rGO, (b) Au-NP, (c) rGO:Au-NP(0.08 at%), (d) rGO:Au-NP(0.11 at.%), (e) rGO:Au-NP(0.22 at.%) and (f) rGO:Au-NP(4.88 at.%). The indicated peaks show the relevant core level transitions.

Figure 4.3.13 shows the wide scan XPS spectra for all the samples considered in this study. The wide scan indicates the components that are present in the sample. The relevant peaks representing the transition core level states are indexed from previous reports [2, 59]. The peak positions for higher concentration of Au are the same as that of the lower concentration. The unindexed peaks depicted at approximately 370 eV and 1100 eV can be attributed to Auger effects resulting from intra-state transitions of electrons in the excited atoms [60].

The actual concentration of the samples was confirmed by XPS quantification as indicated in table 4.3.4. The core level spectra showing the binding energies for the constituent transition state are depicted in the table 4.3.6. Here, the transition states consist of C 1s, O 1s and Au 4f in the case of rGO:Au-NPx (x=0.08 at.%, 0.11 at.%, 0.22 at.% and 4.88 at. %).

From table 4.3.4, the concentration of O 1s is much higher in C 1s for rGO:Au-NP (0.11 at. %). This can be attributed to strong bonding between carbon and the oxygen atoms i.e C−O, C=O [29]. The weight percentage supports the concentration of different component that are contained in the composites.

Table 4.3.4: The values of the concentration of Au in rGO in atomic percentages as determined by XPS.

	Atomic percentages		
Sample	C 1s	O 1s	Au-4f
rGO	53.37 ± 0.9	46.64 ± 0.9	
rGO:Au-NP(0.08 at.%)	68.04 ± 0.7	31.88 ± 0.7	0.08 ± 0.01
rGO:Au-NP(0.11 at.%)	45.48 ± 1.0	54.52 ± 1.0	0.11 ± 0.01
rGO:Au-NP(0.22 at.%)	61.65 ± 0.8	38.34 ± 0.8	0.22 ± 0.01
rGO:Au-NP(4.88 at.%)	71.14 ± 0.7	23.99 ± 0.5	4.88 ± 0.08

Table 4.3.5: The values of the concentration of Au in rGO in weight percentages as determined by XPS

	Weight percentages		
Sample	C 1s	O 1s	Au-4f
rGO	46.21 ± 0.9	53.79 ± 0.8	
rGO:Au-NP(0.08 at.%)	61.47 ± 0.7	38.45 ± 0.7	0.08 ± 0.01
rGO:Au-NP(0.11 at.%)	38.46 ± 0.9	61.42 ± 0.9	0.11 ± 0.01
rGO:Au-NP(0.22 at.%)	54.57 ± 0.8	45.42 ± 0.8	0.22 ± 0.01
rGO:Au-NP(4.88 at.%)	38.85 ± 0.5	17.45 ± 0.3	43.7 ± 0.4

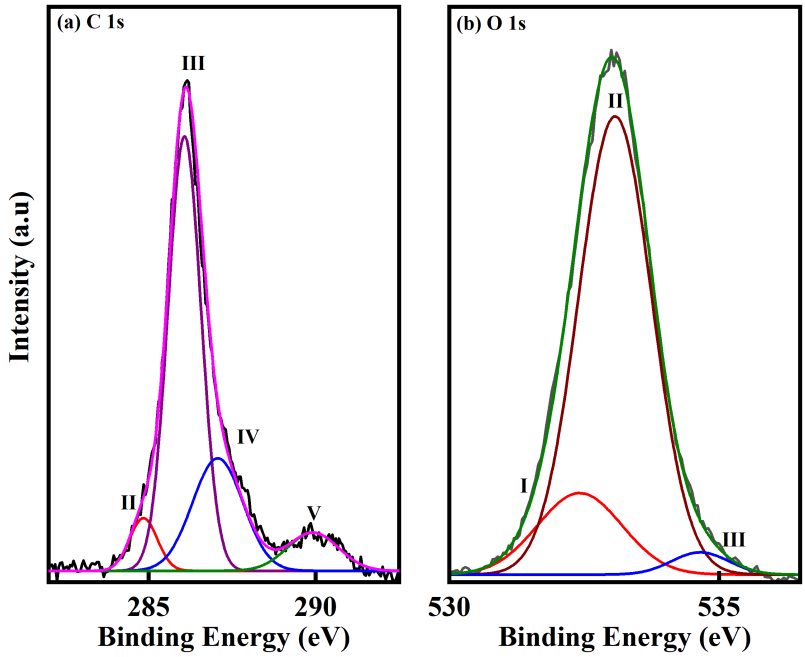

i

*Figure 4.3.14: C 1s and O 1s XPS spectra of rGO without functionalization. (a) C 1s with peak II-*284.8 eV*, III-*286.0 eV*, IV-*287.8 eV *and V -* 289.9 eV *and (b) O 1s with peak I-*532.4 eV*, II -* 533 eV *and III -* 534.6 eV*. The colours differentiates the fitted peak positions.*

The assignment of the C 1s, O 1s and Au 4f peaks in the current study is based on previously reported literature [29]. Figure 4.3.14 shows the de-convoluted XPS spectra for rGO with C 1s and O 1s peak positions using Gaussian function from Originlab software. The various peak positions for all the considered samples are shown in the table 4.3.6.

The C 1s has four prominent peaks which are located at 284.8 eV, 286.07 eV, 287.06 eV and 289.9 eV. The peaks are assigned to the C=C sp^2 clusters, C−O, HO−C=O and

Table 4.3.6: Table showing the extrapolated values for C 1s for all the samples considered. The assignment of the peak position is based on previous literature [2, 59].

	C 1s XPS (binding energy in eV)				
Sample	I	II	III	IV	V
rGO		284.8 ±0.1	286 ±0.1	287 ±0.1	289.9 ±0.1
rGO:Au-NP(0.08 at.%)		284.8 ±0.1	286.1 ±0.1	287.6 ±0.1	290.2 ±0.1
rGO:Au-NP(0.11 at.%)		284.6 ±0.1	285.7 ±0.1	287.1 ±0.1	290 ±0.1
rGO:Au-NP(0.22 at.%)		285.3 ±0.1	285.9 ±0.1	287.2 ±0.1	
rGO:Au-NP(4.88 at.%)	284.1 ±0.1	285.4 ±0.1	286.4 ±0.1	287.6±0.1	288.5±0.1

Table 4.3.7: Table showing the extrapolated values for O 1s for all the samples considered. The assignment of the peak position is based on previous literature [2, 59].

	O 1s XPS (eV)		
Sample	I	II	III
rGO	532.4 ±0.1	533.0 ±0.1	534.0 ±0.1
rGO:Au-NP(0.08 at.%)	532.2 ±0.1	533.0 ±0.1	534.4 ±0.1
rGO:Au-NP(0.11 at.%)	532.0 ±0.1	532.8 ±0.1	534.3 ±0.1
rGO:Au-NP(0.22 at.%)	531.9 ±0.1	532.9 ±0.1	534.3 ±0.1
rGO:Au-NP(4.88 at.%)	532.6 ±0.1	533.5 ±0.1	534.5 ±0.1

O−C=O, respectively [61–63].

Figure 4.3.14 (b) shows the peak position for O 1s spectra which includes peaks at 532.4 eV, 533 eV and 534.6 eV which are assigned to C=O, C−O, C−O [61–63] and chemiabsorbed water molecules [64], respectively. Figure 4.3.15 shows the C 1s and O 1s XPS spectra for rGO:Au-NP(0.08 at. %) where, there is a slight shift to higher binding energy (289.9 eV → 290.2 eV). There is a corresponding downward shift in the O 1s peak positions. The chemical shift in the peak position can be attributed to the effect that Au interaction with carbon atoms in the rGO network. The interaction between C and Au results in weak attachment of Au onto C atoms and redistributions of the atoms in the carbon matrix [65]. A fractional decrease in the energy is observed with Au (0.11 at.%) nanocomposites (shown in Figure 4.3.16) with all the peaks been retained. There is a slight decrease in the peak position 284.8 eV → 284.6 eV which is assigned to $sp^2 - C$ for low values of Au nanocomposites introduction to rGO.

The increase in the concentration of Au causes an increase in the oxidation of carbon atoms. This can be observed in the abrupt increase in the intensity of O 1s peak in comparison with the previous concentration (Au-NP (0.08 at.%)).

The oxidation process of graphene, in some cases, causes a shift in the binding energy and leads to formation of extra peaks in carbon-oxygen bonding structure [61, 66]. Although, the peaks are retained in this case, the cases of (Au-NP (0.11 at.%)) shown in Figures 4.3.16 show similar behavior with (Au-NP (0.08 at. %)) where the peaks are retained with the position undergoing a shift to lower binding energy. In the case of (Au-NP (0.22 at. %)) shown in Figure 4.3.17, shift to higher binding energy with a

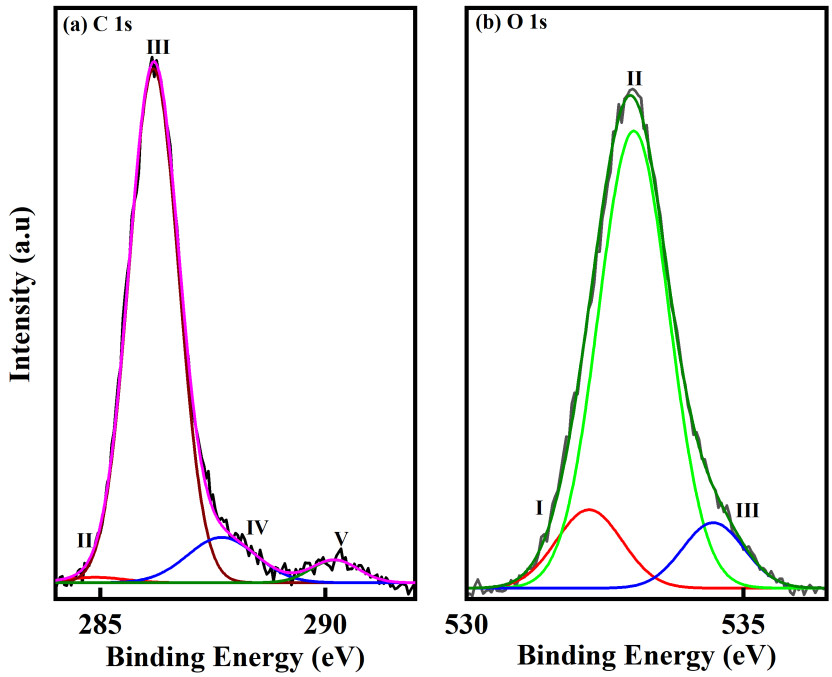

*Figure 4.3.15: XPS spectra for rGO:Au-NP(0.08 at%) with C 1s and O 1s transition states with peak II-*284.8 eV*, III-*286.0 eV*, IV-*287.8 eV *and V -* 290.2 eV *and (b) O 1s with peak I-*532.2 eV*, II -* 533 eV *and III -* 534.4 eV *remained intact with respect to rGO however, a slight shift in the energy levels was observed. The different colours differentiate the fitted peak positions.*

disappearance of peak V. The disappearance of the peak can be attributed to removal of some of the oxygen moieties [29].

For the case of (Au-NP (4.88 at. %)) shown in Figure 4.3.18, peak V reappears signifying an increase in the oxidation of the carbon atoms leading to a reduction in the sp^2 clusters and invariably enhances sp^3 clusters. In terms of the peaks positions, an extra peak is observed at 284.1 eV which is assigned to C−Au. The appearance of C−Au peak is a consequence of the Au atoms attachment to sp^2 clusters [67]. The effect of the attachment causes a decrease in the peak intensity of sp^2-C, which is located at 285.4 eV. The 285.4 eV represents a shift from lower energy in comparison with rGO (284.8 eV). The 285.4 eV peak which is also referred to as defect peak occurs from structural defects of carbon as well as metal intercalation in graphite related defects [67]. There are chances of Au nanocomposites weakly bonding to sp^2 carbon atoms. As indicated by Estrade [67], the bonds between carbon atoms arising from sp^2 configuration

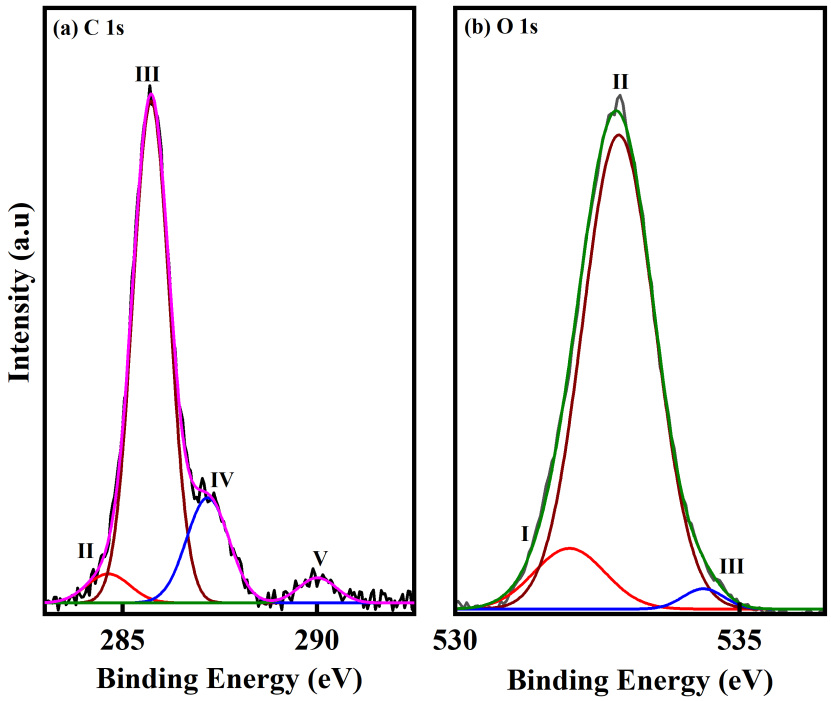

*Figure 4.3.16: The XPS spectra for rGO:Au-NP(0.11 at. %) with C 1s and O 1s transition states with peak II-*284.6 eV*, III-*285.7 eV*, IV-*287.1 eV *and V -* 290.0 eV *and (b) O 1s with peak I-*532.0 eV*, II -* 532.8 eV *and III -* 534.3 eV*. The peak position were retained with a slight shift in the energy positions. The colours differentiate the fitted peak positions.*

can lead to an appearance of a C 1s peak at approximately 285 eV. This C 1s peak is consistent with carbon atoms experiencing sp^2/sp^3 hybridization state transition [68]. In terms of the C−Au peak, there is possibility of Au-atoms participating in transition between carbon (C−C) atoms within ≈ 0.4 eV across a diffusion barrier [69]. The transition can easily occur at ambient temperature hence the weak bonding of C-Au peak that is observed in the spectra [69]. Furthermore, the O 1s also experiences a shift to higher binding energy transitions indicating structural defects from the increase in the concentration of Au-NP [58].

4.3.6 Ultraviolet photoelectron spectroscopy

The ultraviolet photoelectron spectroscopy (UPS) enables the quantification of the density of states (DOS) of the valence electrons in terms of their bonding and transitions

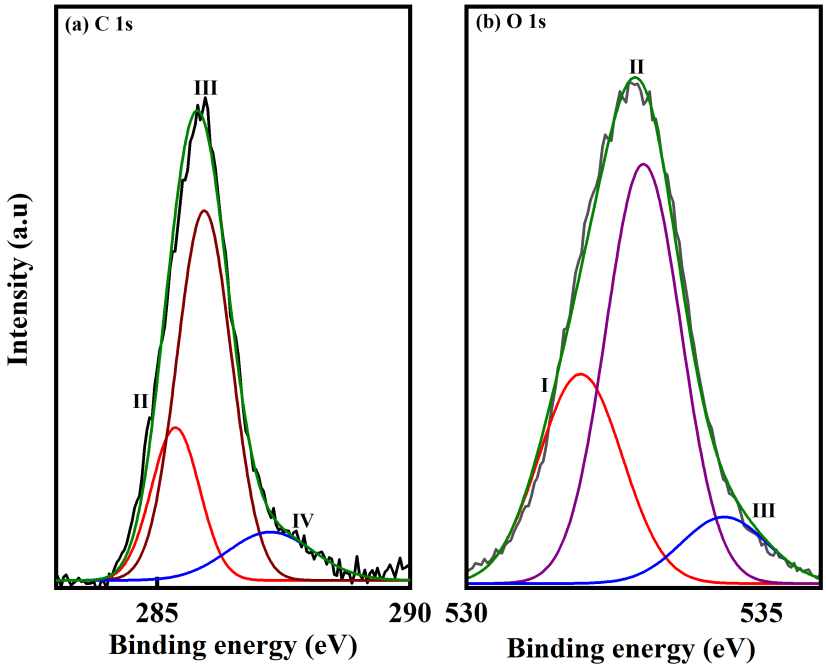

*Figure 4.3.17: The XPS spectra for rGO:Au-NP(0.22 at.%) with C 1s and O 1s transition states with peak II-*285.3 eV*, III-*285.9 eV *and IV-*287.2 eV *and (b) O 1s with peak I-*531.9 eV*, II -* 532.9 eV *and III -* 534.3 eV*. The colours differentiate the fitted peak positions.*

[29]. The UPS spectra were recorded using KRATOS-SUPRA spectrometer with He I ($hv = 20.2\,\text{eV}eV$) and He II ($hv = 40.8\,\text{eV}$) with base pressure of 1.2×10^{-8} Torr. All the measurements were performed at room temperature.

Figure 4.3.19 shows the Fermi levels which describes the highest energy state occupied by the electrons at room temperature. The Fermi levels in the Figure 4.3.19 (a)-(d) indicates the Fermi edges. The tabulated values indicated in Table 4.3.8 show the shift in the Fermi edge of rGO:Au-NPx nanocomposites in comparison with rGO. For instance, in Figure 4.3.19 (a), there is almost an overlap between rGO and rGO:Au-

Table 4.3.8: The Fermi shift of rGO:(Au-NP)x extrapolation in comparison with rGO as obtained from UPS spectra in figure 4.3.19.

Sample	Fermi shift (eV)	Intensity diff. (a.u)	VBM (eV)
rGO	-	-	3.92
Au-NP	-	-	-
rGO:Au-NP(0.08 at.%)	0.17	0.3	4.12
rGO:Au-NP(0.11 at.%)	0.51	4.28	3.67
rGO:Au-NP(0.22 at.%)	0.62	4.12	3.31
rGO:Au-NP(4.88 at.%)	0.73	11.74	3.69

NP(0.08 at.%) which implies insignificant impact on the energy state of rGO caused by Au electrons due to low concentration of Au-NP. Increase in the concentration of Au-NP leads to significant shift away from the Fermi level in comparison with rGO, signifying an increase in the lowest unoccupied molecular orbital (LUMO) states of rGO [70].Figure 4.3.20 and Table 4.3.8 show the extrapolation and values of the VBM. An increase in the concentration of Au results in an increase in intensity of rGO:Au-NP, indicating a disturbance in the electronic configuration of rGO due to the presence of Au atoms. An earlier report [71] showed that the chemical functionalizaton of graphene by donors or acceptors does not impair the material. However, the position of the dirac points undergoes a shift which is consistent with the current study where the Fermi level shift slightly towards higher energy. As reported by Schedin *et al.* [71], the shift in the Fermi level is attributed to the transfer of Au atoms to the $sp^2 - C$ clusters.

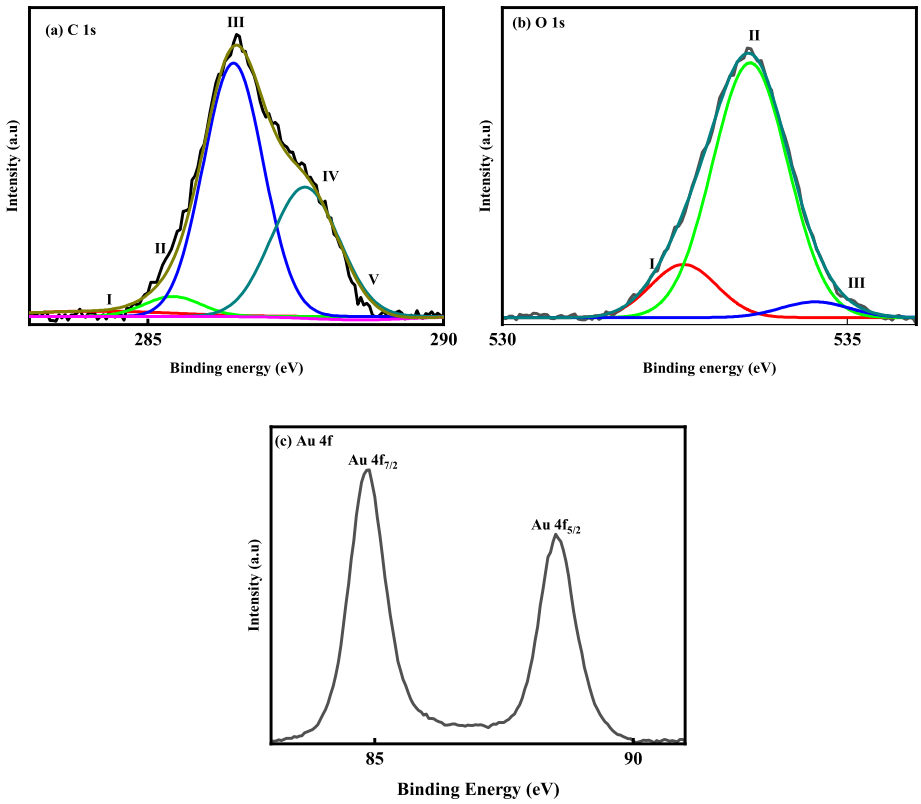

*Figure 4.3.18: The XPS core-level spectra for rGO:Au-NP(4.88 at.%) with C 1s having peak I-*284.1 eV*, peak II-*285.4 eV*, III-*286.4 eV*, IV-*287.6 eV *and V -* 288.5 eV*, (b) O 1s with peak I-*532.6 eV*, II -* 533.5 eV *and III -* 534.5 eV *and (c) Au 4f transition states. The colours differentiate the fitted peak positions.*

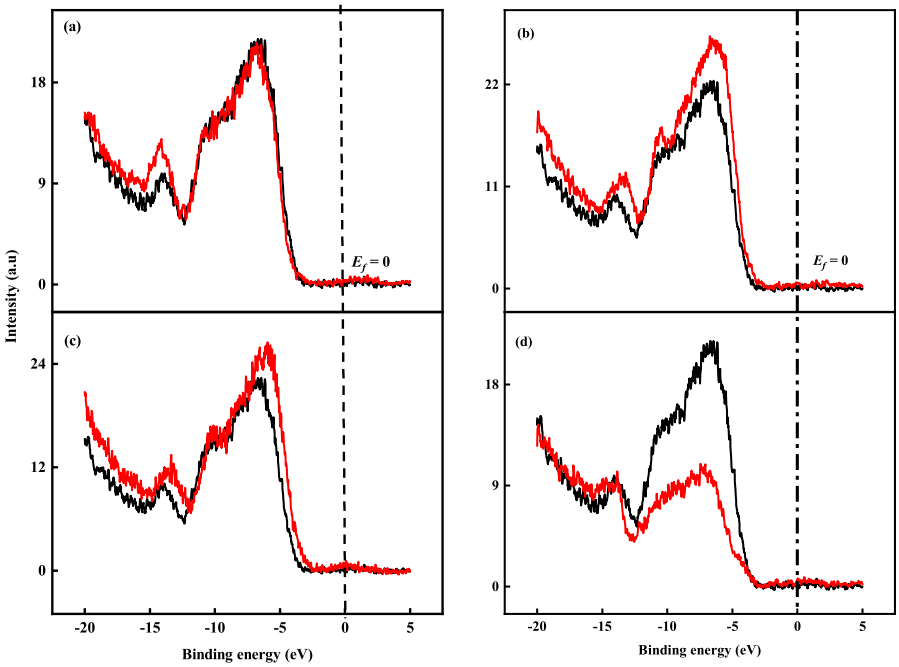

Figure 4.3.19: UPS plot showing the relationship between the Fermi end shift of rGO (black) and rGO:(Au-NP)x (red) where (a) rGO and rGO:Au-NP(0.08 at.%), (b) rGO and rGO:Au-NP(0.11 at.%), (c) rGO and rGO:Au-NP(0.22 at.%) and (d) rGO and rGO:Au-NP(4.88 at.%). The broken line indicates the Fermi level position.

This is consistent with the C−Au peak that is observed in the XPS spectra in section 4.3.5.

The valence band maximum (VBM) which gives the relationship between the electronic structure and carrier transport is an important parameter. The VBM can be uniquely extrapolated from valence band photoelectron spectroscopy (VB-PES) at the point where the density of states (DOS) approaches zero. The technique is described elsewhere [72]. The described extrapolation technique was used for the VBM determination for rGO and rGO:(Au-NP)x from He I. The influence of the defects induced by Au nanocomposites in rGO is evident in the change of the the extrapolated VBM values as the Au concentration changes. With low concentration of Au(0.08 at%), the VBM values deflect from the Fermi edge E_f. However, with further increase in the concentration, the VBM shift towards E_f. The deflection from the Fermi edge by the low concentration is possibly attributed to high band bending at the surface of rGO [73]. Since the VBM is associated with transition of electrons from the valence band

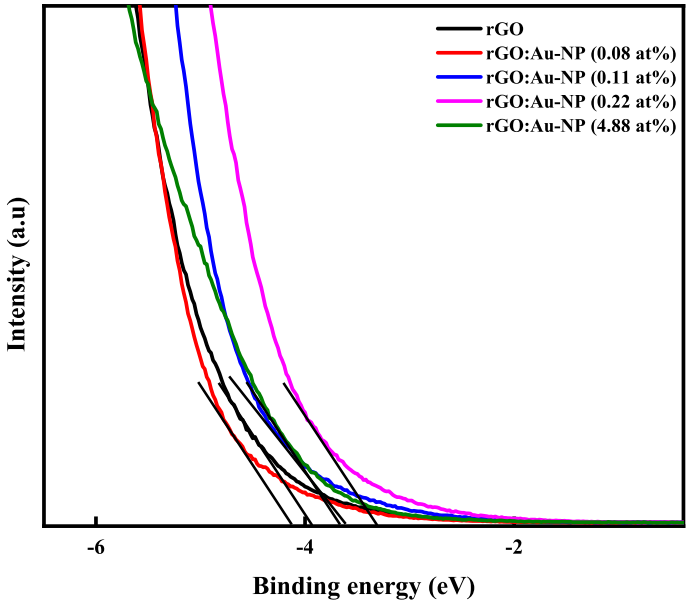

Figure 4.3.20: The extrapolated values of VBM from UPS He I for rGO and rGO:Au-NPx.

to the conduction band, a shift in the Fermi level could contribute to the narrowing of the bandgap of rGO thereby causing band bending [73].

The electronic structure-charge carrier relationship can be seen to be consistency with the VBM and electrical conductivity of rGO and rGO:(Au-NP)x. Figure 4.3.21 and Table 4.3.9 show the UPS He II prominent deconvoluted peaks from the UPS spectra using Gaussian function from Originlab software which identifies the hybridized state of rGO as it relates with Au-NP functionalization.

Using Au-NP as reference, the following prominent peaks can be established. The peaks are $2p-(\pi-\sigma)$ overlap located at $\approx 5.60\,\text{eV}\pm0.02$, $2\pi-\sigma$ appearing at $\approx 6.80\,\text{eV}\pm0.02$, $2s-2p$ mixed state which is located at $\approx 9.60\,\text{eV}\pm0.02$ and $2s$ state which appears at $\approx 14.10\,\text{eV}$. Considering rGO and rGO:Au-NPx, the de-convoluted peaks include $2p-\sigma$ which is prominent at $6.70\,\text{eV}\pm0.02$. Other prominent peaks are assigned to $\approx 4.60-5.60\,\text{eV}\pm0.02$ $(2p-(\pi-\sigma))$ overlap, $\approx 5.90-6.80\,\text{eV}\pm0.02$ assigned to $2p-\sigma$. $\approx 7.90-9.60\,\text{eV}\pm0.02$ is assigned to $2s-2p$ state whereas $\approx 13.60-14.10\,\text{eV}$ is attributed to $2s$ state [74].

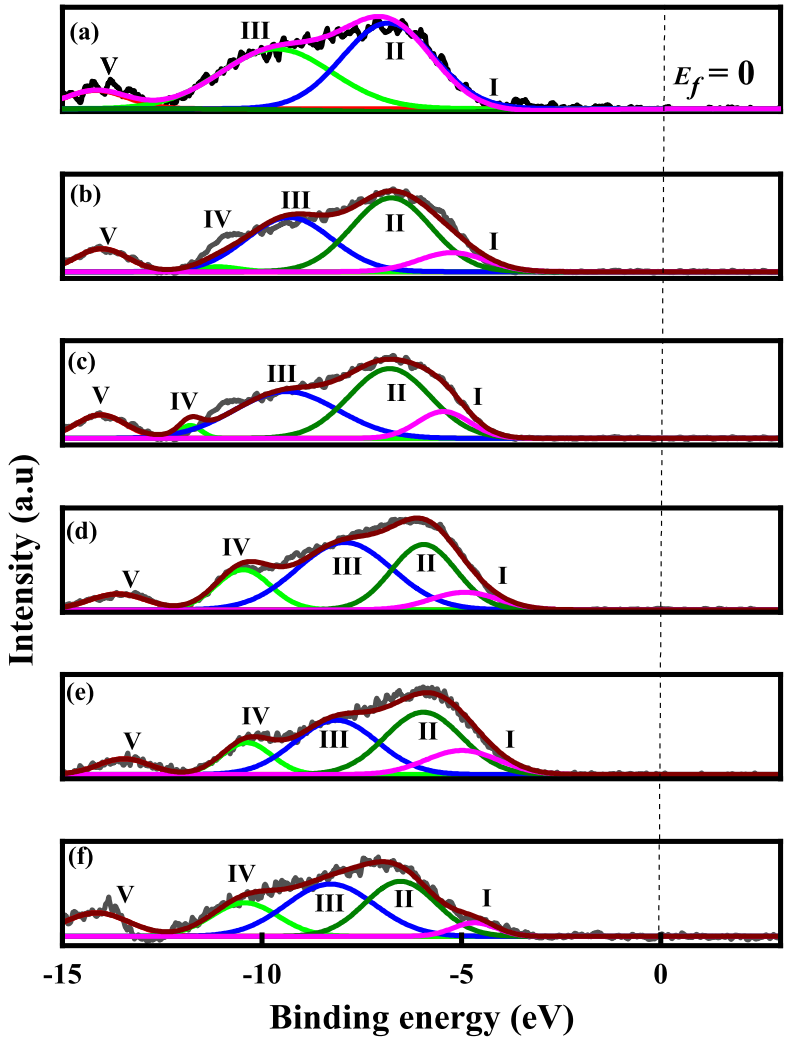

Figure 4.3.21: UPS He II spectra for the density of state measurement below the Fermi level for rGO and rGO:(Au-NP)x. (a) rGO (b) rGO:Au-NP(0.08 at.%) (c) rGO:Au-NP(0.11 at.%) (d) rGO:Au-NP(0.22 at.%) and (e) rGO:Au-NP(4.88 at.%). Peaks: I- 2p-($\pi - \sigma$) overlap, II-2p-σ, III- 2s-2p, IV-2s and V-2s.

The peaks appearing between $\approx 10.1 \pm 0.02$ eV and $\approx 14.1 \pm 0.02$ eV are associated with σ and π bonding of C=O and C−O pair [75–77]. An upward shift towards the Fermi edge is observed for low concentration of Au-NP whereas a downward shift from the Fermi edge is observed for higher concentration of Au-NP. The shift in the transition state of rGO is due to the change in the density of state (DOS) of rGO, resulting from electron transfer between C, O and Au [78]. There is a broadening of the He-II photoemission cross section for $C - 2p$ and $C - 2s$ electrons and it may be likened with corresponding estimations [79]. The DOS increases with respect to π electrons

of rGO:Au-NP(4.88 at.%) as indicated in the downward shift of the $2p - (\pi - \sigma)$ overlap band [79]. The decrease in the $2p - (\pi - \sigma)$ overlap simultaneously causes a blue shift of $2p - \sigma$ band [80]. The decrease in the mixed state overlap and blue shift can be associated with increase in carbon related graphitic networks in rGO. A broadening of the peaks with a decrease in the intensity is observed with an increase in the concentration of Au. A decrease in the intensity is consistent with Raman spectroscopy where the I_D/I_G (rGO:Au-NP(4.88 at.%) decreases in comparison to that of unfunctionalized rGO. Since the formation of carbon lone pair with Au is highly unlikely due to the divacancy pore nature of oxygen [81–83], the oxygen divacancy pores cannot easily bond with Au atoms due to the self-passivation of the oxygen atoms in GO [81–83]. However, the Au atoms tend to attach themselves to the edges of C−O atoms. These new formations can impact the overall properties of GO significantly. Density functional theory has suggested the mechanism of Au weak attachment to carbon [69]. For instance, there have been recent theoretical report by Kobashi [84] where the shift of Fermi level due to impurity doping in diamond was calculated using Korringa-Kon-Rostoker model. Their results showed a shift in the Fermi level as a result of Si and B doping. The shift is presumed to influence the mobility of the carbon atoms since there is a widening or a narrowing of the bandgap. In the current study, the shift in the observed Fermi level due to Au introducion into rGO can also be attributed to attachment on its edges/ surface. The change in the electronic behaviour of rGO due to the influence on Au changes the transition of electrons from the valence

Table 4.3.9: Tabularized prominent peak positions of Au-NP, rGO and rGO:(Au-NP)x as obtained by UPS He II.

Sample	Peak I (eV)	Peak II (eV)	Peak III (eV)
	2p-($\pi - \sigma$) Overlap	2p-σ	2s-2p
Au-NP	5.60 ± 0.02	6.80 ± 0.02	9.60 ± 0.02
rGO	5.20 ± 0.02	6.70 ± 0.02	9.30 ± 0.02
rGO:Au-NP(0.08 at.%)	5.40 ± 0.02	6.80 ± 0.02	9.40 ± 0.02
rGO:Au-NP(0.11 at.%)	4.90 ± 0.02	5.90 ± 0.02	7.90 ± 0.02
rGO:Au-NP(0.22 at.%)	4.90 ± 0.02	5.90 ± 0.02	8.10 ± 0.02
rGO:Au-NP(4.88 at.%)	4.60 ± 0.02	6.50 ± 0.02	8.20 ± 0.02

Table 4.3.10: Prominent peak positions of Au-NP, rGO and rGO:(Au-NP)x as obtained by UPS He II

Sample	Peak IV (eV)	Peak V (eV)
	2s-2p	2s
Au-NP		14.10 ± 0.02
rGO	11.10 ± 0.02	14.0 ± 0.02
rGO:Au-NP(0.08 at.%)	11.70 ± 0.02	14.0 ± 0.02
rGO:Au-NP(0.11 at.%)	10.60 ± 0.02	13.60 ± 0.02
rGO:Au-NP(0.22 at.%)	10.30 ± 0.02	13.40 ± 0.02
rGO:Au-NP(4.88 at.%)	10.40 ± 0.02	14.10 ± 0.02

band to the conduction band [70].

4.3.7 X-rays absorption near edge spectroscopy

The X-rays absorption near edge spectroscopy (XANES) analysis of rGO and rGO:Au-NPx were done using high-energy spherical grating monochromator 20A-beamline at the National Synchrotron Radiation Research Center (NSRRC), Hsinchu, Taiwan. Figure 4.3.22 shows the normalized XANES spectra for rGO and rGO:Au-NPx with the respective π^* and σ^* transition states. As previously reported, the π^* and σ^* are prominent at 284.80 ± 1 eV and 292.10 ± 1 eV, respectively [85–87]. The π^* is the blueprint for an sp^2 C=C bond, whereas σ^* describes the property of an sp^3 tetrahedral C−C bond transition [88]. The transitions indicate the features of a pristine graphitic material indicating three boundaries. The first boundary depicts the π^* transitions which is ascribed to 284.8 eV in the current study. The second boundary comprises of the C−H bond region which is assigned to 288.3 eV and the third region borders the broad region of σ^* transition which is associated with 291.1 eV up till 310 eV [89, 90]. With the action of functionalization, the peak remained intact however, there is an upward shift in the energy levels, as can be observed in Figure 4.3.22. A Gaussian function described in section 3.8 of chapter 3 was fitted to the spectra as shown in Figure 4.3.22 for rGO and rGO:Au-NPx. The peak positions for C K and O K edges are presented in the Table 4.3.11, 4.3.12 and 4.3.13. The Gaussian background was

subtracted to obtain the sp^2 content of π^* transition. The peaks labelled I_1 to I_6 from Figure 4.3.22 are the prominent peaks that describes the bonds that are present in rGO and rGO:(Au-NP)x. Peak I_1 (286.6 ± 1 eV) which is close to the Fermi level is attributed to C−H transition. The transition can be associated with states of π symmetry which lie in the plane of M and L points as observed in the graphene Brillouin zones [91, 92].

Peak I_2 (288.5 eV ± 1) is attributed to C-2p-Au 3d hybridization bonding with the presumable $1s \rightarrow \pi^*$ C=O transition [88, 90, 93]. Moreover, the rGO:Au-NP film is not entirely free of oxygen, hence the peak indicated at I_3 (290.06 eV ± 1) is not C−Au rather C−O−Au. The peak I_3 is attributed to $1s \rightarrow \pi^*$ transitions, which involves the bonding of carbon with oxygenated groups (COOH) [94]. The σ^* peak possesses excitonic features, which may be due to transitions of dispersion-less unoccupied states.

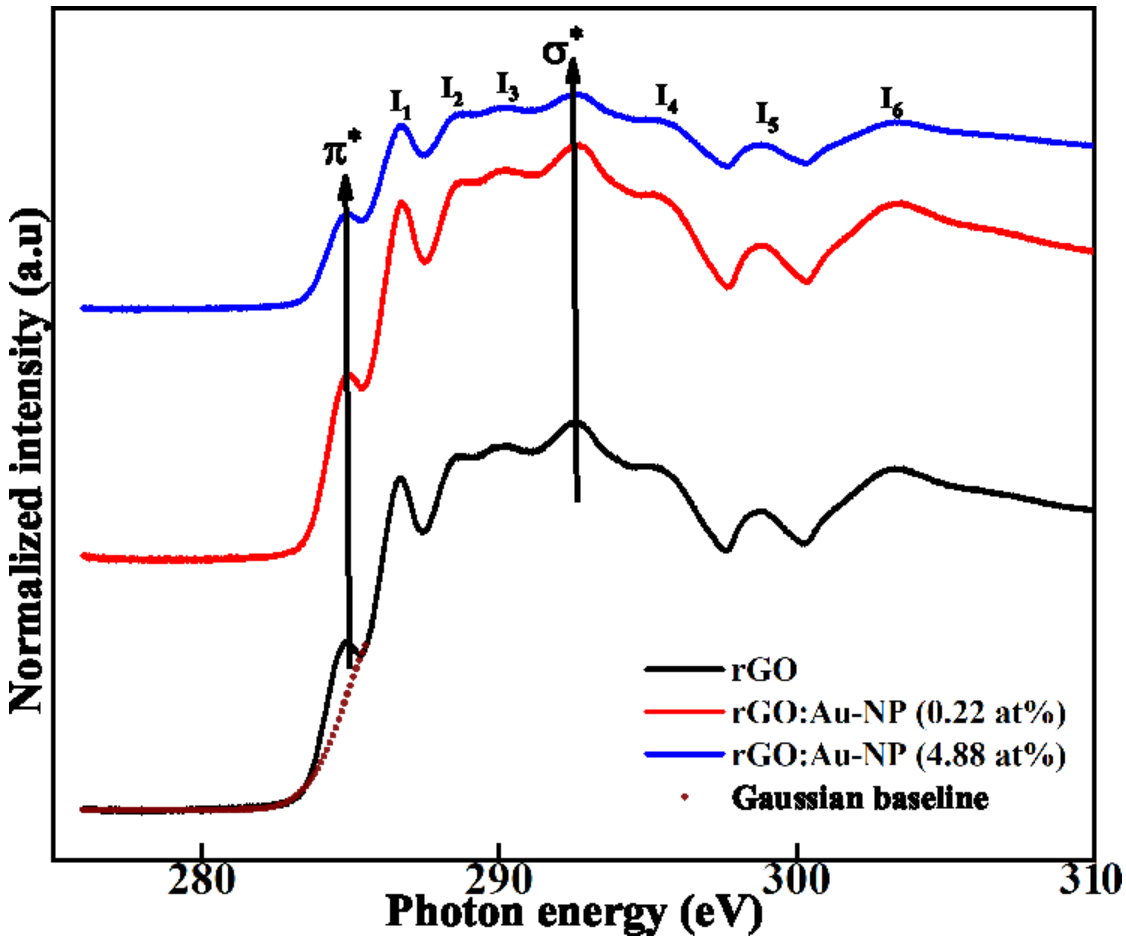

Figure 4.3.22: The C K edge XANES spectra and Gaussian fit used for sp^2 extrapolation for rGO and rGO:Au-NPx (x=0.22 at.% and 4.88 at.%).

The excitonic feature is assumed to have σ symmetry at the Γ point of the graphene Brillouin zone [89, 92]. Peaks above 293 ± 1 eV (Peak $I_4 - I_6$) are mainly attributed to higher-lying conductive states of π and σ symmetry as observed in graphene / graphite density of states [92]. With the inclusion of Au as a functionalizing agent, there is an upward shift 288.58 eV $\rightarrow$288.65 $\pm$1 eV in the energy levels of GO. This can be seen in Figure 4.3.22 with low concentration of Au-NP (0.22 at%).

With further increase in the concentration of Au-NP(4.88 at.%), a shift in the energy levels is observed. Meanwhile, all the bond are consistent for all the samples which clearly indicates a weak attachment of Au-NP to sp^2 carbon atoms. The Au atoms do not substitute the carbon atoms but rather forms an attachment. Figure 4.3.23 shows the normalized O K edge spectra of rGO and rGO:Au-NPx which indicates the bonding activities of carbon with oxygenated groups.

The Gaussian function was also fitted to extrapolate the π^* and σ^* height intensity (shown in Figure 4.3.23). The prominent peaks are represented as π^* (533.7 eV), σ^*(541.3 eV) and I_3 (545.5 eV). The spectra for rGO and rGO:(Au-NP)x show similar trend with an upward shift of peak positions when the concentration of Au increases.

The peak position at 533.7 eV is ascribed to π^* state of C=O originating from carbonyl group which is usually bonded to aromatic rings [86]. Another possibility could be from π^* state of C$-$O which originates from epoxides [86, 95]. Peaks at 541.3 eV and 545.5 eV are assigned to σ^*(C$-$O) and σ^*C=O bonds, respectively [86, 95].

Herein, the carboxyl group (C=O) is mainly due to basal plane bonding of GO [86, 95]. The extrapolated values from the Gaussian fit of C K edge and O K edge are given in

Table 4.3.11: Table showing the approximate extrapolated peak positions of C K edge after Gaussian subtraction.

Samples	C K edge				
	π^* (eV)	I_1 (eV)	I_2 (eV)	I_3 (eV)	σ^*
rGO	284.8 $\pm$1	286.6 $\pm$1	288.5 $\pm$1	290.06 $\pm$1	292.6 $\pm$1
rGO:AuNP(0.22 at.%)	284.7 $\pm$1	286.6 $\pm$1	288.6 $\pm$1	290.1 $\pm$1	292.5 $\pm$1
rGO:AuNP(4.88 at.%)	284.8 $\pm$1	286.6 $\pm$1	288.5 $\pm$1	290.2 $\pm$1	292.4 $\pm$1

Table 4.3.12: The approximate extrapolated $I_4 - I_6$ peak positions of C K edge after Gaussian subtraction for C K edge.

Samples	C K edge		
	I_4 (eV)	$I5$ (eV)	I_6 (eV)
rGO	295.6 ±1	298.7 ±1	303.2 ±1
rGO:AuNP(0.22 at.%)	295.4 ±1	298.8 ±1	303.4 ±1
rGO:AuNP(4.88 at.%)	295.3 ±1	298.8 ±1	303.2 ±1

Table 4.3.14. The corresponding extrapolated sp^2 for C K edge and O K edge are also shown in Figure 4.3.24. The π^*/σ^* ratio shows an increase and eventually drops with respect to rGO:Au-NP((0.22 at.%)). Similar behavior is observed for π^*/σ^* for O K edge. The implication of the behavior is due to the enhancement of sp^3 C−C bond content [93].

4.3.8 Current-voltage technique

In this study, the conductivity of rGO and rGO:Au-NPx were established using the current (I)- voltage (V) technique. The I-V technique was carried out using Keithley model 4200 at Center for Industrial Research (CSIR), Pretoria and Keithley 6487 at University of South Africa, Florida.

The colloidal samples of rGO and rGO:(Au-NP)x (x=0.008 at%, 0.11 at%, 0.22 at% and 4.88 at%) were drop casted on a SiO_2 wafer substrate and air dried. The voltage source was set to voltage range of -1 to 1 volt with an automatic voltage sweep option. The I-V measurements for rGO and rGO:Au-NPx were repeated for 3 cycles for each sample. All measurements were performed at room temperature.

Table 4.3.13: The approximate extrapolated peak positions of O K edge after Gaussian subtraction for O K edge.

Samples	O K edge		
	π^* (eV)	σ^*	I_3 (eV)
rGO	533.7 ±1	541.3 ±1	545.5 ±1
rGO:AuNP(0.22 at.%)	533.7 ±1	541.1 ±1	545.6 ±1
rGO:AuNP(4.88 at.%)	533.6 ±1	541.4 ±1	545.7 ±1

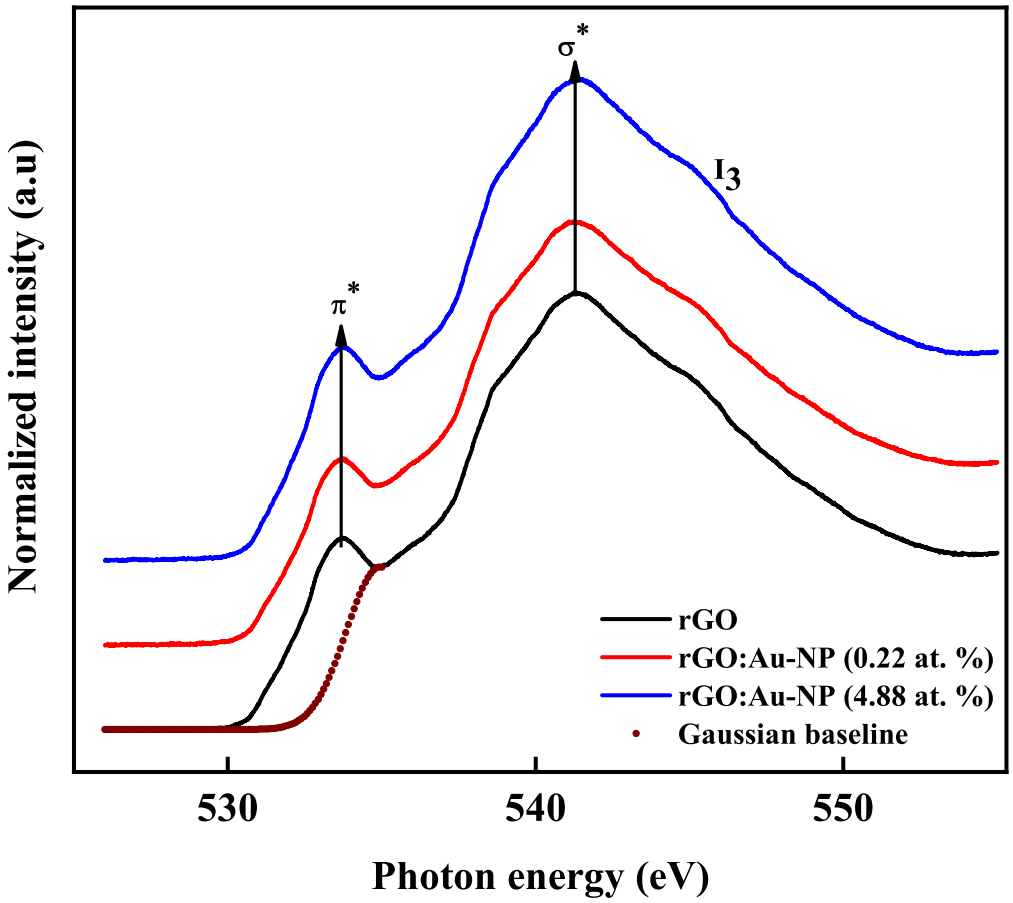

Figure 4.3.23: The O K edge spectra of rGO and rGO:(Au-NP)x fitted with Gaussian function for extrapolation of π^* and σ^*.

Table 4.3.14: Table showing the extrapolated values of π^* and σ^* for rGO and rGO:(Au-NP)x

C K edge				
Samples	$\pi^* sp^2$ content	π^* intensity	σ^* intensity	π^*/σ^* ratio
rGO	0.0090	0.0267	0.0628	0.4251
rGO:Au-NP(0.22 at.%)	0.0106	0.0296	0.0661	0.4475
rGO:Au-NP(4.88 at.%)	0.0110	0.0290	0.0663	0.4378

Samples	O K edge		
	π^* intensity	σ^* intensity	π^*/σ^* ratio
rGO	0.0149	0.0511	0.2918
rGO:AuNP(0.22 at.%)	0.0147	0.0496	0.2969
rGO:AuNP(4.88 at.%)	0.0168	0.0565	0.2980

The I-V curves for rGO and rGO:(Au-NP)x are shown in Figure 4.3.25 and 4.3.26. As indicated in Figure 4.3.26 the current passes through the origin and increases steadily as the voltage increases. These feature are typical of semiconductors [96], which was

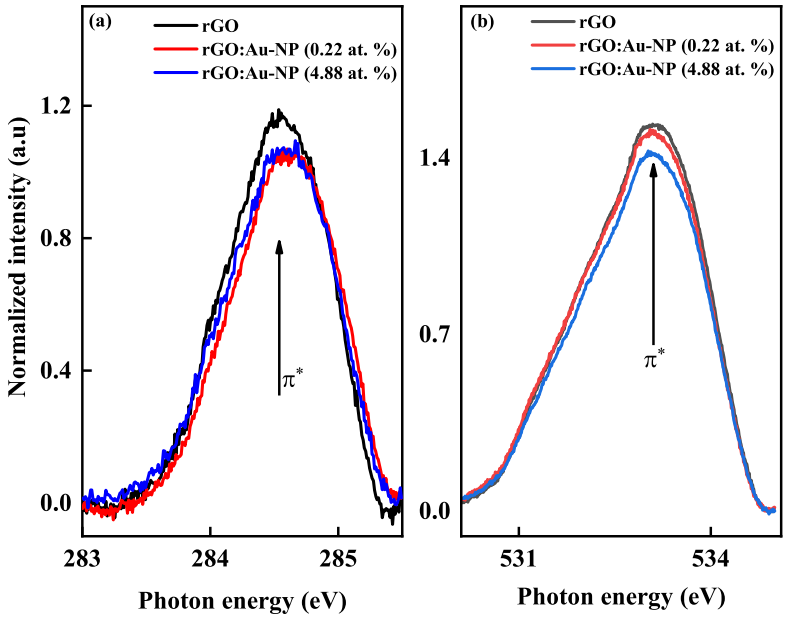

Figure 4.3.24: The extrapolated sp^2 content for C K edge and O K edge with regard to increase in the concentration of Au nanocomposite.

explained briefly in Section 3.9.2. This semiconductor feature is exhibited for both unfunctionalized and functionalized rGO.

It is worth mentioning that in the current study, electrical conductivity was not calculated due to lack of resources for measurement of sheet resistance.The I-V curve gives a picture of the electrical conductivity of the material since both current and voltage are part of the main parameter for consideration for calculating electrical conductivity. Functionalization of rGO with Au changes the electrical conductivity trend of the material as indicated in Figure 4.3.25. With low concentration of Au-NP (0.08), the electrical conductivity feature of rGO:Au-NP composite increases and decreases afterwards with Au-NP concentration (0.11 at.%). The electrical conductivity feature further increased with slight concentration increase (Au-NP: 0.22 at. %) and with higher concentration of Au-NP, the I-V characteristics in terms of electrical conductivity feature of rGO dropped by a significant magnitude as shown in figure 4.3.25. The semiconductor nature of rGO is retained in all the 3 cycles. Although, there is a gap between the forward and reverse bias of the voltage sweep. There is also an overlap of

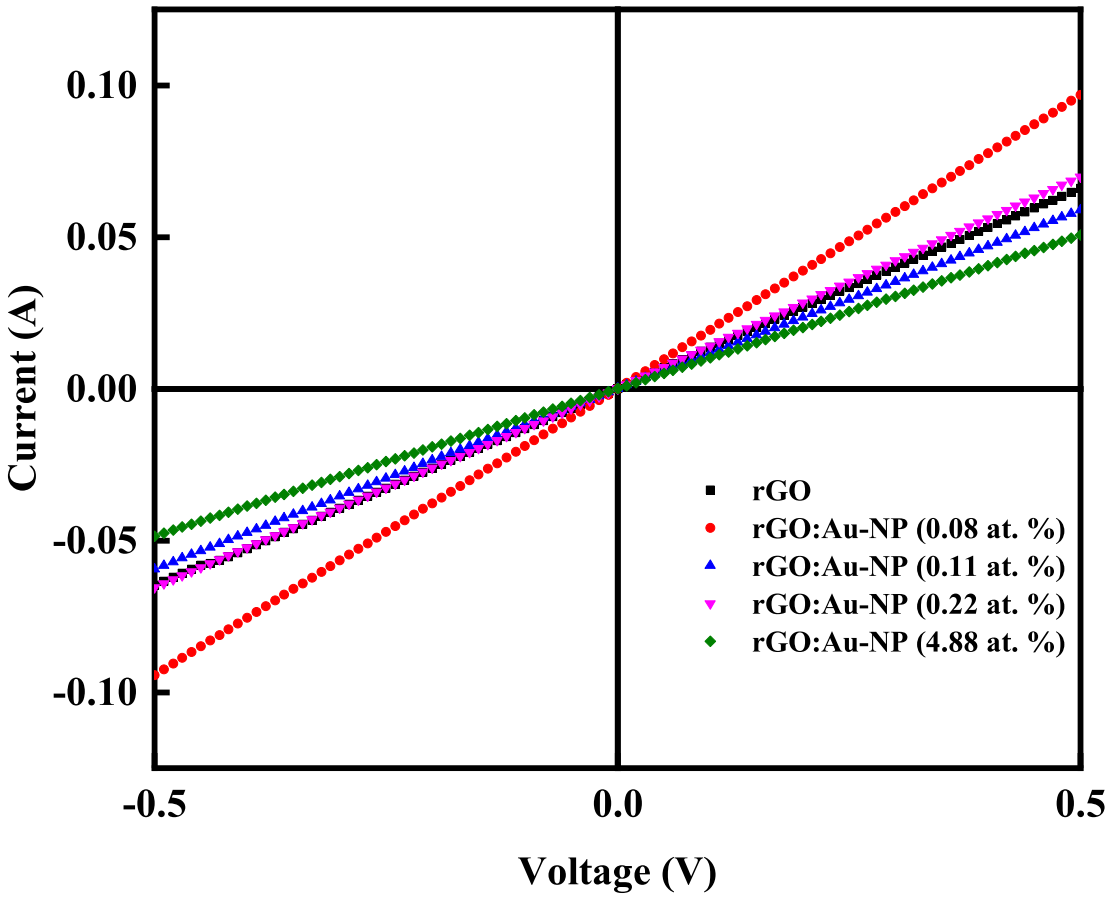

Figure 4.3.25: I-V curve comparison for rGO and functionalized GO with Au for concentrations 0.08 at.%, 0.11 at.%, 0.22 at.% and 4.88 at.%. The plot electrical conductivity levels of rGO:(Au-NP)x in comparison with rGO. Au-NP is conductive as expected and does not necessary compare with rGO.

the curve as the cycle varies. This is mainly due to the charges recombination effect after excitation by the current. Similar effect is observed in functionalized rGO with low concentration of Au (Figure 4.3.27 - 4.3.30). Higher concentrations of Au-NP (4.88 at.%) show different behaviour. The I-V curve of rGO:Au-NP (4.88 at.%) displayed weak ferroelectric behaviour. It is worth mentioning that the behavior is consistent with the previous Section 4.3.4 in Raman spectroscopy. High I_D/I_G values show no sign of ferroelectricity, whereas low I_D/I_G displays ferroelectric behaviour as observed in Figure 4.3.31 , which is consistent with the dielectric charge storage behavior [97]. Charge storage behaviour is feature of semiconductors due to polarization in a dielectric material when an electric field is applied. The effect leads to seperation and alignment

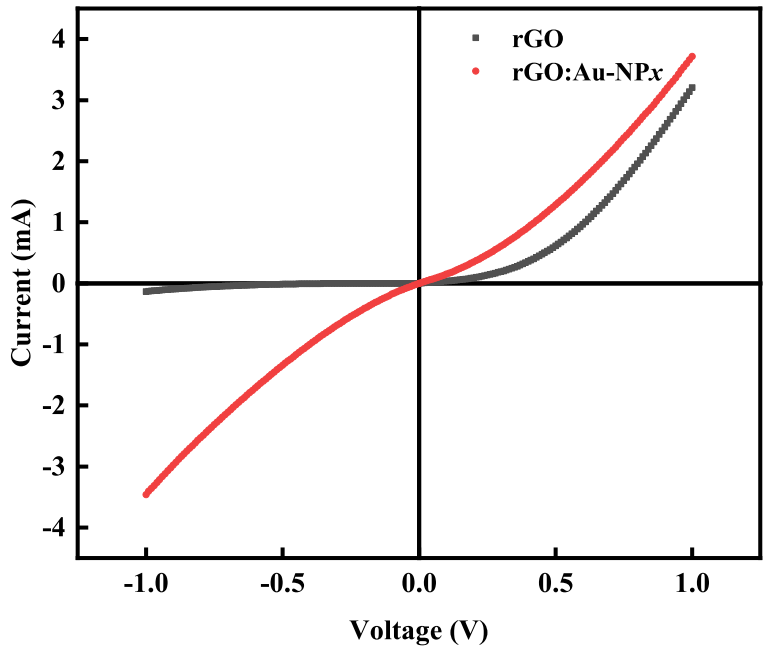

Figure 4.3.26: I-V Curve showing the actual semiconductor behaviour of rGO and rGO:Au-NPx

of electric charges which leads to enhanced charge storage [97]. In the current study, the seperation of the forward and reverse bias is a feature that is similar to charge storage property and can be useful for ferroelectric applications [97]. The semi-logarithm (log) plot shown on the right of each of the I-V plots depicts the variation of the gaps between the reverse and forward bias voltage with respect to the output current. From the semi-log plot (Figure 4.3.27- 4.3.31), no significant difference is observed. This may be attributed to the low defect density in GO due weak attachment of Au-NP to the carbon graphitic network [98]. Another reason for the similar behavior in the log plot could be due to the recombination of electron and holes. Since the recombination is dependent on the voltage sweep time [99], there is possibility of the trend been unaffected since the voltage sweep in the current is automated for the entire I-V measurement.

In general terms, the reduction in the conductivity of graphene can be attributed to reduction in the sp^2 bonding cluster with an increase in the sp^3 cluster [29]. In other words, the reduction in the conductivity of rGO through the displacement of graphene sp^2 clusters with replacement/ attachment of Au-NP. This is in correlation with the work of Xioming *et al.* [49] where the impact of Au-NP caused a red shift (decreased

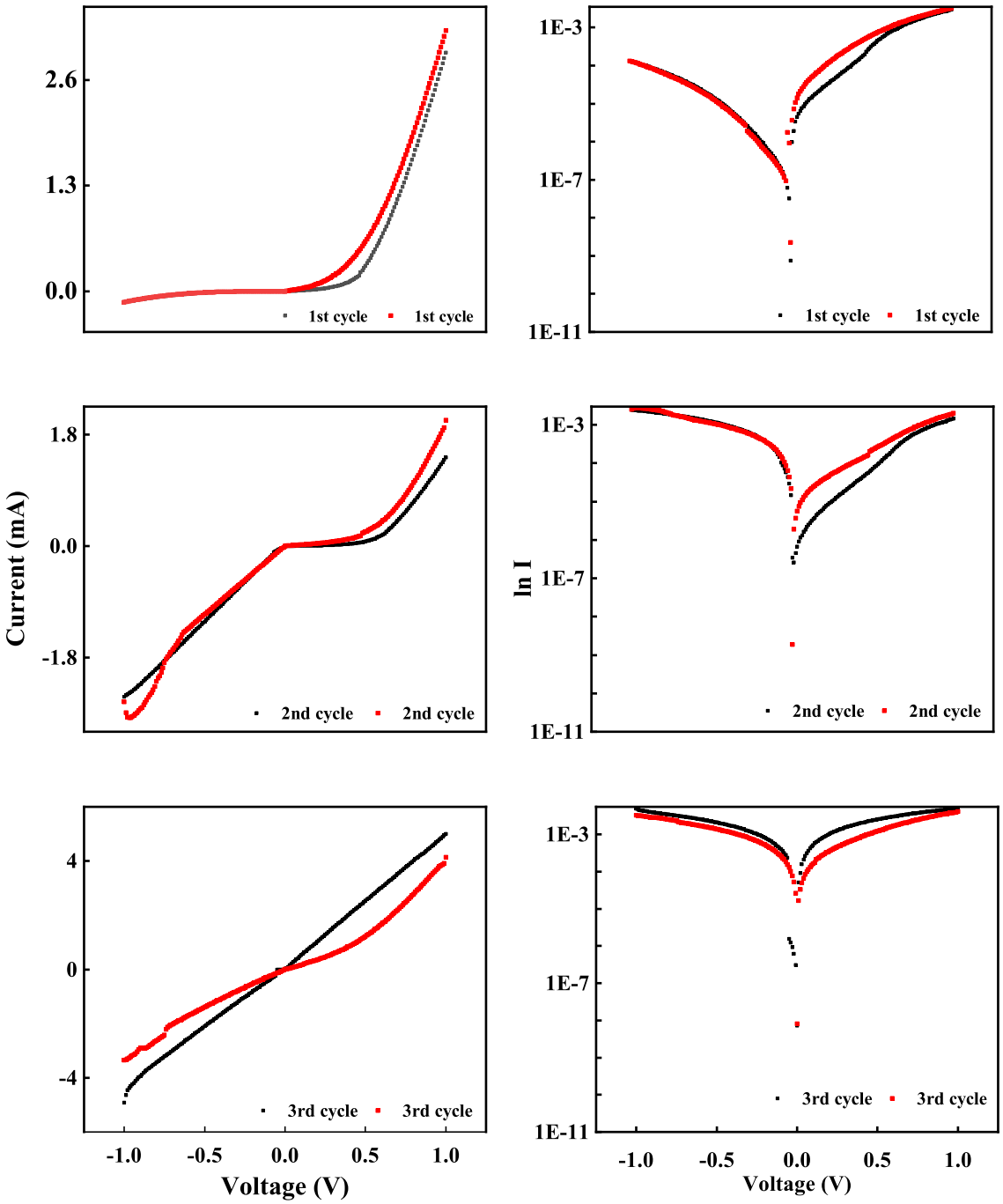

Figure 4.3.27: The 3 cycles I-V curve for rGO without Au functionalization. The red colour represents forward bias and the black represents reverse bias.

in frequency of photon interactions due to defects) in the Raman spectroscopy. The reduction in the I_D/I_G in the Raman secton (see Section 4.3.4) is a consequence of the red shift. As previously mentioned in Section 2.1, graphene is characterized with high electron mobility [10].

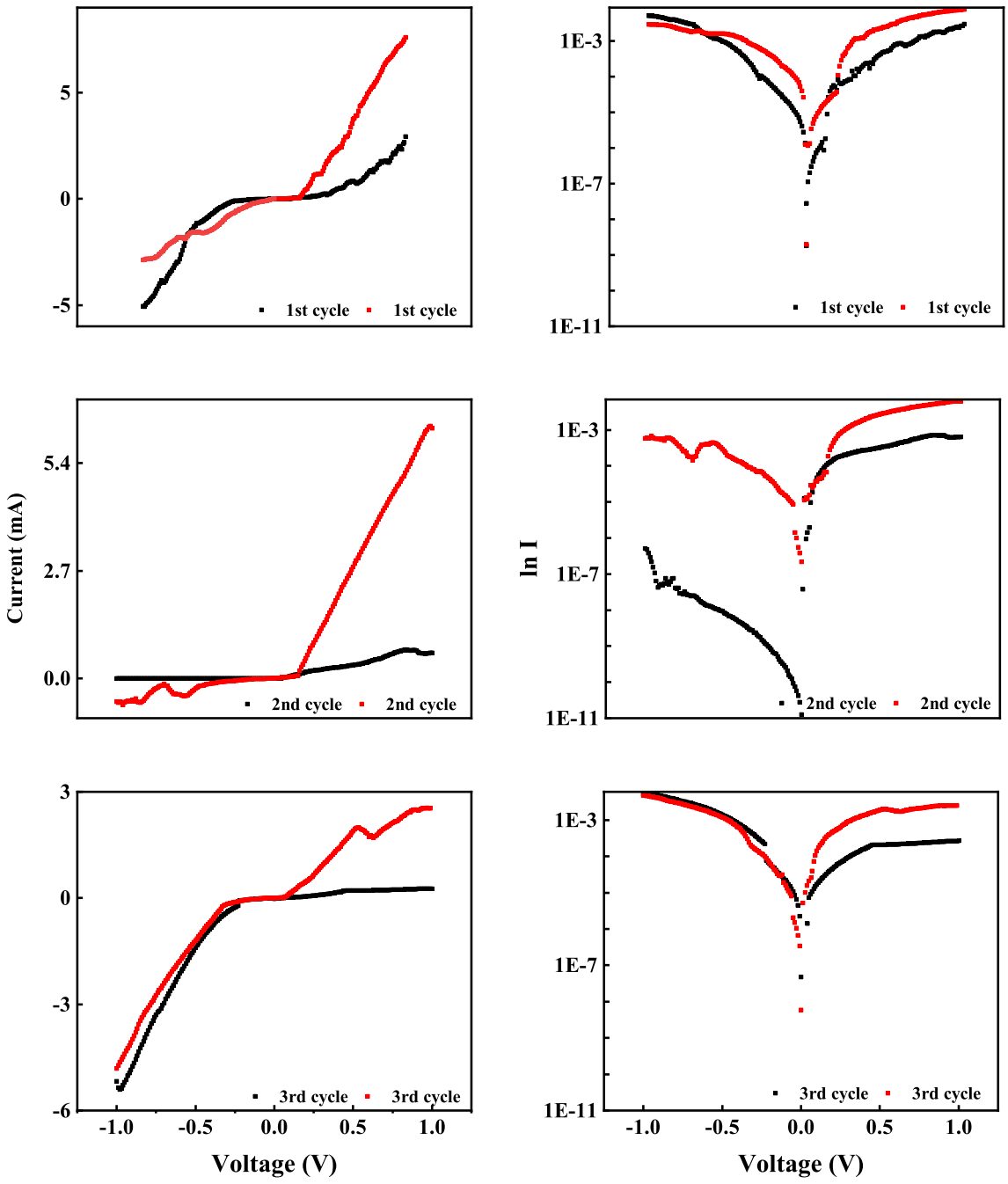

Figure 4.3.28: The 3 cycles of I-V curve for rGO functionalized with Au-NP (0.08 at.%). The red colour represents forward bias and the black represents reverse bias.

The implication of the increase in the graphitic sp^2 cluster will increase the mobility of the inherent electrons however, with the reduction in the sp^2 cluster and eventual increase in the sp^3 clusters of rGO will inevitably lower the mobility of the electrons and lower the conductivity of rGO as suggested by the findings of the present study. Due to the non-uniformity of the structure of rGO, the material comprises clusters

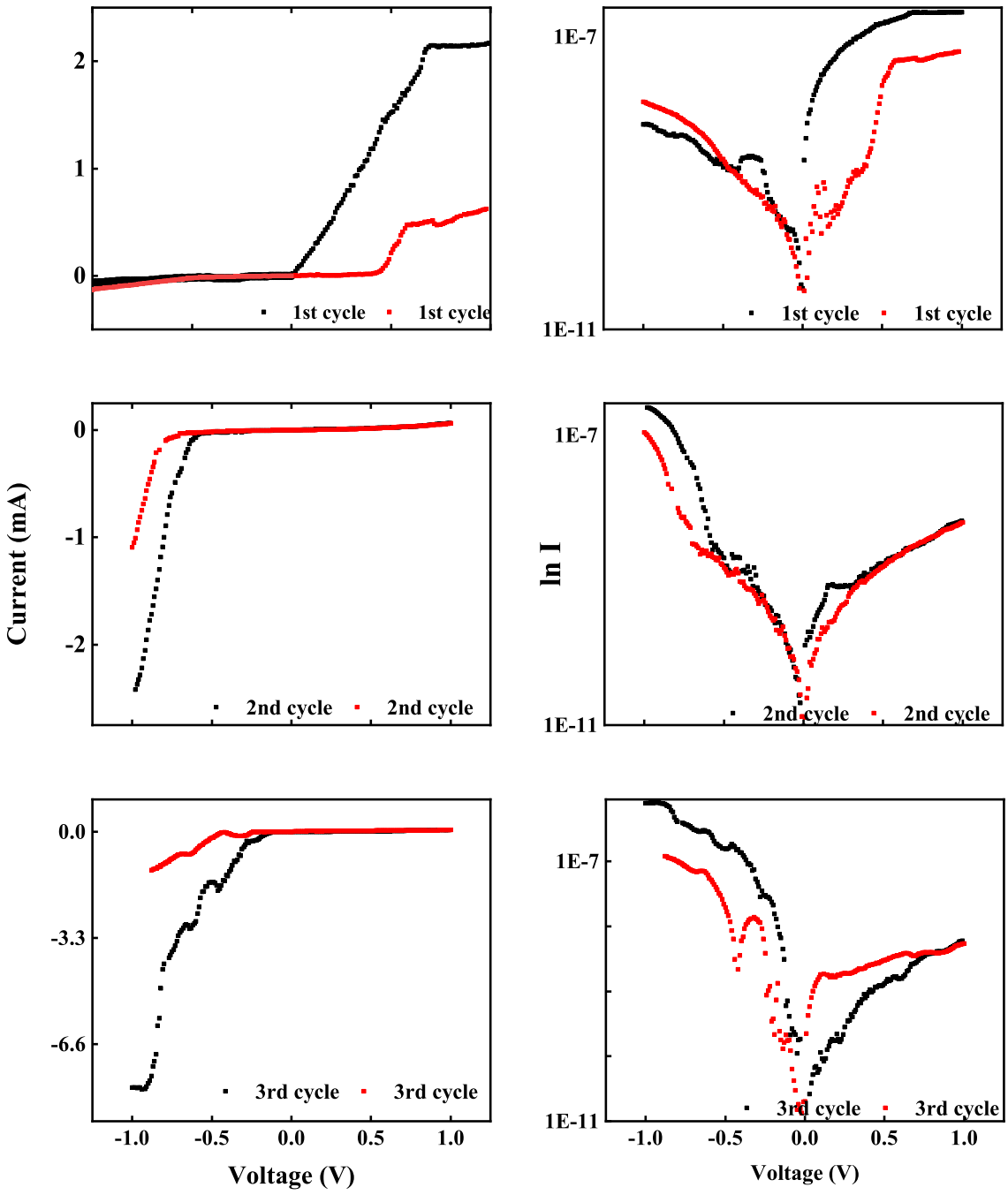

Figure 4.3.29: The 3 cycles of I-V curve for rGO functionalized with Au-NP (0.11 at.%). The red colour represents forward bias and the black represents reverse bias.

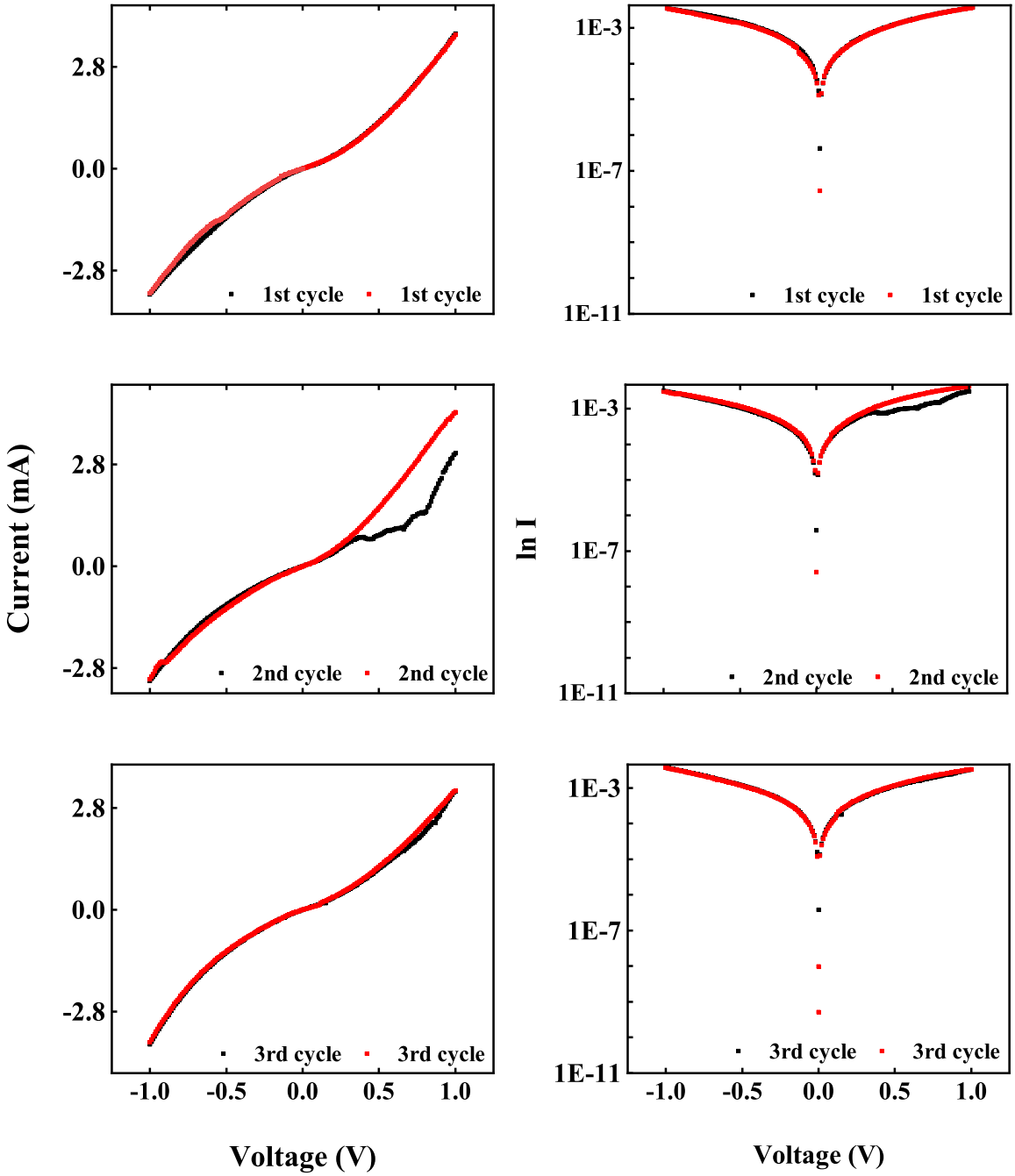

Figure 4.3.30: The 3 cycles of I-V curve for rGO functionalized with Au-NP(0.22 at.%). The red colour represents forward bias and the black represents reverse bias.

of non-deformed part and parts with oxidized graphene. The oxidized part is highly dense and contains the oxygenated function groups (hydroxyl, carbonyl and epoxy) [100]. Regarding theoretical formulations, the oxidized part of graphene produces a dielectric matrix with embedded graphene inclusions [101]. These inclusions create

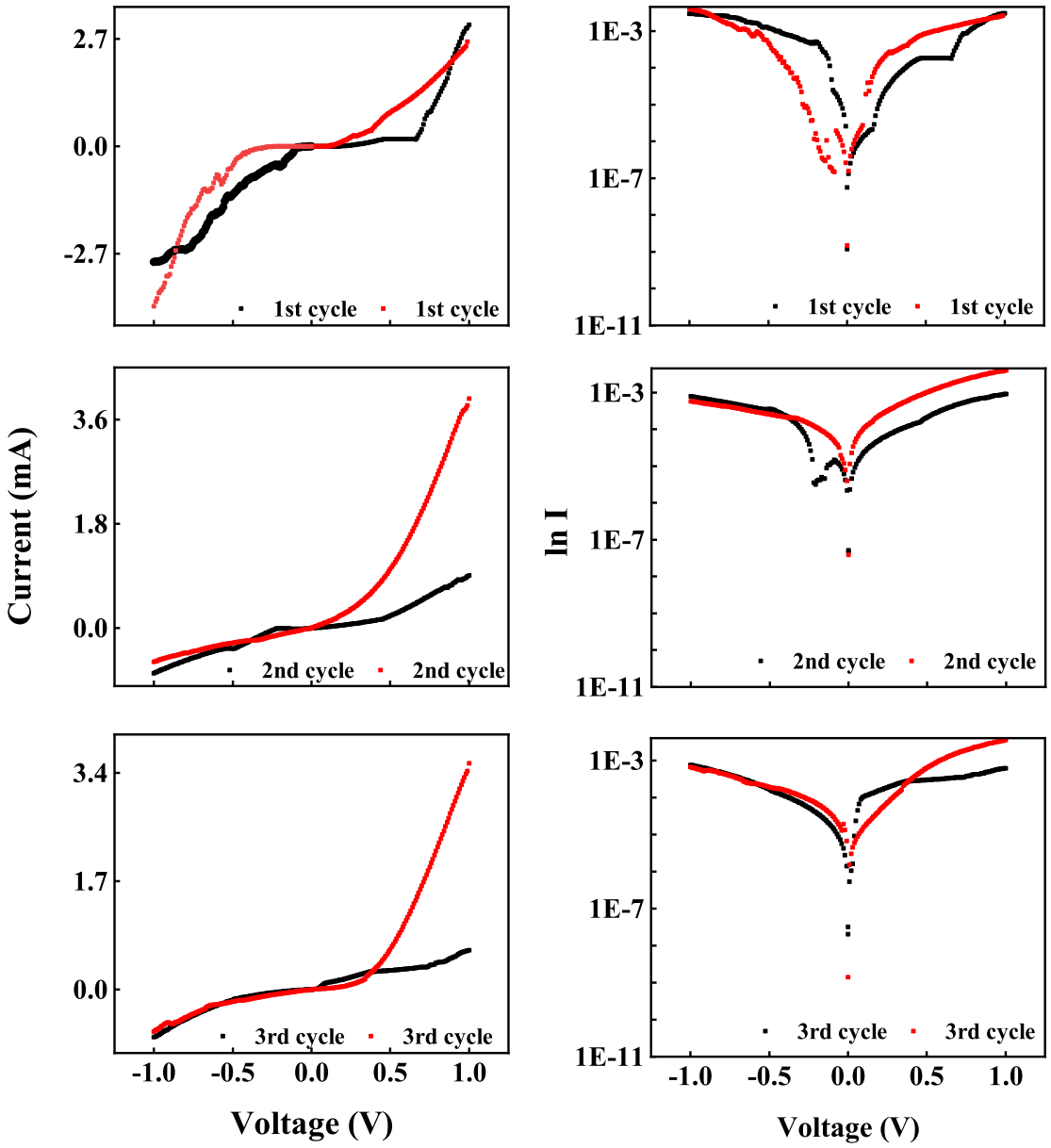

Figure 4.3.31: The 3 cycles I-V curve for rGO functionalized GO with Au-NP (4.88 at.%). The red colour represents forward bias and the black represents reverse bias.

a charge carrier capturing effect (electron and hole traps). This effect also occurs in chemical bonds of rGO and can lower the electrical conductivity of rGO [101].

In summary, with low concentration of Au in rGO, limited impact is induced in the semiconductor behavior of graphene with possible redistribution of atoms whereas at higher concentration, the semiconductor begins to exhibit a ferroelectric property. In the situation where the increase of conductivity of GO is paramount, then low concentration of Au is recommended otherwise high concentration of Au is required to

facilitate the formation of ferro-electric tendency in rGO. This result is also consistent with the reduction in the I_D/I_G value (1.22 to 0.98) in the Raman spectroscopy result given in Table 4.3.2. Although, the I-V measurements did not account for polarization, the ferroelectric behavior suggests that the material studies may be useful in memory devices.

4.3.9 Magnetic properties

The magnetic measurement enables the establishment of the magnetic properties of a material. The M-H loop characterization of rGO:(Au-NP)x in the current study was conducted using a superconducting quantum interference device (SQUID), which is available at the Department of Physics, University of Johannesburg. The SQUID device has a sensitivity of $< \times 10^{-8}$ emu with a base pressure of $< \times 10^{-6}$ Torr and 1 kV power supply. The magnetic field was applied at temperatures ranging between 40 and 300 K. The M-H loop was performed for rGO, Au-NP and rGO:Au-NPx (x=0.22 at.% and 4.88 at.%) at temperature 300 K, 40 K and 2 K. The M-T loop for rGO:(Au-NP)x (x = 0.08 at% and 4.88 . %) was performed to ascertain the possible magnetic phase transition as the temperature varies.

There is a possibility of diamagnetic effect been introduced into the actual magnetization of Au-NP, which is associated with the bulk gold [102]. These diamagnetic effects are mainly due to the silicon wafer substrate, which exhibits diamagnetic properties [103]. The effect was corrected by the background subtraction of the silicon wafer contribution for Au-NP, rGO, and rGO:Au-NP(0.22 at.%) over the entire temperature range. Background subtraction was performed using the method proposed by O'Hara *et al.* [104]. However, the method was ineffective for the case of rGO:Au-NP(4.88 at.%) where there are paramagnetic contribution in the region 5000 - 10000 Oe. Hence, the plots were presented without further analysis.

Figure 4.3.32 shows the M-H loop for Au-NP for temperatures 1.8 K, 40 K and 300 K.

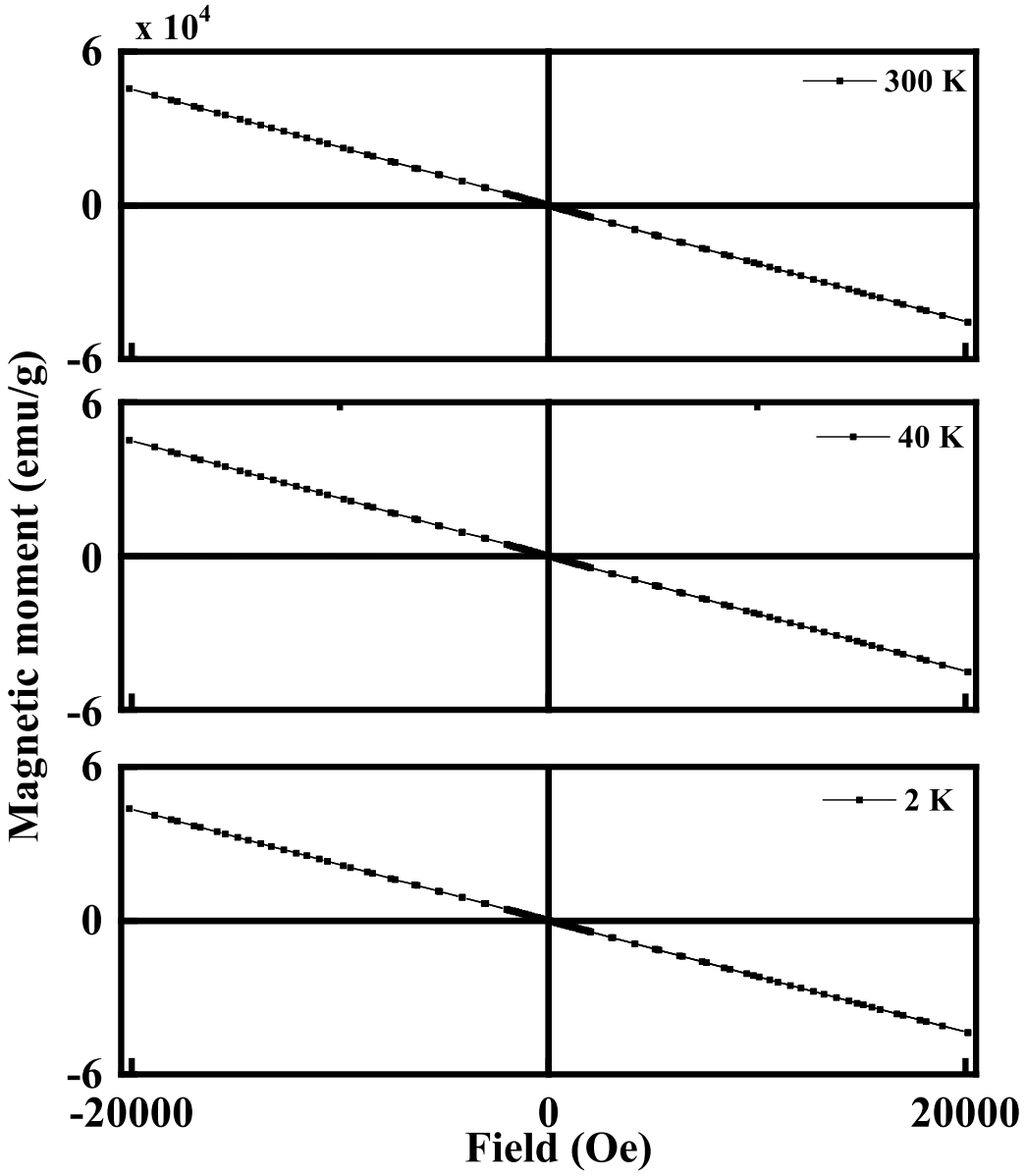

Figure 4.3.32: 36 M-H loop for Au-NP showing diamagnetic properties for temperature 1.8 K, 40 K and 300 K.

It is obvious in all cases that Au-NP remains diamagnetic irrespective of the temperature [102]. The ferromagnetic behavior of other metals is mainly due to the electronic configuration of the 3d energy level [105]. Since there is an imbalance of spin down and spin up electron population during the exchange interaction, a net magnetization is produced [105]. Meanwhile, Au has electronic configuration with outer shells of $4f^{14}5d^{10}6s^{1}$ that also gives an imbalance in the spin dynamic populations. However, from density of state calculations indicates balance dynamics of the spins, thus con-

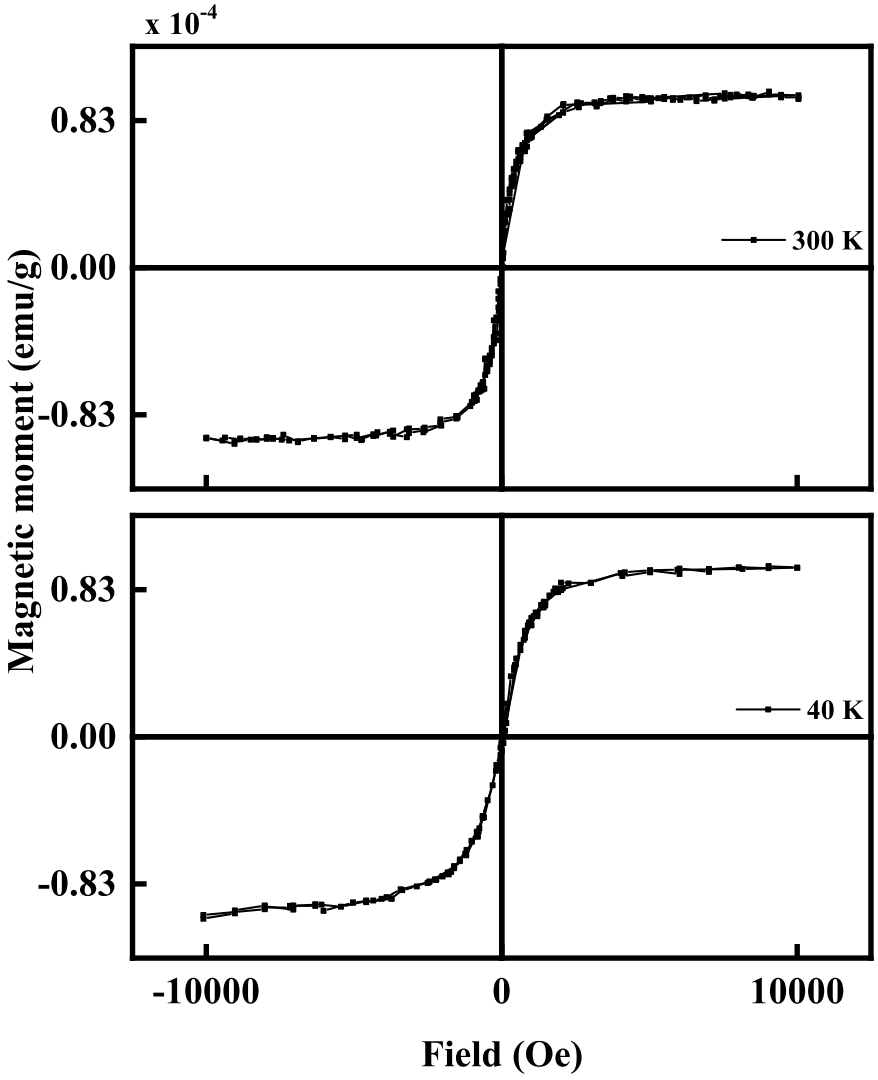

Figure 4.3.33: The diamagnetic corrected M-H loop for rGO for temperature 300 K and 40 K showing weak ferromagnetic property.

firming its diamagnetic magnetic properties [3, 106, 107].

Furthermore, from the direct relationship of magnetization and the applied field of a magnetic material, the susceptibility, which gives the magnetic response of material can easily be extrapolated from the slope. Here, the extrapolated susceptibility is negative, as expected with a magnitude range of -2.18 to -2.27 (dimension-less). [108]. Figure 4.3.33 shows the M-H loop for rGO without functionalization for temperatures 40 K and 300 K. The saturation of the M-H loop was evident, which indicates a significant magnetization [21]. Due to the absence of intrinsic magnetic moment and zero band gaps in GO, it was expected that GO should be nonmagnetic [109]. However, magneti-

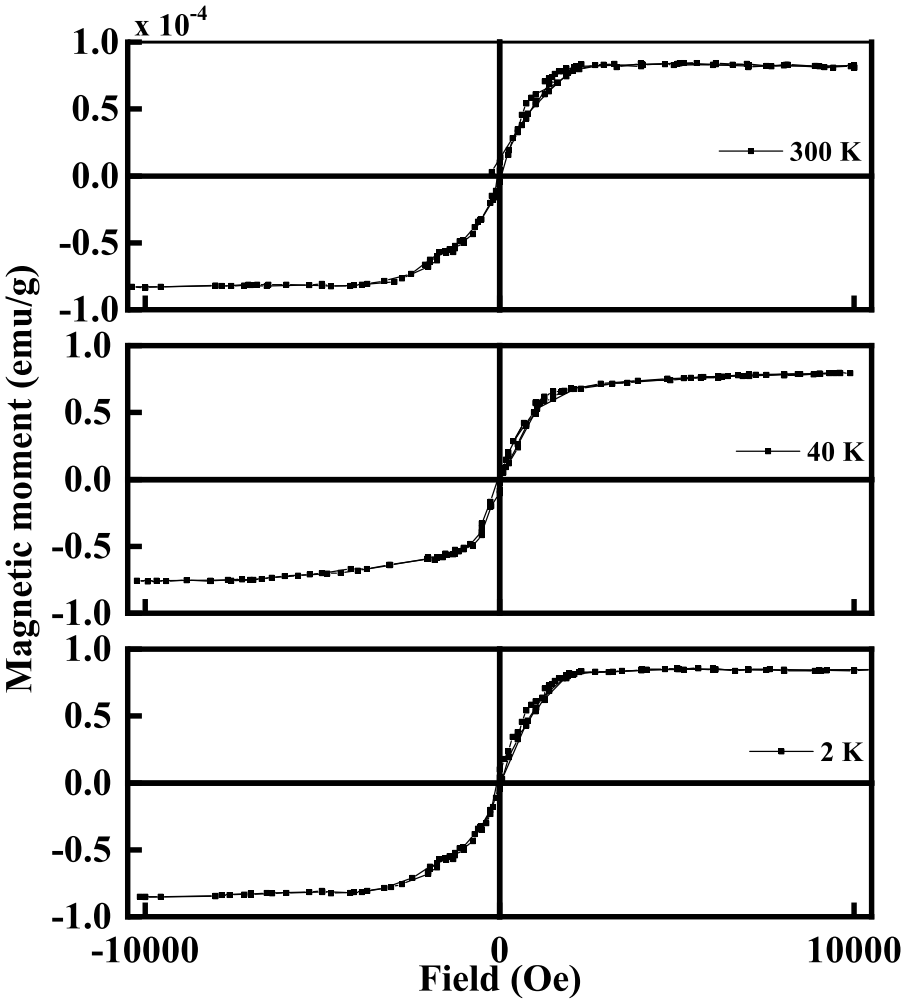

Figure 4.3.34: The M-H loops for rGO functionalized with low concentration of Au (0.22 at.%) showing similar characteristics as rGO at various constant temperatures.

zation is induced due to the oxidation of carbon atoms during the chemical reduction of GO to rGO. The process leads to carbon bonding with oxygenated groups [110], where some of the carbon atoms gain magnetic moments due to O-bonding in the hydroxyl group. In accordance with Lieb's theory [111], the hydroxyl group can easily bond with one carbon atom, which leads to the inducement of local magnetic moment that is observed in Figure 4.3.33. With the inclusion of Au at low concentration (Figure 4.3.34), there is an insignificant change in the magnetic feature compared with rGO and remains the same at room temperature.

Previous reports have indicated that the magnetic signal is attributed to atomic scale structural defects which are induced by surfactant attachment [110]. The defect in-

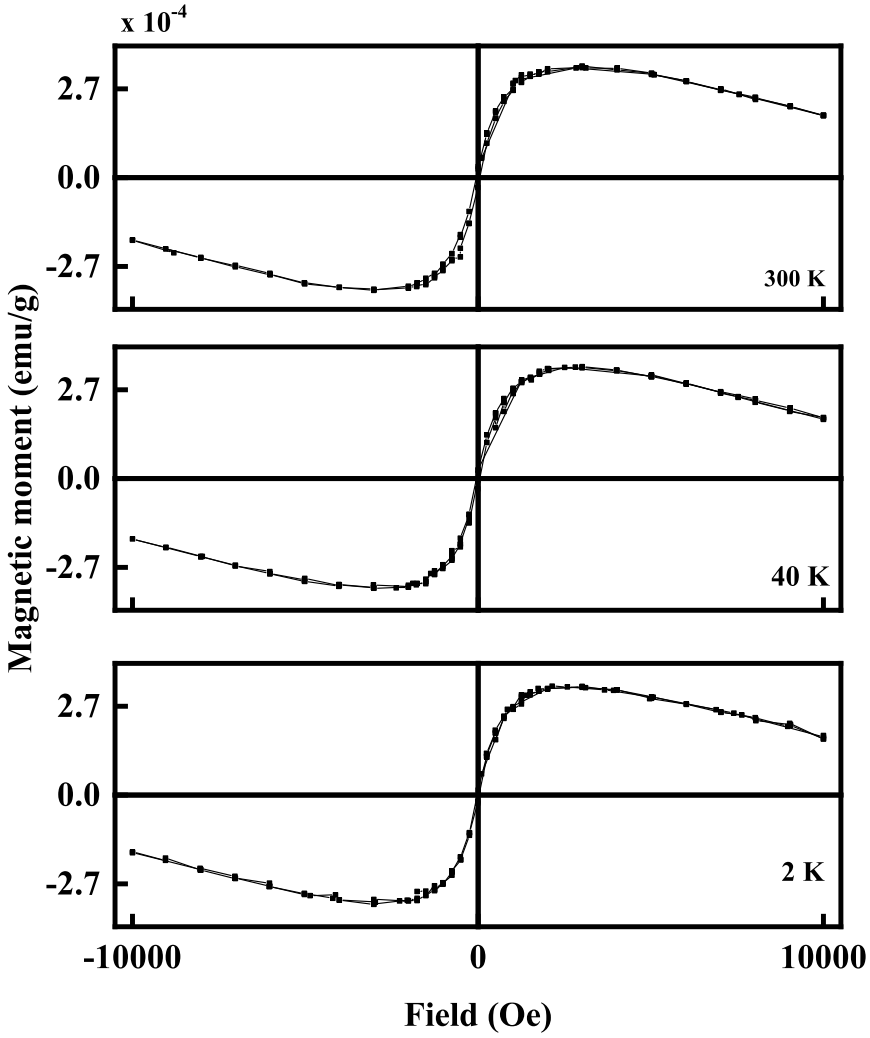

Figure 4.3.35: The M-H loops for rGO:Au-NP(4.88 at.%) at constant temperature 2 K, 40 K and 300 K.

trusion through rGO functionalization can cause an imbalance in the lattice, thereby enhancing the magnetic properties of the parent material [110]. Since the change is insignificant, presumably, the atomic bonding between C, O, and Au is not enough to create an imbalance in the magnetic spins for magnetic enhancement. The insignificant induced defect can be the reason for the insignificant change in magnetization. The further increase in the concentration of Au-NP (4.88 at. %) changes the magnetic properties of rGO significantly. The weak ferromagnetic property of rGO was enhanced due to exchange interaction of C, O, and Au electrons. Since the atomic radius of Au is

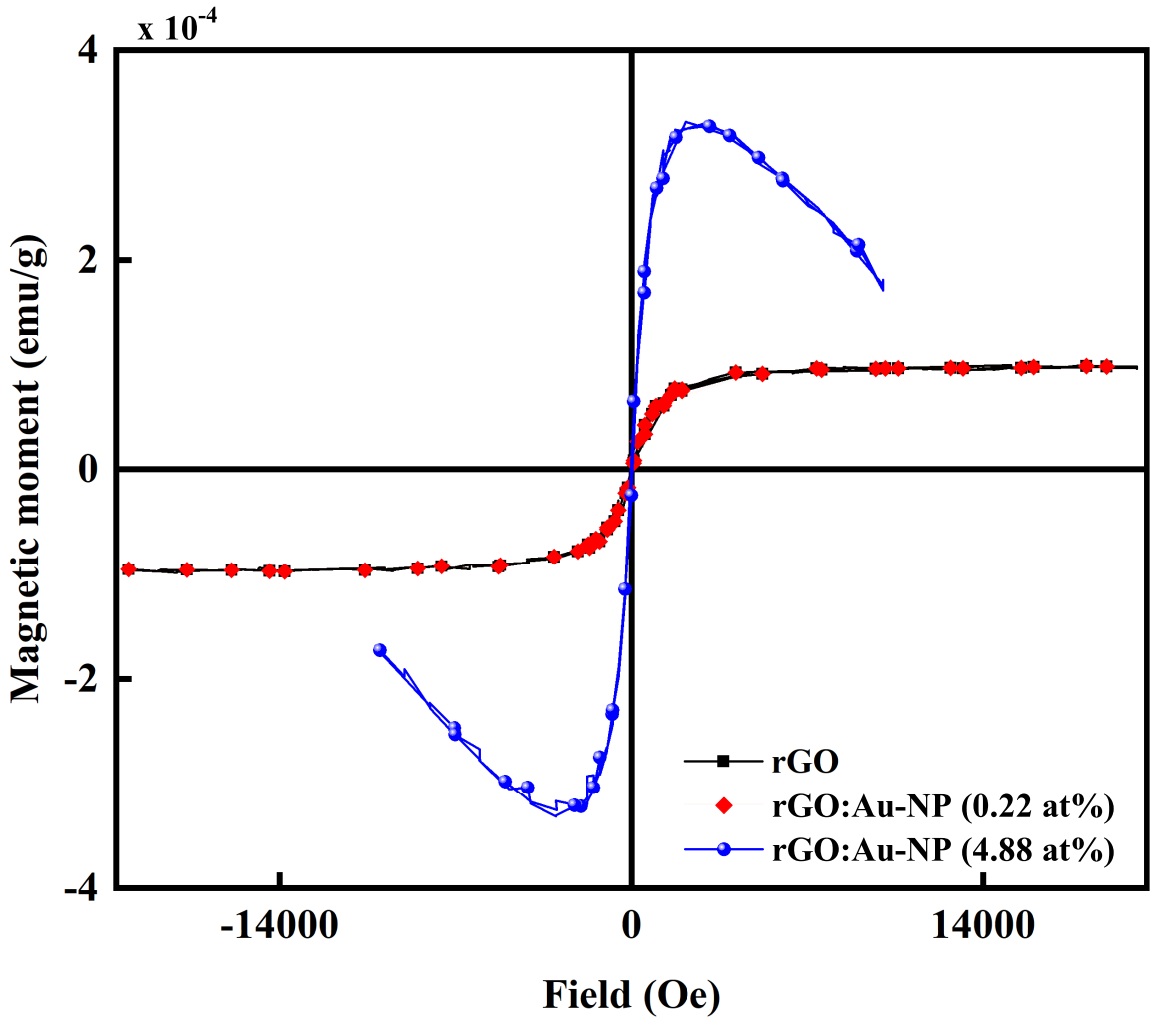

Figure 4.3.36: The comparison of M-H of rGO and rGO:(Au-NP)x to ascertain the enhancement of the magnetization at 300 K.

approximately double that of C, the formation of a lone pair of C-Au bonds is unlikely, however, C-O-Au bond can be formed [112]. Bulk Au exhibits diamagnetic features, however, the spins are re-aligns to ferromagnetic when the size of the particles is reduced [113].

The Coulomb interaction between the C, O, and Au electrons can lead to the enhanced magnetization. With the variation in temperature, ferromagnetic property seemed stable, as seen in the similarity of the saturation magnetization. The improved magnetization can be attributed exchange interaction between the electrons local induced moment of rGO and Au atoms. The enhancement can be easily observed from Figure 4.3.36. The magnetization is seen to be tripled when the concentration of Au-NP is

Table 4.3.15: The extrapolated values indicating the susceptibility and magnetization saturation of the rGO and rGO:(Au-NP)x.

Sample	Susceptibility			Saturation magnetization (emu/g)		
	300 K	40 K	2 K	300 K	40 K	2 K
Au-NP	-2.27	-2.25	-2.18	-	-	-
rGO	-	-	-	8.5×10^{-5}	8.5×10^{-5}	-
rGO:Au-NP(0.22 at%)	-	-	-	9×10^{-5}	9×10^{-5}	9×10^{-5}
rGO:Au-NP(4.88 at%)	-	-	-	2.9×10^{-4}	2.9×10^{-4}	2.9×10^{-4}

increased to 4.88 at. %. Table 4.3.15 shows the extrapolated saturation parameters for rGO and rGO:(Au-NP)x. The saturation magnetization (M_s) , which is the point where the magnetization value becomes constant at the applied field depends on the temperature T [114]. Other properties such as coercity and remanence magnetization are used to qualify the magnetic nature of a material.

As shown in Figure 4.3.33 - 4.3.35, the curves indicate a narrow hysteresis loop with a slight variation in M_s with the inclusion of Au-NP. There is no clear rationale for the variance of saturation, however, disordered surface spin structure has been suggested by Kodama *et al.* [115]. Additionally, magnetism in Figure 4.3.33 - 4.3.35 can be classified as either ferromagnetic or superparamagnetic. It can be considered weak ferromagnet due to the presence of remanence M_r and coercivity (H_c) indicated in Table 4.3.16 and the zoomed in narrow hysteresis loop shown in Figure 4.3.37, 4.3.38 and 4.3.39. The weak ferromagnetic properties are consistent with previous studies [116, 117] and cannot be completely ignored.

The magnetic features can also be considered as superparamagnetic by virtue of the particle size (10-15 nm) as previously mentioned in Section 4.3.1 and the weak remanence and coercivity [118]. Superparamagnetism is a magnetism type that occurs in weak ferromagnetic or ferrimagnetic nanoparticles [119]. Superparamagnetism occurs in nanocomposites comprising of single magnetic domain where the diameter of the material is in the range 3 nm to 50 nm. Hence, the nanocomposite magnetization is assumed to contain giant magnetic moment, where each atom possesses magnetic moments [119]. The weak remanence and coercivity indicated in Table 4.3.16 is an indication that rGO and rGO:(Au-NP)x shows consistency of superparamagnetic be-

Table 4.3.16: The extrapolated values indicating the remanence and coercivity of rGO and rGO:(Au-NP)x.

Samples	Remanence (emu/g) $\times 10^{-5}$			Coercivity (Oe) ($\times 10^5$)		
	300 K	40 K	2 K	300 K	40 K	2 K
rGO	4.1	2.1		32.9	18.4	
rGO:Au-NP(0.22 at.%)	9.4	6.2	1.01	106.1	91.7	127.7
rGO:Au-NP(4.88 at.%)	14.4	25.5	39.1	17.5	55.9	53.9

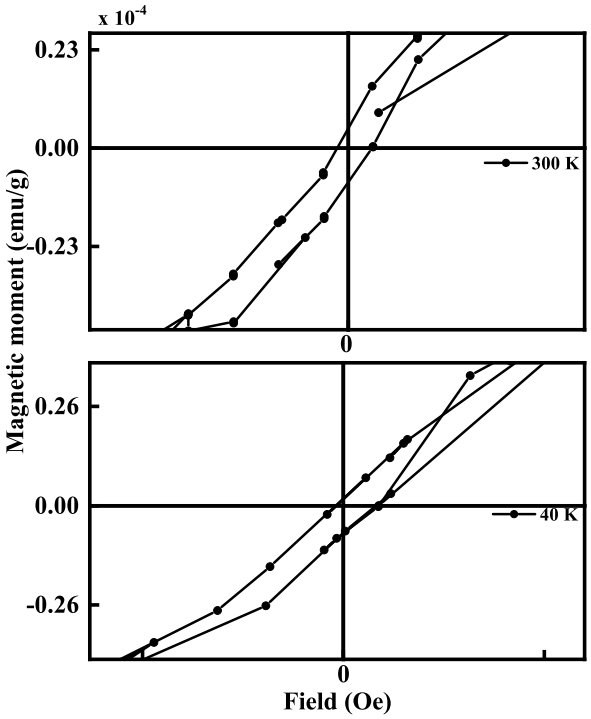

Figure 4.3.37: The zoomed in hysteresis of rGO showing weak remanence and coercivity features.

havior, which was previously reported by Gong *et al.* [120] and the report of Kumar and Bhatnagar [118].Low coercivity and remanence have been reported to be pre-requisites for superparamagnetic properties [121] , which is consistent with the extrapolated values given in Table 4.3.16 and further supports the particle size requirements of the nanocomposites. Considering both categories of magnetism, rGO and rGO:(Au-NP)x can be classified as soft magnetic materials applicable for nano-magnetic applications (biomedicine) [122], memory reading heads [123]. One of the draw-back of superparamagnetism is zero magnetization when the room-temperature thermal noise becomes larger than the magnetic anisotropy [124].

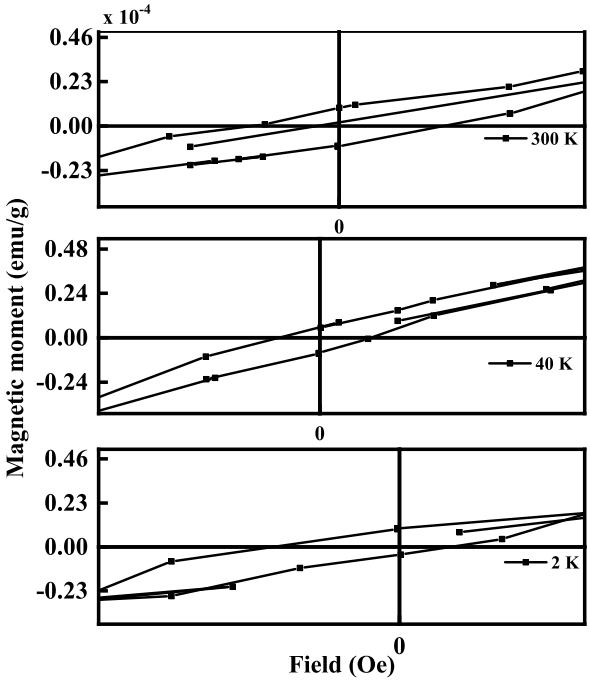

Figure 4.3.38: The zoomed in hysteresis of rGO:Au-NP(0.22 at.%) showing weak remanence and coercivity features.

However, there has been a successful attempt in the inducement of electric field using electric-field-induced strain in a magnetoelectric composite [125]. The technique proved useful in the switching of the net magnetization (On and Off). The implication of the results of Kim *et al* [125] is the usefulness of superparamagnetic materials for nanospintronic applications implying the potential of the rGO:(Au-NP)x for nanospintronics applications.

Figure 4.3.40 (a) and (b) shows the magnetization-temperature (M-T) loop for high and low concentrations of Au-NP in rGO. In both cases, a steady increase in magnetization as temperature increases from 0 K to 50 K. It saturates between 50 K and 80 K then increases and saturates at 100 K. A saturation region is then observed and increases afterward. The transition in the region 45 K to $\approx$ 85 K indicates a paramagnetic transition to ferromagnetic behavior , which is in proximity of 72 K that was previously reported by Li *et al.* [126]. Considering the magnetic transition between paramagnetism and ferromagnetism, the magnetic features of rGO:Au-NPx can be classified as superparamagnetic [127]. The transitions at higher temperatures in the

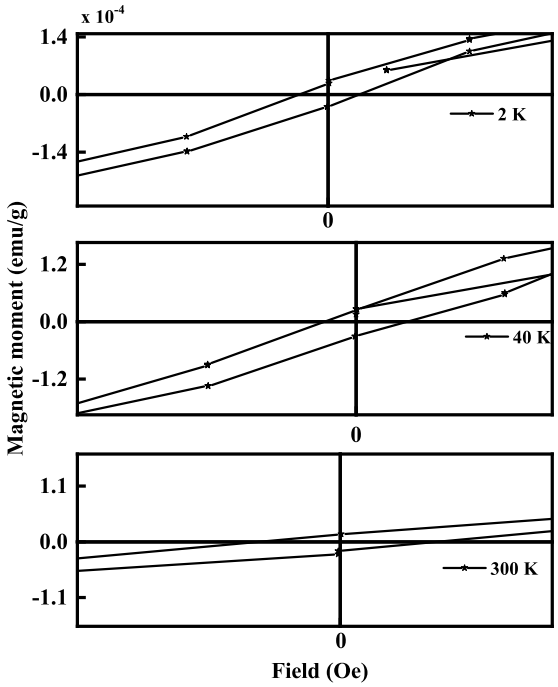

Figure 4.3.39: The zoomed in hysteresis of rGO:Au-NP(4.88 at.%) showing weak remanence and coercivity features.

range 150 K to ≈ 320 K due to the quality of the data is not explicit. However, reports of Alazmi *et al.* [128] proposed possible transition between superparagmetism and ferromagnetism. This transition may be due to threshold transition from a single domain to multi-domain structure in rGO [128].

4.4 Summary

This study seeks to establish rGO:Au-NP as a potential material for electronic device applications. To achieve this aim, the electronic structure, electrical and magnetic properties of GO functionalized with Au-NP was studied. rGO and rGO:Au-NPx (x= 0.08, 0.11, 0.22 and 4.88 at. %) was synthesized using modified Hummers method and characterized by several techniques. The XRD spectra, TEM, SEM images and EDX spectra indicate the formation of the intended material (rGO and rGO:(Au-NP)x).

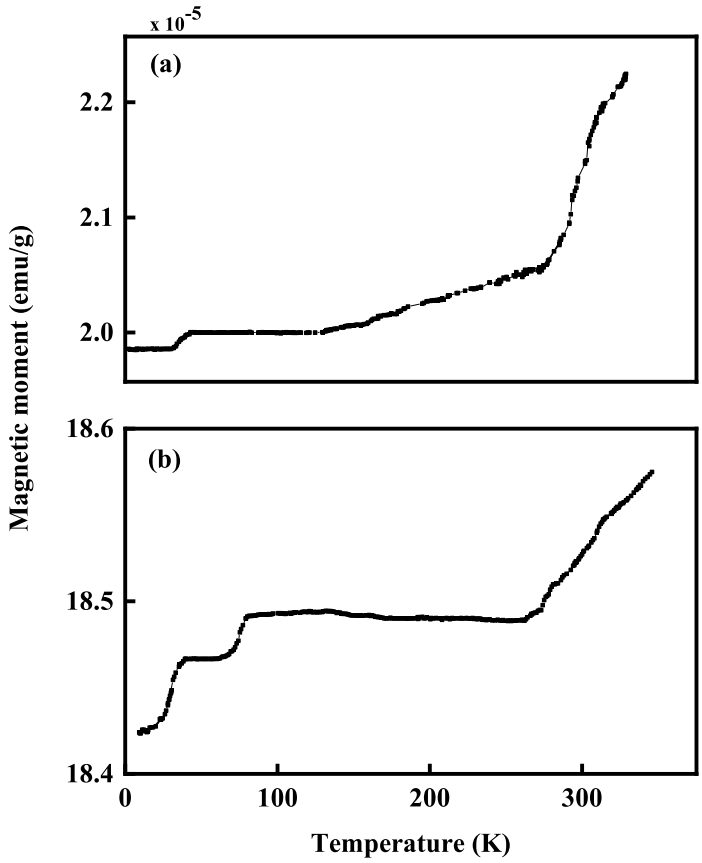

Figure 4.3.40: M-T loop for low and high concentrations of Au-NP showing the formation of the magnetic transitions where (a) rGO:Au-NP(0.22 at. %) and rGO:Au-NP(4.88 at. %).

The presence of the components (C, O, and Au) were observed as expected.

Raman spectroscopy showed the relevant D and G resonance vibrations as obtainable for graphene-related materials. The I_D/I_G ratio, which describes the level of defects that are induced from the functionalization was extrapolated. A significant decrease in the value ($1.22 \rightarrow 0.98$) of rGO with respect to the variation of the concentration of Au-NP was observed.

The XPS spectrum analysis showed that the actual quantity of the concentrations of C, Au, and O are present in each sample. The elemental composition was depicted in the core level i.e., C 1s, O 1s, and Au 4f. The core-levels spectra also indicated the relevant bonding structure of GO, which inevitably is responsible for the observed electrical and magnetic behavior. The UPS results were used to calculate the valence band

maximum (VBM), which showed a variation as the concentration of Au changes. The implication of which showed that the VBM of GO can easily be tuned with Au atoms as surfactants. Since GO is a poor conductor, the reduction of GO and introduction of Au-NP surfactants enabled significant mobility of the electrons. The mobility can be seen in the increase in VBM of rGO when it is functionalized with Au-NP. The improved mobility iterated by Fermi-level shift extrapolations. Fermi-level shift indicates an increase in the density of states (DOS). Both parameters indicate the possibility of an increase in the conductivity of GO. The behaviour is seen in the lower concentration (0.08 at%, 0.11 at% and 0.22 at%) of rGO:Au-NP.

The XANES results also showed consistency with the core-level bonding present in rGO and rGO:(Au-NP)x. The core levels showed a C−Au bond, which is an indication of C attaching to Au atoms. With normalized spectra of XANES, the content of sp^2 as it changes with the concentration of Au-NP was extrapolated. The increase in the sp^2 content means the weak attachment of Au to C atoms with an enhancement of the sp^3 hybridization.

The electrical conductivity of GO was measured using the I-V characterization technique. The conductivity represented by the I-V features of GO increased when functionalized with low concentration of Au-NP (except Au-NP (0.11 at%)). However, it dropped significantly when the concentration of Au-NP was increased. Hence, if the motivation of the electrical conductivity of rGO is toward its improvement, a low concentration of Au-NP is recommended. Nonetheless for ferroelectric properties, high concentration of Au-NP is recommended.

The M-H loop also indicates a significant improvement in terms of the ferromagnetic behavior of rGO. With low concentration of Au, ferromagnetic behavior remained unchanged with low saturation magnetization. However, with high concentration of Au, and the ferromagnetism of rGO significantly improved with a magnitude of $\times 3$. The magnetic nature of rGO:(Au-NP)x can also be considered as superparamagnetic, which comprises fractions of weak ferromagnetism and paramagnetism.

The improvement of the ferromagnetism or superparamagnetic properties of GO can be

attributed to the enhancement of sp^3 clusters of rGO. The implication of this effect is the possible ferroelectric behavior of rGO:Au-NP as depicted in the I-V curve when the concentration of Au increased significantly (4.88 at.%). With this ferroelectric and superparagmagnetic/ferromagnetic property, the material may prove useful in electronic device applications and memory-reading devices.

Bibliography

[1] Zhu Yanwu, Murali Shanthi, Cai Weiwei, Li Xuesong, Suk Ji Won, Potts Jeffrey R, and Ruoff Rodney S. Graphene and graphene oxide: synthesis properties and applications. *Advanced Materials*, 22(35):3906–3924, 2010.

[2] Kar Prasenjit, Sardar Samim, Liu Bo, Sreemany Monjoy, Lemmens Peter, Ghosh Srabanti, and Pal Samir Kumar. Facile synthesis of reduced graphene oxide–gold nanohybrid for potential use in industrial waste-water treatment. *Science and Technology of Advanced Materials*, 17(1):375–386, 2016.

[3] Gao Wei. The chemistry of graphene oxide. In *Graphene Oxide*, pages 61–95. Springer, 2015.

[4] Marcano Daniela C, Kosynkin Dmitry V, Berlin Jacob M, Sinitskii Alexander, Sun Zhengzong, Slesarev Alexander, Alemany Lawrence B, Lu Wei, and Tour James M. Improved synthesis of graphene oxide. *ACS Nano*, 4(8):4806–4814, 2010.

[5] Eda Goki, Mattevi Cecilia, Yamaguchi Hisato, Kim HoKwon, and Chhowalla Manish. Insulator to semimetal transition in graphene oxide. *The Journal of Physical Chemistry C*, 113(35):15768–15771, 2009.

[6] Mkhoyan K Andre, Contryman Alexander W, Silcox John, Stewart Derek A, Eda Goki, Mattevi Cecilia, Miller Steve, and Chhowalla Manish. Aatomic and electronic structure of graphene-oxide. *Nano Letters*, 9(3):1058–1063, 2009.

[7] Kim Jaemyung, Cote Laura J, Kim Franklin, Yuan Wa, Shull Kenneth R, and Huang Jiaxing. Graphene oxide sheets at interfaces. *Journal of the American Chemical Society*, 132(23):8180–8186, 2010.

[8] Daniel R Dreyer, Sungjin Park, Christopher W Bielawski, and Rodney S Ruoff. The chemistry of graphene oxide. *Chemical Society Reviews*, 39(1):228–240, 2010.

[9] Sabina Drewniak, Roksana Muzyka, Agnieszka Stolarczyk, Tadeusz Pustelny, Michalina Kotyczka-Moranska, and Maciej Setkiewicz. Studies of reduced graphene oxide and graphite oxide in the aspect of their possible application in gas sensors. *Sensors*, 16(1):103, 2016.

[10] Dreyer Daniel R, Todd Alexander D, and Bielawski Christopher W. Harnessing the chemistry of graphene oxide. *Chemical Society Reviews*, 43(15):5288–5301, 2014.

[11] Bhattacharya Gourav, Kandasamy Ganeshlenin, Soin Navneet, Upadhyay Ravi Kant, Deshmukh Sujit, Maity Dipak, McLaughlin James, and Roy Susanta Sinha. Novel π-conjugated iron oxide/reduced graphene oxide nanocomposites for high performance electrochemical supercapacitors. *RSC Advances*, 7(1):327–335, 2017.

[12] Lizhao Liu, Junfeng Zhang, Jijun Zhao, and Feng Liu. Mechanical properties of graphene oxides. *Nanoscale*, 4(19):5910–5916, 2012.

[13] Bolotin KI. Electronic transport in graphene: towards high mobility. In *Graphene*, pages 199–227. Elsevier, 2014.

[14] Ali of khazraei Mahmood, Milne William I, Ozkan Cengiz S, Mitura Stanislaw, Gervasoni Juana L, and Ali Nasar. *Graphene Science Handbook: Electrical and Optical Properties*. CRC press, 2016.

[15] Jie Zhao, Ruijun Pan, Rui Sun, Chenyu Wen, Shi-Li Zhang, Biao Wu, Leif Nyholm, and Zhi-Bin Zhang. High-conductivity reduced-graphene-oxide/copper aerogel for energy storage. *Nano Energy*, 60:760–767, 2019.

[16] Yilin Wang, Yanan Chen, Steven D Lacey, Lisha Xu, Hua Xie, Tian Li, Valencia A Danner, and Liangbing Hu. Reduced graphene oxide film with record-high conductivity and mobility. *Materials Today*, 21(2):186–192, 2018.

[17] Stankovich Sasha, Dikin Dmitriy A, Dommett Geoffrey HB, Kohlhaas Kevin M, Zimney Eric J, Stach Eric A, Piner Richard D, Nguyen SonBinh T, and Ruoff Rodney S. Graphene-based composite materials. *Nature*, 442(7100):282–286, 2006.

[18] Pei Songfeng and Cheng Hui-Ming. The reduction of graphene oxide. *Carbon*, 50(9):3210–3228, 2012.

[19] Corbelli Gabriele, Ghisleri Cristian, Marelli Mattia, Milani Paolo, and Ravagnan Luca. Highly deformable nanostructured elastomeric electrodes with improving conductivity upon cyclical stretching. *Advanced Materials*, 23(39):4504–4508, 2011.

[20] Tombros Nikolaos, Jozsa Csaba, Popinciuc Mihaita, Jonkman Harry T, and Van Wees Bart J. Electronic spin transport and spin precession in single graphene layers at room temperature. *Nature*, 448(7153):571–574, 2007.

[21] Tang Tao, Liu Fuchi, Liu Yuan, Li Xinyu, Xu Qinghua, Feng Qian, Tang Nujiang, and Du Youwei. Identifying the magnetic properties of graphene oxide. *Applied Physics Letters*, 104(12):123104–123109, 2014.

[22] Yang T-Y, Balakrishnan J, Volmer F, Avsar A, Jaiswal M, Samm J, Ali SR, Pachoud A, Zeng M, Popinciuc M, et al. Observation of long spin-relaxation times in bilayer graphene at room temperature. *Physical Review Letters*, 107(4):047206–047210, 2011.

[23] Ney Andreas, Papakonstantinou Pagona, Kumar Ajay, Shang Nai-Gui, and Peng Nianhua. Irradiation enhanced paramagnetism on graphene nanoflakes. *Applied Physics Letters*, 99(10):102504–102508, 2011.

[24] Nair RR, Sepioni M, Tsai I-Ling, Lehtinen O, Keinonen J, Krasheninnikov AV, Thomson T, Geim AK, and Grigorieva IV. Spin-half paramagnetism in graphene induced by point defects. *Nature Physics*, 8(3):199–202, 2012.

[25] Eng Alex Yong Sheng, Poh Hwee Ling, Sanek Filip, Marysko Miroslav, Matejkova Stanislava, Sofer Zdenek, and Pumera Martin. Searching for magnetism in hydrogenated graphene: using highly hydrogenated graphene prepared via birch reduction of graphite oxides. *Acs Nano*, 7(7):5930–5939, 2013.

[26] Santos Elton JG, Ayuela Andrés, and Sánchez-Portal Daniel. Universal magnetic properties of sp3-type defects in covalently functionalized graphene. *New Journal of Physics*, 14(4):043022–043035, 2012.

[27] Chen Lianlian, Guo Liwei, Li Zhilin, Zhang Han, Lin Jingjing, Huang Jiao, Jin Shifeng, and Chen Xiaolong. Towards intrinsic magnetism of graphene sheets with irregular zigzag edges. *Scientific Reports*, 3:2599–2605, 2013.

[28] Wang Min and Li Chang Ming. Magnetism in graphene oxide. *New Journal of Physics*, 12(8):083040–083040, 2010.

[29] David O Idisi, Haydar Ali, JA Oke, Sweety Sarma, SJ Moloi, Sekhar C Ray, HT Wang, Nikhil R Jana, WF Pong, and Andre M Strydom. Electronic, electrical and magnetic behaviours of reduced graphene-oxide functionalized with silica coated gold nanoparticles. *Applied Surface Science*, 483:106–113, 2019.

[30] Suneev Anil Bansal, Vanish Kumar, Javad Karimi, Amrinder Pal Singh, and Suresh Kumar. Role of gold nanoparticles in advanced biomedical applications. *Nanoscale Advances*, 2(9):3764–3787, 2020.

[31] Qura Tul Ain, Samina Hyder Haq, Abeer Alshammari, Moudhi Abdullah Al-Mutlaq, and Muhammad Naeem Anjum. The systemic effect of peg-ngo-induced oxidative stress in vivo in a rodent model. *Beilstein journal of nanotechnology*, 10(1):901–911, 2019.

[32] Andy Nieto, Ankita Bisht, Debrupa Lahiri, Cheng Zhang, and Arvind Agarwal. Graphene reinforced metal and ceramic matrix composites: a review. *International Materials Reviews*, 62(5):241–302, 2017.

[33] Yan Wang, Zhihui Wen, Huoli Zhang, Guohua Cao, Qi Sun, and Jianliang Cao. Cuo nanorods-decorated reduced graphene oxide nanocatalysts for catalytic oxidation of co. *Catalysts*, 6(12):214–221, 2016.

[34] Sunatkari AL, Talwatkar SS, Tamgadge YS, and Muley GG. Synthesis characterization and optical properties of l-arginine stabilized gold nanocolloids. *Nanoscience and Nanotechnology*, 5(2):30–35, 2015.

[35] Ezra Feilden, Esther García-Tuñón Blanca, Finn Giuliani, Eduardo Saiz, and Luc Vandeperre. Robocasting of structural ceramic parts with hydrogel inks. *Journal of the European Ceramic Society*, 36(10):2525–2533, 2016.

[36] Jili Wu, Xiaoping Shen, Lei Jiang, Kun Wang, and Kangmin Chen. Solvothermal synthesis and characterization of sandwich-like graphene/zno nanocomposites. *Applied Surface Science*, 256(9):2826–2830, 2010.

[37] Lili Feng, Guo Gao, Peng Huang, Xiansong Wang, Chunlei Zhang, Jiali Zhang, Shouwu Guo, and Daxiang Cui. Preparation of pt ag alloy nanoisland/graphene hybrid composites and its high stability and catalytic activity in methanol electrooxidation. *Nanoscale research letters*, 6(1):1–10, 2011.

[38] MV Wenzl, G Wölkart, H Stessel, M Beretta, K Schmidt, and B Mayer. Different effects of ascorbate deprivation and classical vascular nitrate tolerance on aldehyde dehydrogenase-catalysed bioactivation of nitroglycerin. *British journal of pharmacology*, 156(8):1248–1255, 2009.

[39] Shadpour Mallakpour, Amir Abdolmaleki, and Sedigheh Borandeh. Covalently functionalized graphene sheets with biocompatible natural amino acids. *Applied Surface Science*, 307:533–542, 2014.

[40] Joshy Jose and M Abdul Khadar. Role of grain boundaries on the electrical conductivity of nanophase zinc oxide. *Materials Science and Engineering: A*, 304:810–813, 2001.

[41] Amartya Acharya, Koyel Bhattacharya, Chandan Kumar Ghosh, Achintesh Narayan Biswas, and Sanjib Bhattacharya. Charge carrier transport and electrochemical stability of li2o doped glassy ceramics. *Materials Science and Engineering: B*, 260:114612, 2020.

[42] N Lee, RD Hartschuh, D Mehtani, A Kisliuk, JF Maguire, M Green, MD Foster, and AP Sokolov. High contrast scanning nano-raman spectroscopy of silicon. *Journal of Raman Spectroscopy: An International Journal for Original Work in all Aspects of Raman Spectroscopy, Including Higher Order Processes, and also Brillouin and Rayleigh Scattering*, 38(6):789–796, 2007.

[43] Thi Khanh Thu Vu, Quang Dong Nguyen, Thanh Dinh Nguyen, Thi Hue Trinh, et al. Preparation of metal nanoparticles for surface enhanced raman scattering by laser ablation method. *Advances in Natural Sciences: Nanoscience and Nanotechnology*, 3(2):025016–025021, 2012.

[44] Lazzeri Michele, Attaccalite Claudio, Wirtz Ludger, and Mauri Francesco. Impact of the electron-electron correlation on phonon dispersion: Failure of lda and gga dft functionals in graphene and graphite. *Physical Review B*, 78(8):081406–081410, 2008.

[45] Wang K-A, Rao AM, Eklund PC, Dresselhaus MS, and Dresselhaus G. Observation of higher-order infrared modes in solid c 60 films. *Physical Review B*, 48(15):11375–11381, 1993.

[46] Isaac Childres, Luis A Jauregui, Wonjun Park, Helin Cao, and Yong P Chen. Raman spectroscopy of graphene and related materials. *New developments in photon and materials research*, 1:1–20, 2013.

[47] Gupta Vaishali, Sharma Neeraj, Singh Udai, Arif Mohd, and Singh Arun. Higher oxidation level in graphene oxide. *Optik-International Journal for Light and Electron Optics*, 143:115–124, 2017.

[48] Bruna Matteo, Anna K, Ijas Mari, Yoon Duhee, Sassi Ugo, and Ferrari Andrea C. Doping dependence of the raman spectrum of defected graphene. *Acs Nano*, 8(7):7432–7441, 2014.

[49] Zheng Xiaoming, Chen Wei, Wang Guang, Yu Yayun, Qin Shiqiao, Fang Jingyue, Wang Fei, and Zhang Xue-Ao. The raman redshift of graphene impacted by gold nanoparticles. *AIP Advances*, 5(5):057133–057140, 2015.

[50] Sahoo Rasmita and Mishra Rashmi Ranjan. Phonon dispersion for armchair and zigzag carbon nanotubes. *Graphene*, 3(02):14–20, 2014.

[51] Tuinstra F and Koenig J Lo. Raman spectrum of graphite. *The Journal of Chemical Physics*, 53(3):1126–1130, 1970.

[52] Wang Yingying, Ni Zhenhua, Hu Hailong, Hao Yufeng, Wong Choun Pei, Yu Ting, Thong John TL, and Shen Ze Xiang. Gold on graphene as a substrate for surface enhanced raman scattering study. *Applied Physics Letters*, 97(16):163111–163114, 2010.

[53] Philipp Vecera, Julio C Chacón-Torres, Thomas Pichler, Stephanie Reich, Himadri R Soni, Andreas Gorling, Konstantin Edelthalhammer, Herwig Peterlik, Frank Hauke, and Andreas Hirsch. Precise determination of graphene functionalization by in situ raman spectroscopy. *Nature Communications*, 8(1):1–9, 2017.

[54] Wei Liu and Giorgio Speranza. Tuning the oxygen content of reduced graphene oxide and effects on its properties. *ACS Omega*, 6(9):6195–6205, 2021.

[55] Georgakilas Vasilios. *Functionalization of Graphene*. John Wiley & Sons, 2014.

[56] R Al-Gaashani, A Najjar, Y Zakaria, S Mansour, and MA Atieh. Xps and structural studies of high quality graphene oxide and reduced graphene oxide prepared by different chemical oxidation methods. *Ceramics International*, 45(11):14439–14448, 2019.

[57] F Priante, M Salim, L Ottaviano, and F Perrozzi. Xps study of graphene oxide reduction induced by (100) and (111)-oriented si substrates. *Nanotechnology*, 29(7):075704, 2018.

[58] Dongxing Yang, Aruna Velamakanni, Gülay Bozoklu, Sungjin Park, Meryl Stoller, Richard D Piner, Sasha Stankovich, Inhwa Jung, Daniel A Field, Carl A Ventrice Jr, et al. Chemical analysis of graphene oxide films after heat and chemical treatments by x-ray photoelectron and micro-raman spectroscopy. *Carbon*, 47(1):145–152, 2009.

[59] Fairley Neal, Carrick Alan, and Fairly Neal. *The casa cookbook*, volume 1. Acolyte Science Cheshire, 2005.

[60] M Al-Hada, L Gregoratti, M Amati, and M Neeb. Pristine and oxidised ag-nanoparticles on free-standing graphene as explored by x-ray photoelectron and auger spectroscopy. *Surface Science*, 693:121533, 2020.

[61] Dimiev Ayrat M and Eigler Siegfied. *Graphene oxide: Fundamentals and Applications*. John Wiley & Sons, 2016.

[62] Pan Fei, Chen Dandan, Zhuang Xuming, Wu Xuran, Luan Feng, Zhang Shuang, Wei Jiaru, Xia Shuang, and Li Xiao. Fabrication of gold nanoparticles/l-cysteine functionalized graphene oxide nanocomposites and application for nitrite detection. *Journal of Alloys and Compounds*, 744:51–56, 2018.

[63] Shin Young-Eun, Sa Young Jin, Park Seungyoung, Lee Jiwon, Shin Kyung-Hee, Joo Sang Hoon, and Ko Hyunhyub. An ice-templated ph-tunable self-assembly route to hierarchically porous graphene nanoscroll networks. *Nanoscale*, 6(16):9734–9741, 2014.

[64] O Akhavan. The effect of heat treatment on formation of graphene thin films from graphene oxide nanosheets. *Carbon*, 48(2):509–519, 2010.

[65] Wang Yu, Li Sisi, Yang Haiyan, and Luo Jie. Progress in the functional modification of graphene/graphene oxide: a review. *RSC Advances*, 10(26):15328–15345, 2020.

[66] Ganguly Abhijit, Sharma Surbhi, Papakonstantinou Pagona, and Hamilton Jeremy. Probing the thermal deoxygenation of graphene oxide using high-resolution in situ x-ray-based spectroscopies. *The Journal of Physical Chemistry C*, 115(34):17009–17019, 2011.

[67] Estrade-Szwarckopf Henriette and Rousseau Bernard. Photoelectron core level spectroscopy study of cs-graphite intercalation compounds—i. clean surfaces study. *Journal of Physics and Chemistry of Solids*, 53(3):419–436, 1992.

[68] Haerle Rainer, Riedo Elisa, Pasquarello Alfredo, and Baldereschi Alfonso. sp^2/sp^3 hybridization ratio in amorphous carbon from c 1 s core-level shifts: X-ray photoelectron spectroscopy and first-principles calculation. *Physical Review B*, 65(4):045101–045110, 2001.

[69] da Silva Antônio JR, Faria J Carrijo, da Silva Edison Z, Fazzio A, et al. Adsorption of gold atoms on carbon nanotubes. In *Nanotech Technical Proceedings of the 2003 Nanotechnology Conference and Trade Show*, volume 3, pages 165–168, 2003.

[70] Frédéric Joucken, Luc Henrard, and Jérôme Lagoute. Electronic properties of chemically doped graphene. *Physical Review Materials*, 3(11):110301, 2019.

[71] Schedin F, Geim AK, Morozov SV, Hill EW, Blake P, Katsnelson MI, and Novoselov KS. Detection of individual gas molecules adsorbed on graphene. *Nature Materials*, 6(9):652–655, 2007.

[72] Chambers Scott A, Droubay T, Kaspar Tiffany C, and Gutowski M. Experimental determination of valence band maxima for srtio 3 tio 2 and sro and the

associated valence band offsets with si (001). *Journal of Vacuum Science & Technology B: Microelectronics and Nanometer Structures Processing Measurement and Phenomena*, 22(4):2205–2215, 2004.

[73] Xia Yuqi, Qian Dong, Hsieh David, Wray L, Pal Arijeet, Lin Hsin, Bansil Arun, Grauer DHYS, Hor Yew San, Cava Robert Joseph, et al. Observation of a large-gap topological-insulator class with a single dirac cone on the surface. *Nature Physics*, 5(6):398–402, 2009.

[74] Bianconi A, Hagström SBM, and Bachrach RZ. Photoemission studies of graphite high-energy conduction-band and valence-band states using soft-x-ray synchrotron radiation excitation. *Physical Review B*, 16(12):5543–5548, 1977.

[75] Becerril Héctor A, Mao Jie, Liu Zunfeng, Stoltenberg Randall M, Bao Zhenan, and Chen Yongsheng. Evaluation of solution-processed reduced graphene oxide films as transparent conductors. *ACS nano*, 2(3):463–470, 2008.

[76] Larciprete R, Gardonio S, Petaccia L, and Lizzit S. Atomic oxygen functionalization of double walled c nanotubes. *Carbon*, 47(11):2579–2589, 2009.

[77] Luo Zhiqiang, Lim Sanhua, Tian Zhiqun, Shang Jingzhi, Lai Linfei, MacDonald Brian, Fu Chao, Shen Zexiang, Yu Ting, and Lin Jianyi. Pyridinic n doped graphene: synthesis electronic structure and electrocatalytic property. *Journal of Materials Chemistry*, 21(22):8038–8044, 2011.

[78] Leibo Hu, Xianru Hu, Xuebin Wu, Chenlei Du, Yunchuan Dai, and Jianbo Deng. Density functional calculation of transition metal adatom adsorption on graphene. *Physica B: Condensed Matter*, 405(16):3337–3341, 2010.

[79] Bhattacharyya Somnath, Vallee C, Cardinaud C, and Turban G. Structure of nitrogenated carbon films prepared from acetylene and nitrogen mixture in electron cyclotron resonance plasma. *Journal of Applied Physics*, 87(10):7524–7532, 2000.

[80] Sutar DS, Singh Gulbagh, and Divakar Botcha V. Electronic structure of graphene oxide and reduced graphene oxide monolayers. *Applied Physics Letters*, 101(10):103103–103108, 2012.

[81] Koo Hye Young, Lee Ha-Jin, Noh Yong-Young, Lee Eui-Sup, Kim Yong-Hyun, and San Choi Won. Gold nanoparticle-doped graphene nanosheets: sub-nanosized gold clusters nucleate and grow at the nitrogen-induced defects on graphene surfaces. *Journal of Materials Chemistry*, 22(15):7130–7135, 2012.

[82] Muszynski Ryan, Seger Brian, and Kamat Prashant V. Decorating graphene sheets with gold nanoparticles. *The Journal of Physical Chemistry C*, 112(14):5263–5266, 2008.

[83] Yang Huanping, Zhou Weiwei, Yu Bo, Wang Yingying, Cong Chunxiao, and Yu Ting. Uniform decoration of reduced graphene oxide sheets with gold nanoparticles. *Journal of Nanotechnology*, 2012:1–8, 2012.

[84] Kobashi Koji. Shift of fermi level by substitutional impurity-atom doping in diamond and cubic-and hexagonal-boron nitrides ii. generalized gradient approximation. *arXiv preprint arXiv:1412.6716*, 1:1–14, 2014.

[85] Chen Da, Feng Hongbin, and Li Jinghong. Graphene oxide: Preparation, functionalization, and electrochemical applications. *Chemical Reviews*, 112(11):6027–6053, 2012.

[86] Pacile D, Meyer JC, Rodriguez A Fraile, Papagno M, Gomez-Navarro C, Sundaram RS, Burghard M, Kern K, Carbone C, and Kaiser U. Electronic properties and atomic structure of graphene oxide membranes. *Carbon*, 49(3):966–972, 2011.

[87] Zhao Jijun, Liu Lizhao, and Li Fen. *Graphene Oxide: Physics and Applications*. Springer, 2015.

[88] Ray SC, Pao CW, Tsai HM, Bose B, Chiou JW, Pong WF, and DasGupta D. Orientation of graphitic planes during annealing of "dip deposited" amorphous carbon film: A carbon k-edge x-ray absorption near-edge study. *Carbon*, 44(10):1982–1985, 2006.

[89] Eda Goki, Fanchini Giovanni, and Chhowalla Manish. Large-area ultrathin films of reduced graphene oxide as a transparent and flexible electronic material. *Nature Nanotechnology*, 3(5):270–274, 2008.

[90] Ray Sekhar C, Soin Navneet, Pong Way-Faung, Roy Susanta S, Strydom Andre M, McLaughlin James A, and Papakonstantinou Pagona. Plasma modification of the electronic and magnetic properties of vertically aligned bi-/tri-layered graphene nanoflakes. *RSC Advances*, 6(75):70913–70924, 2016.

[91] Lee Vincent, Whittaker Luisa, Jaye Cherno, Baroudi Kristen M, Fischer Daniel A, and Banerjee Sarbajit. Large-area chemically modified graphene films: electrophoretic deposition and characterization by soft x-ray absorption spectroscopy. *Chemistry of Materials*, 21(16):3905–3916, 2009.

[92] Rosenberg RA, Love PJ, and Rehn Victor. Polarization-dependent c (k) near-edge x-ray-absorption fine structure of graphite. *Physical Review B*, 33(6):4034–4038, 1986.

[93] Ray Sekhar Chandra, Pao CW, Tsai HM, Chiou JW, Pong WF, Tsai MH, Okpalugo TIT, Papakonstantinou P, and Pi TW. Enhancement of sp3-bonding in high-bias-voltage grown diamond-like carbon thin films studied by x-ray absorption and photoemission spectroscopy. *Journal of Physics: Condensed Matter*, 19(17):176204–176210, 2007.

[94] Saxena Sumit, Tyson Trevor A, and Negusse Ezana. Investigation of the local structure of graphene oxide. *The Journal of Physical Chemistry Letters*, 1(24):3433–3437, 2010.

[95] Szabó Tamás, Berkesi Ottó, Forgó Péter, Josepovits Katalin, Sanakis Yiannis, Petridis Dimitris, and Dékány Imre. Evolution of surface functional groups in a series of progressively oxidized graphite oxides. *Chemistry of materials*, 18(11):2740–2749, 2006.

[96] Sze Simon Min. *Semiconductor Devices: Physics and Technology*. John Wiley & Sons, 2008.

[97] Chang-Hyun Lee, Sung-Hoi Hur, You-Cheol Shin, Jeong-Hyuk Choi, Dong-Gun Park, and Kinam Kim. Charge-trapping device structure of sio2/sin/ high-k dielectric al2o3 for high-density flash memory. *Applied Physics Letters*, 86(15):152908–152911, 2005.

[98] Rance GA and Khlobystov AN. Interactions of carbon nanotubes and gold nanoparticles: the effects of solvent dielectric constant and temperature on controlled assembly of superstructures. *Dalton Transactions*, 43(20):7400–7406, 2014.

[99] Peykov P, Aceves M, and Diaz T. Determination of recombination lifetime in mos structures using a lineal voltage-sweep technique. *Superficies y vacio*, 17(2):29–31, 2004.

[100] Kotin IA, Antonova IV, Orlov OM, and Smagulova SA. Origin of hole and electron traps in graphene oxide. *Materials Research Express*, 3(6):066301–066307, 2016.

[101] Zebrev GI, Melnik EV, and Tselykovskiy AA. Influence of interface traps and electron-hole puddles on quantum capacitance and conductivity in graphene field-effect transistors. *arXiv preprint arXiv:1011.5127*, 1:1–17, 2010.

[102] P Crespo, Rojas Litrán, TC Rojas, M Multigner, JM De la Fuente, JC Sánchez-López, MA García, A Hernando, S Penadés, and A Fernández. Permanent mag-

netism, magnetic anisotropy, and hysteresis of thiol-capped gold nanoparticles. *Physical Review Letters*, 93(8):087204, 2004.

[103] A Roy, M Turner, and MP Sarachik. Susceptibility of si: P across the metal-insulator transition. i. diamagnetism. *Physical Review B*, 37(10):5522, 1988.

[104] Dante Jamal O'Hara, Tiancong Zhu, and Roland Kenji Kawakami. Importance of paramagnetic background subtraction for determining the magnetic moment in epitaxially grown ultrathin van der waals magnets. *IEEE Magnetics Letters*, 9:1–5, 2018.

[105] Trudel Simon. Unexpected magnetism in gold nanostructures: making gold even more attractive. *Gold Bulletin*, 44(1):3–13, 2011.

[106] Di Ventra M, Pantelides ST, and Lang ND. First-principles calculation of transport properties of a molecular device. *Physical Review Letters*, 84(5):979–983, 2000.

[107] Ghosh Partha, Han Gang, De Mrinmoy, Kim Chae Kyu, and Rotello Vincent M. Gold nanoparticles in delivery applications. *Advanced Drug Delivery Reviews*, 60(11):1307–1315, 2008.

[108] V Cannella and JA Mydosh. Magnetic ordering in gold-iron alloys. *Physical Review B*, 6(11):4220–4237, 1972.

[109] Ray Sekhar. *Applications of Graphene and Graphene-Oxide Based Nanomaterials*. William Andrew, 2015.

[110] Sarkar SK, Raul KK, Pradhan SS, Basu S, and Nayak A. Magnetic properties of graphite oxide and reduced graphene oxide. *Physica E: Low-dimensional Systems and Nanostructures*, 64:78–82, 2014.

[111] Lieb Elliott and Mattis Daniel. Theory of ferromagnetism and the ordering of electronic energy levels. In *Inequalities*, pages 33–41. Springer, 2002.

[112] ElMetwally M Abdelrazek, Amr M Abdelghany, Shalabya I Badr, and Mohamed A Morsi. Structural, optical, morphological and thermal properties of peo/pvp blend containing different concentrations of biosynthesized au nanoparticles. *Journal of materials research and technology*, 7(4):419–431, 2018.

[113] Mikhail Agrachev, Sabrina Antonello, Tiziano Dainese, Marco Ruzzi, Alfonso Zoleo, Edoardo Apra, Niranjan Govind, Alessandro Fortunelli, Luca Sementa, and Flavio Maran. Magnetic ordering in gold nanoclusters. *ACS Omega*, 2(6):2607–2617, 2017.

[114] Lu HM, Zheng WT, and Jiang Q. Saturation magnetization of ferromagnetic and ferrimagnetic nanocrystals at room temperature. *Journal of Physics D: Applied Physics*, 40(2):320–326, 2007.

[115] Kodama Richard H, Berkowitz Ami E, McNiff Jr EJ, and Foner S. Surface spin disorder in nife 2 o 4 nanoparticles. *Physical Review Letters*, 77(2):394–397, 1996.

[116] Sarma Sweety, Ray Sekhar C, and Strydom André M. Electronic and magnetic properties of nitrogen functionalized graphene-oxide. *Diamond and Related Materials*, 79:1–6, 2017.

[117] Navneet Soin, Sekhar C Ray, Sweety Sarma, Debarati Mazumder, Surbhi Sharma, Yu-Fu Wang, Way-Faung Pong, Susanta Sinha Roy, and Andre M Strydom. Tuning the electronic and magnetic properties of nitrogen-functionalized few-layered graphene nanoflakes. *The Journal of Physical Chemistry C*, 121(26):14073–14082, 2017.

[118] A Sendil Kumar and Anil K Bhatnagar. Magnetism from fe 2 o 3 nanoparticles embedded in amorphous sio 2 matrix. *Applied Nanoscience*, 8(1):79–87, 2018.

[119] Marghussian Vahak. *Nano-Glass Ceramics: Processing Properties and Applications*. William Andrew, 2015.

[120] Pengyu Gong, Qingyun Chen, Kaimin Shih, Changzhong Liao, Lielin Wang, Hua Xie, and Sihao Deng. Ultra-low remanence and weak magnetic agglomeration of superparamagnetic magnetite nanoparticles caused by high magnetic moment tb 3+ doping. *Journal of Materials Science: Materials in Electronics*, 30(24):20970–20978, 2019.

[121] Tristan D Clemons, Roland H Kerr, and Alexander Joos. Multifunctional magnetic nanoparticles: Design, synthesis, and biomedical applications. In *Comprehensive nanoscience and nanotechnology: Volume 3: Biological nanoscience*, pages 193–210. Elsevier BV, 2019.

[122] Jesus MDLF and Grazu V. *Nanobiotechnology: Inorganic Nanoparticles Vs Organic Nanoparticles*, volume 4. Elsevier, 2012.

[123] Comstock Larry. Magnetic information-storage materials. In *Springer Handbook of Electronic and Photonic Materials*, pages 1155–1191. Springer, 2006.

[124] Bean CP and Livingston undJ D. Superparamagnetism. *Journal of Applied Physics*, 30(4):S120–S129, 1959.

[125] Kim Hyungsuk KD, Schelhas Laura T, Keller Scott, Hockel Joshua L, Tolbert Sarah H, and Carman Gregory P. Magnetoelectric control of superparamagnetism. *Nano Letters*, 13(3):884–888, 2013.

[126] Lingwei Li, Ye Yuan, Yikun Zhang, Rainer Pöttgen, and Shengqiang Zhou. Magnetic phase transitions and large magnetic entropy change with a wide temperature span in hozn. *Journal of Alloys and Compounds*, 643:147–151, 2015.

[127] Xu Jie, Wang Jin-Feng, Jiao Long, Ji Weijing, Zhou Jian, Gu Zheng-Bin, Chen YB, Yao Shu-Hua, Zhang Shan-Tao, and Chen Yan-Feng. Magnetic and electrical transport properties of pb1-xlaxti1-xmnxo3 ceramics. *AIP Advances*, 2(3):032156–032165, 2012.

[128] Amira Alazmi, Venkatesh Singaravelu, Nitin M Batra, Jasmin Smajic, Mram Alyami, Niveen M Khashab, and Pedro MFJ Costa. Cobalt ferrite supported on reduced graphene oxide as a t 2 contrast agent for magnetic resonance imaging. *RSC advances*, 9(11):6299–6309, 2019.

Chapter 5

Graphene oxide functionalized with iron oxide nanoparticles

The importance of graphene/metal nanocomposites has been topical recently due to the advantages that they proffer in today's applications. The applications of graphene/metal nanocomposites have found usefulness in biomedicine [1], catalysis [2], optoelectronics [3, 4], and recently in spintronics [5].

As iterated earlier in former chapters, due to the difficulty in obtaining graphene sheets, other techniques have been employed. One of such technique involves the exfoliation of graphite sheets, which oxidizes the carbon atoms. The oxidation of the carbon atoms decreases the electrical conductivity of graphene (in the form of graphene oxide). Furthermore, the absence of intrinsic magnetic moment of graphene also leads to the nonmagnetism feature, thereby limiting the functionality of graphene in related applications. However, the weak spin-orbit coupling of graphene results in long spin life time , which is advantageous in terms of graphene been used for ferroelectric electronic device applications [6].

Sequel to the previous chapter, Au-NP was used for enhancing the magnetic properties of rGO. This chapter takes it further by enhancing the weak ferromagnetic or superparamagnetic properties of GO. Thereafter, the structural, electronic, electrical and magnetic properties of GO with iron nanoparticles (Fe-NP) are explored.

One of the major challenges posed by Fe-NP is its reactivity when it interacts with water and oxygen. This setback is prevalent in iron nanoparticles leading to overall ox-

idation in air [7]. The oxidized Fe-NP comes in the form of iron (III) oxide Fe_2O_3, Iron (II,III) oxide Fe_3O_4 Fe_2O_3 nanoparticles, which is the focus of this part of the study is a material having advantages such as easy accessibility, cheap, nontoxic. Fe_2O_3 is a semiconductor characterized by a 2.2 eV band gap [8].

Owing to Fe_2O_3 component being anchored on GO as a composite offers an avenue for enhancing the properties of GO. Different techniques have been employed in the synthesis of GO-Fe_2O_3 composite. One of the techniques involves encapsulating Fe_2O_3 into GO through high-pressure pyrolysis of ferrocene using pristine graphene sheets [9]. The sol-gel technique is useful in the synthesis of GO-Fe_2O_3 composite. The procedure can be done without any reducing agent [10]. The use of sodium dodecylbenzenesulphate (NaDDBS) for the reduction can lower the effect of impurities that can occur from iron oxide 3D clusters. The thermal deposition is another technique , which involves the use of high temperatures. The technique outcome gives a crystalline and highly monodisperse composite [11, 12]. An easier technique, which is the chosen technique for this study is the chemical co-precipitation method. The chemical-co-precipitation technique is cheap and yields a high throughput composite precipitate [13, 14].

Furthermore, there has been various capping agents for attaching surfactants to GO. One relevant technique is the 2-aminoterephthalic acid (ATA). ATA is a derivative of Terephthalic (TPA), which is a compound for production of condensation polymers [15]. ATA on the other hand is useful for the formation of organic networks of materials [16]. For instance, Bhattacharya *et al.* used ATA as a coating agent for iron oxide (Fe_3O_4) nanoparticles on rGO for supercapacitor applications [17]. The network shown in figure 5.0.1 shows a typical GO-Fe_3O_4 network , which is similar to Fe_2O_3.

Their results showed good attachment of Fe_3O_4 and GO. The structural properties of GO-Fe_2O_3 has been demonstrated by Tian *et al.* [18]. Their findings indicate a homogeneous attachment of Fe_2O_3 on GO (shown in figure 5.0.2). It is pertinent to note the importance of GO reduction as the properties of rGO behaves similarly to pristine graphene. Although the results of Tian *et al.* [18] shows homogeneity between

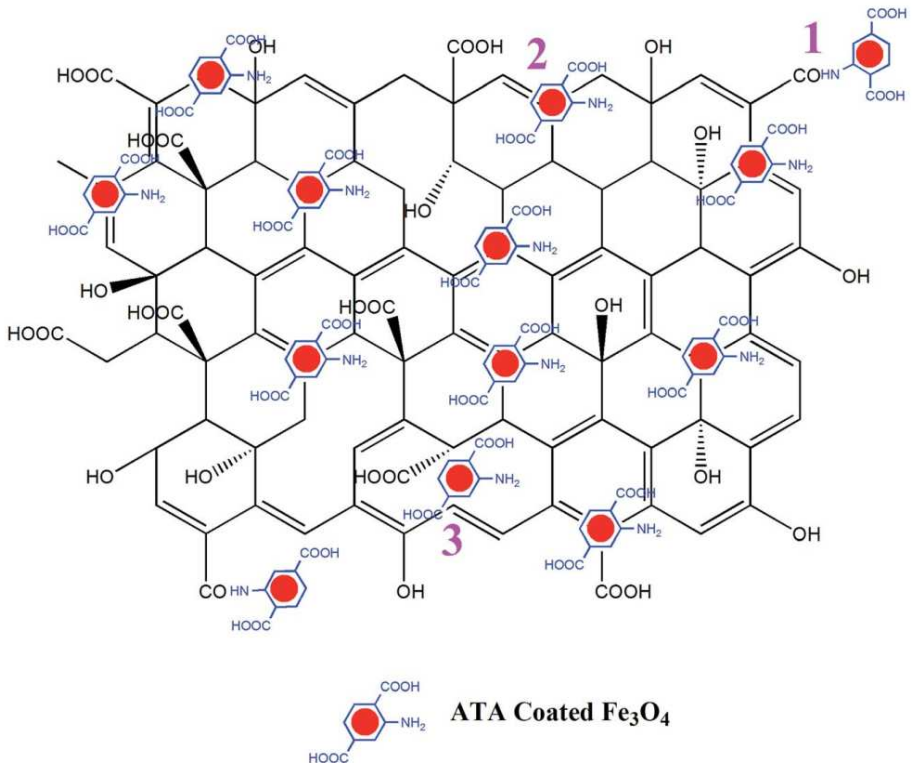

Figure 5.0.1: The GO- Fe_3O_4 network formed from ATA capping agent . Image adapted from [17]

Figure 5.0.2: The structural properties of GO—Fe_2O_3 showing homogeneous arrangement of Fe atoms on the edges of GO. Image adapted from Leilei et al. [18].

GO and Fe_2O_3, it did not account for rGO. The structural properties of GO-(α-Fe_2O_3) composite was recently considered by Zhang *et al.* [19]. The results showed uniform distribution of Fe_2O_3 in GO clusters.

The electrical conductivity of Fe_2O_3 has been a topic of interest for several decades. Precisely with the work of Warnes *et al.* [20] that studied the electrical conductivity and Seebeck effect of α- Fe_2O_3. The results showed intrinsic semiconductor behaviour at temperatures above 923 K. The semiconductor behaviour was due to the inter-

action between the electrons and holes with the α-Fe_2O_3 component. These results amongst others could be the reason behind the enormous electrochemical applications [21]. The electrical insight of GO-Fe_2O_3 composite is mostly geared towards super capacitance and catalysis [22, 23]. Not much is known about the ferroelectric property of GO−Fe_2O_3.

The magnetic property of Fe in the pure or oxidized state is one attribute that has led to it receiving much attention in the recent era [24]. Depending on the phase (i.e α, γ and ϵ), Fe_2O_3 shows magnetic properties. Recently, Tadic *et al* [25] studied the magnetic properties of $\alpha-$ Fe_2O_3 nanocomposites. The results showed a superparamagnetic property at 300 K. Similar studies of Zolghadr [26] used GO-α-Fe_2O_3 and indicated different magnetic transitions. For instance, with the increase in the concentration of GO in GO-α-Fe_2O_3 composite, there is observed paramagnetic and superparamagnetic properties afterwards. All these attempts did not explore the electrical studies which might give an insight into the ferroelectric features of the GO−Fe composite.

The semiconductor characteristics of Fe_2O_3 has made it useful for physicochemical processes and water splitting applications [27, 28]. The electrochemical properties of nanoscale Fe_2O_3 has been greatly explored in lithium-ion battery applications in the recent era [9, 29, 30]. The Li-ion applications are mainly due to the noncovalent bonding of graphene/Fe_2O_3 composite, whereas electrochemical properties have enabled the GO-Fe_2O_3 composite to be very handy as a catalyst for degradation of organic contaminant applications [31].

All the aforementioned applications are very useful in energy and water quality needs [32, 33]. However, the increase in data storage needs is an evolving issue waiting to escalate. There is a need for improvement of the current memory-related materials for faster, efficient and durable storage.

The current study seeks to use the GO-Fe_2O_3 composite for possible applications in electronic and contrast agent related applications. Here, the current study as a follow-up study of rGO−(Au−NP) is geared towards investigating the electronic, electrical and magnetic properties of GO-Fe_2O_3. Moreover, to alleviate the issue of instability associ-

ated with α-Fe_2O_3, the study seeks to approach the structural and electronic properties of GO-Fe_2O_3 with ATA as stabilizing agent. Furthermore, the study in another light seeks to probe the electrical and ferroelectric behaviour of GO-Fe_2O_3 nanocomposite composite. In summary, the study aims to establish the suitability of rGO-ATA-Fe_2O_3 composite material for possible applications in ferroelectric electronic device and MRI contrast agent applications.

5.1 Sample preparation

The materials used for the synthesis of the GO−Fe_2O_3 composites includes ferrous chloride, ferric chloride, 2-aminoterephthalic 99 % acid (ATA), ammonium hydroxide 99 % (NH_4OH), potassium hydroxide 99 % (KOH) and graphene oxide (GO) 99 % powder. The chemicals were commercially obtained from Fisher Scientific and Sigma Aldrich. The aqueous related colloids were synthesized using ultrapure water.

5.1.1 Reduced graphene oxide

Reduced graphene oxide (rGO) in colloidal form was prepared from GO powder. 20 ml of aqueous GO was magnetically stirred at the rate of 500 rpm under 70 °C. The stirring process was left for $\approx$ 6 hrs. The reduction process of GO was done using ammonia hydroxide (NH_4OH). 3 ml of NH_4OH was added in drops to the magnetically stirred GO solution overnight. The obtained rGO solution was centrifuged at 5000 rpm. The centrifuge was done to eliminate large crumbs or clusters. The obtained colloid was washed several times with water and ethanol to neutralize the impact of ammonia impurity. The final product of rGO was collected by drying the colloidal rGO at 60 °C and used for the synthesis of rGO-ATA-Fe_2O_3.

5.1.2 Preparation of ATA-Fe_2O_3 and rGO-ATA-Fe_2O_3 nanocomposites

The synthesis of ATA-Fe_2O_3 and rGO-ATA-Fe_2O_3 nanocomposites is as follows:
A mixture of 1.17 g of $FeCl_2{\cdot}6H_2O$, 0.43 g of $FeCl_2{\cdot}4H_2O$ and 0.82 g of ATA were poured into a 150 ml round flask. The mixture was mixed with 22.5 ml of distilled water. The total mixture was stirred using a magnetic stirrer bar for 1 h at 60 °C under N_2 gas supply. 2.5 ml of NH_4OH at 25% was immediately added to the stirred mixture in order to form iron oxide nanoparticle clusters. The chemical reaction was maintained at a pH in the range $10 - 11$ whilst stirring for another 1 h at 80 °C.
The stirred mixture was cooled to ambient temperature. The nucleated nanoparticles were separated using a magnetic technique. To reduce the effect of impurities, the precipitate was washed several times with ethanol and distilled water. The obtained ATA-Fe_2O_3 nanoclusters were attached to rGO to form the composite as described below.
In the case of rGO-ATA-Fe_2O_3, colloidal portion of ATA-Fe_2O_3 in the ratio of rGO:ATA-Fe_2O_3= 1 : 2 nanocomposites was used. The mixture was ultrasonicated on a low power 50 W bath sonicator at room temperature for approximately 30 mins. The precipipate was dried and collected as rGO-ATA-Fe_2O_3.
The samples rGO-ATA-Fe_2O_3 I and II nanocomposites were prepared to account for different concentration of Fe in the rGO composite using weight ratios in the form of rGO-ATA-Fe_2O_3: rGO i.e (1:2, 1:1). To maintain the homogeneity of rGO-ATA-Fe_2O_3 I and II nanocomposites, both aqueous solutions were ultrasonicated in a low power bath set at room temperature for approximately 30 min.

5.2 Sample characterizations

The structural and morphology of Fe_2O_3 nanoparticle composite was studied using X-ray diffraction (XRD), scanning electron microscopy (SEM) and transmission electron microscopy (TEM). The electronic properties was explored using Raman microscopy, Fourier transform infra-red spectroscopy (FTIR), X-ray photoelectron spectroscopy (XPS), X-ray absorption near edge structure (XANES). The electrical conductivity was studied using a current-voltage (I-V) setup and the magnetic property was established using M-H loop measurement from a superconducting quantum interference device (SQUID) magnetometer. The structural characterization of the samples was performed using Rigaku Smartlab X-ray diffractometer (0.154 nm Cu $K\alpha$ line). The morphology of the samples was obtained using transmission electron microscopy (TEM) Jeol JEM 2100 and Field emission scanning electron microscope Jeol JSM-7800F. The core-shell electronic structure were obtained using KRATOS-SUPRA spectrometer with monochromatic Al $K\alpha$ (photon source $hv = 83.87\,\text{eV}$) and base pressure 1.2×10^{-9} Torr.

Valence band photoemission and density of states (DOS) were probed using KRATOS-SUPRA ultraviolet photoelectron (UPS) spectrometer He II ($hv = 40.8\,\text{eV}$). The M-H hysteresis loop of the samples was measured using a SQUID-type magnetometer with sensitivity $< 5 \times 10^{-8}$ emu.

5.2.1 X-ray diffraction

The X-ray diffraction spectra of graphite, GO, rGO and rGO- ATA-Fe_2O_3 is shown Figure 5.2.1.The prominent peaks for graphite and GO include 14.3°, 26.4° and 30.2°. The peaks are associated with C(002), C(100) and C(200) respectively. The peak appearing at 33.2°, 45° and 54.7° are attributed to C(111) [34], C(100) and C(004) reflections

[35], respectively. The C(100) reflections are due to convolution of carbon nanocrystals whereas the C(004) peak are related to the second order diffraction of the C(002) peak [35]. The peak located at 54.7° which is prominent in all the samples with the exception of rGO-ATA-Fe_2O_3 is assigned to C(211) [36]. Meanwhile, for ATA-Fe_2O_3 and rGO-ATA-Fe_2O_3, two peaks indicated at 43.1° and 50.4° are prominent. Both peaks are due to Fe atoms and are assigned to (311) and (400) respectively [17, 37, 38]. There is a possibility of an overlap between C(002) and Fe (110) [39] indicating the attachment of C and Fe atoms. The XRD pattern of rGO-ATA-Fe_2O_3 shows consistency with with spinel phase of Fe_3O_4 with JCPDS card no. 19-0629 [40].

As discussed in Section 4.3.1, the Debye-Sherrer equation was used in the estimation of the crystallite size. With focus on C(002) reflection peak and using pseudovoigt function in Originlab software, the estimated particle size of graphite powder, GO, rGO and ATA-Fe_2O_3 were extrapolated (see Table 5.2.1). Steady increase in the crystallite size is observed as carbon atoms undergoes different chemical treatment. The increase in the particle size can be attributed to graphite exfoliation, GO reduction and functionalization. The particle size increase is consistent with the previous report of Li *et al.* [42]. Furthermore, the steady increase indicates redistribution of atoms and formation of new bonds as indicated in later Section 5.2.6 in XPS data. The size distribution of the GO and rGO-ATA-Fe_2O_3 indicate the clusters been in the nanoscale and confirms the formation of the nanocomposite. Furthermore, the hump-like pattern indicates the presence of few layers of graphene in GO [43]. The intensity of the hump decreases with the action of functionalization signifying an increase in the sp^3 cluster of GO.

Table 5.2.1: The extrapolated estimated values of particle size of graphite, GO, rGO and ATA-Fe_2O_3 from XRD spectra using C(002) reflection plane.

Samples	2θ (degree)	FWHM	Particle size (nm)
Graphite	30.3	0.113 ±0.08	76.1
GO	30.3	0.107 ±0.08	80.3
rGO	30.2	0.097 ±0.08	88.6
ATA-Fe_2O_3	30.2	0.092 ±0.08	93.4

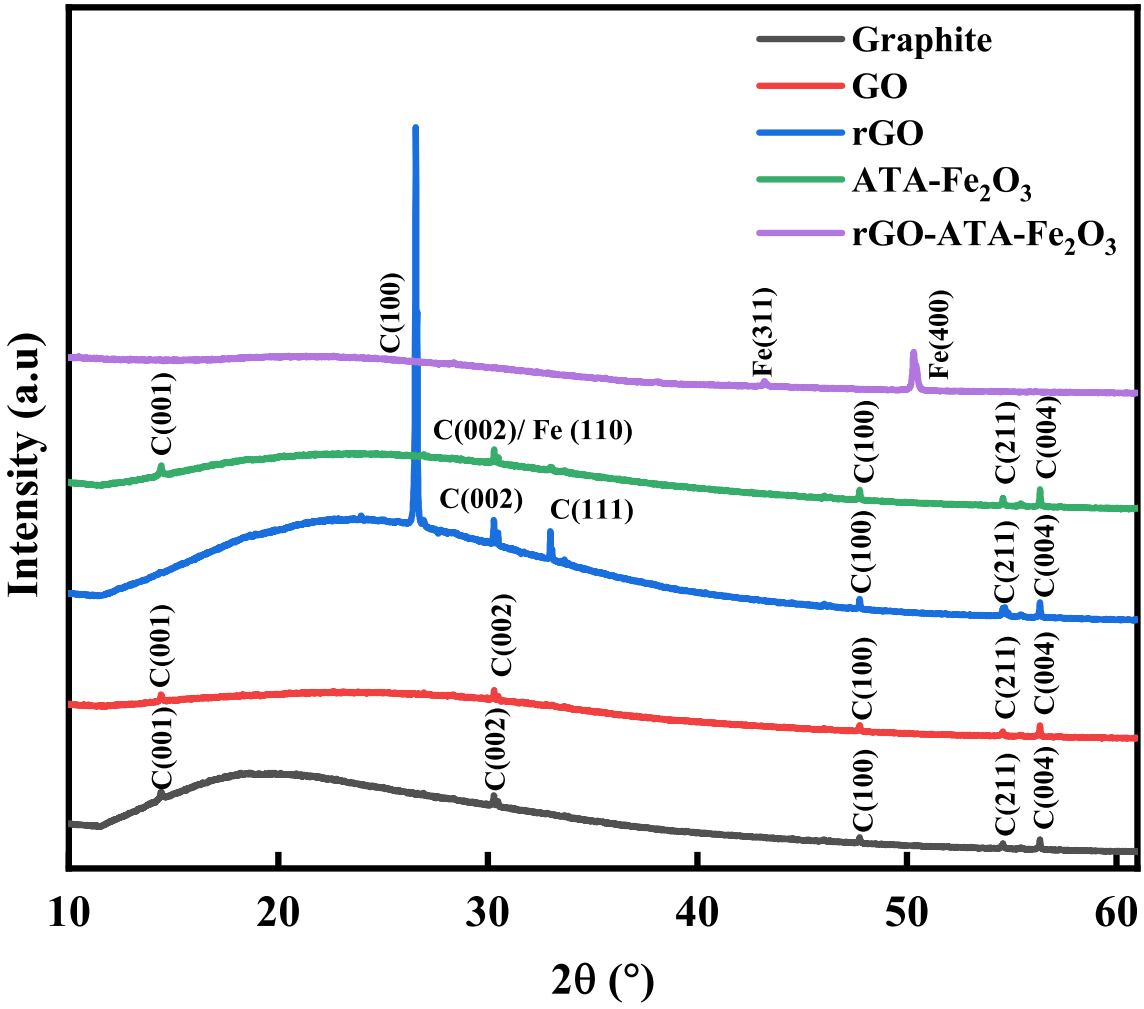

Figure 5.2.1: The X ray diffraction spectra of GO, rGO and rGO- ATA-Fe_2O_3. The XRD plots for all the samples are stacked, hence, the intensities (y axis) can not be compared.

5.2.2 Transmission electron microscopy

The TEM images as indicated in Figure 5.2.2 (a)-(c) shows the morphology of ATA-Fe_2O_3 at various magnifications, whereas (d) shows the selected area electron diffraction (SAED) pattern. All the samples in this Section were not imaged by the TEM technique due to a lack of characterization resources. The particle sizes were manually extrapolated from the TEM images and are within the $8 - 10$ nm range which is consistent with the composite being in the nanoscale range as indicated in XRD measurements. The bright spot in the SAED image confirms the weak amorphicity of Fe_2O_3, which

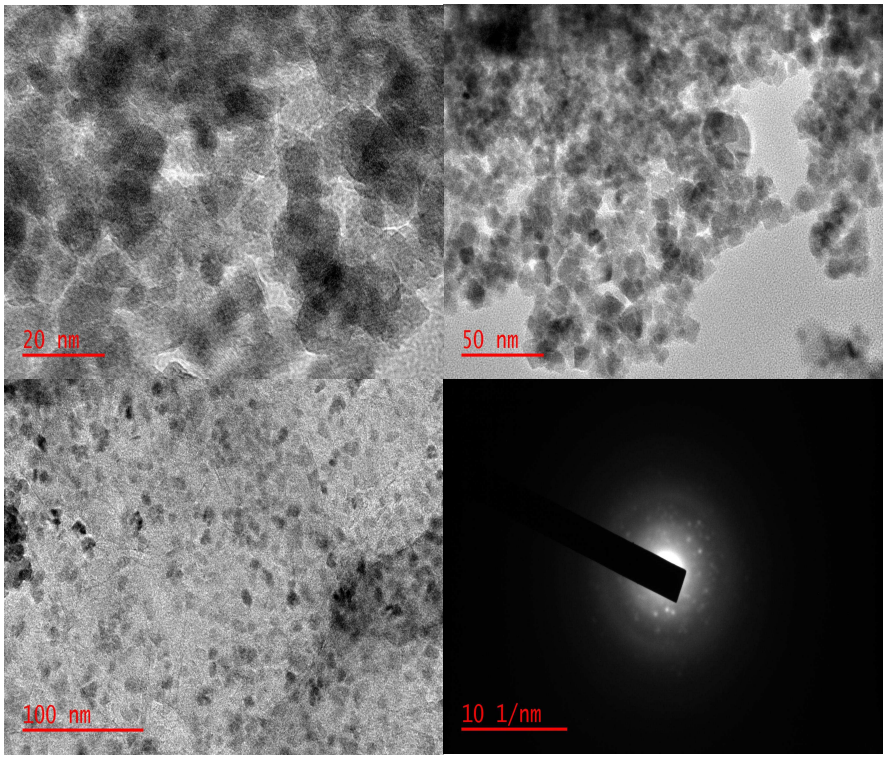

Figure 5.2.2: The TEM images of ATA-Fe_2O_3 at various magnification (a) magnification at 20 nm, (b) magnification at 50 nm, (c) magnification at 100 nm and (d) SAED images indicating the amorphous nature of ATA-Fe_2O_3.

may have been induced by the impact of the capping agent [44], whereas the dots (crystallinity) forming a ring around the bright spot are the reflections of Fe(311) and Fe(400) as indicated in the XRD spectra [44].

The morphology of rGO-ATA-Fe_2O_3 (Figure 5.2.3) displays a similar pattern with adequate dispersivity of the particles. The grey area surrounding the spheres indicates graphene oxide [45]. The crystallinity of rGO-ATA-Fe_2O_3 is more pronounced as indicated in the SAED images. Similarly, the rings represent the Fe (311) and Fe (400) reflection planes. The appearance of the bright spot is mostly from rGO contributions. The weak agglomeration present in the composite is depicted by the pocket of space in the images. Figure 5.2.4 shows the particle size distribution of ATA-Fe_2O_3 and rGO-ATA-Fe_2O_3 (II) extrapolated using ImageJ software. As indicated, the particle mean distribution size spans the range 14-15 nm , which is the intended composite for the current study. The main distinction between both images is the presences of the GO sheet in figure 5.2.3 at the top left corner. The surface to volume ratio property of GO

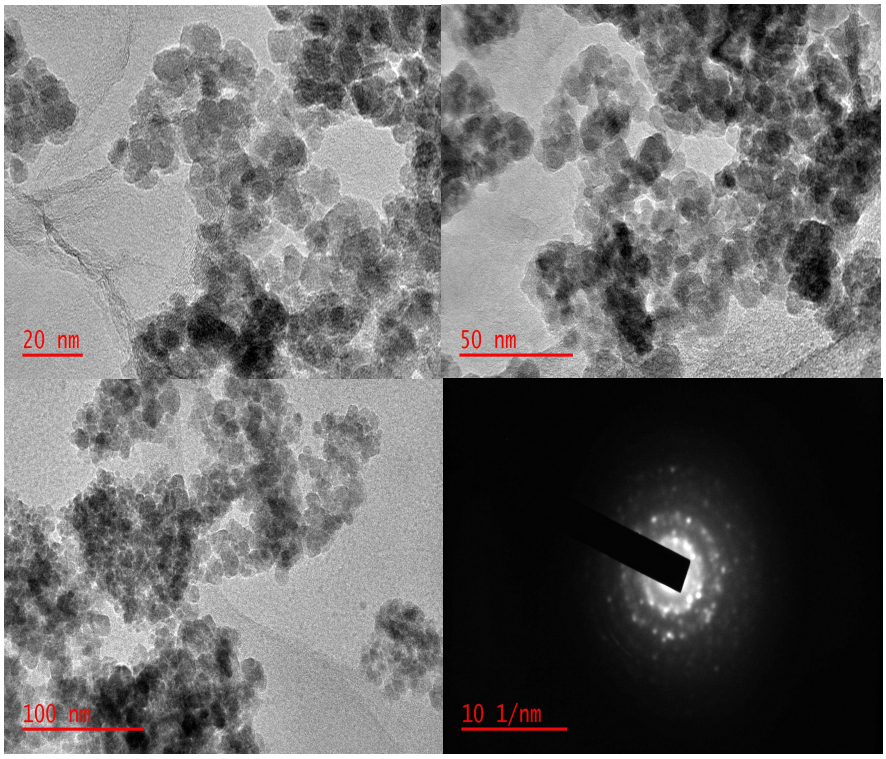

Figure 5.2.3: The TEM images of rGO-ATA-Fe_2O_3 with various magnification. (a) magnification at 20 nm, (b) magnification at 50 nm, (c) magnification at 100 nm and (d) SAED images indicating the crystallinity of the nanocomposite.

sheets [46] allows for easy clustering of the Fe_2O_3 particles on its surface.

The discrepancy in particle size between the XRD and TEM measurements. The size from XRD spectra using the Sherrer equation is an estimate and does not account for error corrections which could be responsible for the higher value in particle size. Hence, the extrapolations from TEM images are considered more accurate [47].

5.2.3 Scanning electron microscopy

Further study of the morphologies of GO, rGO and rGO-ATA-Fe_2O_3 is shown in the FESEM images. Figure 5.2.5 shows the SEM images and EDX spectra for graphite powder. The images show the typical flake-type particles exhibited by graphitic materials [48]. The particles are tightly packed with little space in-between. The implication of the tight packing may prove useful in electron mobility. The EDX spectra indicate

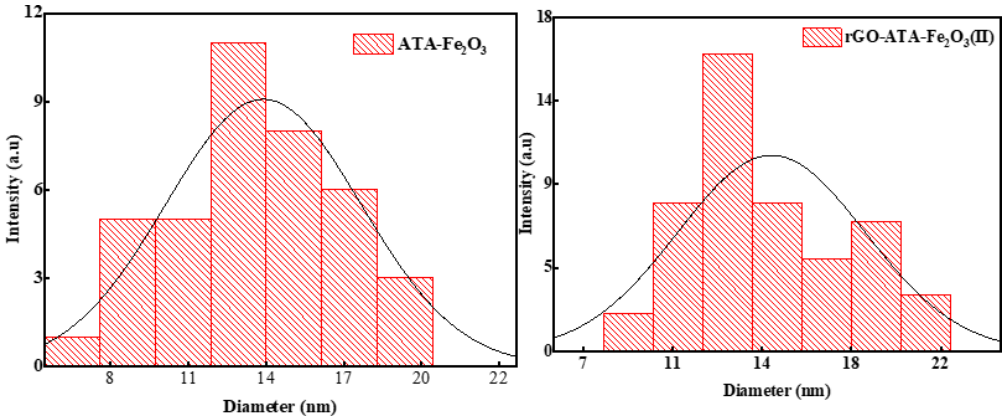

Figure 5.2.4: Histogram showing the particle size distribution for ATA-Fe_2O_3 and rGO-ATA-Fe_2O_3 (II).

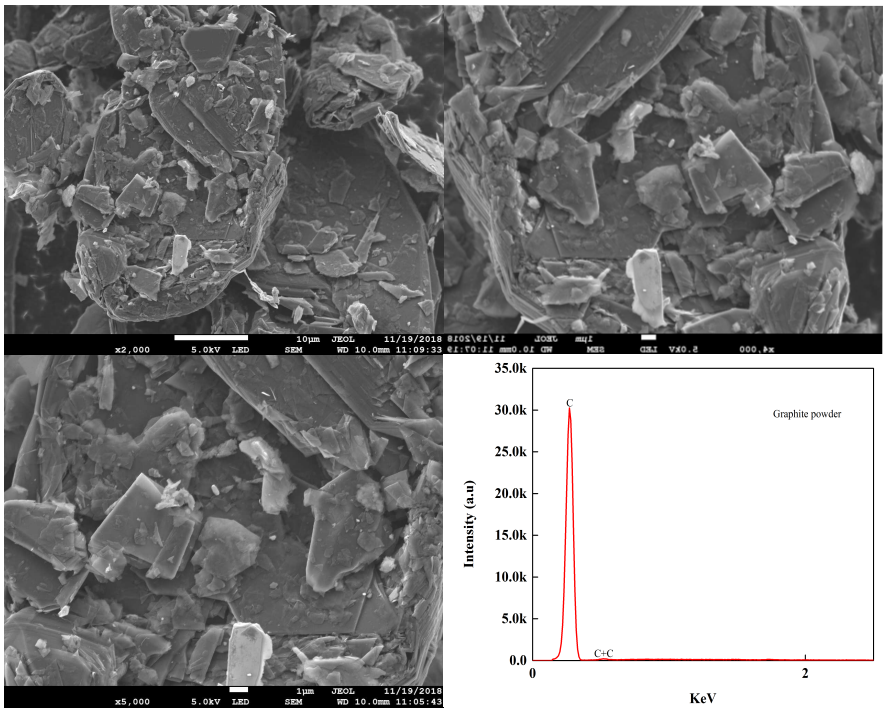

Figure 5.2.5: The SEM images for graphite powder for several magnifications. (a) magnification at ×2000, (b) magnification at ×4000, (c) magnification at ×5000 and (d) The EDX spectra showing the approximate elemental composition of the sample.

the presence of carbon which is in agreement with typical graphite material. The effect of graphite powder exfoliation can be easily observed in GO as shown in Figure 5.2.6. In the case of GO (see Figure 5.2.6), the particles exhibit sphere-like shape. The particles are sparsely arranged and may easily influence electron mobility behaviour. The EDX spectra indicate carbon and oxygen as expected. The oxygen component accounts for the oxygen functional groups that are easily found in the edge and basal planes of

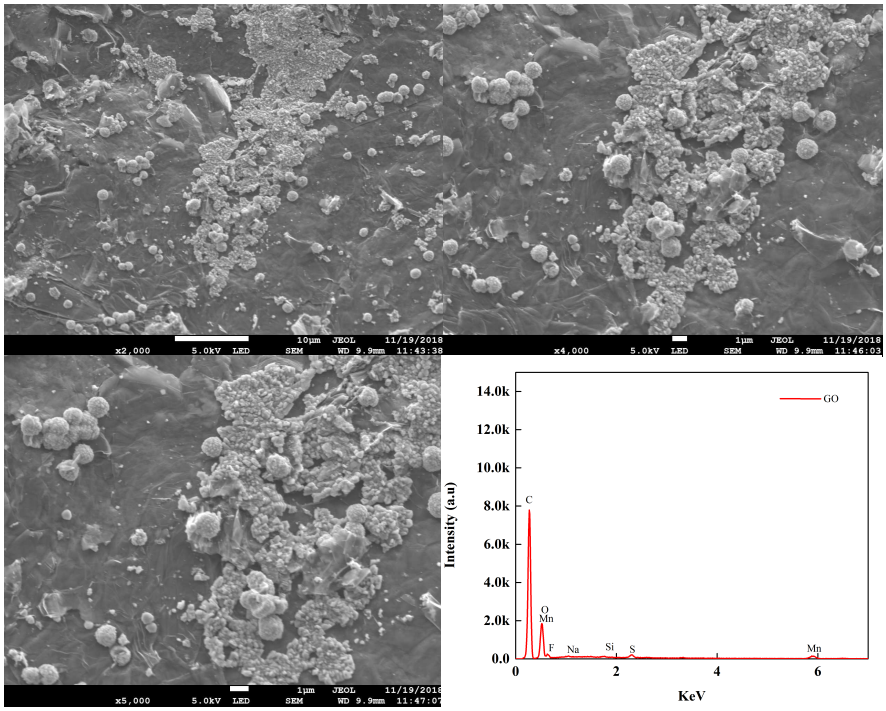

Figure 5.2.6: SEM images for GO with different magnifications (a) magnification at ×2000, (b) magnification at ×4000, (c) magnification at ×5000 and (d) EDX spectra showing the element component of the sample.

GO. The other elemental components are due to impurities from the drop-casting process. The film deposition process is reliant on air-drying, which allows easy deposition of trace elements from the air. Even though care has been taken to reduce the impact, it is completely unavoidable.

The reduction of GO with NH_4OH also impacts the morphology of GO. As observed in 5.2.7, the shape of the particles seemed flaked-like with tight packing. The EDX spectra show the presence of carbon and oxygen as expected. Another appearance of impurities is mainly due to the reduction process and the silicon wafer drop-casting process. The tight packing of the particles is an indication of weak agglomeration. As noted earlier, the tight packing has an enormous influence on the electrical conductivity of GO [49].

Figure 5.2.8 shows the SEM images of ATA-Fe_2O_3 nanoparticles for various magnifications. The spherical shape of the particles shows consistency for magnetic Fe_3O_4 [50]. The other flake-like particles may be the carbon coating used for the reduction of the charging effect during SEM measurement [51]. Figure 5.2.8 (d) is the EDX spectra

showing the elemental components for ATA-Fe_2O_3 nanoparticles. The appearance of carbon is mainly from the spin coating of the silicon substrate for charging effect reduction. Furthermore, Figure 5.2.9 shows the SEM images for rGO-ATA-Fe_2O_3 nanocomposite. The SEM images for rGO-ATA-Fe_2O_3 show similarity with ATA-Fe_2O_3. The observed distinction is seen in the distribution and arrangement of the spherical and flake-like particles. The obvious reason is attributed to the inclusion of rGO in the composite which allows for formation of the Fe_2O_3 clusters on the GO by virtue of its large surface area [46]. As iterated earlier from TEM images, the particle distribution describes weak agglomeration of the particles which may inevitably allow easy electron mobility. Figure 5.2.9(d) also shows the EDX spectra for rGO-ATA-Fe_2O_3 nanocomposite.

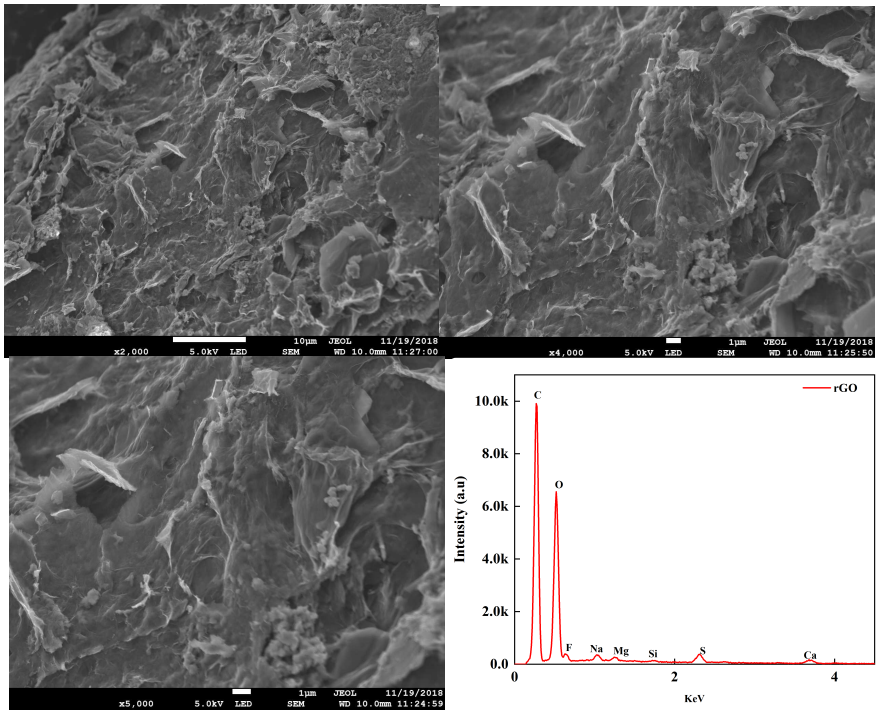

Figure 5.2.7: The SEM images for rGO at diffent magnifications (a) magnification at ×2000, (b) magnification at ×4000, (c) magnification at ×5000 and (d) EDX spectra showing the elemental components contained in the sample.

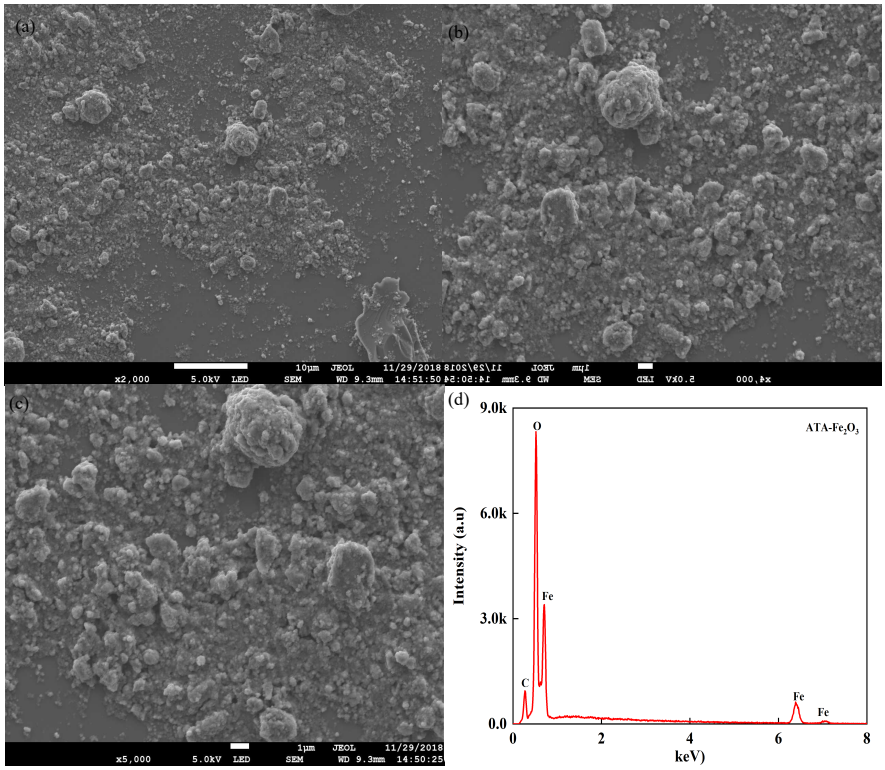

Figure 5.2.8: The SEM images for ATA-Fe_2O_3 at different magnifications (a) magnification at $\times$2000*, (b) magnification at* $\times$4000*, (c) magnification at* $\times$5000 *and (d) EDX spectra showing the elemental components contained in the sample.*

5.2.4 Raman spectroscopy

The Raman scattering spectra for all samples considered are shown in Figure 5.2.10. The D and G peak , which corresponds to the defect and E_{2g} breathing mode are present at $\approx$ 1332 and 1560 cm^{-1}, respectively, for graphite powder. Likewise, the D and G peaks manifest in all graphene related material [52] with a downward or upward Raman shift. The defect D peak is mainly due to the disordered atomic arrangement from sp^3 carbon atomic configurations, whereas the E_{2g} breathing mode G peak is due to sp^2 carbon atomic configuration usually associated with 2-dimension lattice graphene-like materials [53].

The upward or downward shift in the Raman scattering can be attributed to sp^3 enhancement from the impact of NH_4OH reduction and Fe_2O_3 functionalization [45]. However, the case of ATA-Fe_2O_3 does not show any D or G peak since it is not graphitic as

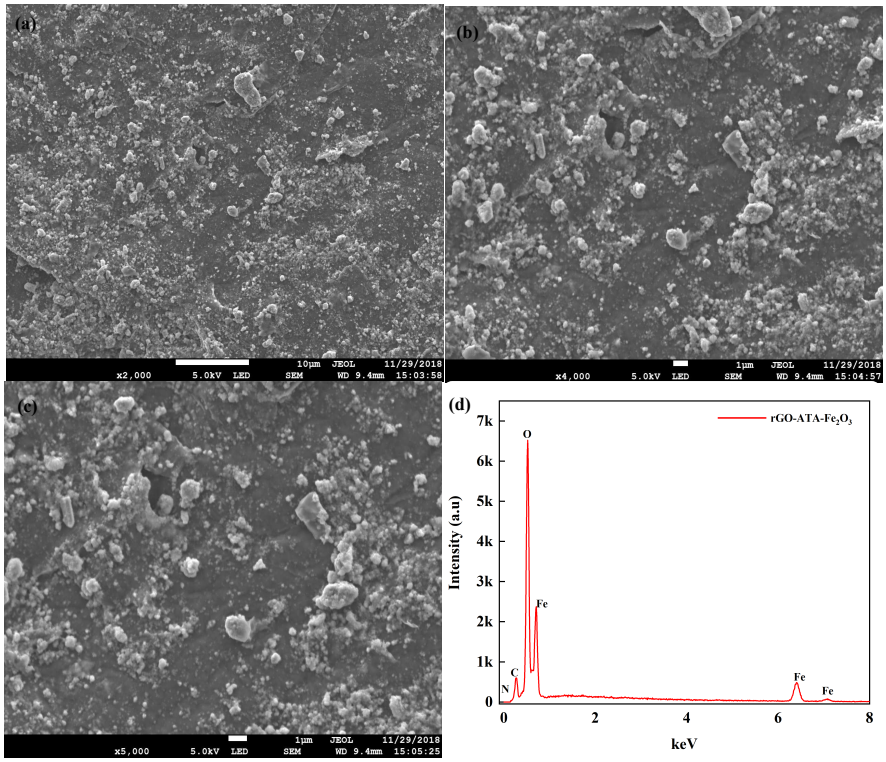

Figure 5.2.9: The SEM images for rGO- ATA-Fe_2O_3 at different magnifications (a) magnification at ×2000, (b) magnification at ×4000, (c) magnification at ×5000 and (d) EDX spectra showing the elemental components contained in the sample.

in the case of carbon materials that possesses C=C and C−C , which are responsible for D and G band [54].

Table 5.2.2 and 5.2.3 represents the extrapolated parameters, i.e. peak position, area and width from the deconvoluted peaks fitted using a Gaussian function from Originlab software. The ratio I_D/I_G , which iterates the degree of defect in the material due to oxidation, reduction and functionalization was calculated from the peak intensities. As

Table 5.2.2: The extrapolated parameters from the G bands where X_D, A_D and W_D are the position, area and width, respectively

Samples	D Peak		
	$X_D(\text{cm}^{-1})$	A_D	$W_D(\text{cm}^{-1})$
Graphite	1332 ±2.4	8.9 ±0.5	7.2 ±2.4
GO	1334 ±2.3	1.7 ±0.5	0.6±0.01
rGO	1314 ±2.4	12.8 ±0.4	0.6 ±0.01
rGO-ATA-\ch{Fe2O3}(I)	1342 ±2.4	9.2 ±0.5	0.2 ±0.01
rGO-ATA-\ch{Fe2O3}(II)	1313 ±2.4	0.6 ±0.5	0.8 ±0.01

indicated in Table 5.2.3, the value for graphite powder gives 0.82. With the oxidation

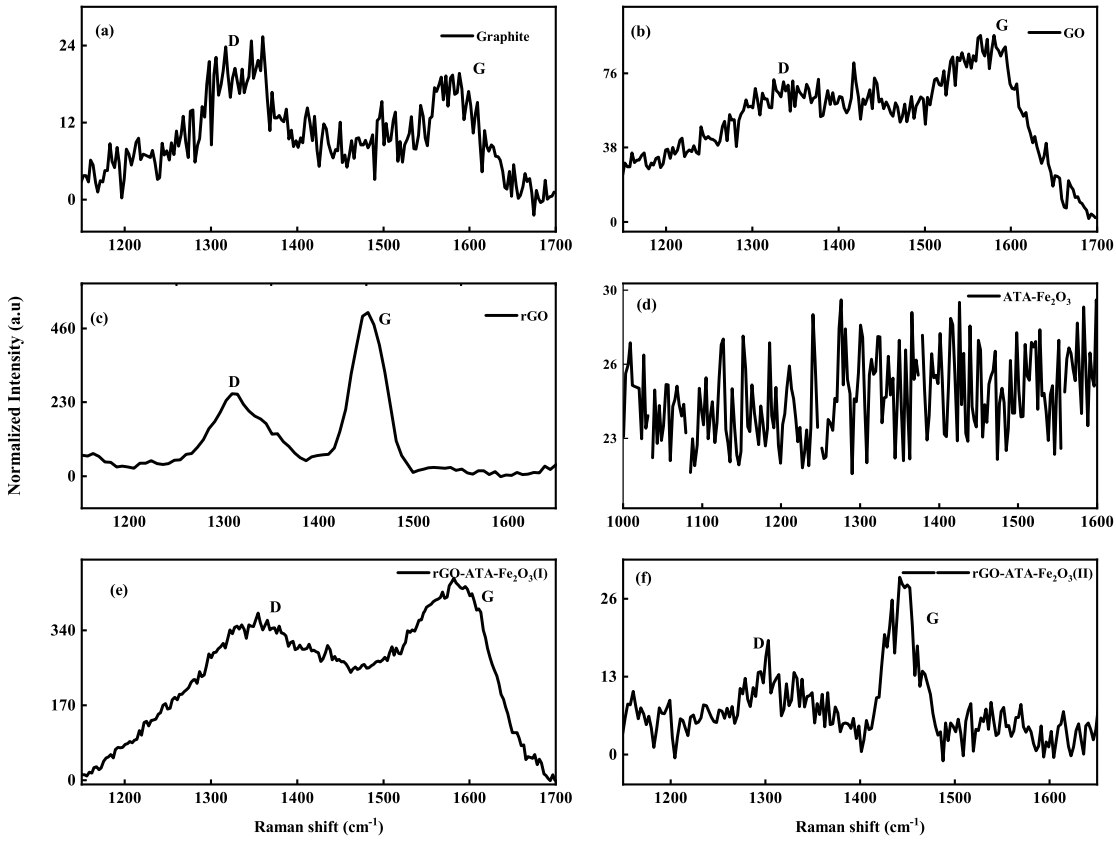

Figure 5.2.10: The Raman spectroscopy measurement for all the samples where (a) graphite powder, (b) GO, (c) rGO, (d) ATA-Fe_2O_3, (e) rGO- ATA-Fe_2O_3 (I) and (f) rGO- ATA-Fe_2O_3 (II).

Table 5.2.3: The extrapolated parameters from the G bands where X_D, A_D and W_D are the position, area and width, respectively.

Samples	G peak		
	$X_G(\mathrm{cm}^{-1})$	A_G	$W_G(\mathrm{cm}^{-1})$
Graphite	1580 ±2.4	9.6 ±0.4	7.0 ±0.4
GO	1568 ±2.4	4.5 ±0.4	8.5 ±0.4
rGO	1452 ±2.4	20.2 ±2.4	0.3 ±0.1
rGO-ATA-\ch{Fe2O3}(I)	1573 ±2.4	9.6 ±1.4	1.9 ±0.4
rGO-ATA-\ch{Fe2O3}(II)	1444 ±2.4	1.0 ±0.4	0.3 ±0.1

D+D'			2D			I_D/I_G
$X_{D+D'}(\mathrm{cm}^{-1})$	$A_{D+D'}$	$W_{D+D'}(\mathrm{cm}^{-1})$	$X_{2D}(\mathrm{cm}^{-1})$	A_{2D}	$W_{2D}(\mathrm{cm}^{-1})$	
2531.0 ±2.4	8.3 ±0.4	242.9 ±0.4	2792.0 ±2.4	2.7 ±0.4	0.7 ±0.1	0.82
						0.46
2725.0 ±2.9	1.6 ±0.4	59.6 ±0.4	2922.2 ±2.2	16.8 ±2.4	0.1 ±0.01	0.45
						0.83
2684.0 ±3.4	0.2 ±0.01	25.3 ±0.1	2911 ±2.4	13.06 ±2.4	0.1 ±0.01	0.43

of the carbon atoms, the value decreases (0.82 → 0.46). With the reduction of GO using NH_4OH, the sp^3 is enhanced and can be seen with a slight decrease (0.46 → 0.45). However, with the functionalization of GO with ATA-Fe_2O_3 (Figure 5.2.11 (d)), an abrupt increase (0.45 → 0.83) in the defect D peak is observed. The increase in the

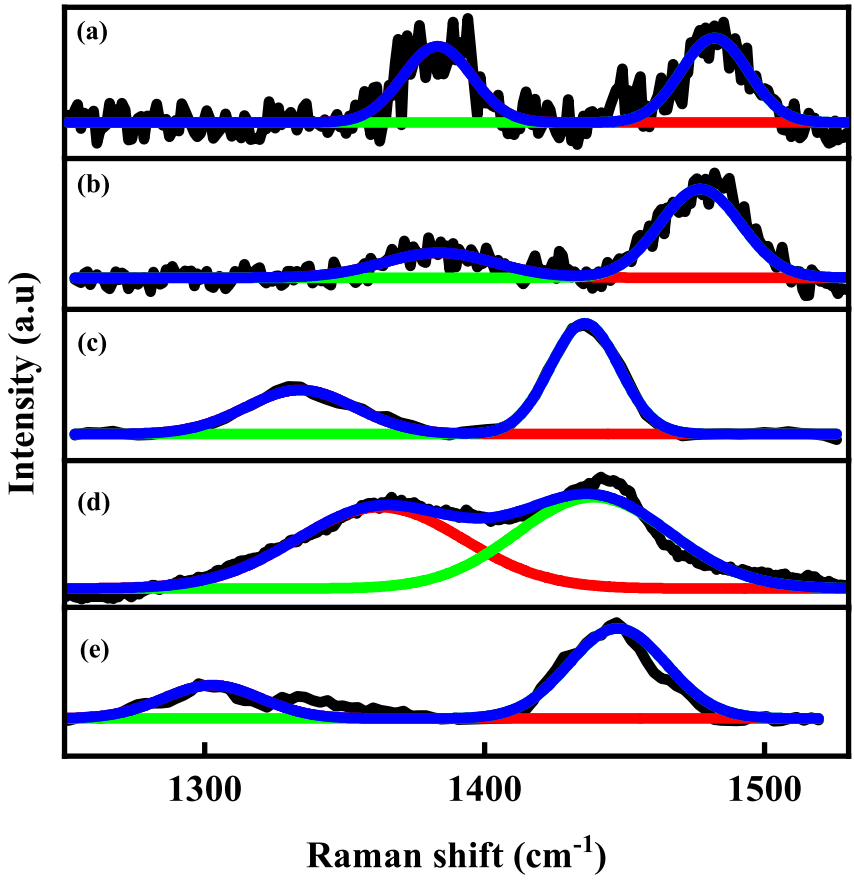

Figure 5.2.11: The deconvoluted D and G peak position for all the samples considered where (a) graphite powder, (b) GO, (c) rGO, (d) rGO-ATA-Fe_2O_3(I) and (e) rGO-ATA-Fe_2O_3(II)

defect of the carbon network causes an abrupt jump in the value of I_D/I_G [55]. The increase in the intensity of the D band can be attributed to the reduction in the in-base plane functional group [56].

The induced defect in GO from the impact of functionalization is shown in Figure 5.2.12. The appearance of D' can be attributed to vacancies created by 5-8-5 defects [57]. The 5-8-5 defects are attributed to the pentagonal and octagonal rings [55, 56]. A further decrease in the I_D/I_G is observed when the concentration of Fe_2O_3 is increased.

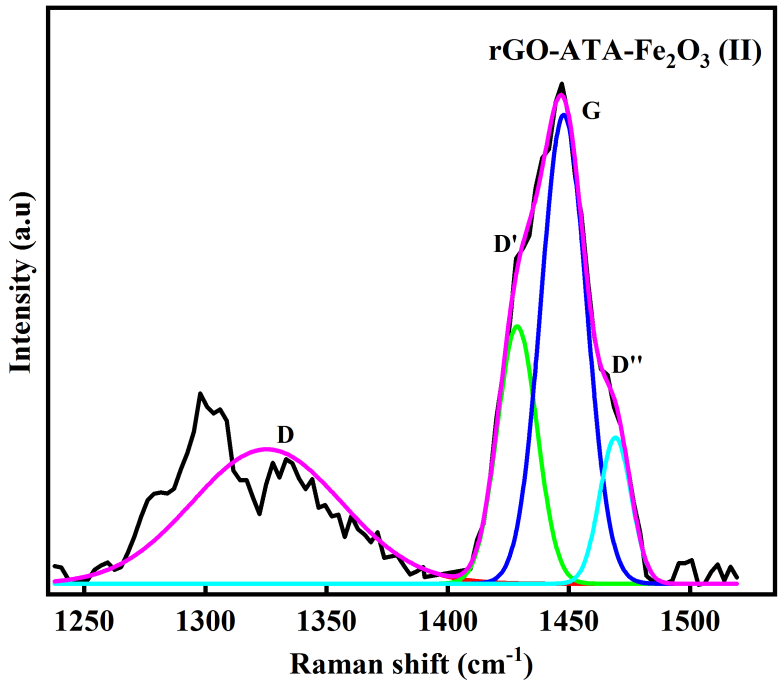

Figure 5.2.12: The deconvoluted Raman spectra for rGO-ATA-Fe_2O_3 (II) showing defect disorder in GO from the effect of functionalization. The colours differentiate the peak positions.

The decrease can be due to the stability of the carbon network with possible recovery in the carbon backbone, which is associated with pristine graphene [58].

Figure 5.2.13 shows the 2D peak prominent for graphite, rGO and rGO-ATA-Fe_2O_3 (II) appearing at 2792 cm^{-1}, 2922 cm^{-1} and 2911 cm^{-1}, respectively [59]. The 2D peak for GO and rGO-ATA-Fe_2O_3 (I) was not prominent. The absence of the 2D peak may be due to the defect induced by the exfoliation process and functionalization. Although, the samples were prepared using the same process, however, the atomic interaction with the incident light, which results in the Raman scattering behaves differently. The distribution of the atoms within the structure of GO and rGO-ATA-Fe_2O_3 (I) and light interaction may not have created significant phonon vibrations that could cause the appearance of the 2D overtone [54]. The case of rGO-ATA-Fe_2O_3 (I) is consistent with the high value of I_D/I_G. The 2D peak is a D peak overtone, which is due to two lattice phonon vibrations [59]. The electron dispersion spectra of graphene indicates a two-phonon assisted-defect process, which can produce weak peak as observed in figure 5.2.13 [59]. The mechanism behind the activation of the $D'D'$ is mainly attributed to

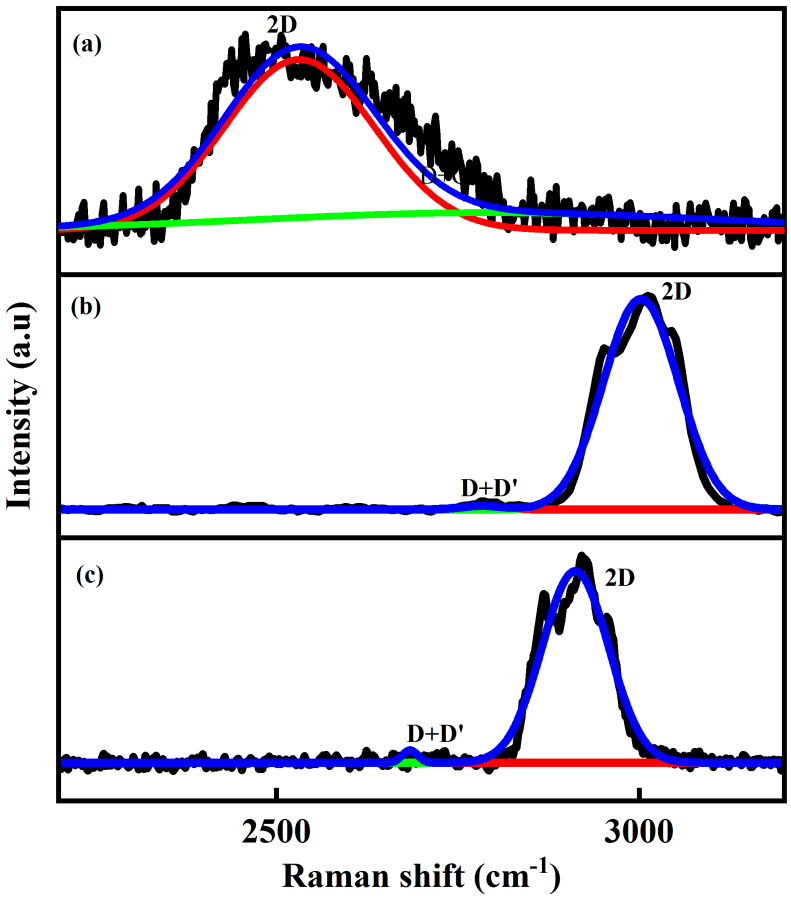

Figure 5.2.13: The 2D and D+G peak raman spectra where (a) graphite powder, (b) rGO and (c) rGO-ATA-Fe_2O_3 (II) nanocomposite.

double resonance [60].

The effect of GO reduction and functionalization is evident in the wavenumber shift. For instance, the 2D position shifts to higher wavenumbers and eventually shift backwards. The process of reduction causes bond stretching, which in turn leads to phonon vibrations. The impact of the phonon vibration leads to a shift in the peak position, which is observed in this case. The higher or lower shift in the Raman peak positions is mostly due to chemical bond length inherent in the material. A short bond length results in higher wavenumber shift, whereas long bond length gives the backward shift with regard to the reference material [61]. Here, the degree of oxidation of carbon and sp^3 enhancement due to Fe and O_2 atomic attachment may be the reason for the long and short bond lengths.

5.2.5 Fourier transform infra red spectroscopy

As iterated earlier in Section 3.5, the Fourier transform infrared (FTIR) spectroscopy is a non-destructive tool that can probe the bonding that exists within a material. Figure 5.2.14 and Table 5.2.4 shows the FTIR spectra of GO, rGO and rGO-ATA-Fe_2O_3. As indicated in the Table 5.2.4, the prominent peaks are indicated at wavenumbers 1060, 1186, 1456, 1619 cm^{-1} which are assigned to C−O alkoxy group, C−O epoxy group, O−H bending and C=C stretching, respectively. Whereas the peaks 1704-1740, 2851-2940, 3460 cm^{-1} are assigned to C=O stretching vibrations, symmetric and asymmetric stretching from $-CH_2$ bonds and −OH stretching vibrations respectively [62]. All these aforementioned peaks have strong prominence in GO and rGO.

The oxygen functional groups also appear for ATA-Fe_2O_3 and rGO-ATA-Fe_2O_3 with two extra peaks of 570 and 663 cm^{-1} which are assigned to Fe−O bonds [63]. The reduction in the intensity and disappearance of some bonds is attributed to the substitution of oxygen groups with Fe atoms [64]. The case of graphite powder shows feeble activity. The FTIR spectra confirm the formation of GO and rGO-ATA-Fe_2O_3 nanocomposite as expected.

Table 5.2.4: The bond stretching and formations for GO, rGO and rGO-ATA-Fe_2O_3 as indicated by FTIR spectra.

Wavenumber (cm^{-1})	Functional group
1060	C-O alkoxy group
1186	C-O epoxy group
1456	O-H bending
1619	C=C stretching
1704-1740	C=O stretching vibration
2851-2940	Symmetric and asymmetric stretching
3360, 3460	-OH stretching vibration
570	Fe-O
663	Fe-O

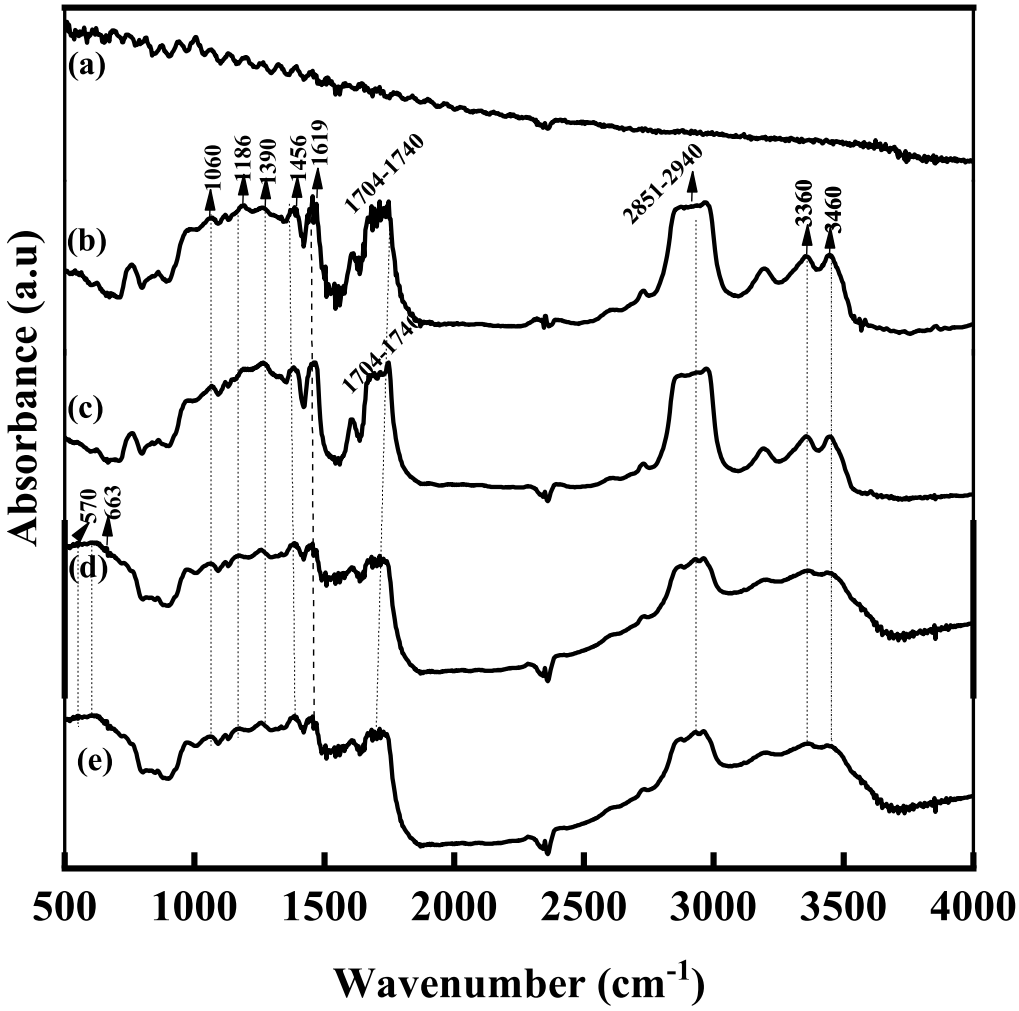

Figure 5.2.14: The FTIR spectra for all the samples considered. (a) Graphite powder, (b) GO, (c) rGO, (d) ATA-Fe_2O_3 and (e) rGO-ATA-Fe_2O_3.

5.2.6 X-ray photoelectron spectroscopy

Figure 5.2.15 shows the XPS-wide scan of GO, rGO and rGO-ATA-Fe_2O_3 nanocomposite. The wide scan shows the indexed core–shell state present in the sample as well as the elemental components. In the case of graphite powder, the prominent core shells include Si 2p, Si 2s, C 1s, O 1s, and O KLL shells. The core shells show silicon, carbon, oxygen atoms as expected.

The Si 2p and Si 2s represents the silicon substrate in which the sample was deposited (drop-cast) on. The C and O 1s represents the carbon and oxygen atoms, respectively.

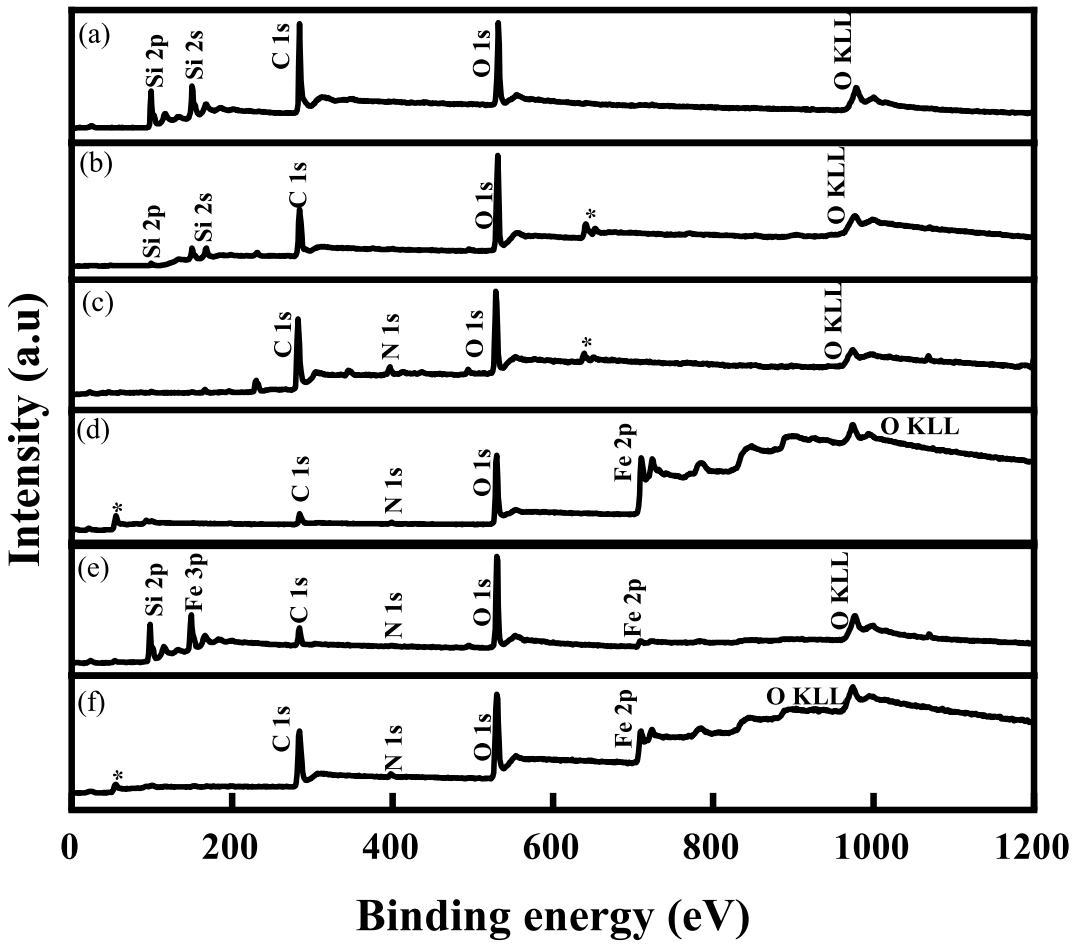

Figure 5.2.15: The XPS wide scan of all the samples considered. (a) Graphite powder (b) GO (c) rGO (d) ATA-Fe_2O_3 (e) rGO-ATA-Fe_2O_3 (I), (f)rGO-ATA-Fe_2O_3 (II) nanocomposite.

The presence of oxygen may be from the drop-casting process when the powder was dissolved with methanol [65]. A similar trend is observed for GO and rGO.; however, the N 1s, which represent the presence of nitrogen is mainly due to the NH_4OH reducing agent. The features labelled asteriks are unknown can be attributed to Auger effect resulting from intra-state transitions of electrons in the excited atoms [66]. The possibility of the presence of N 1s in ATA-Fe_2O_3 is likely and may be due to impurities introduced from the 2-aminoterephthalic acid (ATA) capping , whereas the Fe 2p and O 1s indicate the formation of Fe_2O_3 nanoparticles. Meanwhile, the N 1s becomes prominent for rGO-ATA-Fe_2O_3 (I) and (II), which confirms the formation of the nanocomposite with rGO [45, 67].

Table 5.2.5: The composition and quantification of GO composites obtained from XPS spectra.

Sample	C 1s	O 1s	N 1s	Fe 2P
Graphite powder	75.21 ± 0.39	24.79 ± 0.39		
GO	63.75 ± 0.38	36.25 ± 0.38		
rGO	69.34 ± 0.48	26.17 ± 0.36	4.49 ± 0.46	
ATA-Fe_2O_3	25.85 ± 0.70	48.87 ± 0.58	2.24 ± 0.40	23.04 ± 0.36
rGO-ATA-Fe_2O_3 (I)	34.63 ± 0.96	60.76 ± 0.98	1.76 ± 0.68	2.85 ± 0.27
rGO-ATA-Fe_2O_3 (II)	60.89 ± 0.41	31.92 ± 0.33	2.17 ± 0.38	5.01 ± 0.18

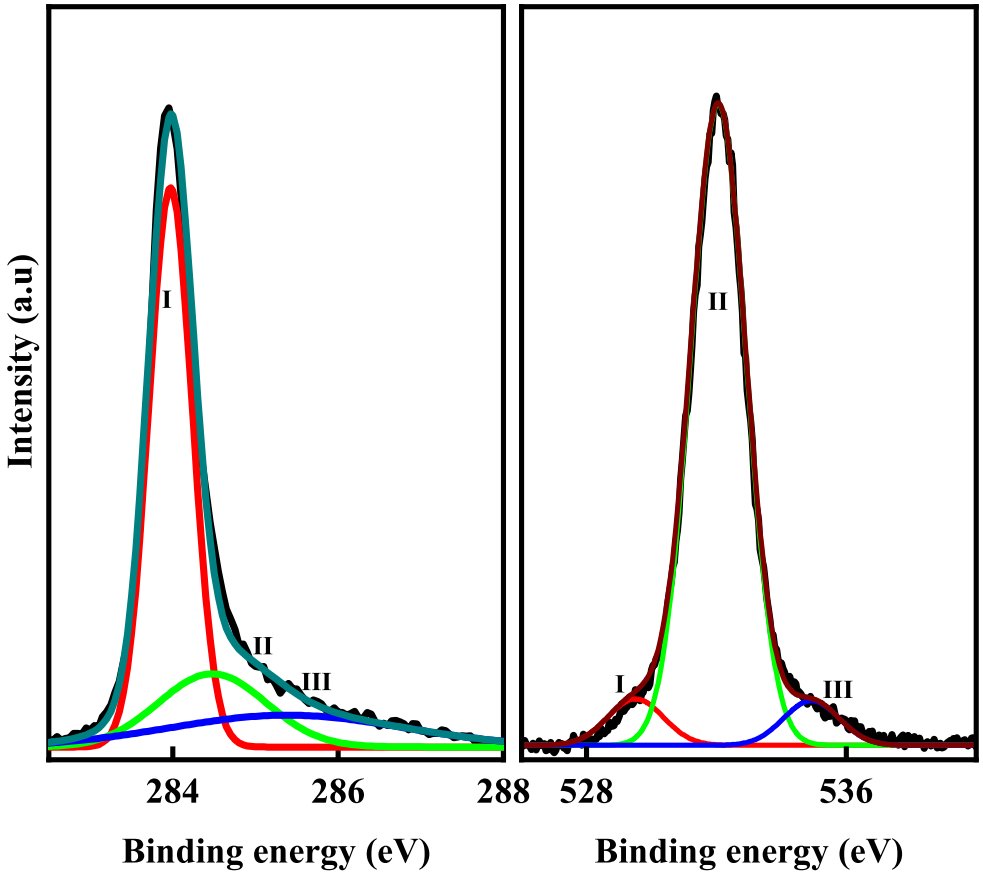

Figure 5.2.16: The C 1 s and O 1s core shells of graphite powder showing the prominent peaks of C=C sp^2 clusters. Peak I (C=C), Peak II (C−OH), peak III (C=O) and peak IV (O=C−OH. for O 1s, Peak I (O=C−OH), peak II (C=O) and peak III (C−OH. The different colours differentiates the peak positions.

The elemental quantification of the GO and composites are presented in Table 5.2.5. Figure 5.2.16 shows the C and O 1s core shells for graphite. The de-convoluted peaks are labeled as indicated in the Figure 5.2.16 and tabulated in Table 5.2.6. The resulting C 1s peak positions are 284.0 eV ± 0.1, 285.2 eV ± 0.1 and 286.3 eV ± 0.1 and are assigned to C=C sp^2, C-O and C=O, respectively [68]. The C-O and C=O are mainly

Table 5.2.6: The de-convoluted peak positions of all the samples indicating the binding energies (eV) for C 1s core-levels.

	C 1s X ray photoelectron spectroscopys (binding energy in eV)			
Samples	Peak I C=C	Peak II C-OH	Peak III C=O	Peak IV O=C-OH
Graphite	284.0 ± 0.1	285.2 ± 0.1	286.3 ± 0.1	
GO	283.7 ± 0.1	285.7 ± 0.1	287.1 ± 0.1	291.5 ± 0.1
rGO	281.5 ± 0.1	283.2 ± 0.1	284.5 ± 0.1	285.8 ± 0.1
ATA-Fe_2O_3	284.1 ± 0.1	285.6 ± 0.1	286.2 ± 0.1	287.9 ± 0.1
GO-ATA-Fe_2O_3(I)	283.2 ± 0.1	284.7 ± 0.1	285.5 ± 0.1	286.3 ± 0.1
GO-ATA-Fe_2O_3(II)	282.8 ± 0.1	284.5 ± 0.1	284.9 ± 0.1	286.1 ± 0.1

due to the interaction of carbon and oxygen atoms [69]. For O 1s, the peak positions are 530.1 eV ± 0.1, 532.0 eV ± 0.1 and 535.0 eV ± 0.1 where the peaks are assigned to O=C-OH, C=O and C-OH. The rich hydroxyl presence signifies graphitic platelets, which is consistent with features of graphite oxide [70].

Figure 5.2.17 shows C and O 1s spectra of GO with the splitting of the sp^2 C-C bond. The splitting of the peaks in C 1s of GO as shown in Figure 5.2.17 is mainly due to the impact of graphite exfoliation. The extra peak located at ≈ 285.8 eV ± 0.1 is assigned to O=C-O bond [46]. A slight decrease and increase in the peak position of graphite → GO is observed i.e 284 → 283.7, 285.2 → 285.7 and 286.32 → 287.1 (eV). The emergence of the new bond and the shift in the binding energy positions is due to the carbon sheet oxidation of GO. The case of O 1s shows a slight decrease in the position when GO compares with graphite. In correlation to the particle size increase given by the XRD analysis, the increase in the cluster size is mainly attributed to carbon atoms oxidation resulting in clustering or agglomeration. This size increase can impact the electronic and electrical properties of GO [71]. The N 1s peak is mainly from the NH_4OH reduction of GO. As indicated in Table 5.2.8, the N 1s peaks include 398.9 eV, 397.02 eV and 395.3 eV. The peaks are assigned to N-C=O, N=C and N-C respectively [72]. The N 1s bond indicates the attachment of nitrogen to carbon atoms, which invariably can impact the properties of rGO. The C 1s peak positions indicated as 281.5 eV, 283.3 eV, 284.5 eV and 285.8 eV are attributed to pre-sp^2-C, sp^2-C, sp^2-C and C-O respectively [73–75].

The core shells for C 1s, O 1s, N 1s, and Fe 2p for ATA-Fe_2O_3 are shown in Figure 5.2.19. The appearance of C 1s is mainly due to impurities during the film preparation. The most relevant peaks are O 1s, N 1s, and Fe 2p, which indicate the formation of iron oxide composite. The N 1s are mainly contributions from the 2-aminoterephthalic

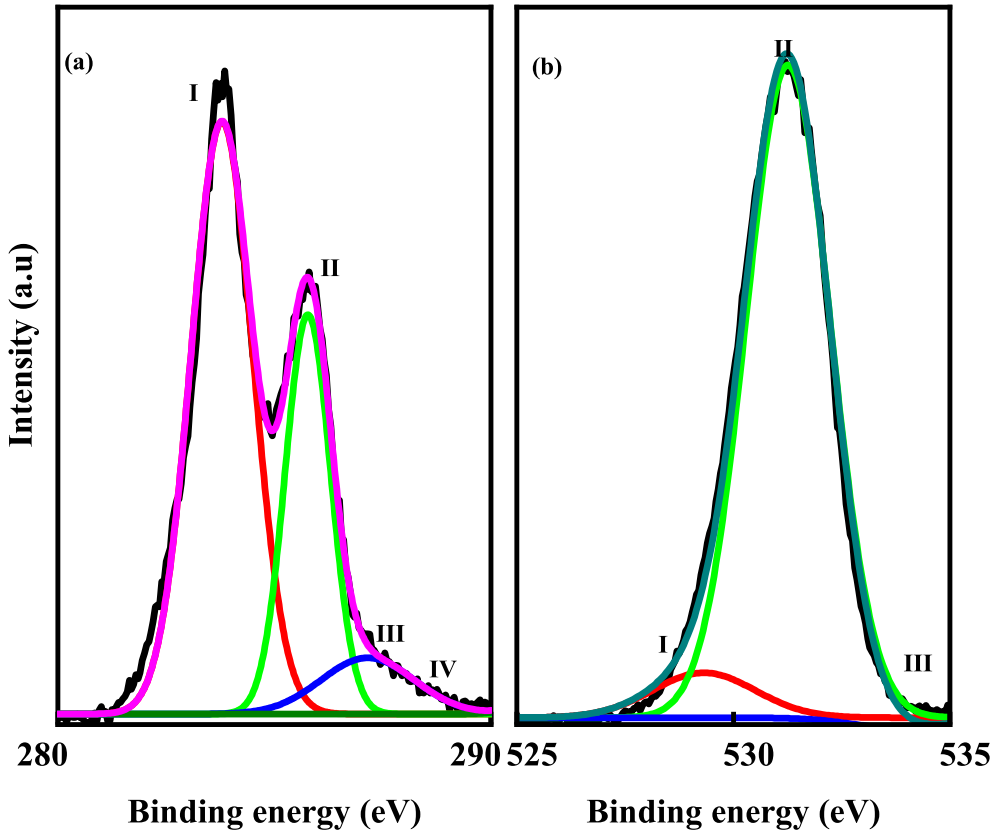

Figure 5.2.17: The C 1s and O 1s core shells of GO showing the de-convoluted peak positions where (a) C 1s and (b) O 1s. For C 1s the peaks are as follows: Peak I (C=C), Peak II (C−OH), peak III (C=O) and peak IV (O=C−OH. for O 1s, Peak I (O=C−OH), peak II (C=O) and peak III (C−OH. The different colours differentiates the peak positions.

Table 5.2.7: The de-convoluted peak positions of all the samples indicating the binding energies (eV) for O 1s core-levels.

	O 1 s X ray photoelectron spectroscopy (eV)		
Samples	Peak I O=C-OH	Peak II C=O	Peak III C-OH
Graphite	530.1 ± 0.1	532.0 ± 0.1	535.0 ± 0.1
GO	528.6 ± 0.1	531.1 ± 0.1	535.0 ± 0.1
rGO	527.6 ± 0.1	529.1 ± 0.1	530.3 ± 0.1
ATA-Fe_2O_3	529.5 ± 0.1	530.9 ± 0.1	531.7 ± 0.1
GO-ATA-Fe_2O_3(I)	529.8 ± 0.1	530.5 ± 0.1	531.3 ± 0.1
GO-ATA-Fe_2O_3(II)	528.1 ± 0.1	530.08 ± 0.1	531.1 ± 0.1

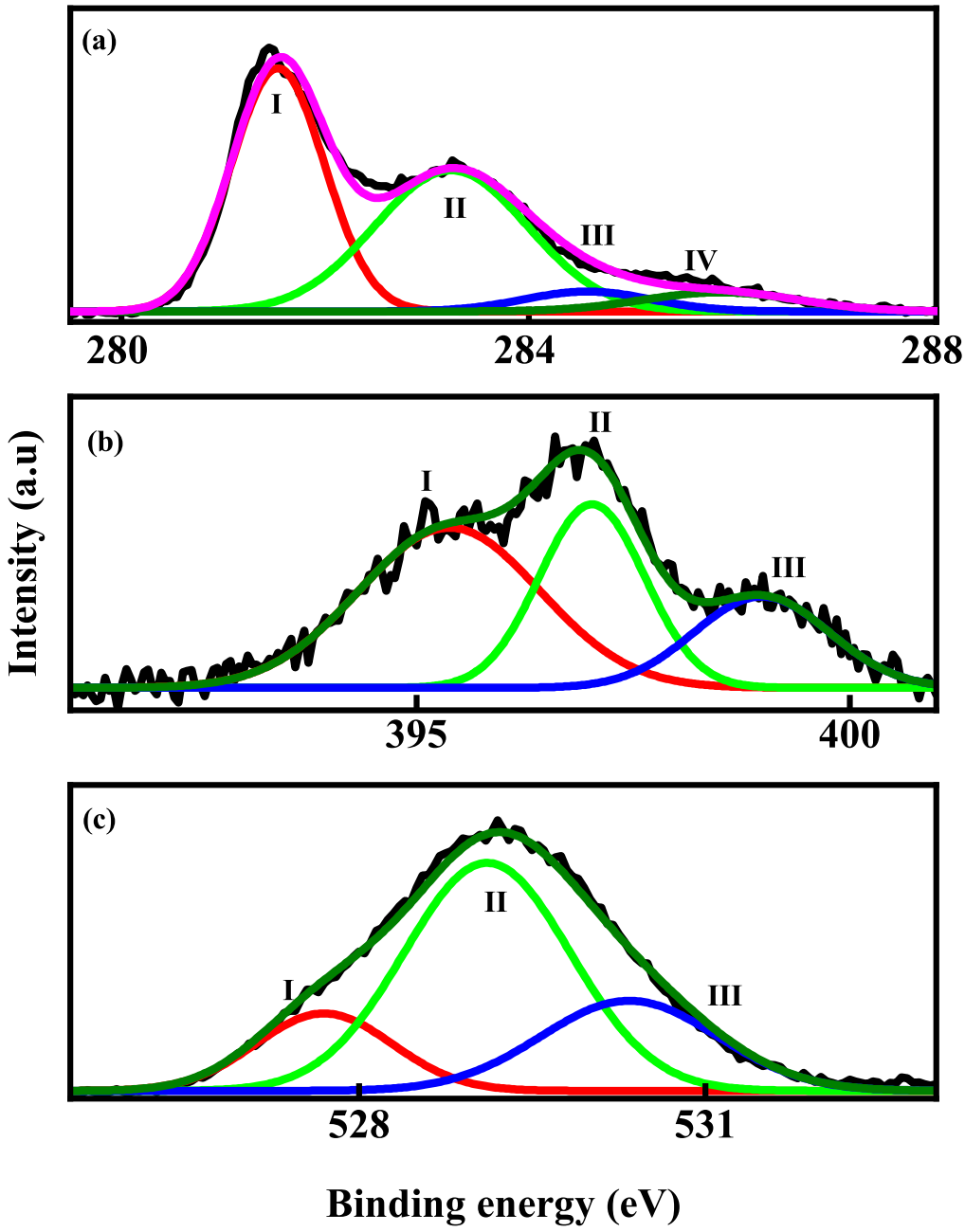

Figure 5.2.18: The core shells for rGO where (a) C 1s, (b) N 1s and (c) O 1s. For C 1s the peaks are as follows: Peak I (C=C), Peak II (C−OH), peak III (C=O) and peak IV (O=C−OH. for O 1s, Peak I (O=C−OH), peak II (C=O) and peak III (C−OH. The different colours differentiate the peak positions.

acid (ATA) capping agent. The peak indicated at 398.7 eV indicates the formation of F−Nx bond [76] whereas 398.7 eV and 398.5 eV are associated with N=C and N-C, respectively. Figure 5.2.19(d) shows the Fe 2p core shells of ATA-Fe_2O_3 composite. The two main peaks indicate at 710.7 eV and 724.09 eV are assigned to Fe^{2+} and Fe^{3+}

Table 5.2.8: Table showing the de-convoluted peak position of Fe 2p for rGO and rGO nanocomposites.

	N 1s X-ray photoelectrospectropy (eV)		
Sample	Peak I N-C=O	Peak II N=C	Peak III N-C
Graphite			
GO			
rGO	398.9 ± 0.1	397.02 ± 0.1	395.4 ± 0.1
ATA-\ce{Fe2O3}	399.9 ± 0.1	398.8 ± 0.1	398.6 ± 0.1
rGO-ATA-\ce{Fe2O3} (I)	400.7 ± 0.1	398.3 ± 0.1	396.6 ± 0.1
rGO-ATA-\ce{Fe2O3} (II)	400.8 ± 0.1	399.01 ± 0.1	397.4 ± 0.1

Table 5.2.9: Table showing the de-convoluted peak position of Fe 2p for rGO nanocomposites.

Fe 2p X-ray photoelectrospectropy (eV		
Sample	Peak I Fe $2p_{3/2}$	Peak II Fe $2p_{1/2}$
Graphite		
GO		
rGO		
ATA-\ce{Fe2O3}	710.7 ± 0.1	724.1 ± 0.1
rGO-ATA-\ce{Fe2O3} (I)	709.7 ± 0.1	723.1 ± 0.1
rGO-ATA-\ce{Fe2O3} (II)	709.9 ± 0.1	723.6 ± 0.1

peaks. Two weak peaks located at 718.2 eV and 732.2 eV are satellite peaks that can be assigned to Fe^{3+} [77]. Furthermore, the Fe^{3+} and Fe^{2+} corresponds to the Fe $2p_{3/2}$ and Fe $2p_{1/2}$ doublet states. Usually, the Fe $2p_{3/2}$ peak is much larger than Fe $2p_{1/2}$ (see Figure 5.2.19). The difference is mainly due to the (j-j) spin orbit couplings [77]. The Fe $2p_{3/2}$ state is assumed to possess four state degeneracy, whereas Fe $2p_{1/2}$ has two states [77].

The peak structure C 1s, O and N 1s show similarity with rGO and ATA-Fe_2O_3 for the case of rGO-ATA-Fe_2O_3 (see Figure 5.2.20). However, with the impact of Fe_2O_3, new bonds are observed; for instance, the peak positions at 283.2 eV ±0.1 and 284.7 eV ±0.1 are attributed to Fe−C and C−Fe bonds respectively [78]. Peak III at 285.5 eV ±0.1 and peak IV at 286.3 eV ±0.1 are assigned to the epoxy group and C=O, respectively. The difference between rGO-ATA-Fe_2O_3 (I) and rGO-ATA-Fe_2O_3 (II) is the concentration of Fe. Hence, the impact of the increase in the concentration of Fe atoms can be observed from the decrease in the peak positions of C and O 1s.

A slight increase is observed for N 1s and Fe 2p transitions. This shift in the peak

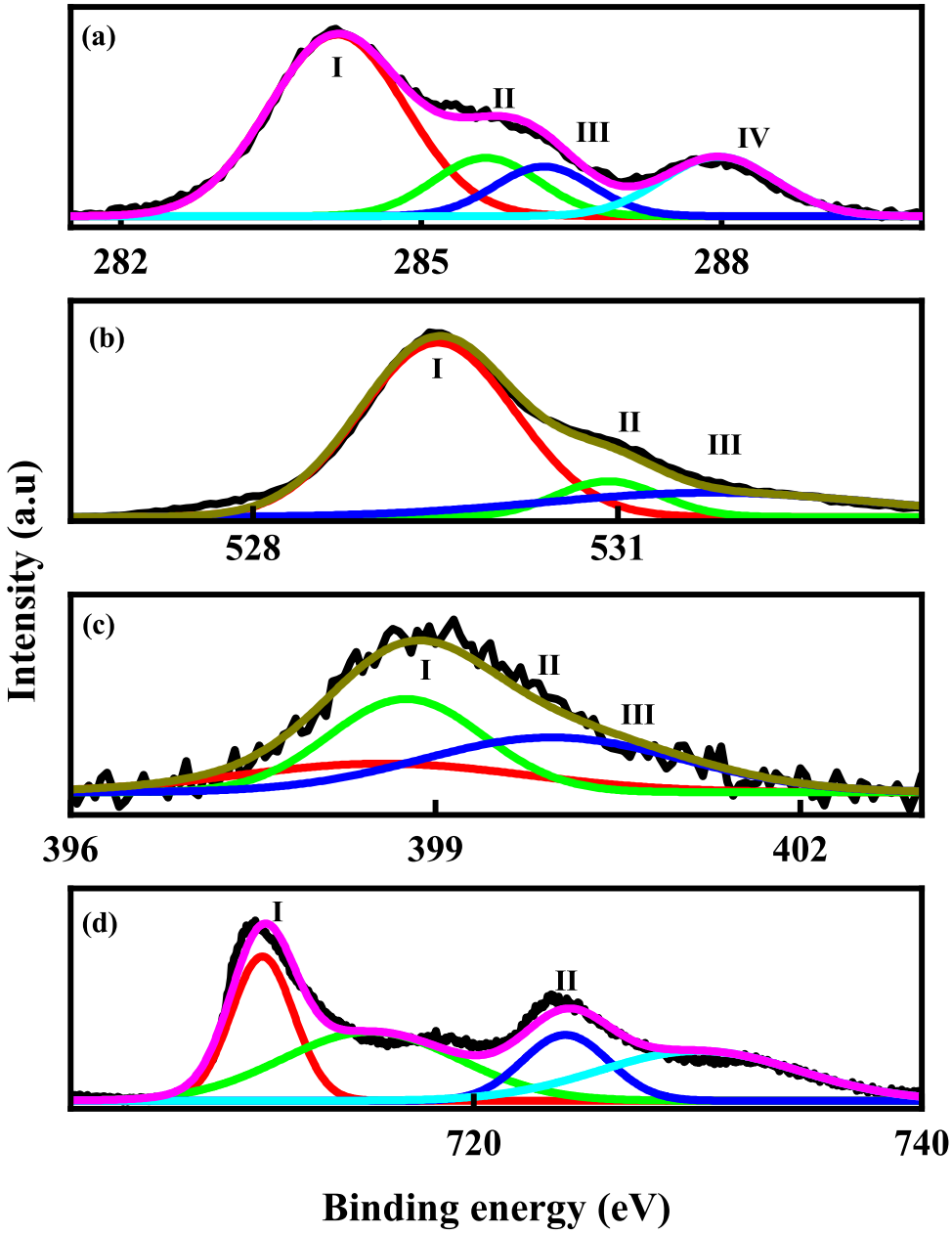

Figure 5.2.19: The core shells for ATA-Fe_2O_3 showing the prominent peaks where (a) C 1s, (b) O 1s, (c) N 1s and (d) Fe 2p. For C 1s the peaks are as follows: Peak I (C=C), Peak II (C−OH), peak III (C=O) and peak IV (O=C−OH. For O 1s, Peak I (O=C−OH), peak II (C=O) and peak III (C−OH. For N 1s, Peak I (N−C=O, Peak II (N=C and Peak III (N−C. For Fe 2p, Peak I and II are doublet state Fe $2p_{3/2}$ and Fe $2p_{1/2}$ The different colours differentiate the peak positions.

positions can be observed from the de-convoluted peaks of rGO-ATA-Fe_2O_3 (II) from Figure 5.2.21. The Fe−C and C−Fe bonds from rGO-ATA-Fe_2O_3(I) nanocomposite is retained; however, the increase in the concentration of Fe atoms can increase the population of the attached carbon-oxygen atoms [45]. The increased C-O atomic bonds are

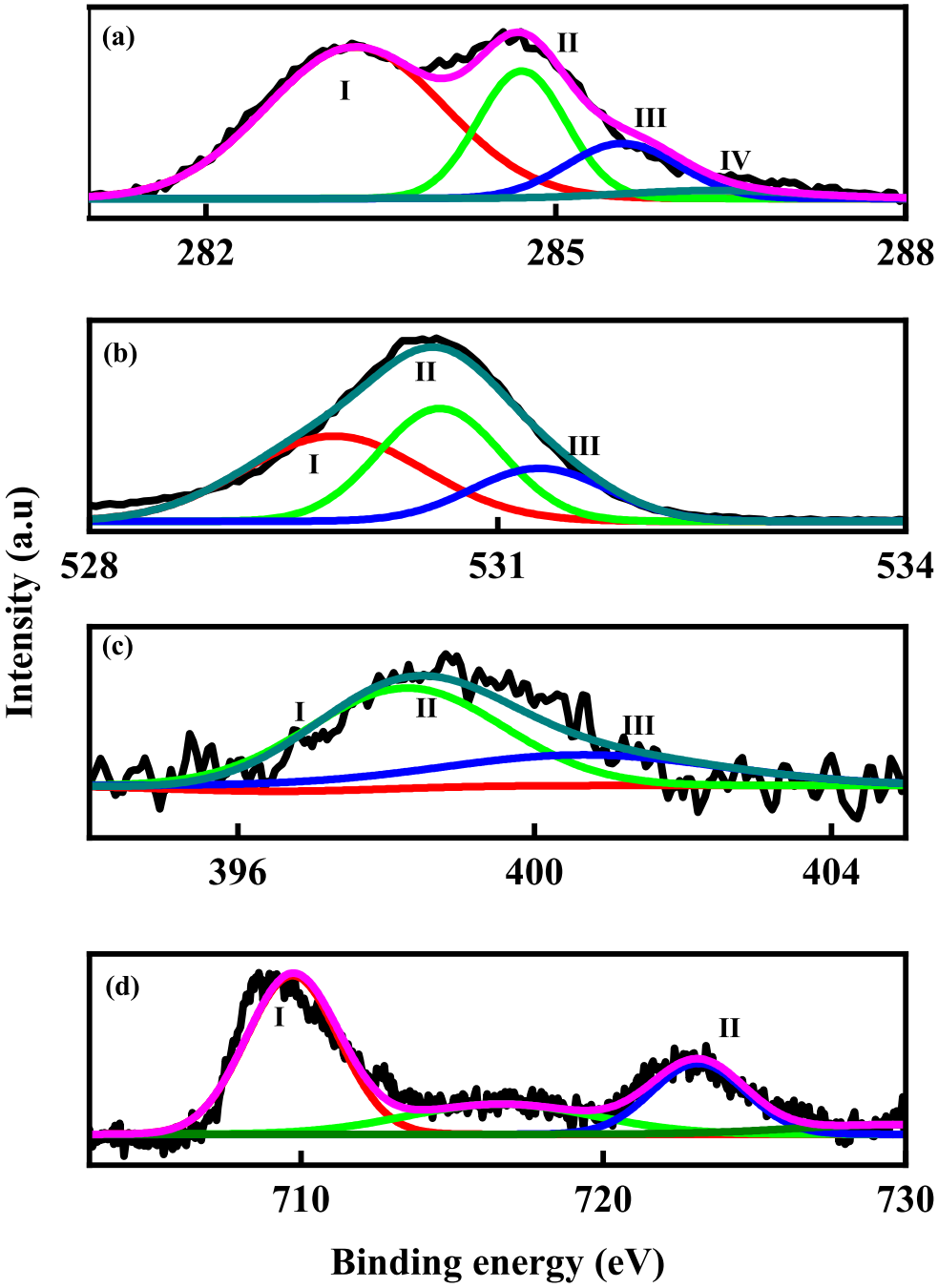

Figure 5.2.20: The core shells for rGO- ATA-Fe_2O_3 (I) showing the prominent peaks where (a) C 1s, (b) O 1s, (c) N 1s and (d) Fe 2p. For C 1s the peaks are as follows: Peak I (C=C), Peak II (C−OH), peak III (C=O) and peak IV (O=C−OH. For O 1s, Peak I (O=C−OH), peak II (C=O) and peak III (C−OH. For N 1s, Peak I (N−C=O, Peak II (N=C and Peak III (N−C. For Fe 2p, Peak I and II are doublet state Fe $2p_{3/2}$ and Fe $2p_{1/2}$. The different colours differentiate the peak positions.

consistent with the increase in the particle size as indicated by XRD and TEM images ($8 \rightarrow 10\,\text{nm}$).

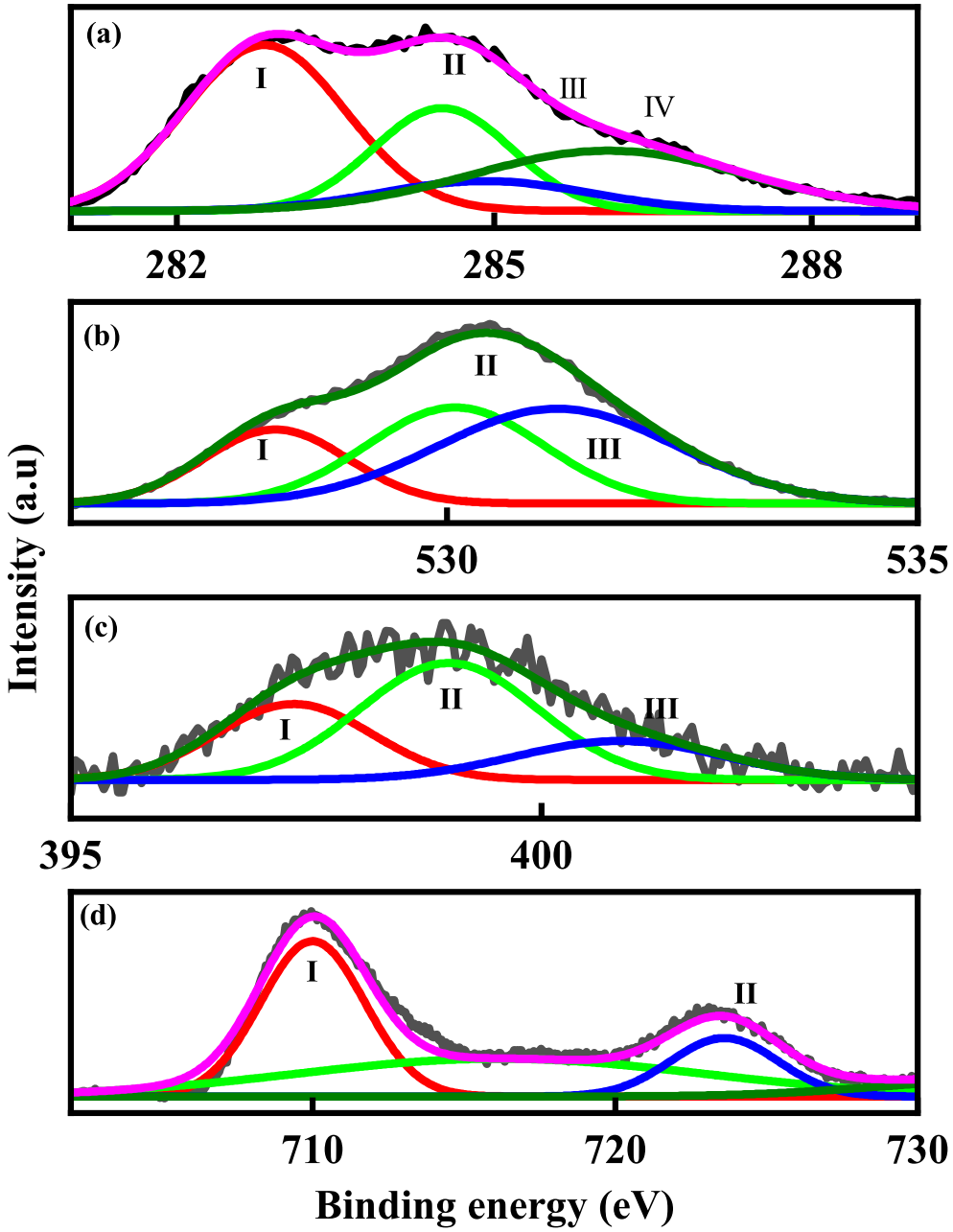

Figure 5.2.21: The core shells for rGO- ATA-Fe_2O_3 (II) showing the prominent peaks where (a) C 1s, (b) O 1s, (c) N 1s and (d) Fe 2p. For C 1s the peaks are as follows: Peak I (C=C), Peak II (C−OH), peak III (C=O) and peak IV (O=C−OH. For O 1s, Peak I (O=C−OH), peak II (C=O) and peak III (C−OH. For N 1s, Peak I (N−C=O, Peak II (N=C and Peak III (N−C. For Fe 2p, Peak I and II are doublet state Fe $2p_{3/2}$ and Fe $2p_{1/2}$. The different colours differentiate the peak positions.

The O 1s configuration is similar for GO, rGO, rGO-ATA-Fe_2O_3 (I) and rGO-ATA-Fe_2O_3 (II) nanocomposites. The main O 1s peaks for GO include 528.6 and 531.1 (eV) ±0.1. The peaks are assigned to the quinone group, oxygen doubly-aromatic carbon

bonds (C=O), respectively. The 535 ± 1 eV is assigned to oxygen singly-aliphatic and phenolic carbon bonds. The decrease and increase in the binding energy is mainly due to the effect of reduction and functionalization. Meanwhile, for the case of 527.6 eV ± 0.1 and 528.1 eV ± 0.1 for rGO and rGO-ATA-Fe_2O_3 nanocomposite, the peak positions occur due to carbon-oxygen and iron oxide bonds [79].

5.2.7 Ultraviolet photoelectron spectroscopy

The UPS technique uses the same equipment as XPS, hence, the intensity of the spectra does not necessarily reflect the sample composition. In most cases, high intensity of the spectra depends on the applied accelerating voltage of the X-rays. Hence, the intensity of the orbital state spectra and valence band maximum is ignored. Additionally, the red and blue shift in the peak position is insignificant ($\approx 0.5 - 2.0$ eV) [80, 81]. Hence, the errors in the peak positions are ignored.

Figure 5.2.22 shows the Fermi shift of the composite with GO been the reference. The C=C bonds can be observed by the shift of the Fermi level toward the edge with ≈ 1.74 eV. The edge shift can be attributed to an increase in the DOS due to increase in the disorder of GO when it undergoes reduction with NH_4OH. A previous report suggested an increase in the average DOS of graphene when there is increase disorder in its structure [82]. Although ATA-Fe_2O_3 is unintentional carbon-based composites since the intended original component lacks carbon, however, the presence of carbon contamination offers the opportunity to study the importance of high concentrations of Fe atoms in GO composites.

A shift away from the Fermi edge (Figure 5.2.22(b)) of ≈ 2.79 eV is observed, which indicates the decrease in the DOS of GO. The case of low concentration of Fe atoms is observed in Figure 5.2.22 (c) and (d). The shift (≈ 1.56 eV and ≈ 0.85 eV) away from the Fermi edge is less significant compared to the latter case.

To further quantify the composite core-level state responsible for the variation of the

DOS, the spectra were de-convoluted using a Gaussian function of Originlab software into four peaks, as shown in Figure 5.2.23. The de-convoluted peaks are given in Table 5.2.10 showing four prominent peak positions. In the case of graphite, the peak position is $\approx 10.9\,\text{eV}$, $\approx 8.8\,\text{eV}$, $\approx 6.8\,\text{eV}$ and $\approx 4.9\,\text{eV}$. The peaks are assigned to $C-2(s-p)$ mixed state, $C-2p_{\sigma}$, $2p-(\pi-\sigma)$ overlap and $C-2p_{\pi}$, respectively [80].

The effect of graphite sheet exfoliation (GO) did not shift the states significantly. Although an increase for peak II ($8.8\,\text{eV} \rightarrow 9.2\,\text{eV}$) $\pm$ 0.1, peak III ($6.8\,\text{eV} \rightarrow 6.9\,\text{eV}$)

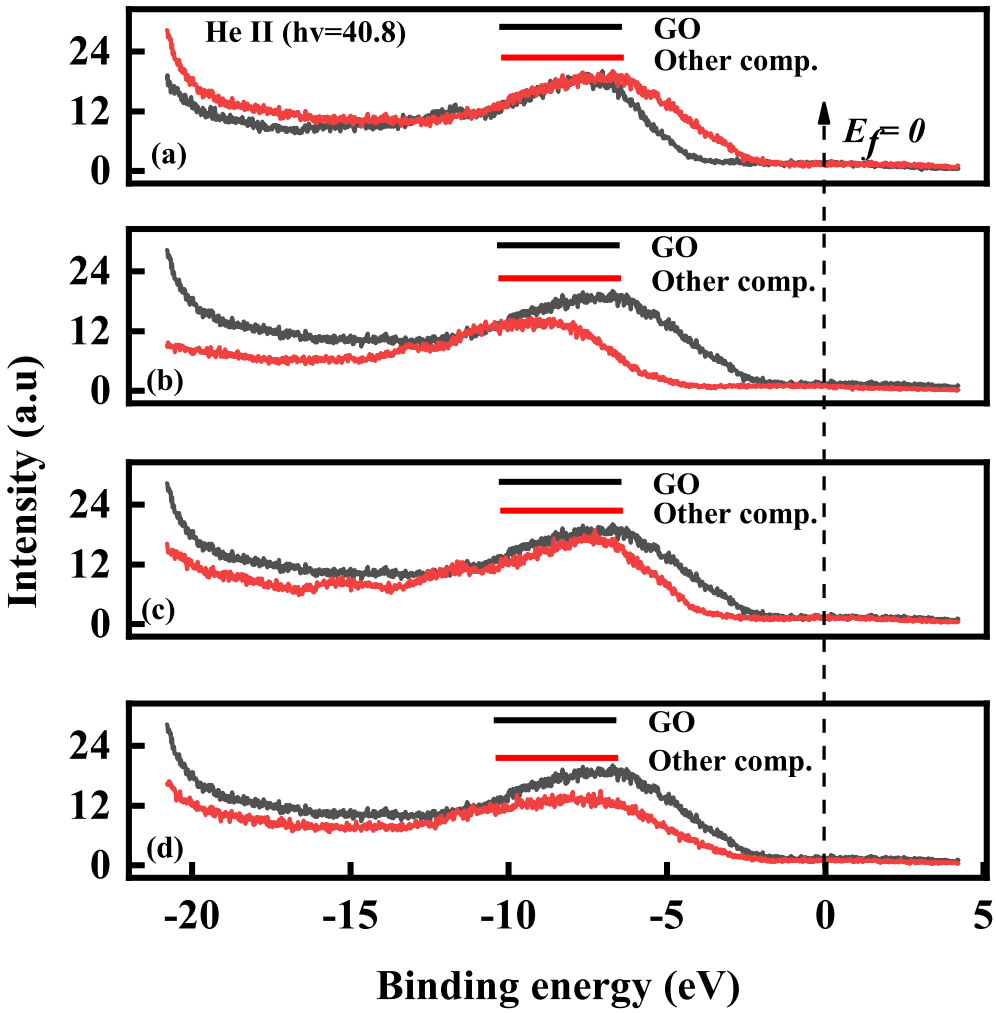

Figure 5.2.22: The observed shift of the fermi energy level in comparison with GO. (a) GO and rGO, (b) GO and ATA-Fe_2O_3, (c) GO and rGO-ATA-Fe_2O_3 (I), and (d) GO and rGO-ATA-Fe_2O_3 (II).

Table 5.2.10: The UPS spectra de-convoluted peak positions showing the hybridization state of GO and rGO-ATA-Fe_2O_3 nanocomposites.

Samples	Peak I eV	Peak II eV	Peak III eV	Peak IV eV
Graphite	10.9 ± 0.1	8.8 ± 0.1	6.8 ± 0.1	4.9 ± 0.1
GO	10.9 ± 0.1	9.2 ± 0.1	6.9 ± 0.1	5.4 ± 0.1
rGO	11.8 ± 0.1	10.6 ± 0.1	9.3 ± 0.1	8.02 ± 0.1
GO-ATA-Fe_2O_3(I)	15.1 ± 0.1	12.1 ± 0.1	9.4 ± 0.1	7.2 ± 0.1
GO-ATA-Fe_2O_3(II)	12.2 ± 0.1	10.6 ± 0.1	7.3 ± 0.1	5.8 ± 0.1

± 0.1 and peak IV (4.9 eV → 5.4 eV ± 0.1) , which indicates an increase in the DOS of GO. A further increase in the DOS of GO is observed as indicated by the shift in the peak position for rGO. The increase in DOS may be due to the removal of oxygen functionalities with slight recovery of graphitic carbon networks [83].

The impact of GO functionalization results in a new scenario where the peak position

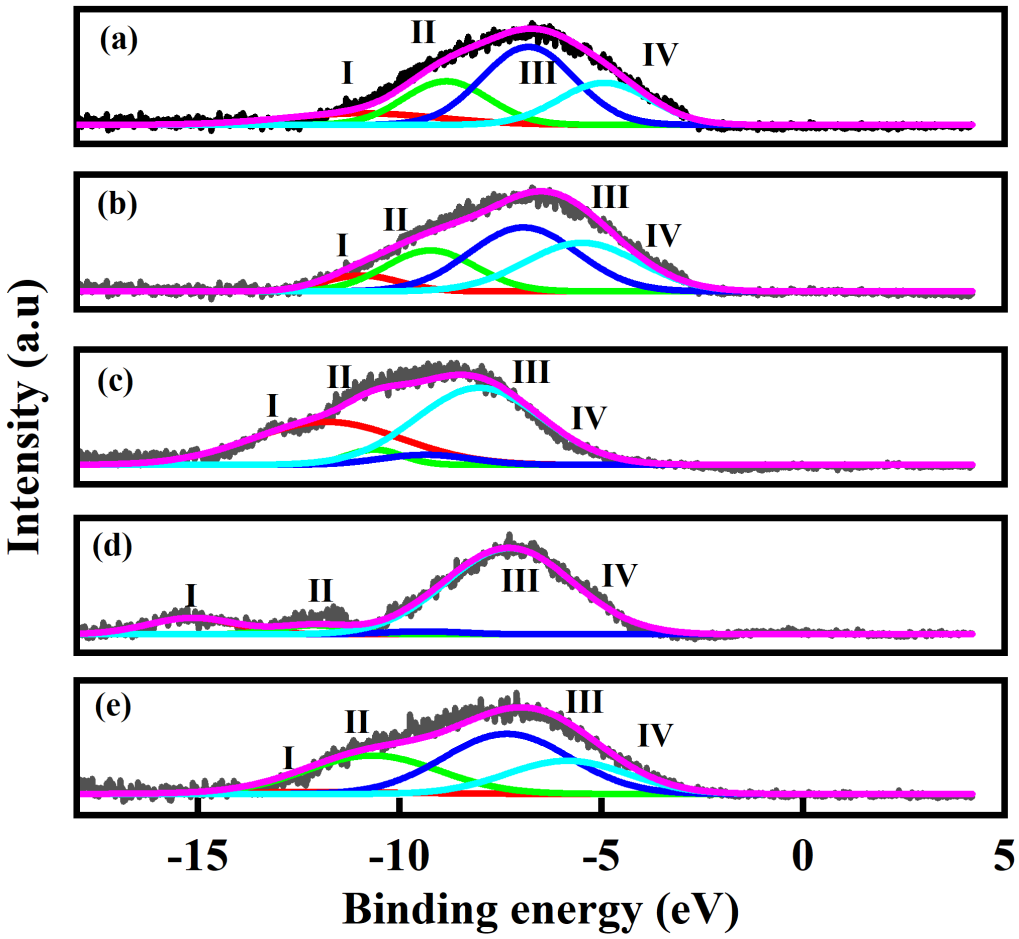

Figure 5.2.23: The deconvoluted spectra showing the different orbital state where (a) graphite powder, (b) GO, (c) rGO, (d) rGO-ATA-Fe_2O_3 (I) and (e) rGO-ATA-Fe_2O_3 (II).

shifted to higher binding energies. For instance, Peak I (10.9 eV ± 0.1 → 15.1 eV ± 0.1), peak II (9.2 eV ± 0.1 → 12.1 eV ± 0.1), peak III (6.9 eV ± 0.1 → 9.4 eV ± 0.1) and peak IV (5.4 eV ± 0.1 → 7.2 eV ± 0.1) is consistent with an increase in the π electron DOS with corresponding appearance of $\pi - \sigma$ overlaps and a blue shift of $2p - \sigma$ band [80]. The over all increase is attributed to the graphitic carbon network and hence invalidates the impact of oxygen moieties in influencing the valence band structure of GO [80]. Meanwhile, the 15.1 eV and 12.1 eV are attributed to σ and π bonds, which occur from C=O and O lone pairs [84–86].

The effect of the shift in the DOS of GO is explored by valence band maximum and work function (WF) extrapolation. Both quantities can elucidate the relative position of the Fermi level of GO. Figure 5.2.24 and 5.2.25 show the UPS He I (hv = 21.2 eV) spectra for GO and rGO-ATA-Fe_2O_3 nanocomposite. The extrapolated values for the work function (WF) and valence band maximum (VBM) are given in Table 5.2.11. As indicated in the table, the WF of graphite is ≈ 3.1 eV ± 0.1, which is in proximity to the theoretical value of ≈ 4.5 eV ± 0.1 [87, 88]. Whereas, the WF for GO is estimated to be 3.8 eV ± 0.1, which is also in close proximity of the reported values of 4.3 eV ± 0.1 [88].

Recent reports indicates the viability of GO for feasible applications with low WF [89]. The tunability of WF of GO offers an avenue to further lower the WF. For instance, the effect of functionalization can lower the WF of GO. As indicated, the WF of GO reduces steadily with high concentration of Fe_2O_3 (3.3 eV ±0.1) and 3.4 eV ±0.1 with lower Fe_2O_3 concentration. The value increases abruptly for a further increase in the

Table 5.2.11: Table showing the extrapolated values of work function, valence band maximum and Fermi level shift.

Samples	WF (eV)	VBM	Fermi shift
Graphite	3.1	3.6	
GO	3.84	1.8	
rGO	-	3.9	1.7
ATA-Fe_2O_3	3.36	2.1	2.7
rGO-ATA-Fe_2O_3 (I)	3.46	2.4	1.5
rGO-ATA-Fe_2O_3 (II)	4.1	2.5	0.8

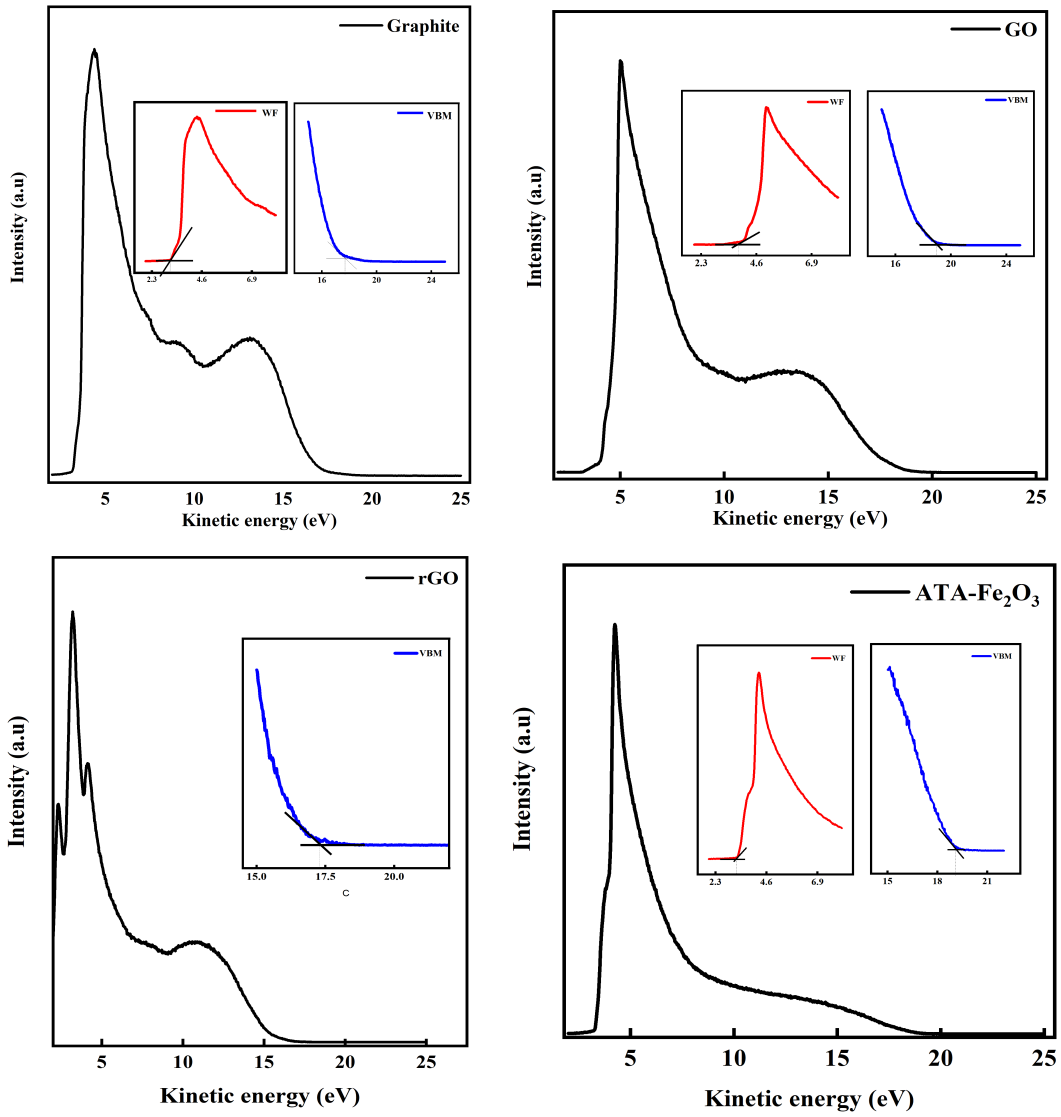

Figure 5.2.24: The UPS He I spectra of graphite powder, GO, rGO and ATA-Fe_2O_3 showing the work function and the valence band maximum.

concentration of Fe_2O_3. The increase may be due to the increase in the recovery of carbon network, as indicated in Table 5.2.5. Meanwhile, VBM is a quantity that is related to the band gap and the Fermi level of GO and have a direct influence on the electronic behaviour of GO. The variation in the value of VBM of GO gives a picture regarding electron mobility between atoms in GO electronic structure [90].

There is a dependence of the electro-optical properties of GO on the delocalized electrons [91] which are related to the VBM in terms of the electronic structure. The increase or decrease in the value of the VBM could be linked with either narrowing or

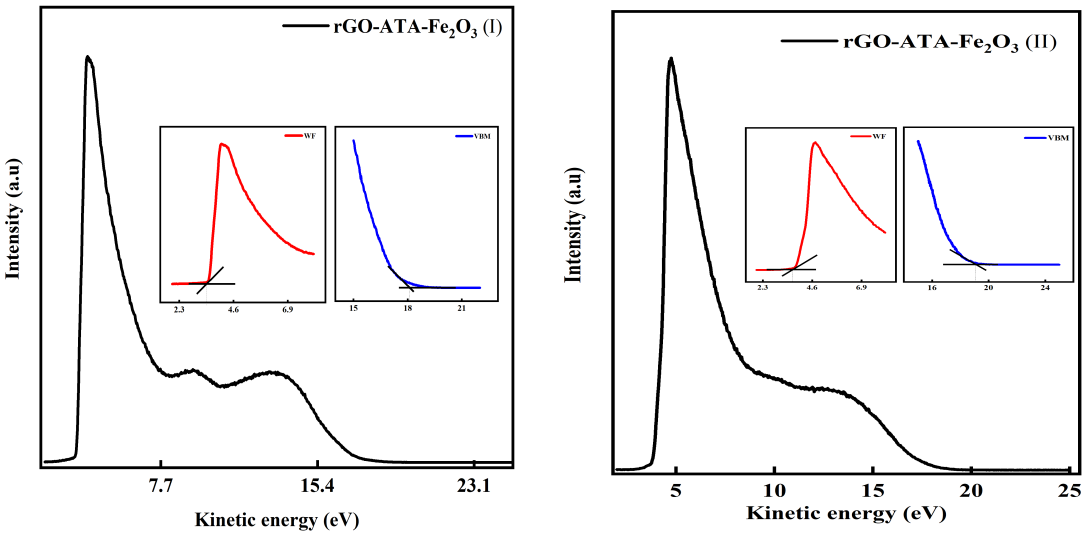

Figure 5.2.25: The UPS He I spectra of rGO-ATA-Fe_2O_3 I and II showing the work function and the valence band maximum.

widening of the band gap [92]. As can be seen from the extrapolated VBM values (Table 5.2.11), the value increases from 1.8 eV → 3.9 eV. The low VBM value supposedly should reduce the band gap, which presumably increases electron mobility. In contrast, mobility was hampered for GO as indicated in the electrical conductivity measurement (see Section 5.2.9). The poor conductivity of GO may be due to the oxygen moieties that are attached to the carbon atoms [45]. The case of rGO gives a different result with the increased VBM value. Electrons can easily transit between atoms, possibly due to the acceptors and donors from nitrogen atoms present in the carbon network of GO [67].

The effect of GO functionalization with Fe_2O_3 can be observed from the drop in the VBM of GO giving value range of 2.1 - 2.5 eV. The resultant impact on the band gap can be observed in the increase electrical conductivity of GO. In general terms, the functionalization of GO-Fe_2O_3 of different concentrations offers an avenue for tuning the band gap of GO, which can be useful for various applications.

5.2.8 X-ray absorption near edge structure spectroscopy

It is important to note the impact of accelerating voltage on the intensity of the spectra of all the edges. In some cases, the high intensity depends on the applied accelerating voltage during measurements. The parameter of interest is the prominent edges and the shift in the peak positions. This is the main reason behind the omission of the intensity in the y axis of the C and K edges figures in this Section.

Figure 5.2.26 shows the XANES spectra for C K edge of GO and rGO-ATA-Fe_2O_3 nanocomposites. The C K edge displays the main peaks consistent with carbon-related materials. The peaks are located at 285 eV and 290.7 eV and are assigned to the unoccupied π^* and σ^* states, respectively. The unoccupied π^* and σ^* states are mainly due to C=C transitions [85, 86]. With the action of reduction and functionalization, the peak tends to shift slightly with approximately $0.1 - 0.3$ eV. Whereas, the σ^* peak is attributed to the sp^3 tetrahedral C−C bond [85].

A pre-edge located at ≈ 283.3 eV was also observed in the spectra. The pre-edge is due to imperfections in the carbon network configuration or bound states lying below the bonding and antibonding states of the carbon atoms [93, 94]. Other prominent peaks marked as $I_1(286.9\,\text{eV})$, $I_2(288.3\,\text{eV})$ are assigned to C−H and C−O bonds respectively [85]. The C−H and C−O bond are due to the bonding of carbon atoms to −OH and −O radicals as expected from GO. Higher energy peaks appearing at ≈ 293.4 eV and ≈ 293.4 eV are carbon atoms attached to oxygen atoms with a possibility of C−O−Fe formation [95].

Figure 5.2.27 shows the O K edge of GO and rGO-ATA-Fe_2O_3 nanocomposites with unoccupied π^* and σ^* states as expected in carbon-related materials [96]. The O K edge spectra confirm the presence of O 2p states , which enable the bonding of carbon atoms to Fe and N atoms, as indicated in the C and N 1s spectra of rGO-ATA-Fe_2O_3 nanocomposites.To further clarify the effect of oxidation of sp^2 of GO, a Gaussian line was used to extrapolate the $\pi^* sp^2$ content of each composite. Figure 5.2.28 shows

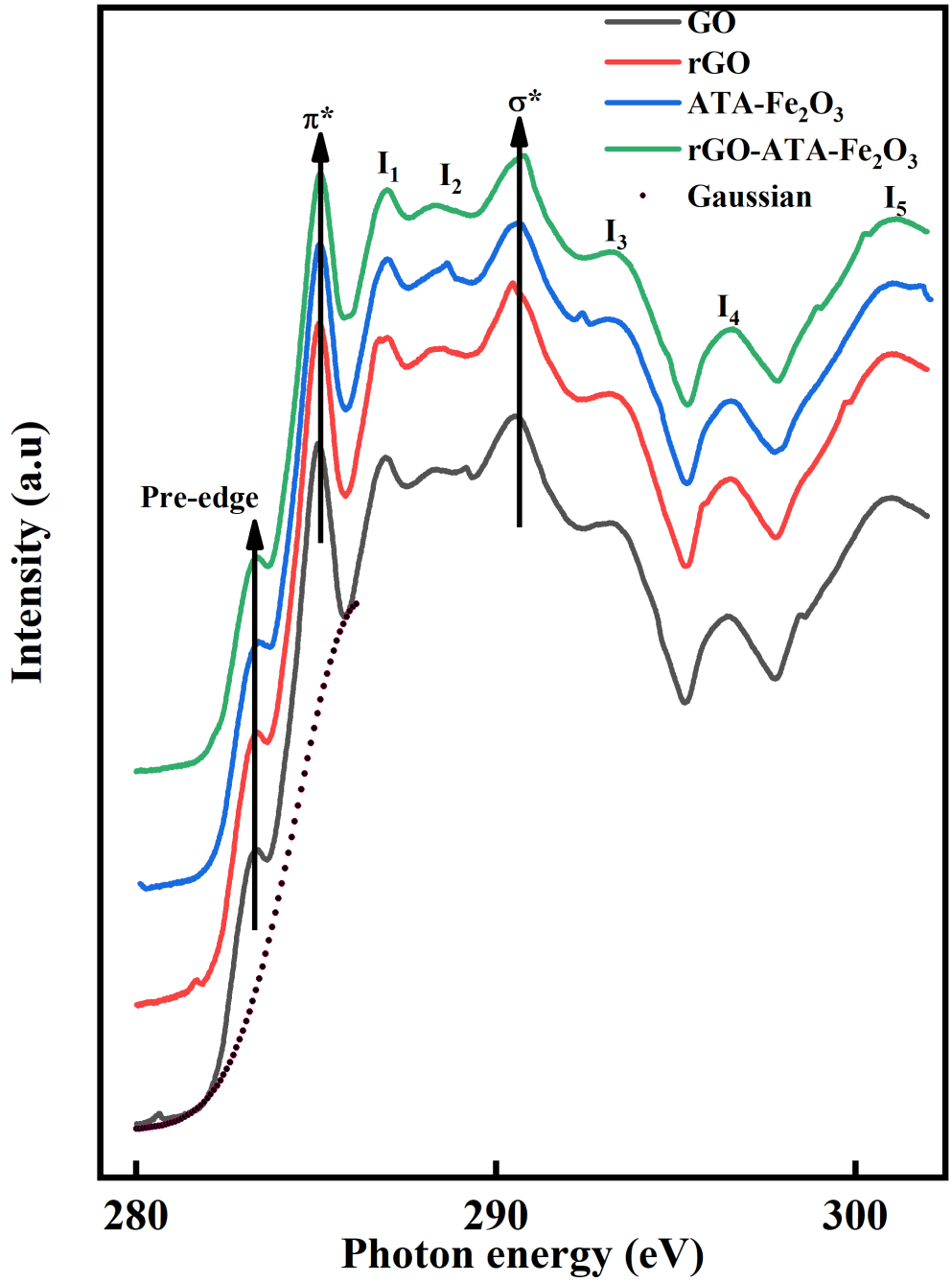

Figure 5.2.26: The C K edge XANES spectra for GO and rGO-ATA-Fe_2O_3 nanocomposites showing the unoccupied π^* and σ^* states.

the extrapolated $\pi^* sp^2$ content after Gaussian subtraction. Table 5.2.12 and 5.2.13 indicate the extrapolated values of the π^*/σ^*, which gives a reflection of the rate of oxidation. As indicated in the case of C K edge, an abrupt drop in sp^2 content with corresponding π^*/σ^* values is observed. Consequently, a decrease is also observed for

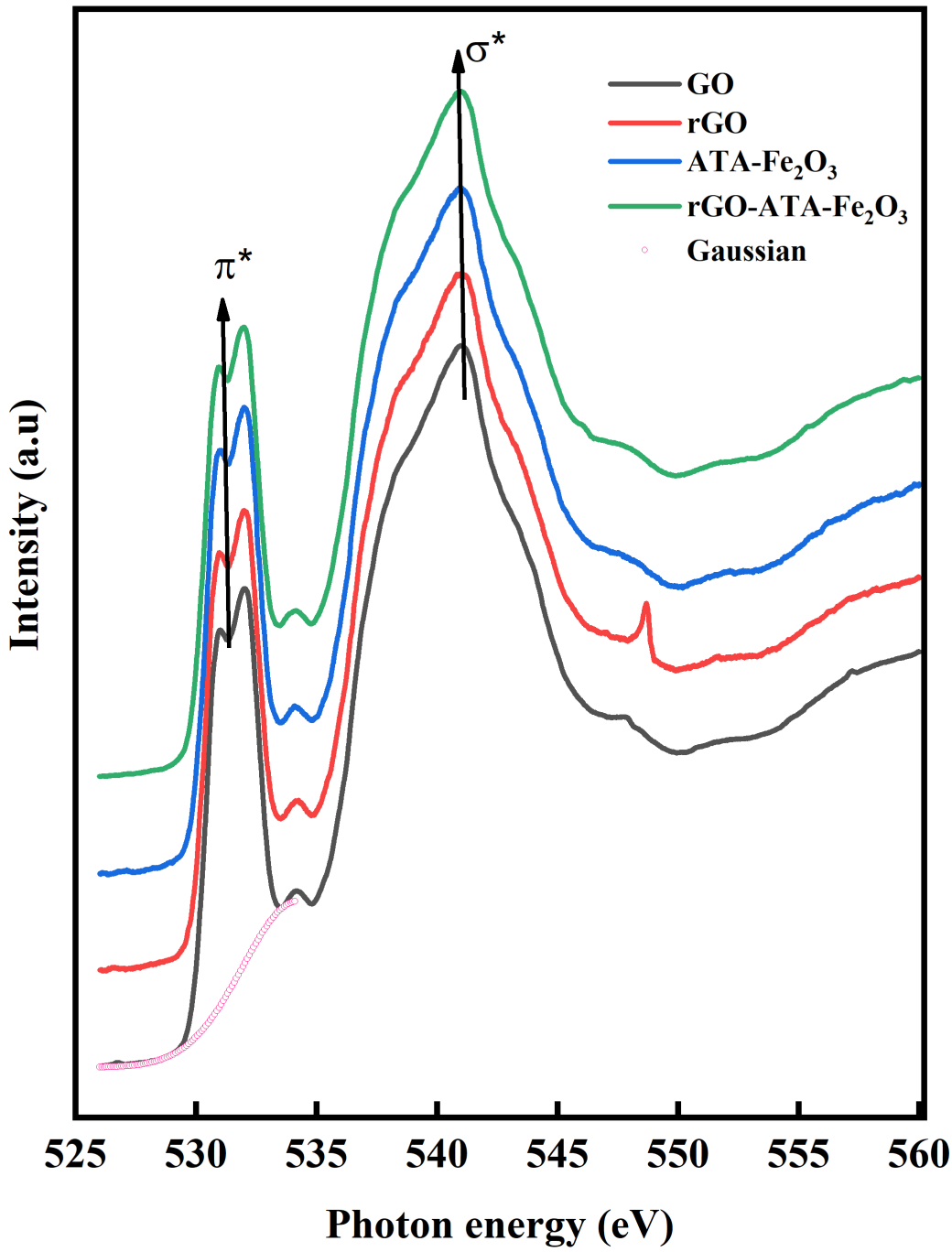

Figure 5.2.27: The O K edge XANES spectra for GO and rGO-ATA-Fe_2O_3 nanocomposites showing the unoccupied π^* and σ^* states.

the O K edge, which indicates the formation of new bonds with nitrogen as depicted by appearance of N 1s from XPS analysis. An increase is observed for the case of ATA-Fe_2O_3 , which implies the composite leaning toward more graphitic nature with a possibility of formation of bonds such as C−Fe and Fe−C. With increase in the carbon

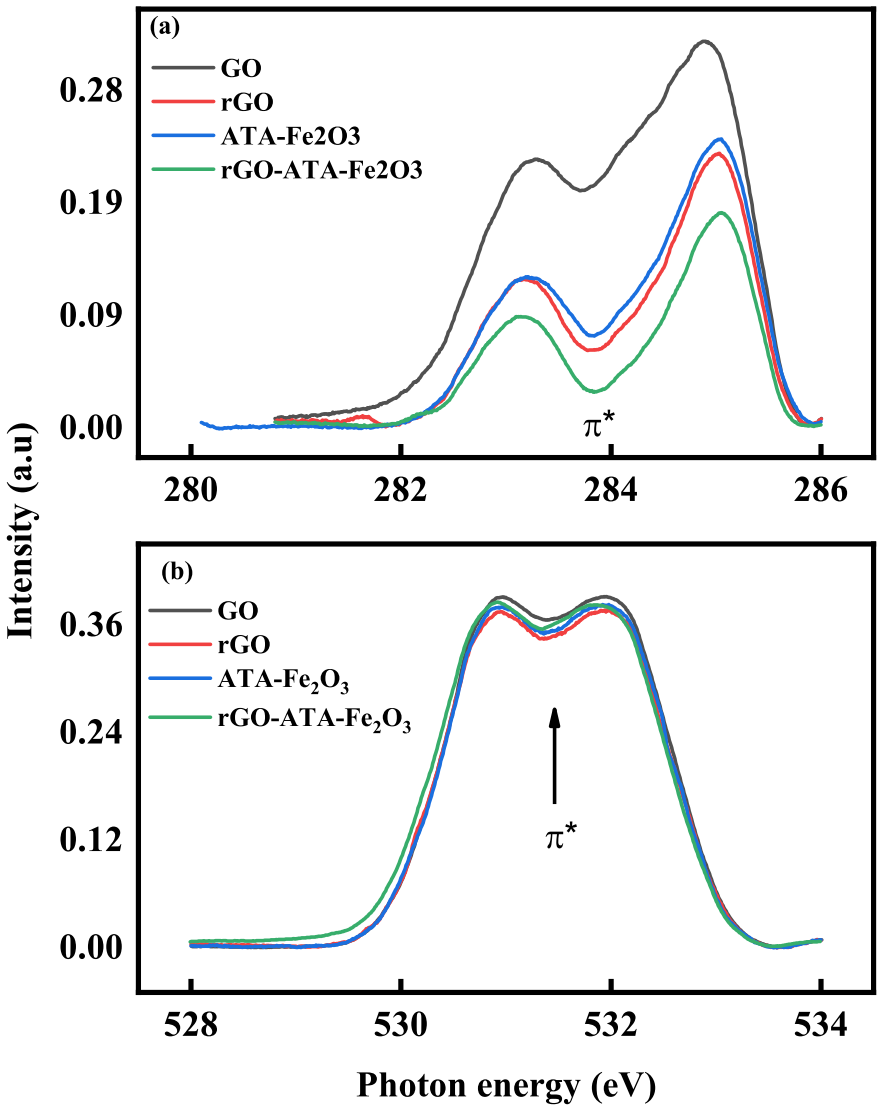

Figure 5.2.28: The extrapolated sp^2 content of C K edge and O K edge of GO and rGO-ATA-Fe_2O_3 nanocomposite.

Table 5.2.12: The extrapolated values of sp^2 content, π^*/σ^* and π^*/σ^* for C K edge for all samples.

		From intensity		
Samples	sp^2-Content (a.u)	π^* (a.u)	σ^* (a.u)	π^*/σ^*
GO	0.0715	0.0322	0.0576	0.5609
rGO	0.0383	0.0229	0.0585	0.3914
ATA-Fe_2O_3	0.0418	0.0241	0.0538	0.4479
rGO-ATA-Fe_2O_3	0.0275	0.0179	0.052	0.3442

content as indicated in the Table 5.2.5, the populations of C−Fe, C−Fe, N−C increase in the composite. The enhanced electrical and magnetic properties, as discussed in

the latter Section 5.2.10 can be attributed to the newly formed bonds. Meanwhile, the XANES spectra also indicate L edges of Fe_2O_3, Fe_3O_4 and FeO (see Figure 5.2.29). The L edge is due to the similarity in the electronic bond structure between the three iron oxide materials [67]. The two main observed peaks represent the Fe $L_3(2p_{3/2})$ and Fe $L_2(2p_{1/2})$ states, respectively. The states are consistent with the XPS Fe 2p peak, as shown in Figure 5.2.21(d). The Fe−O spectra confirms the formation of iron oxides in the rGO-ATA-Fe_2O_3 nanocomposite. Regarding the physical properties of the presence of the three L edges, there is insignificant disparity, since the valence orbitals (Fe-$3d^6 4s^2$ and O- $2s^2 2p^4$) , which contributes to the magnetization and electron mobility are the same for all of them.

5.2.9 Current-Voltage characterization

Figure 5.2.30 shows the I-V curve of graphite powder exhibiting semiconductor feature, which is consistent with the behaviour of narrow band gap graphite [97]. Since graphene is considered a zero band gap material, electrons can be easily generated at the conduction band zone. For this reason, a voltage sweep as in the current study can create a transition of electrons from the valence to the conduction band. For the obtained I-V curve for GO and rGO-ATA-Fe_2O_3 nanocomposites, a non-linear curve is observed for all samples.

The effect of oxidation, reduction and functionalization of carbon sheets causes a decrease and increase in the I-V features i.e., tending toward ohmic nature, as can be

Table 5.2.13: The extrapolated values of sp^2 content, π^*/σ^* and π^*/σ^* for O K edge for all samples.

		From O K edge intensity		
Samples	sp^2-Content (a.u)	π^* (a.u)	σ^* (a.u)	π^*/σ^*
GO	0.091	0.0391	0.0751	0.5206
rGO	0.0874	0.0374	0.0728	0.5164
ATA-Fe_2O_3	0.0884	0.0382	0.0707	0.5403
rGO-ATA-Fe_2O_3	0.0906	0.0385	0.0718	0.5362

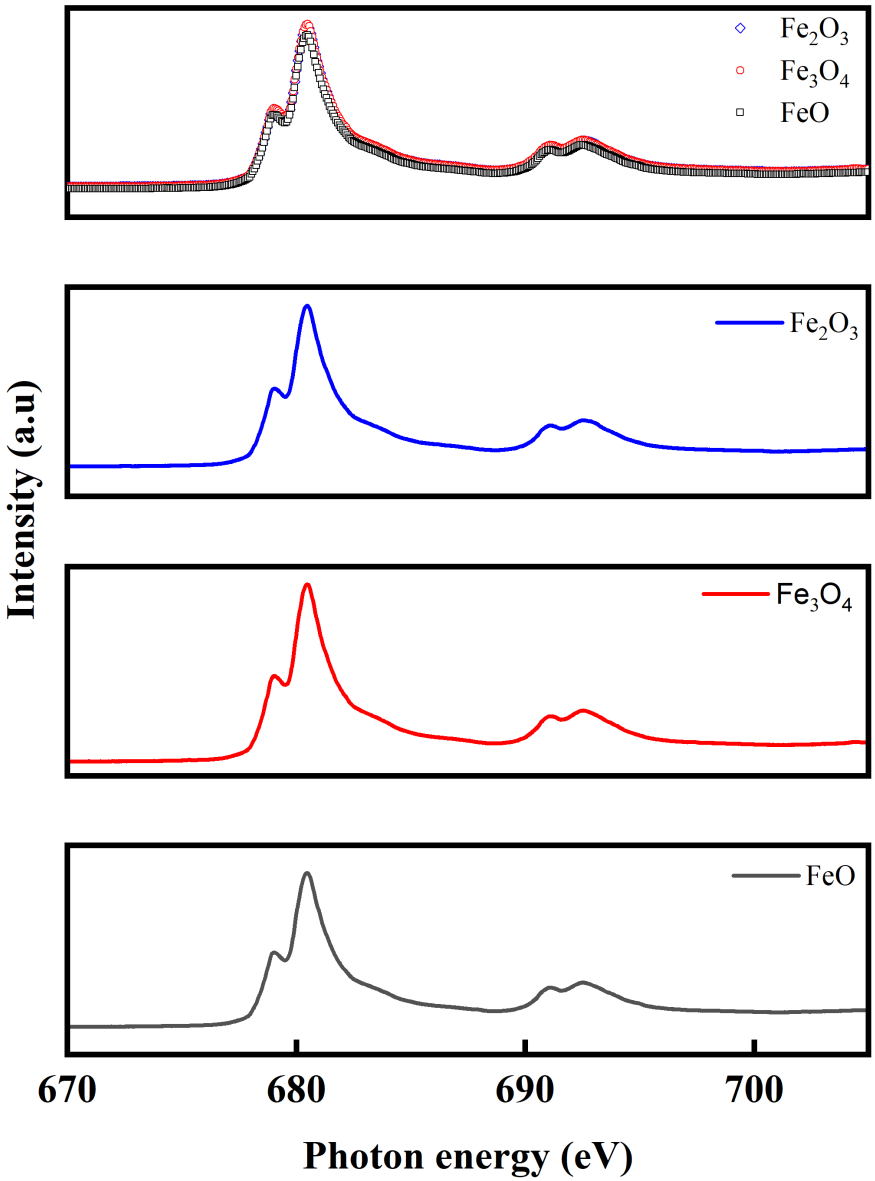

Figure 5.2.29: The XANES L edge spectra showing the presence of Fe_2O_3, Fe_3O_4 and FeO composites.

seen in the case of graphite [98]. The WF and VBM (given as 3.1 eV and 3.6 eV, respectively) are relatively low, which supports the semiconductor behavior of graphite. To ascertain possible hysteresis behavior, which is associated charge storage properties, and the I-V sweep was repeated for 3 cycles. A very weak hysteresis was observed which may not be useful for ferroelectric and memresistive device application [99].

The case of GO (see Figure 5.2.31) shows a slight drop in the conductivity as reflected in the I-V characteristics. The decrease in conductivity may be due to the oxidation

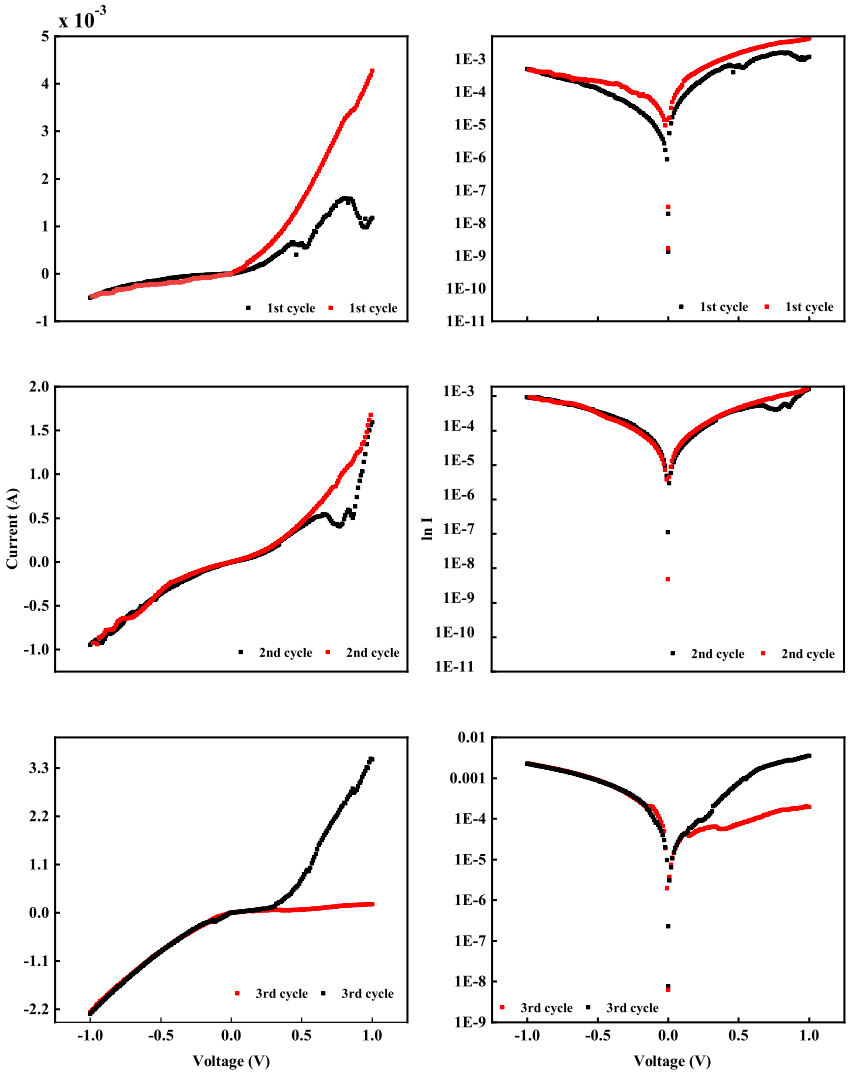

Figure 5.2.30: The I-V curve and semi-logarithm plot for graphite powder showing semiconductor features. The red colour indicates forward bias, whereas the black colour indicates reverse bias.

of carbon atoms as previously reported [100]. As indicated by the repetition of the I-V measurement cycles, the hysteresis becomes more prominent.

The impact of GO reduction on the electrical conductivity is shown from the I-V curve of rGO (see figure 5.2.32). There is no significant change in the electrical conductivity of rGO in comparison with GO, which implies the electron transport in GO is less dependent on the presence of oxygen moieties. Figure 5.2.33 shows the I-V curve of ATA-Fe_2O_3 composite where high concentration of Fe atoms is present. The electrical conductivity is quite low in comparison with GO which could be due to the long chain of the 2-aminoterephthalic acid and high concentration of oxygen presence as

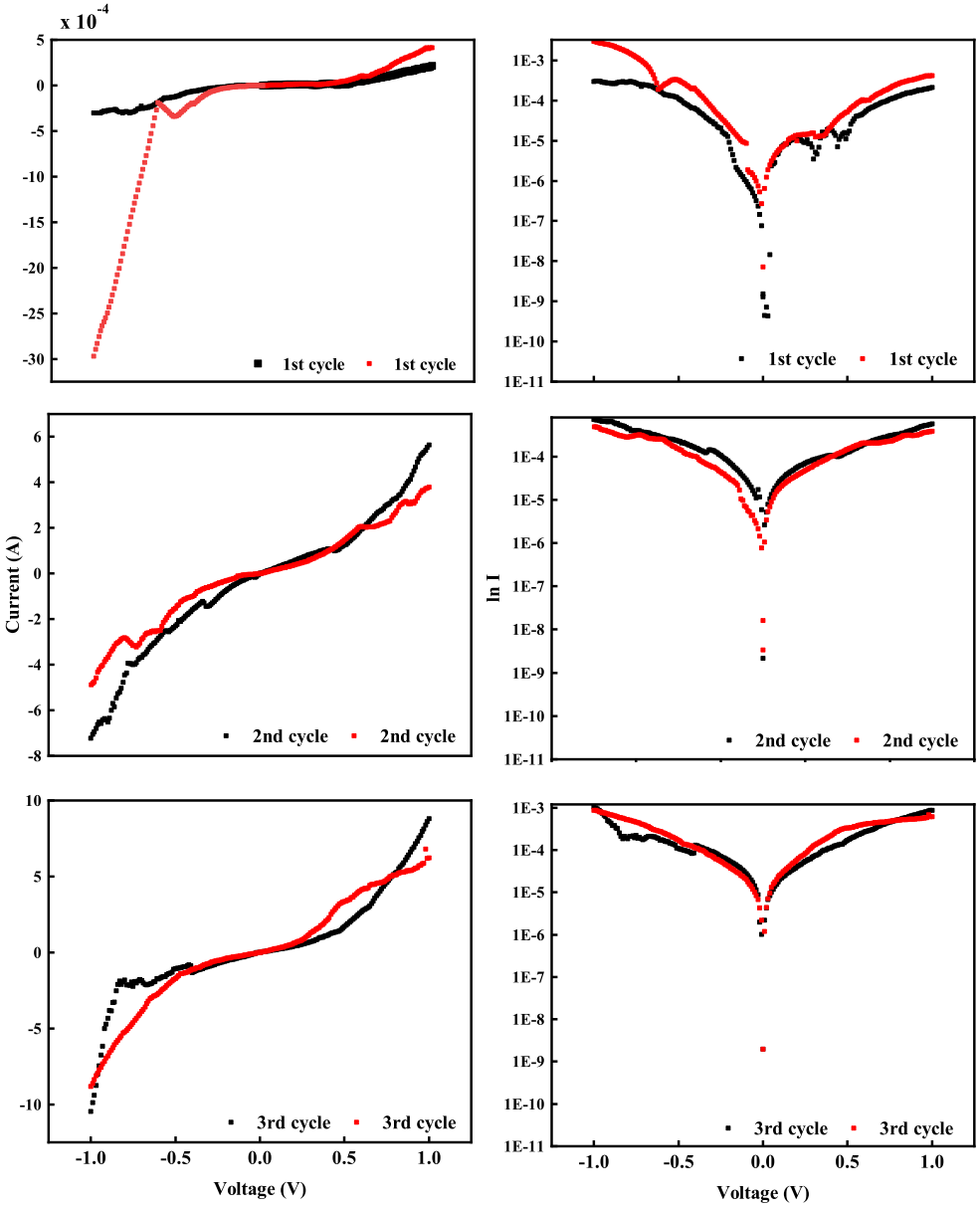

Figure 5.2.31: The I-V curve (left) and semi-logarithm (right) plot for GO showing semiconductor features. The red colour indicates forward bias, whereas the black colour indicates reverse bias.

indicated in the Table 5.2.5. A previous report has shown the possibility of site scattering inducement, which can create high density electron-hole puddles in non-covalent functionalization [101]. These puddles can create easy electron-hole traps that can inevitably affect the electrical conductivity [101]. The case of ATA-Fe_2O_3 also involves non-covalent attachments of ATA and Fe, which can be the reason for the reduced electrical conductivity.

The impact of GO functionalization with Fe_2O_3 is evident where significant enhance-

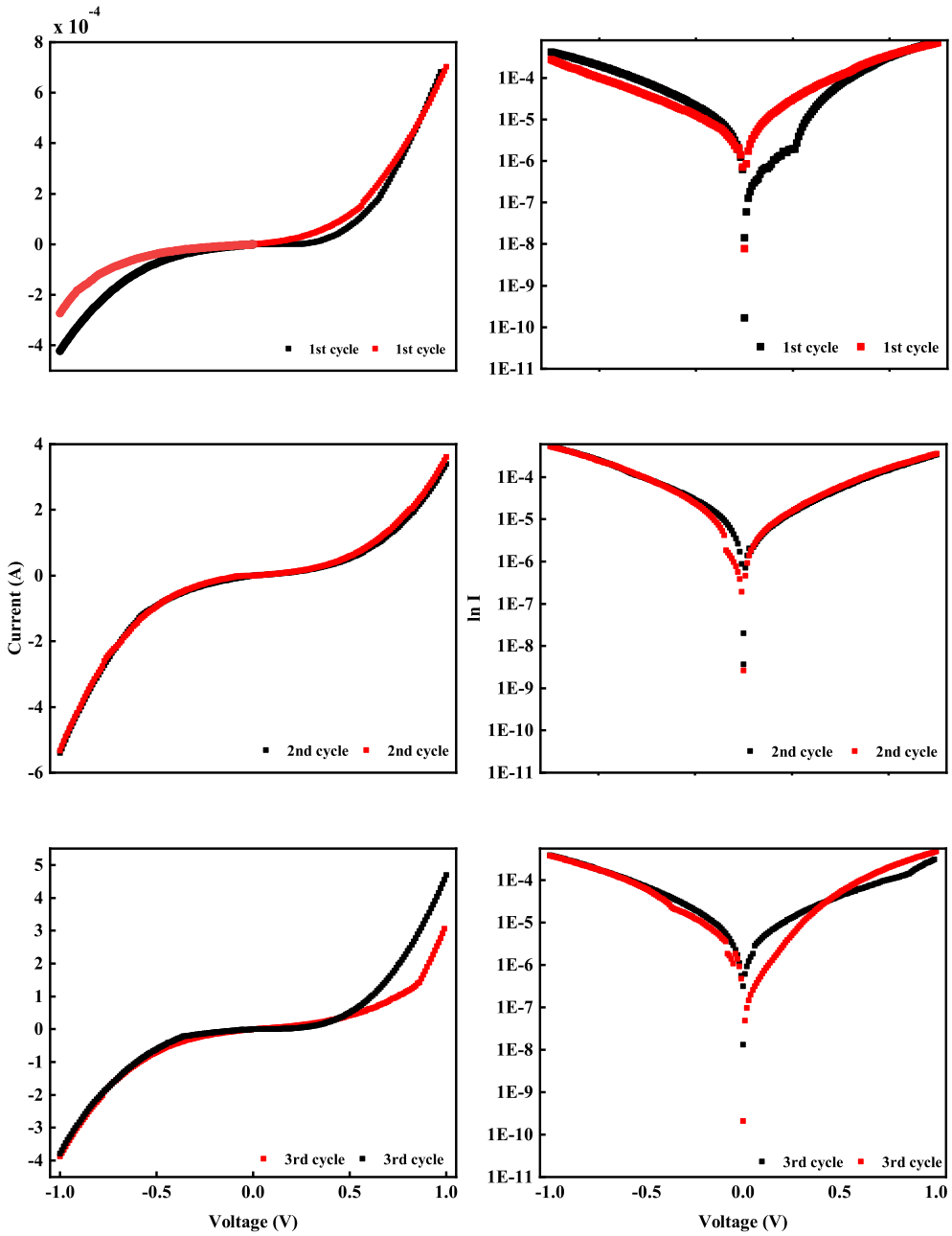

Figure 5.2.32: The I-V curve (left) and semi-logarithm (right) plot for rGO showing the features of a semiconductor. The red colour signifies forward voltage sweep (forward bias) and black colour represents backward voltage sweep (reverse bias).

ment of the electrical conductivity is observed in the I-V features (see Figure 5.2.34).

Furthermore, the increase in Fe atomic concentration only improved the electrical conductivity of GO as shown in the I-V characteristics of Figure 5.2.35. A previous report has shown improved electrical conductivity of Fe_2O_3 when the temperature is above 1071 K [20]. This implies that the improvement of the conductivity of Fe_2O_3 is

much dependent on temperature rather than concentration. Meanwhile, the enhanced electrical conductivity can be attributed to contributions from Fe and N atoms, which are consistent with C−Fe, Fe−C and N−C bonds from XPS measurements. Recent reports showed an enhanced electrical conductivity of GO-nitrogen composites [102]. Similarly, the attachment of nitrogen atoms to the surface of GO can influence the electrical conductivity of GO, even though the intention of the study does not rely on

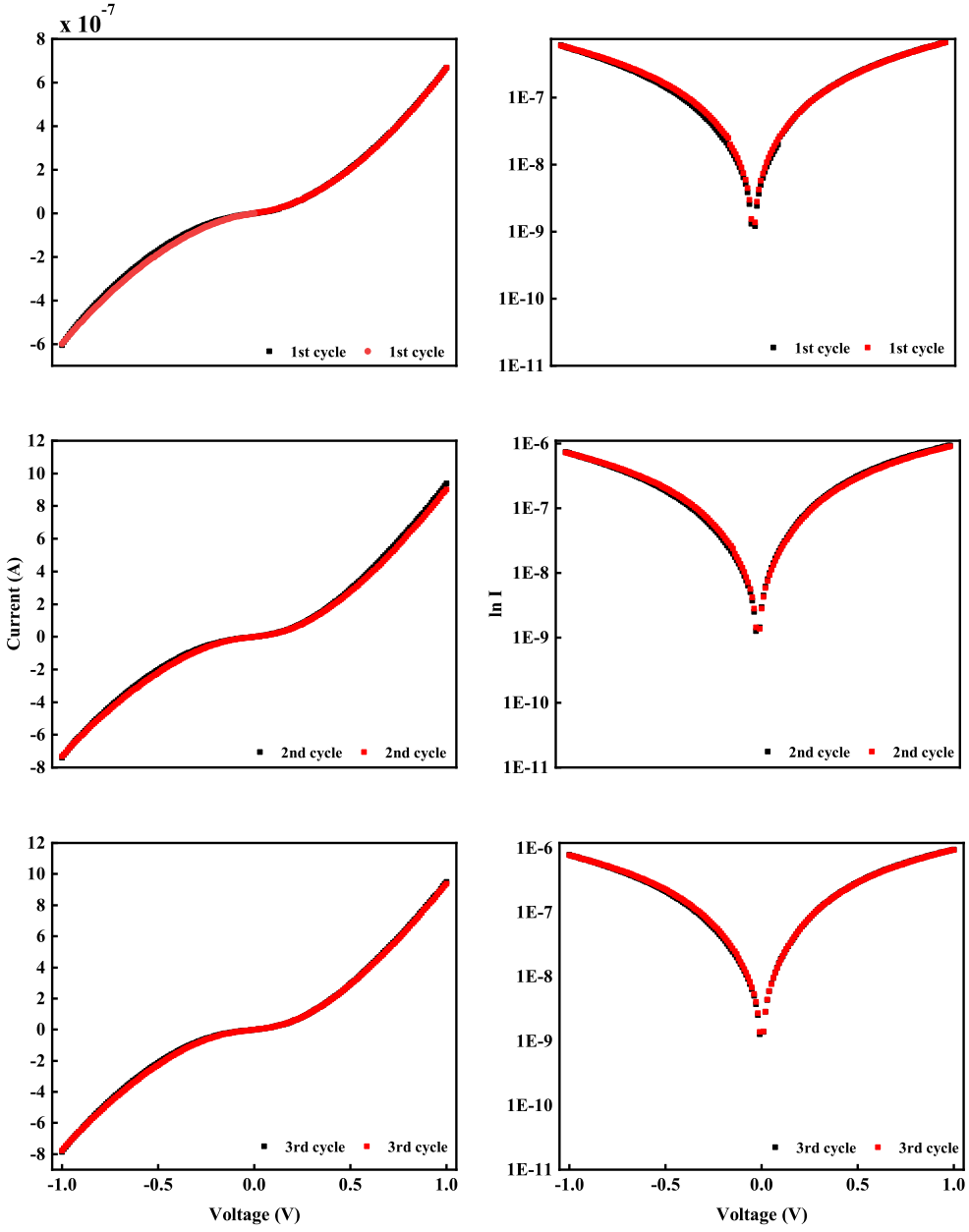

Figure 5.2.33: The I-V curve(left) and semi-logarithm plot (right) of ATA-Fe_2O_3 showing semiconductor features. The red colour signifies forward voltage sweep (forward bias) and black colour represents backward voltage sweep (reverse bias).

nitrogen.

A weak hysteresis feature is observed for rGO-ATA-Fe_2O_3 nanocomposite. However, the features become less prominent when the cycles are repeated severally. The disappearance of the loop may be due to the effect of coulomb blockade [103]. Presumably, the effects seem to occur for graphene nanomaterials [103] and metal oxides [104]. The issue of Coulomb blockade, which can improve the ferroelectric properties can easily

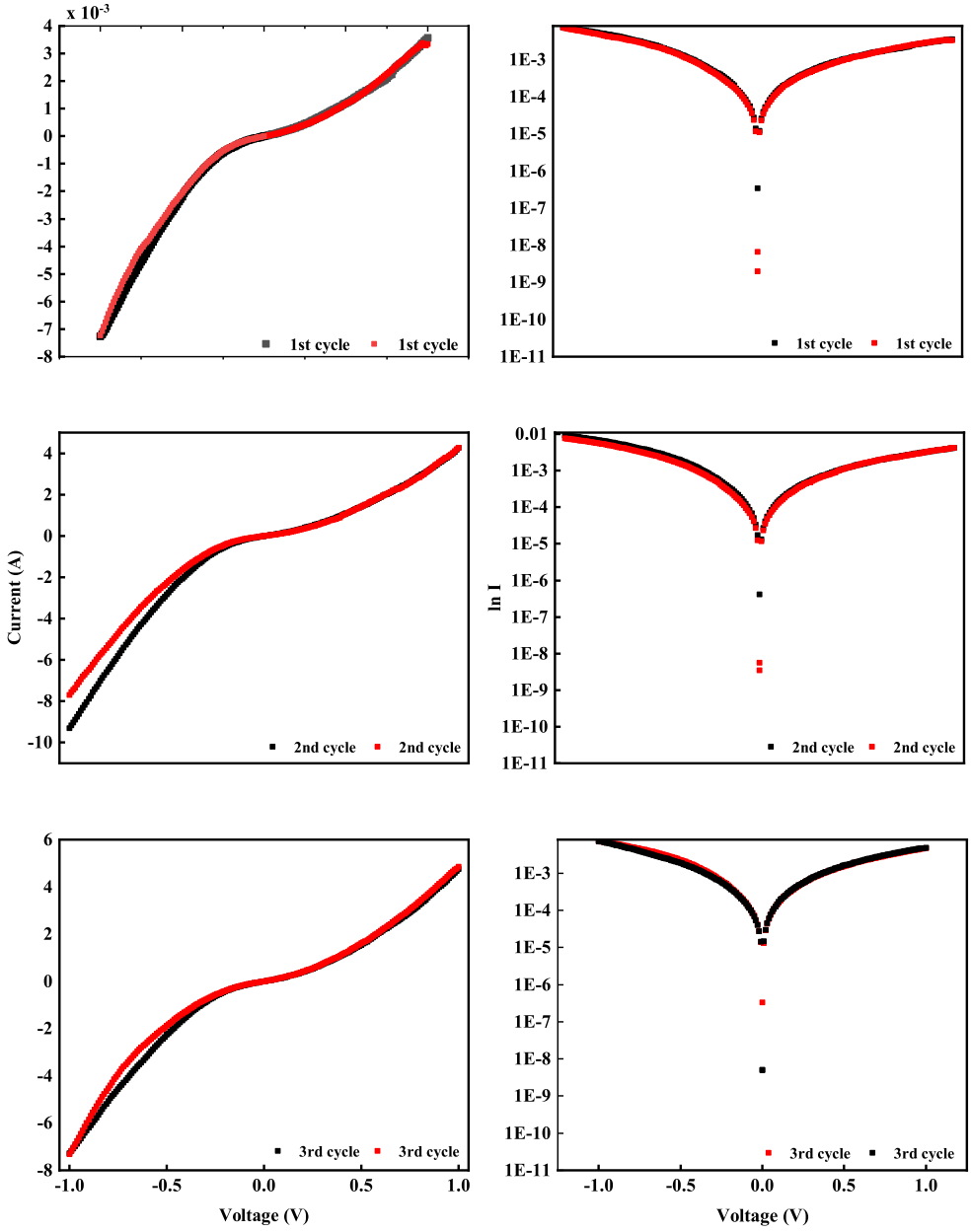

Figure 5.2.34: The I-V curve(left) and semi-logarithm plot (right) of rGO-ATA-Fe_2O_3(I) showing semiconductor features. The red colour signifies forward voltage sweep (forward bias) and black colour represents backward voltage sweep (reverse bias).

be alleviated as proposed by Udalov and Beloborodov [104]. They suggested that the application of external field can be used to manipulate the dielectric constant and the Coulomb interaction, which eventually can help reduce the impact of the Coulomb blockade effect [104].

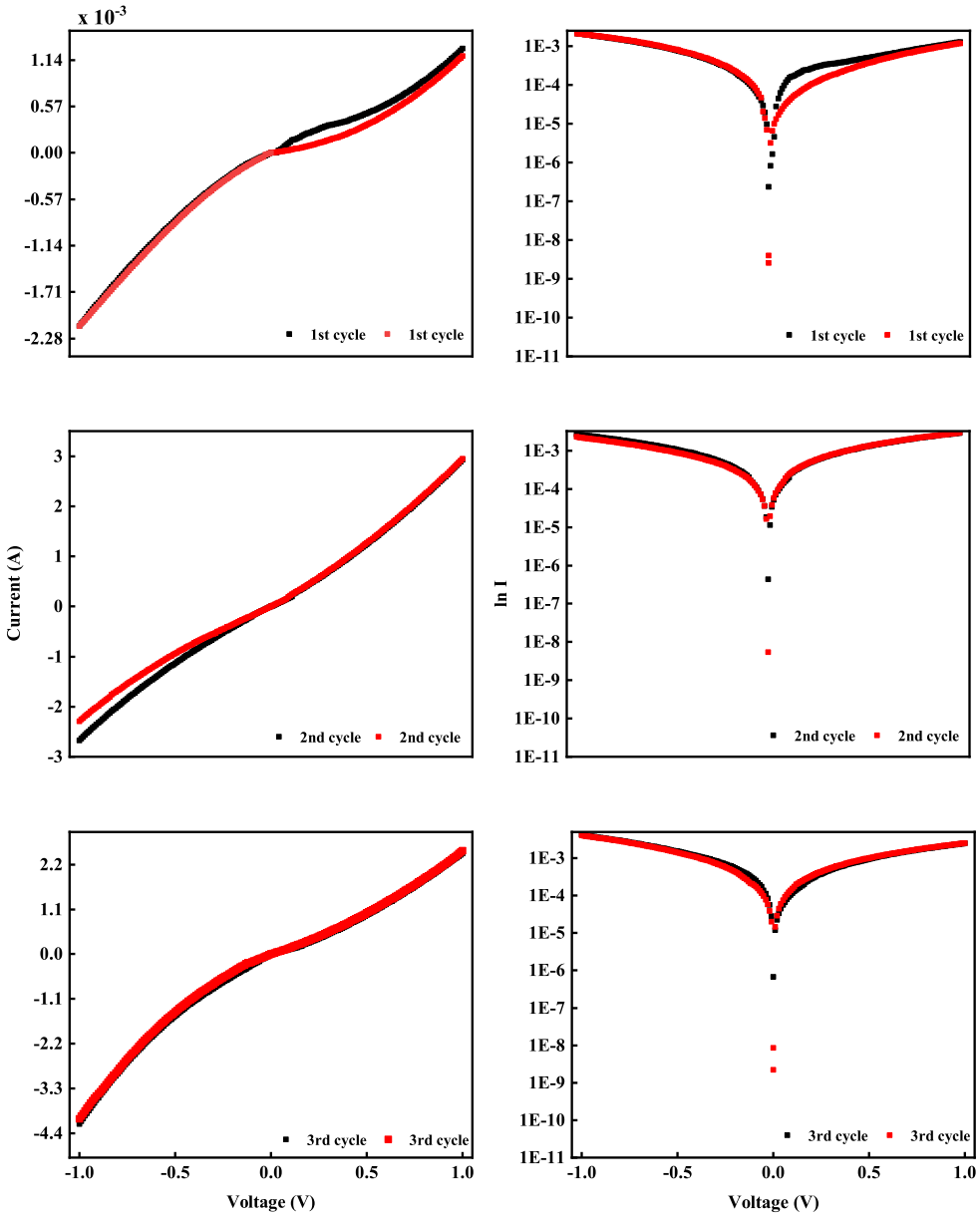

Figure 5.2.35: The I-V curve(left) and semi-logarithm plot (right) of rGO-ATA-Fe_2O_3(II) showing semiconductor features. he red colour signifies forward voltage sweep (forward bias) and black backward voltage sweep (reverse bias).

5.2.10 Magnetic behaviors

Figure 5.2.36 shows the M-H curve for graphite powder for temperatures 300 K, 40 K and 1.8 K. A coercivity of $\approx$ 255 Oe with temperature-dependent Ms values is observed, which indicates a ferromagnetic behaviour. The saturation magnetization (Ms) increases with decreasing temperature i.e 300 K $\rightarrow$ 5.5emu/g, 40 K $\rightarrow$ 6.01emu/g and 1.8 K $\rightarrow$ 10.2emu/g. The increase-decrease effect of Ms-T is mainly due to magnetic alignments since the saturation signifies complete alignment of the moments with regard to the field direction, the magnetic spins can be easily altered by Brownian motion [106]. The resulting effect causes decreased saturation, however, at low temperature, the Zeeman energy is more prominent with respect to thermal energy. The resulting effect leads to an increased Ms magnetization [107]. The origin of magnetism in carbon materials is still a controversy but in this case, the magnetization can be attributed to defective graphite as previously suggested [108]. From the EDX spectra, the peak indicated by C+C can be attributed to carbon defects. Although, the magnetization of graphite seem significant but it possesses high population of layers which is a huge deviation from pristine graphene.

The effect of the graphene sheet exfoliation can be observed in the M-H loop of GO (see Figure 5.2.37). The magnetization features show weak paramagnetic behaviour for temperatures 300 K and 40 K. Meanwhile, a weak ferromagnetic feature is observed at lower temperature at 1.8 K. The origin of the magnetization at low temperature is mainly due to the easy spin relaxation. Previous reports have indicated easy alignment of magnetic spins at low temperature [109, 110].

Figure 5.2.38 shows the M-H loop of rGO. The removal of oxygen moieties from the surface of GO does not improve the magnetization of GO rather a decrease is observed. The reduction is magnetization can be attributed to GO becoming more pristine graphene-like in nature [110]. The decrease in magnetization also validates the role of oxygen vacancies in influencing the electrical and magnetic properties of GO.

As in the case of electrical conductivity, the change in the properties of GO in this case is mainly due to the influence of Fe and nitrogen atom attachment.

The magnetic features of rGO show similarity with GO possessing weak ferromagnetic behavior at low temperature. The magnetic features can also be attributed to easy alignment of magnetic moments at low temperature. To further clarify the effect of Fe atoms on the magnetization of GO, consider the M-H loop of ATA-Fe_2O_3 shown in Figure 5.2.39. It is worth mentioning that ATA-Fe_2O was unintended for consideration as a complete GO composite. However, due to the high concentration of Fe and carbon

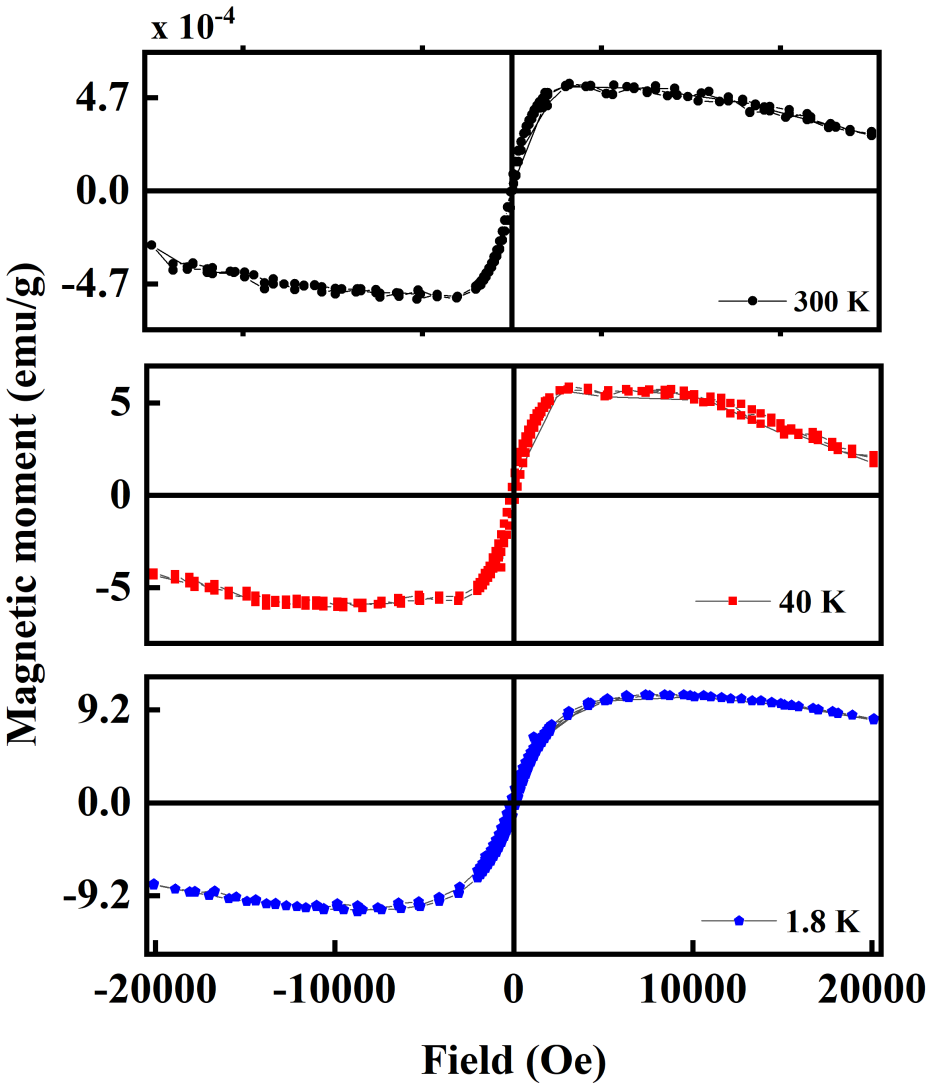

Figure 5.2.36: The M-H hysteresis loop for graphite powder for temperatures 300 K, 40 K *and* 1.8 K.

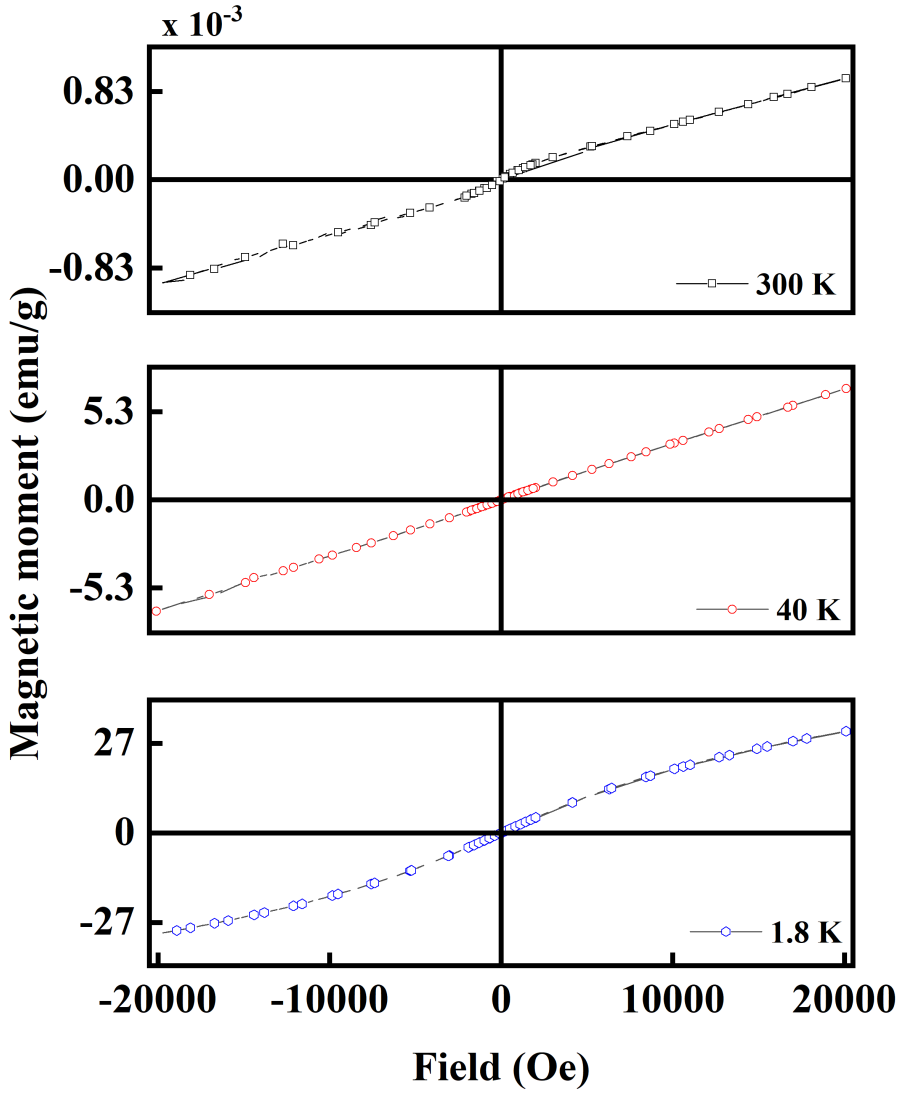

Figure 5.2.37: The M-H hysteresis loop for GO for temperatures 300 K, 40 K *and* 1.8 K.

impurities, it is considered for the sake of emphasis. The magnetization of GO in the case was significantly enhanced, which again validates the origin of magnetization in the composite. The magnetic features leaned toward ferromagnetism mainly because of the size of the Fe atomic clusters ($\approx 14 - 15$ nm) as indicated in average particle distribution in Section 5.2.2.

Figure 5.2.40 shows the M-H loop for rGO-ATA-Fe_2O_3 nanocomposites for temperature range 300 K, 40 K and 5 K. The Ms values for rGO-ATA-Fe_2O_3 nanocomposites are $\approx 6.8 \times 10^{-2}$ emu/g which is mainly due to Fe atoms as well as the amount of Fe_2O_3

deposited on the surface of GO. Furthermore, the value of remanence magnetization and coercivity are given in Table 5.2.14 after zooming into the M-H loops (see Figures 5.2.41, 5.2.42 and 5.2.43). As iterated earlier in Section 4.3.9, one of the pre-requisite for superparamagnetism is low remanence and coercivity. The values recorded in Table 5.2.14 are in proximity with the values that were previously reported [111].

The case of GO revealed negligible value of remanence and coercivity signifying the paramagnetic features of GO. Interestingly, the values for coercivity for ATA-Fe_2O_3

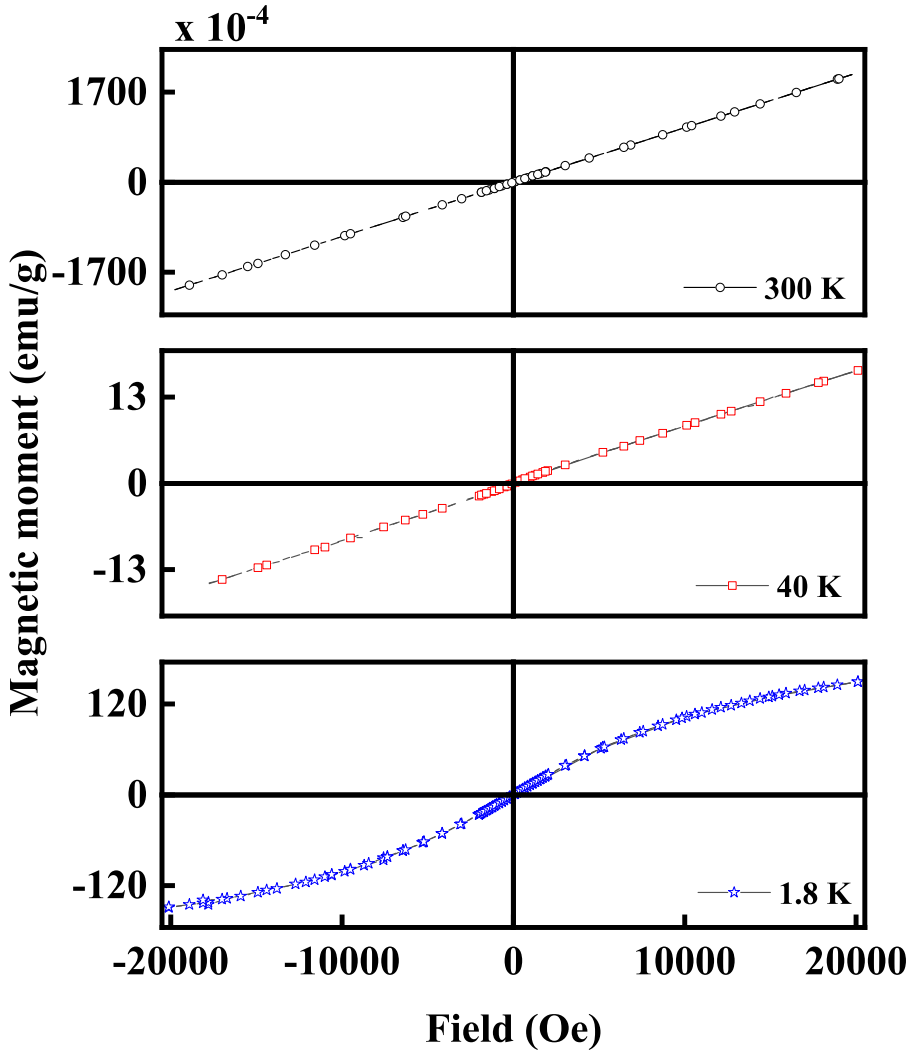

Figure 5.2.38: The M-H hysteresis loop for reduced GO for temperature range 300 K, 40 K *and* 1.8 K.

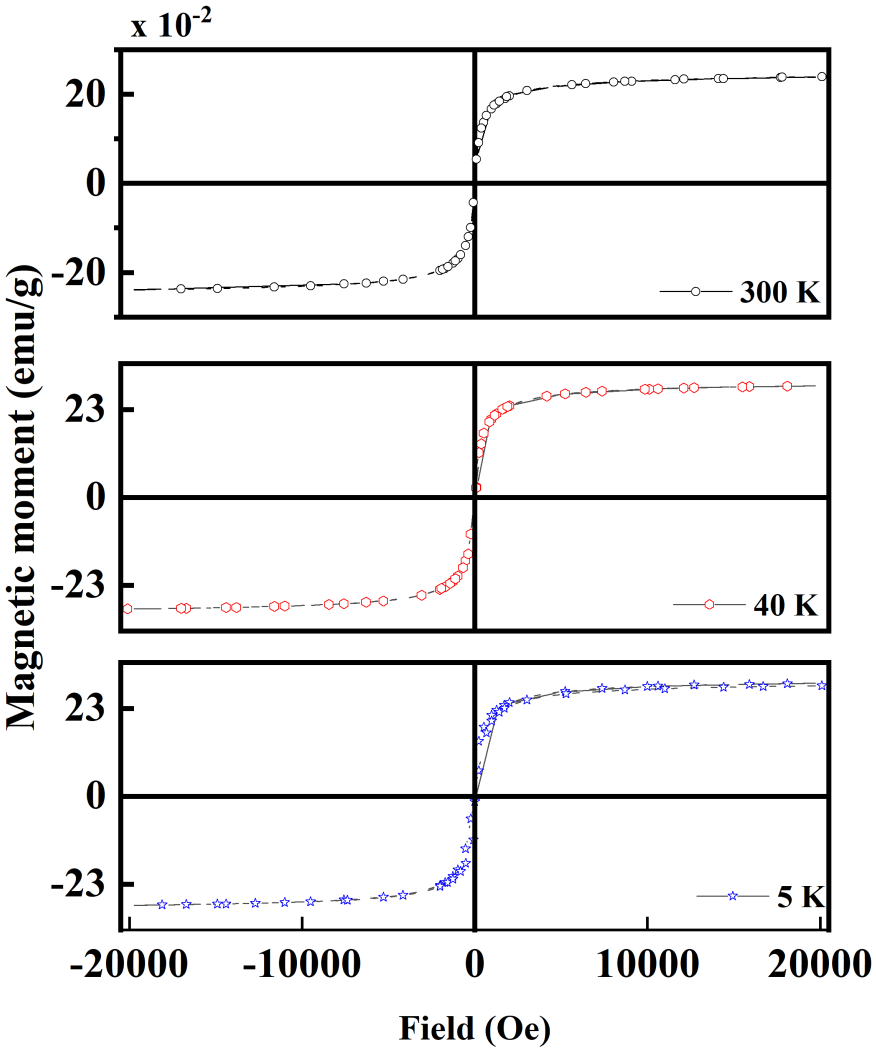

Figure 5.2.39: The M-H hysteresis loop for$ATA\text{-}Fe_2O_3$ for temperature range 300 K, 40 K *and* 5 K.

and rGO-ATA-Fe_2O_3 are higher in comparison with graphite at low temperature signifying the impact of lower temperature in favouring the alignment of magnetic spins [109, 110].. As earlier noted in the Section 4.3.9, ferromagnetic features can become superparamagnetic when the size of the particle is less than 50 nm. By virtue of the particle size distribution given in Section 5.2.2, the magnetic type of rGO-ATA-Fe_2O_3 nanocomposite can be classified as superparamagnetic.

As indicated in electronic structure from XANES in Section 5.2.8, there is presence of FeO, Fe_2O_3 and Fe_3O_4 signifying the actual origin of magnetism in rGO-ATA-Fe_2O_3 nanocomposite. This validates recent report of the conversion of Fe^{2+} to Fe^{3+} [112].

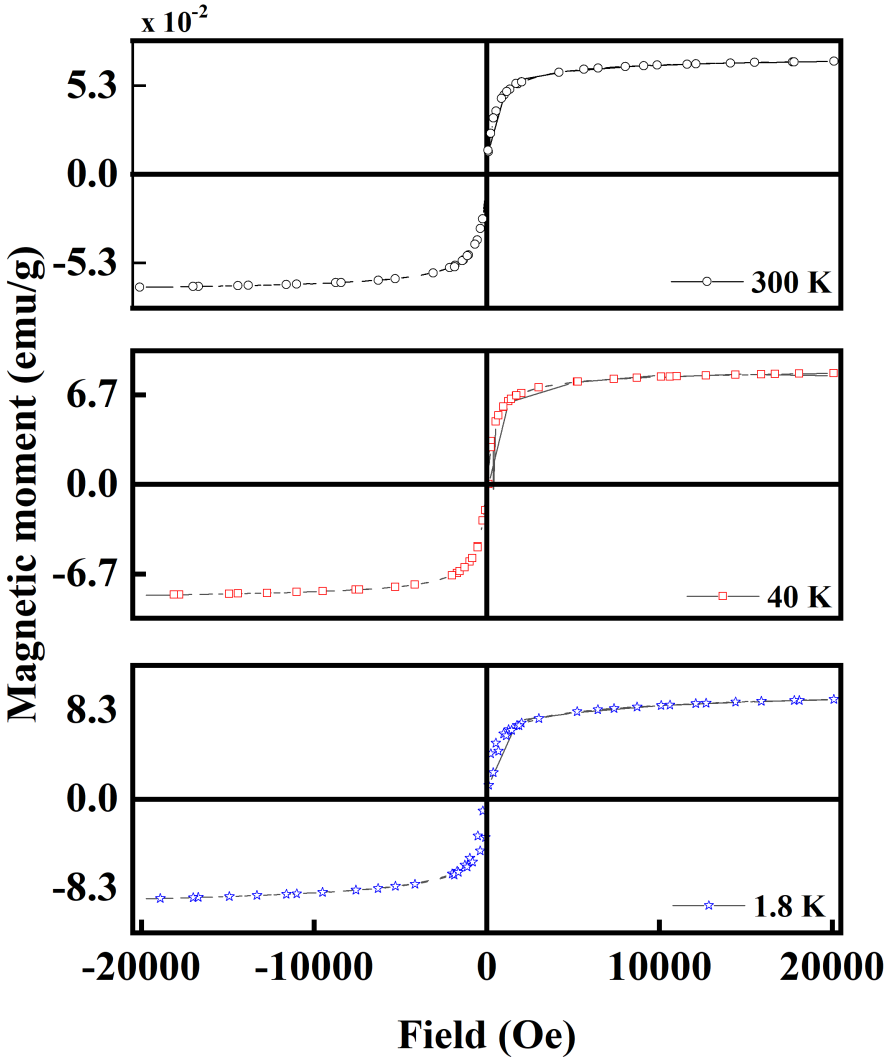

Figure 5.2.40: The M-H hysteresis loop for rGO-ATA-Fe_2O_3 nanocomposites for temperature range 300 K, 40 K *and* 5 K.

Figure 5.2.44 shows the field cooled M-T curve for GO, rGO and rGO-ATA-Fe_2O_3 nanocomposite for temperature range $0 - 400$ K. The curves show similarity for all the samples except ATA-Fe_2O_3. The M-T trends show a steady drop in magnetization

Table 5.2.14: Table showing the values of remanence and coercvity for graphite, ATA-Fe_2O_3 and rGO-ATA-Fe_2O_3 after zooming into the M-H loops.

Samples	Remanence (emu/g) $\times 10^{-5}$			Coercivity (Oe) $(\times 10^5)$		
	300 K	40 K	2 K	300 K	40 K	2 K
Graphite	4.19	8.0	8.0	77.1	155.2	155.2
GO	-	-	-	-	-	-
ATA-\ch{Fe2O3}	4.7	2.6	5	8.7	48.2	48
rGO-ATA-\ch{Fe2O3}(II)	1.7	5.1	2	8.2	30.4	107.5

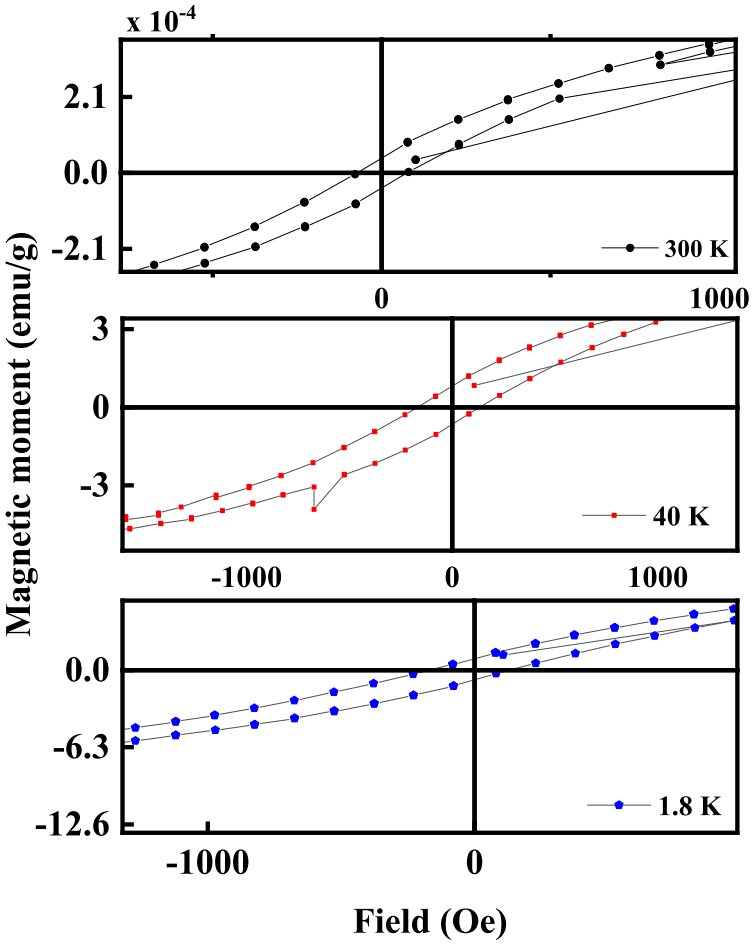

Figure 5.2.41: The zoomed in features of M-H loops of graphite indicating remanence magnetization and coercity.

with an increase in temperature and saturate between $17 - 305\,\mathrm{K}$ and decreases with respect to increase with temperature.

Meanwhile, blocking temperature T_B is an important parameter that is exhibited by magnetic materials. T_B is the temperature where the thermal energy of a single domain material becomes smaller leading to blocked magnetic moments. Below the blocking temperature, the orientation of superparamagnetic materials loses their polarizations [113]. There is a blocking temperature at $\approx 47\,\mathrm{K}$ for all the samples except for rGO-ATA-Fe_2O_3 $\approx (34\,\mathrm{K})$ where there is a decrease in the blocking temperature. The decrease in the blocking temperature may be due to a decrease in magnetic coupling between the particles of Fe atoms [114]. This feature of the blocking temperature

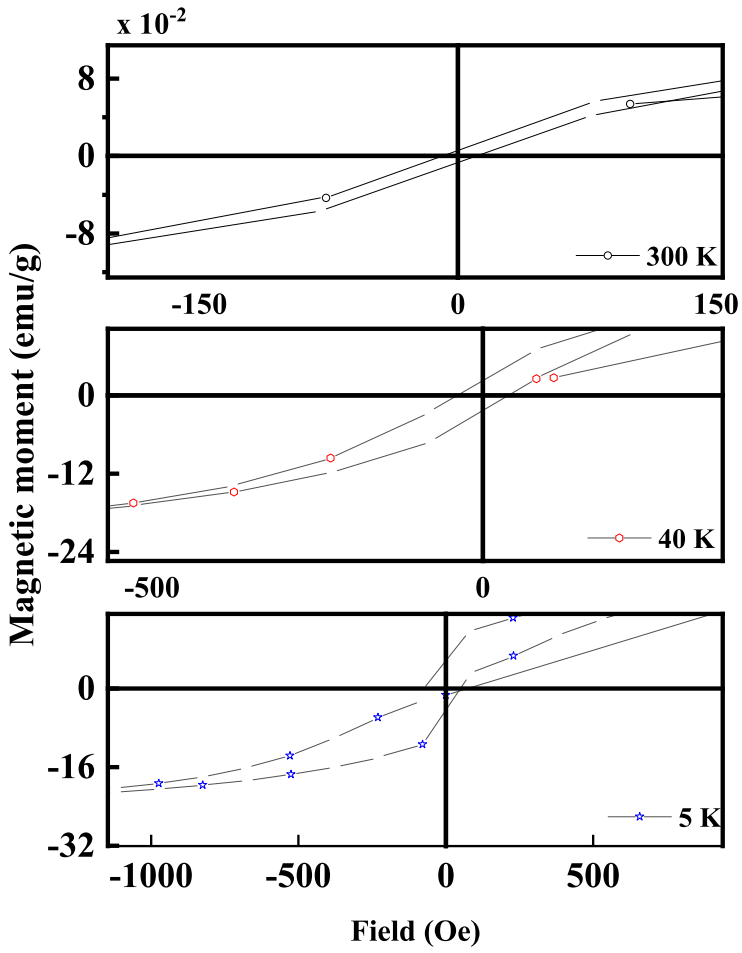

Figure 5.2.42: The zoomed in features of M-H loops of ATA-Fe_2O_3 indicating remanence magnetization and coercity.

is consistent with superparamagnetic behaviour [113, 115], whereas the case of ATA-Fe_2O_3 shows zero-field cooled M-T curve exhibiting similar behaviour with an increase in magnetization as temperature increased. At approximately 47 K, the magnetization saturates and decreases steadily at approximately 180 K.

Since Fe_2O_3 forms part of the spinel group, it occurs in the magnetite cubic structure which has a similar behavior as Fe_3O_4. The Fe_3O_4 spin dynamics can be analyzed as follows: Consider the cubic inverse spinel structure of Fe_3O_4 expressed as $(Fe[1])_A[Fe[2], Fe[3]_BO_4$ where Fe[1] possesses four nearest O^{2-} attached ions. These ions tend to occupy the tetrahedral lattice structure. Meanwhile, the Fe[2] and Fe[3] also possess six nearest O^{2-} attached ions which sits at the octahedral sites. The O^{2-} ions are

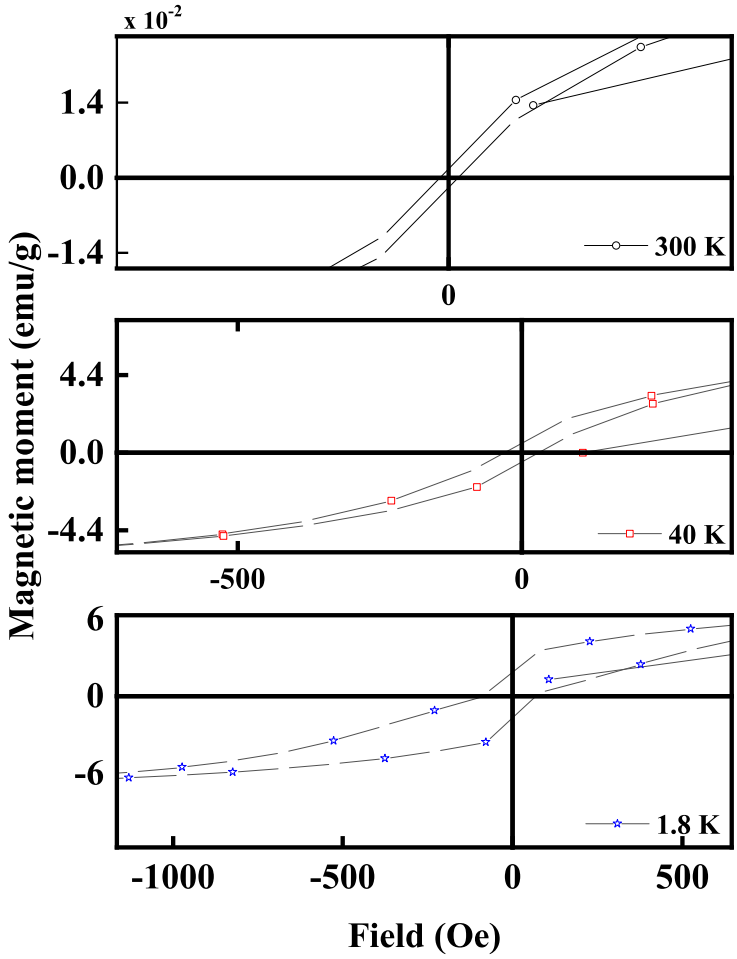

Figure 5.2.43: The zoomed in features of M-H loops of rGO-ATA-Fe_2O_3 indicating remanence magnetization and coercity.

tightly packed in the cubic lattice such that the Fe ions are in-between. Furthermore, the Fe^{3+} tend to occupy the A site whereas the combined Fe^{2+} and Fe^{3+} occupy the B sites implying more B site population [112]. Hence, Fe[1] can be assigned to Fe^{3+} (d^5) having $s = 5/2$ spin moments and the combined Fe^{2+} (d^6) and Fe^{3+} (d^5) (s= 5/2 and $s = 2$) [112]. Considering antiferromagnetic superexchange effect, the stronger interaction can be considered as Fe−Fe which gives Fe[2]-Fe[1] and Fe[1] - Fe[3] sites. In the case of Fe[2] - Fe[3], an unequal population of electrons occupying the nearest ion sites ($d^6 - d^5$) produce a double-bond exchange leading to ferromagnetic interactions. These interactions are responsible for the increased electrical conductivity where the d electrons tend to hop within the lattice [112].

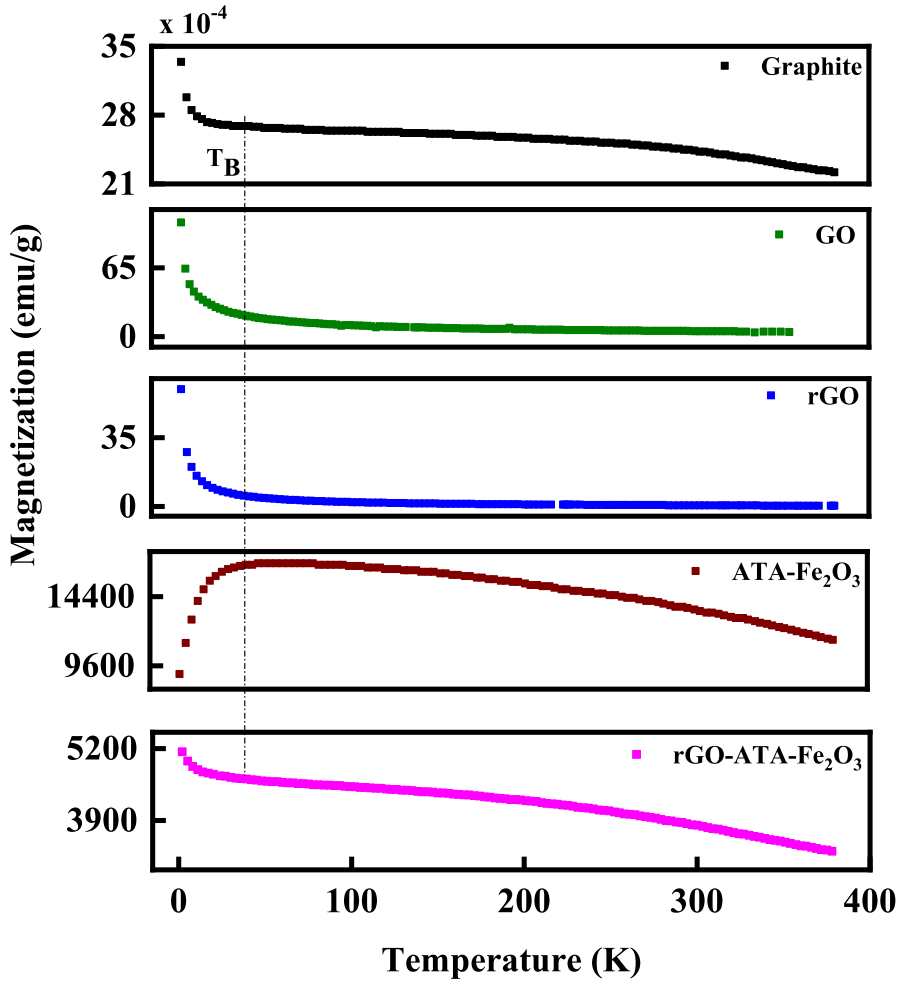

Figure 5.2.44: The field cooled M-T curve for GO, rGO and rGO-ATA-Fe_2O_3 nanocomposite for temperature range $0 - 400\,\mathrm{K}$.

In the case of rGO-ATA-Fe_2O_3 nanocomposite, the volume tend to increase with the formation of high spin state Fe^{3+} where the spin increases from $s = 2$ to $s = 5/2$. The enhanced magnetization in rGO-ATA-Fe_2O_3 nanocomposite can be attributed to magnetic domain size due exchange interaction between C 2p, O 2p an Fe 3d orbital state [116].

5.3 Summary

In this chapter, GO, rGO and rGO-ATA-Fe_2O_3 nanocomposite were synthesized via chemical co-precipitation method and using 2-aminoterephthalic acid (ATA) as a capping agent. The structural, electronic, electrical and magnetic properties were studied using different spectroscopic characterization techniques. There was an appearance of C−Fe, Fe−C and N−C bonds in the XPS measurement which signifies formation of new bonds. The new bonds were due to the impact of reduction and functionalization of GO. The formation of the new bonds offers an avenue for tuning of the electrical and magnetic properties of GO. An enhancement of electrical conductivity was observed for rGO-ATA-Fe_2O_3 nanocomposite in comparison with GO. The magnetic properties of rGO-ATA-Fe_2O_3 nanocomposite also show a superparamagnetic property at room temperature. The obtained result of the superparamagnetic features of rGO-ATA-Fe_2O_3 nanocomposite could be useful in magnetic resonance imaging contrast agent applications as well as electronic device applications by virtue of the weak charge storage property.

Bibliography

[1] Xu Chao, Wang Xin, and Zhu Junwu. Graphene- metal particle nanocomposites. *The Journal of Physical Chemistry C*, 112(50):19841–19845, 2008.

[2] Zhu Yanwu, Murali Shanthi, Cai Weiwei, Li Xuesong, Suk Ji Won, Potts Jeffrey R, and Ruoff Rodney S. Graphene and graphene oxide: synthesis properties and applications. *Advanced Materials*, 22(35):3906–3924, 2010.

[3] Bonaccorso Francesco, Sun Z, Hasan Ta, and Ferrari AC. Graphene photonics and optoelectronics. *Nature Photonics*, 4(9):611, 2010.

[4] Geng Xiumei, Niu Liang, Xing Zhenyuan, Song Rensheng, Liu Guangtong, Sun Mengtao, Cheng Guosheng, Zhong Haijian, Liu Zhenghui, Zhang Zhijun, et al. Aqueous-processable noncovalent chemically converted graphene–quantum dot composites for flexible and transparent optoelectronic films. *Advanced Materials*, 22(5):638–642, 2010.

[5] Han Wei, Kawakami Roland K, Gmitra Martin, and Fabian Jaroslav. Graphene spintronics. *Nature Nanotechnology*, 9(10):794–807, 2014.

[6] Stephan Roche and Sergio O Valenzuela. Graphene spintronics: puzzling controversies and challenges for spin manipulation. *Journal of Physics D: Applied Physics*, 47(9):094011–094015, 2014.

[7] Huber Dale L. Synthesis properties and applications of iron nanoparticles. *Small*, 1(5):482–501, 2005.

[8] RH Misho and WA Murad. Band gap measurements in thin films of hematite fe2o3, pyrite fes2 and troilite fes prepared by chemical spray pyrolysis. *Solar energy materials and solar cells*, 27(4):335–345, 1992.

[9] Sun Zhenyu, Madej Edyta, Wiktor Christian, Sinev Ilya, Fischer Roland A, Van Tendeloo Gustaaf, Muhler Martin, Schuhmann Wolfgang, and Ventosa Edgar. One-pot synthesis of carbon-coated nanostructured iron oxide on few-layer graphene for lithium-ion batteries. *Chemistry–A European Journal*, 21(45):16154–16161, 2015.

[10] Kim Il Tae, Magasinski Alexandre, Jacob Karl, Yushin Gleb, and Tannenbaum Rina. Synthesis and electrochemical performance of reduced graphene oxide/maghemite composite anode for lithium ion batteries. *Carbon*, 52:56–64, 2013.

[11] Hachani Roxanne, Lowdell Mark, Birchall Martin, Hervault Aziliz, Mertz Damien, Begin-Colin Sylvie, and Thanh Nguyen Thi Kim. Polyol synthesis functionalisation and biocompatibility studies of superparamagnetic iron oxide nanoparticles as potential mri contrast agents. *Nanoscale*, 8(6):3278–3287, 2016.

[12] Wang Dan, Ma Qian, and Yang Ping. Synthesis of fe3o4 nanoparticles with tunable and uniform size through simple thermal decomposition. *Journal of Nanoscience and Nanotechnology*, 12(8):6432–6438, 2012.

[13] Petcharoen K and Sirivat A. Synthesis and characterization of magnetite nanoparticles via the chemical co-precipitation method. *Materials Science and Engineering: B*, 177(5):421–427, 2012.

[14] Wu Shen, Sun Aizhi, Zhai Fuqiang, Wang Jin, Xu Wenhuan, Zhang Qian, and Volinsky Alex A. Fe3o4 magnetic nanoparticles synthesis from tailings by ultrasonic chemical co-precipitation. *Materials Letters*, 65(12):1882–1884, 2011.

[15] Astle Melvin Jensen. *The Chemistry of Petrochemicals.* Reinhold, 1956.

[16] Karabacak Mehmet, Cinar Mehmet, Unal Zeliha, and Kurt Mustafa. Ft-ir uv spectroscopic and dft quantum chemical study on the molecular conformation

vibrational and electronic transitions of 2-aminoterephthalic acid. *Journal of Molecular Structure*, 982(1-3):22–27, 2010.

[17] Bhattacharya Gourav, Kandasamy Ganeshlenin, Soin Navneet, Upadhyay Ravi Kant, Deshmukh Sujit, Maity Dipak, McLaughlin James, and Roy Susanta Sinha. Novel π-conjugated iron oxide/reduced graphene oxide nanocomposites for high performance electrochemical supercapacitors. *RSC Advances*, 7(1):327–335, 2017.

[18] Tian Leilei, Zhuang Quanchao, Li Jia, Wu Chao, Shi Yueli, and Sun Shigang. The production of self-assembled fe2o3–graphene hybrid materials by a hydrothermal process for improved li-cycling. *Electrochimica Acta*, 65:153–158, 2012.

[19] Zhang Hao, Yu Li, Li Qun, Du Yu, and Ruan Shuangchen. Reduced graphene oxide/α-fe2o3 hybrid nanocomposites for room temperature no2 sensing. *Sensors and Actuators B: Chemical*, 241:109–115, 2017.

[20] Warnes BM, Aplan FF, and Simkovich G. Electrical conductivity and seebeck voltage of fe2o3 pure and doped as a function of temperature and oxygen pressure. *Solid State Ionics*, 12:271–276, 1984.

[21] A Boudjemaa, S Boumaza, M Trari, R Bouarab, and A Bouguelia. Physical and photo-electrochemical characterizations of α-fe2o3. application for hydrogen production. *International Journal of Hydrogen Energy*, 34(10):4268–4274, 2009.

[22] Liu Shuangke, Chen Zhongxue, Xie Kai, Li Yujie, Xu Jing, and Zheng Chunman. A facile one-step hydrothermal synthesis of α-fe 2 o 3 nanoplates imbedded in graphene networks with high-rate lithium storage and long cycle life. *Journal of Materials Chemistry A*, 2(34):13942–13948, 2014.

[23] Xiao Lisong, Schroeder Matthias, Kluge Sebastian, Balducci Andrea, Hagemann Ulrich, Schulz Christof, and Wiggers Hartmut. Direct self-assembly of fe 2 o 3/reduced graphene oxide nanocomposite for high-performance lithium-ion batteries. *Journal of Materials Chemistry A*, 3(21):11566–11574, 2015.

[24] Everett E Carpenter. Iron nanoparticles as potential magnetic carriers. *Journal of magnetism and Magnetic Materials*, 225(1-2):17–20, 2001.

[25] Tadic Marin, Panjan Matjaz, Damnjanovic Vesna, and Milosevic Irena. Magnetic properties of hematite (α-fe2o3) nanoparticles prepared by hydrothermal synthesis method. *Applied Surface Science*, 320:183–187, 2014.

[26] S. Zolghadr, S. Kimiagar, and A. M. Davarpanah. Magnetic property of α - fe2o3–go nanocomposite. *IEEE Transactions on Magnetics*, 53(12):1–6, 2017.

[27] Gondal MA, Hameed A, Yamani Zain H, and Suwaiyan A. Production of hydrogen and oxygen by water splitting using laser induced photo-catalysis over fe2o3. *Applied Catalysis A: General*, 268(1-2):159–167, 2004.

[28] Guo Sheng, Zhang Gaoke, Guo Yadan, and Jimmy C Yu. Graphene oxide–fe2o3 hybrid material as highly efficient heterogeneous catalyst for degradation of organic contaminants. *Carbon*, 60:437–444, 2013.

[29] Lin Yong-Mao, Abel Paul R, Heller Adam, and Mullins C Buddie. α-fe2o3 nanorods as anode material for lithium ion batteries. *The Journal of Physical Chemistry Letters*, 2(22):2885–2891, 2011.

[30] NuLi Yanna, Zhang Peng, Guo Zaiping, and Liu Huakun. Shape evolution of α-fe2o3 and its size-dependent electrochemical properties for lithium-ion batteries. *Journal of the Electrochemical Society*, 155(3):A196–A200, 2008.

[31] Zhu Xiaoming, Jiang Xiaoyu, Chen Xin, Liu Xiaoling, Xiao Lifen, and Cao Yuliang. Fe2o3 amorphous nanoparticles/graphene composite as high-performance anode materials for lithium-ion batteries. *Journal of Alloys and Compounds*, 711:15–21, 2017.

[32] Lihua Bai, Luyao Yuan, Yi Ji, and Hongxia Yan. Effective removal of phosphate from aqueous by graphene oxide decorated with α-fe2o3: Kinetic, isotherm, ther-

modynamic and mechanism study. *Arabian Journal for Science & Engineering (Springer Science & Business Media BV)*, 43(7), 2018.

[33] Miaomiao Liu and Jing Sun. In situ growth of monodisperse fe 3 o 4 nanoparticles on graphene as flexible paper for supercapacitor. *Journal of Materials Chemistry A*, 2(30):12068–12074, 2014.

[34] Mehwish Qutab, Monas Shahzad, Hamid Latif, Khalid Javed, Saqlain A Shah, and Abdul Waheed Anwar. Plasmonic nano-structured material based on silver and reduced graphene oxide (rgo) for surface enhanced raman spectroscopy. In *Plasmonics III*, volume 10824, page 108240J. International Society for Optics and Photonics, 2018.

[35] Sofiane Sedira and Bilel Mendaci. Hydrothermal synthesis of spherical carbon nanoparticles (cnps) for supercapacitor electrodes uses. *Materials for Renewable and Sustainable Energy*, 9(1):1–9, 2020.

[36] S Ida, P Wilson, B Neppolian, M Sathish, AR Mahammed Shaheer, and P Ravi. Tuning the type of nitrogen on n-rgo supported on n-tio2 under ultrasonication/hydrothermal treatment for efficient hydrogen evolution–a mechanistic overview. *Ultrasonics sonochemistry*, 64:104866, 2020.

[37] PK Sahoo, Bharati Panigrahy, Dan Li, and D Bahadur. Magnetic behavior of reduced graphene oxide/metal nanocomposites. *Journal of Applied Physics*, 113(17):17B525–17B527, 2013.

[38] Kun Zhang, Yue Zhang, and Shiren Wang. Enhancing thermoelectric properties of organic composites through hierarchical nanostructures. *Scientific Reports*, 3:3448–3454, 2013.

[39] Raja Das, Chiran Witanachchi, Zohreh Nemati, Vijaysankar Kalappattil, Irati Rodrigo, José Ángel García, Eneko Garaio, Javier Alonso, Vu Dinh Lam, Anh-

Tuan Le, et al. Magnetic vortex and hyperthermia suppression in multigrain iron oxide nanorings. *Applied Sciences*, 10(3):787, 2020.

[40] Srividhya J Iyengar, Mathew Joy, Chandan Kumar Ghosh, Subhrajyoti Dey, Ravinder K Kotnala, and Swapankumar Ghosh. Magnetic, x-ray and mossbauer studies on magnetite/maghemite core–shell nanostructures fabricated through an aqueous route. *RSC Advances*, 4(110):64919–64929, 2014.

[41] B Ingham and MF Toney. X-ray diffraction for characterizing metallic films. In *Metallic Films for Electronic, Optical and Magnetic Applications*, pages 3–38. Elsevier, 2014.

[42] Mingxin Li and Jie Lian. Microstructure dictating performance: Assembly of graphene-based macroscopic structures. *Accounts of Materials Research*, 2020.

[43] Shubhda Srivastava, Kiran Jain, VN Singh, Sukhvir Singh, N Vijayan, Nita Dilawar, Govind Gupta, and TD Senguttuvan. Faster response of no2 sensing in graphene–wo3 nanocomposites. *Nanotechnology*, 23(20):205501–205507, 2012.

[44] AS Ivanova, EM Slavinskaya, OA Stonkus, RV Gulyaev, TS Glazneva, AS Noskov, and AI Boronin. Highly active and durable pd/fe 2 o 3 catalysts for wet co oxidation under ambient conditions. *Catalysis Science & Technology*, 6(11):3918–3928, 2016.

[45] David O Idisi, JA Oke, Sweety Sarma, SJ Moloi, Sekhar C Ray, WF Pong, and Andre M Strydom. Tuning of electronic and magnetic properties of multifunctional r-go-ata-fe2o3-composites for magnetic resonance imaging (mri) contrast agent. *Journal of Applied Physics*, 126(3):035301, 2019.

[46] Daniel R Dreyer, Sungjin Park, Christopher W Bielawski, and Rodney S Ruoff. The chemistry of graphene oxide. *Chemical Society Reviews*, 39(1):228–240, 2010.

[47] Holger Borchert, Elena V Shevchenko, Aymeric Robert, Ivo Mekis, Andreas Kornowski, Gerhard Grübel, and Horst Weller. Determination of nanocrystal sizes:

a comparison of tem, saxs, and xrd studies of highly monodisperse copt3 particles. *Langmuir*, 21(5):1931–1936, 2005.

[48] Larissa Stieven Montagna, Fabiana de Carvalho Fim, Griselda Barrera Galland, and Nara Regina de Souza Basso. Synthesis of poly (propylene)/graphite nanocomposites by in situ polymerization. In *Macromolecular Symposia*, volume 299, pages 48–56. Wiley Online Library, 2011.

[49] Bernardo Marinho, Marcos Ghislandi, Evgeniy Tkalya, Cor E Koning, and Gijsbertus de With. Electrical conductivity of compacts of graphene, multi-wall carbon nanotubes, carbon black, and graphite powder. *Powder Technology*, 221:351–358, 2012.

[50] Hira Fatima, Dae-Won Lee, Hyun Joong Yun, and Kyo-Seon Kim. Shape-controlled synthesis of magnetic fe 3 o 4 nanoparticles with different iron precursors and capping agents. *RSC Advances*, 8(41):22917–22923, 2018.

[51] TJ Shaffner and RD Van Veld. 'charging'effects in the scanning electron microscope. *Journal of Physics E: Scientific Instruments*, 4(9):633, 1971.

[52] Childres Isaac, Jauregui Luis A, Park Wonjun, Cao Helin, and Chen Yong P. Raman spectroscopy of graphene and related materials. *New Developments in Photon and Materials Research*, 1:1–20, 2013.

[53] Ado Jorio, Erlon H Martins Ferreira, Marcus VO Moutinho, Fernando Stavale, Carlos A Achete, and Rodrigo B Capaz. Measuring disorder in graphene with the g and d bands. *Physica Status Solidi (B)*, 247(11-12):2980–2982, 2010.

[54] LM Malard, Marcos Assunção Pimenta, Gene Dresselhaus, and MS Dresselhaus. Raman spectroscopy in graphene. *Physics reports*, 473(5-6):51–87, 2009.

[55] Adrian Radoń, Patryk Włodarczyk, and Dariusz Łukowiec. Structure, temperature and frequency dependent electrical conductivity of oxidized and reduced

electrochemically exfoliated graphite. *Physica E: Low-dimensional Systems and Nanostructures*, 99:82–90, 2018.

[56] Kalimuthu Vijayarangamuthu, Seungbae Ahn, Hyungtak Seo, Sang-Hee Yoon, Cheol-Min Park, and Ki-Joon Jeon. Temporospatial control of graphene wettability. *Advanced Materials*, 28(4):661–667, 2016.

[57] Konstantin N Kudin, Bulent Ozbas, Hannes C Schniepp, Robert K Prud'Homme, Ilhan A Aksay, and Roberto Car. Raman spectra of graphite oxide and functionalized graphene sheets. *Nano Letters*, 8(1):36–41, 2008.

[58] Young Soo Yun, Gabin Yoon, Min Park, Se Youn Cho, Hee-Dae Lim, Haegyeom Kim, Yung Woo Park, Byung Hoon Kim, Kisuk Kang, and Hyoung-Joon Jin. Restoration of thermally reduced graphene oxide by atomic-level selenium doping. *NPG Asia Materials*, 8(12):e338–e338, 2016.

[59] Andrea C Ferrari and Denis M Basko. Raman spectroscopy as a versatile tool for studying the properties of graphene. *Nature Nanotechnology*, 8(4):235–246, 2013.

[60] Sven Reichardt and Ludger Wirtz. Raman spectroscopy of graphene. In *Optical Properties of Graphene*, pages 85–132. World Scientific, 2017.

[61] Chun-Chung Chen, Wenzhong Bao, Jesse Theiss, Chris Dames, Chun Ning Lau, and Stephen B Cronin. Raman spectroscopy of ripple formation in suspended graphene. *Nano Letters*, 9(12):4172–4176, 2009.

[62] Madhab Bera, Pragya Gupta, Pradip K Maji, et al. Facile one-pot synthesis of graphene oxide by sonication assisted mechanochemical approach and its surface chemistry. *Journal of Nanoscience and Nanotechnology*, 18(2):902–912, 2018.

[63] Fatemeh Ahangaran, Ali Hassanzadeh, and Sirous Nouri. Surface modification of fe 3 o 4@ sio 2 microsphere by silane coupling agent. *International Nano Letters*, 3(1):23–27, 2013.

[64] Vasilica Ţucureanu, Alina Matei, and Andrei Marius Avram. Ftir spectroscopy for carbon family study. *Critical reviews in analytical chemistry*, 46(6):502–520, 2016.

[65] Teresa Iwasita. Electrocatalysis of methanol oxidation. *Electrochimica Acta*, 47(22-23):3663–3674, 2002.

[66] M Al-Hada, L Gregoratti, M Amati, and M Neeb. Pristine and oxidised ag-nanoparticles on free-standing graphene as explored by x-ray photoelectron and auger spectroscopy. *Surface Science*, 693:121533, 2020.

[67] B Ghosh, Sweety Sarma, Mbule Pontsho, and Sekhar C Ray. Tuning of magnetic behaviour in nitrogenated graphene oxide functionalized with iron oxide. *Diamond and Related Materials*, 89:35–42, 2018.

[68] Jong-Pil Jegal, Kwang-Chun Kim, Myeong Seong Kim, and Kwang-Bum Kim. A lithium iron phosphate/nitrogen-doped reduced graphene oxide nanocomposite as a cathode material for high-power lithium ion batteries. *Journal of Materials Chemistry A*, 2(25):9594–9599, 2014.

[69] Wei Gao. The chemistry of graphene oxide. In *Graphene oxide*, pages 61–95. Springer, 2015.

[70] RIR Blyth, Hilmi Buqa, FP Netzer, MG Ramsey, JO Besenhard, Peter Golob, and Martin Winter. Xps studies of graphite electrode materials for lithium ion batteries. *Applied Surface Science*, 167(1-2):99–106, 2000.

[71] B Balamurugan and Toshiro Maruyama. Inhomogeneous effect of particle size on core-level and valence-band electrons: size-dependent electronic structure of cu 3 n nanoparticles. *Applied physics letters*, 89(3):033112–033114, 2006.

[72] Hyung Jin Kim, In-Seob Bae, Sang-Jin Cho, Jin-Hyo Boo, Byung-Cheo Lee, Jinhee Heo, Ilsub Chung, and Byungyou Hong. Synthesis and characteristics of nh

2-functionalized polymer films to align and immobilize dna molecules. *Nanoscale Research Letters*, 7(1):30–36, 2012.

[73] Sasha Stankovich, Dmitriy A Dikin, Richard D Piner, Kevin A Kohlhaas, Alfred Kleinhammes, Yuanyuan Jia, Yue Wu, SonBinh T Nguyen, and Rodney S Ruoff. Synthesis of graphene-based nanosheets via chemical reduction of exfoliated graphite oxide. *carbon*, 45(7):1558–1565, 2007.

[74] Li Qun Xu, Wen Jing Yang, Koon-Gee Neoh, En-Tang Kang, and Guo Dong Fu. Dopamine-induced reduction and functionalization of graphene oxide nanosheets. *Macromolecules*, 43(20):8336–8339, 2010.

[75] Ziyu Yang, Tianshan Zhao, Xiaoxiao Huang, Xin Chu, Tianyu Tang, Yanmin Ju, Qian Wang, Yanglong Hou, and Song Gao. Modulating the phases of iron carbide nanoparticles: from a perspective of interfering with the carbon penetration of fe@fe3o4 by selectively adsorbed halide ions. *Chemical science*, 8(1):473–481, 2017.

[76] Dakai Guo, Sancan Han, Jiacheng Wang, and Yufang Zhu. Mil-100-fe derived n-doped fe/fe3c@ c electrocatalysts for efficient oxygen reduction reaction. *Applied Surface Science*, 434:1266–1273, 2018.

[77] Toru Yamashita and Peter Hayes. Analysis of xps spectra of fe2+ and fe3+ ions in oxide materials. *Applied surface science*, 254(8):2441–2449, 2008.

[78] Martin Magnuson, Ola Wilhelmsson, J-P Palmquist, Ulf Jansson, M Mattesini, S Li, Rajeev Ahuja, and Olle Eriksson. Electronic structure and chemical bonding in ti 2 al c investigated by soft x-ray emission spectroscopy. *Physical Review B*, 74(19):195108–195115, 2006.

[79] Huiying Zeng, Zihang Qiu, Alejandra Dominguez-Huerta, Zoe Hearne, Zhengwang Chen, and Chao-Jun Li. An adventure in sustainable cross-coupling of phe-

nols and derivatives via carbon–oxygen bond cleavage. *ACS Catalysis*, 7(1):510–519, 2016.

[80] DS Sutar, Gulbagh Singh, and V Divakar Botcha. Electronic structure of graphene oxide and reduced graphene oxide monolayers. *Applied Physics Letters*, 101(10):103103–103107, 2012.

[81] Cheng-Hao Chuang, Sekhar C Ray, Debarati Mazumder, Surbhi Sharma, Abhijit Ganguly, Pagona Papakonstantinou, Jau-Wern Chiou, Huang-Ming Tsai, Hung-Wei Shiu, Chia-Hao Chen, et al. Chemical modification of graphene oxide by nitrogenation: An x-ray absorption and emission spectroscopy study. *Scientific reports*, 7(1):1–10, 2017.

[82] Wei Li, Xiaolong Chen, Lin Wang, Yuheng He, Zefei Wu, Yuan Cai, Mingwei Zhang, Yang Wang, Yu Han, Rolf W Lortz, et al. Density of states and its local fluctuations determined by capacitance of strongly disordered graphene. *Scientific reports*, 3(1):1–6, 2013.

[83] Abhijit Ganguly, Surbhi Sharma, Pagona Papakonstantinou, and Jeremy Hamilton. Probing the thermal deoxygenation of graphene oxide using high-resolution in situ x-ray-based spectroscopies. *The Journal of Physical Chemistry C*, 115(34):17009–17019, 2011.

[84] SC Ray, CW Pao, JW Chiou, HM Tsai, JC Jan, WF Pong, R McCann, SS Roy, P Papakonstantinou, and JA McLaughlin. Electronic properties of a-cn x thin films: An x-ray-absorption and photoemission spectroscopy study. *Journal of applied physics*, 98(3):033708–033712, 2005.

[85] SC Ray, CW Pao, HM Tsai, B Bose, JW Chiou, WF Pong, and D Das-Gupta. Orientation of graphitic planes during annealing of "dip deposited" amorphous carbon film: A carbon k-edge x-ray absorption near-edge study. *Carbon*, 44(10):1982–1985, 2006.

[86] Sekhar Chandra Ray, CW Pao, HM Tsai, JW Chiou, WF Pong, MH Tsai, TIT Okpalugo, P Papakonstantinou, and TW Pi. Enhancement of sp3-bonding in high-bias-voltage grown diamond-like carbon thin films studied by x-ray absorption and photoemission spectroscopy. *Journal of Physics: Condensed Matter*, 19(17):176204–176209, 2007.

[87] EV Rut'kov, EY Afanas' eva, and NR Gall. Graphene and graphite work function depending on layer number on re. *Diamond and Related Materials*, 101:107576, 2020.

[88] P Simonov. Physicochemical aspects of preparation of carbon-supported noble metal catalysts. *New York, NY: Marcel Dekker, Inc, 2003.*, pages 409–454, 2003.

[89] Lamprini Sygellou, Georgios Paterakis, Costas Galiotis, and Dimitrios Tasis. Work function tuning of reduced graphene oxide thin films. *The Journal of Physical Chemistry C*, 120(1):281–290, 2015.

[90] Goki Eda, Cecilia Mattevi, Hisato Yamaguchi, HoKwon Kim, and Manish Chhowalla. Insulator to semimetal transition in graphene oxide. *The Journal of Physical Chemistry C*, 113(35):15768–15771, 2009.

[91] DP Singh, V Kumar, A Kumar, R Manohar, Renu Pasricha, B Duponchel, Y Boussoualem, AH Sahraoui, and A Daoudi. Effect of graphene oxide interlayer electron-phonon coupling on the electro-optical parameters of a ferroelectric liquid crystal. *RSC advances*, 7(21):12479–12485, 2017.

[92] Norlida Kamarulzaman, Muhd Firdaus Kasim, and Roshidah Rusdi. Band gap narrowing and widening of zno nanostructures and doped materials. *Nanoscale Research Letters*, 10(1):346–357, 2015.

[93] Clive James. Structural techniques. In *Structural Chemistry of Glasses*, pages 137–183. Elsevier, 2002.

[94] Junqing Xu, Peter Krüger, Calogero R Natoli, Kuniko Hayakawa, Ziyu Wu, and Keisuke Hatada. X-ray absorption spectra of graphene and graphene oxide by full-potential multiple scattering calculations with self-consistent charge density. *Physical Review B*, 92(12):125408–125418, 2015.

[95] Zhijiang Wang, Lina Wu, Jigang Zhou, Zhaohua Jiang, and Baozhong Shen. Chemoselectivity-induced multiple interfaces in mwcnt/fe 3 o 4@ zno heterotrimers for whole x-band microwave absorption. *Nanoscale*, 6(21):12298–12302, 2014.

[96] Aditya Sharma, Sitansu Sekhar Nanda, Jai Parkash, Anshuman Sahai, Shiv Kumar, Deepti Maikhuri, Dong Kee Yi, Hyun-Joon Shin, Keun-Hwa Chae, and Sung Ok Won. Structural and electronic structure investigations on sonication based synthesized graphene oxide and reduced-graphene oxide nano-sheets. *Physica Scripta*, 94(12):125807, 2019.

[97] N García, P Esquinazi, J Barzola-Quiquia, and S Dusari. Evidence for semiconducting behavior with a narrow band gap of bernal graphite. *New Journal of Physics*, 14(5):053015–053029, 2012.

[98] Narek Margaryan, Ninel Kokanyan, and Edvard Kokanyan. Low-temperature synthesis and characteristics of fractal graphene layers. *Journal of Saudi Chemical Society*, 23(1):13–20, 2019.

[99] PK Larsen, R Cuppens, and GACM Spierings. Ferroelectric memories. *Ferroelectrics*, 128(1):265–292, 1992.

[100] Inhwa Jung, Dmitriy A Dikin, Richard D Piner, and Rodney S Ruoff. Tunable electrical conductivity of individual graphene oxide sheets reduced at "low" temperatures. *Nano letters*, 8(12):4283–4287, 2008.

[101] TS Sreeprasad and Vikas Berry. How do the electrical properties of graphene change with its functionalization? *Small*, 9(3):341–350, 2013.

[102] CR Minitha, LR Nivedita, K Asokan, and RT Rajendra Kumar. Tuning the electrical properties of graphene oxide by nitrogen ion implantation: Implication for gas sensing. *Nuclear Instruments and Methods in Physics Research Section B: Beam Interactions with Materials and Atoms*, 450:257–261, 2019.

[103] Daeha Joung, Lei Zhai, and Saiful I Khondaker. Coulomb blockade and hopping conduction in graphene quantum dots array. *Physical Review B*, 83(11):115323–115328, 2011.

[104] OG Udalov and IS Beloborodov. The coulomb based magneto-electric coupling in multiferroic tunnel junctions and granular multiferroics. *AIP Advances*, 8(5):055810, 2018.

[105] Sumanta Bhandary, Olle Eriksson, and Biplab Sanyal. Defect controlled magnetism in fep/graphene/ni (111). *Scientific reports*, 3(1):1–6, 2013.

[106] Charbel Tannous and Jacek Gieraltowski. Magnetic properties: From traditional to spintronic. In *Springer Handbook of Electronic and Photonic Materials*, pages 1–1. Springer, 2017.

[107] Dajie Zhang, KJ Klabunde, CM Sorensen, and GC Hadjipanayis. Magnetization temperature dependence in iron nanoparticles. *Physical Review B*, 58(21):14167–14172, 1998.

[108] J Červenka, MI Katsnelson, and CFJ Flipse. Room-temperature ferromagnetism in graphite driven by two-dimensional networks of point defects. *Nature Physics*, 5(11):840–844, 2009.

[109] CJ Cong, L Liao, QY Liu, JC Li, and KL Zhang. Effects of temperature on the ferromagnetism of mn-doped zno nanoparticles and mn-related raman vibration. *Nanotechnology*, 17(5):1520–1527, 2006.

[110] Tao Tang, Fuchi Liu, Yuan Liu, Xinyu Li, Qinghua Xu, Qian Feng, Nujiang Tang,

and Youwei Du. Identifying the magnetic properties of graphene oxide. *Applied Physics Letters*, 104(12):123104–123108, 2014.

[111] A Sendil Kumar and Anil K Bhatnagar. Magnetism from fe 2 o 3 nanoparticles embedded in amorphous sio 2 matrix. *Applied Nanoscience*, 8(1):79–87, 2018.

[112] Sumit Majumder, Manas Sardar, Biswarup Satpati, Sanjay Kumar, and Sangam Banerjee. Magnetization enhancement of fe3o4 by attaching onto graphene oxide: An interfacial effect. *The Journal of Physical Chemistry C*, 122(37):21356–21365, 2018.

[113] Gerardo F Goya and MP Morales. Field dependence of blocking temperature in magnetite nanoparticles. In *Journal of Metastable and Nanocrystalline Materials*, volume 20, pages 673–678. Trans Tech Publ, 2004.

[114] Klemens Rumpf, Petra Granitzer, Puerto M Morales, Peter Poelt, and Michael Reissner. Variable blocking temperature of a porous silicon/fe 3 o 4 composite due to different interactions of the magnetic nanoparticles. *Nanoscale research letters*, 7(1):1–4, 2012.

[115] J Carvell, E Ayieta, A Gavrin, Ruihua Cheng, VR Shah, and P Sokol. Magnetic properties of iron nanoparticle. *Journal of Applied Physics*, 107(10):103913–103917, 2010.

[116] David O Idisi, James A Oke, Evan M Benecha, Sabato J Moloi, and Sekhar C Ray. Magnetic properties of graphene oxide functionalized with “au” and “fe2o3” nanoparticles: A comparative study. *Materials Today: Proceedings*, 44:5037–5043, 2021.

Chapter 6

Conclusion and future work

GO functionalized with both Au and Fe_2O_3 have shown enormous potential for electronic devices and magnetic resonance imaging contrast agent. Both composites are unique as can be observed in their electrical and magnetic properties. For instance, the electrical conductivity properties of rGO:Au-NP increases with low concentration of Au-NP and drops with high Au concentration. Interestingly, charge storage properties becomes obvious for the high concentration of Au-NP. Whereas in the case of rGO:Fe_2O_3, the electrical conductivity seemed to increase with increased concentration of Fe atoms. However, the charge storage properties of rGO:Fe_2O_3 were not as prominent as observed for rGO:Au-NP. This may be due to weak attachment of Au atoms to the surface of GO and strong attachment of Fe atoms in the case of rGO:Fe_2O_3.

The magnetic properties of both composite also showed enhanced superparamagnetic features which is a consequence of the particle sizes been less than 50 nm alongside low remanence and coercivity. The main distinction between both composites is the magnitude of the enhancement of the magnetization in both cases. The case of rGO:Au-NP showed an enhancement in comparison with rGO in the magnitude of $\approx \times 3$ whereas in the case of rGO:Fe_2O_3, an enormous enhancement ($\approx \times 500$). The reason for both enhancement are due to Au, Fe attachments and their core level contributions as indicated in the UPS measurement.

The exchange interaction of Au 4f, Au 5d and O 2p which are present in rGO:Au-NP plays a role in the electrical and magnetization whereas in the case of rGO:Fe_2O_3, the Coulomb exchange interaction of Fe 2p, Fe 3d and O 2p which are the main contribu-

tors to the observed properties.

In summary, the current project was aimed at functionalizing graphene oxide (GO) with gold and iron oxide nanoparticles for electronic device applications with focus on ferroelectric properties. The project was seperated into two parts where rGO-Au-NP and rGO:ATA-Fe_2O_3 nanocomposites were explored. In the first part, GO was synthesized using modified Hummer's method and reduced with hydrazine hydrate. The obtained rGO powder were chemically functionalized with silica coated Au-NPs for different concentrations. The structural and morphological properties were explored using several characterizations. The electronic, electrical and magnetic properties of the nanocomposites were also considered using different characterization technique.

The obtained results for XRD, TEM and SEM showed the formation of the composites as expected. The Raman spectra of rGO and rGO:Au-NPx showed typical features of D and G peaks of carbon related material. The decrease in value of I_D/I_G from $1.22 \rightarrow 0.98$ depicts an increase in defect of rGO. The implication of which is the reduction in the sp^2 cluster of rGO with increase in the sp^3 clusters as the concentration of Au-NP increases. XPS further clarifies the composites and the bonding structure of rGO and rGO:Au-NPx nanocomposites. Of particular interest is the formation of new bonds of C-Au and Au-O which imparts the properties of GO. The density of state was explored using ultra-violet photoelectron spectroscopy (UPS) He II. Different states such as $2p - \pi$, $2p - (\pi - \sigma)$ overlap, $2p - \sigma$, mixed $2s - 2p$ and $2s$ were observed. The upward and downward observed shift in the states depicted a variation in the density of state of rGO when defects are induced.

X ray absorption near edge spectroscopy was used to probe the electronic structure of rGO and rGO:Au-NPx. The results further clarified the effect of defect induced by rGO functionalization. For instance, the sp^2 decreased steadily with increase in the concentration of Au-NP which implies substitution/ attachment of carbon atoms with Au atoms. The impact of the defects can be seen in the electrical and magnetic properties of rGO and rGO:Au-NP composites. There was a slight decrease in the electrical conductivity of rGO:Au-NP (4.88 at. %) in comparison with rGO. The drop

was mainly due to interfacial electron traps and weak bonding of Au atoms to rGO surface. The magnetic properties displays ferromagnetic/ superparamagnetic features with low remanence and coercivity. The magnetic property of rGO:Au-NP (4.88) was enhanced in comparison to rGO. The Origin of the magnetization was attributed to possible exchange interaction C-Au and C-Au-O atoms. Considering the coercivity and the ferromagnetic characteristics of rGO:Au-NP (4.88 at. %) nanocomposite, the material can be classified as a soft magnetic material. Materials with such behaviour can be good candidate for memory head device and in ferroelectric electronic device.

In the second part, GO and rGO-ATA-Fe_2O_3 were synthesized using modified Hummer's and co-precipitation techniques, respectively. The microstructural analysis from XRD showed an increase in crystallite size $77.1 \rightarrow 83,7\,\text{nm}$ when GO is reduced with NH_4OH. The particle size distribution analysis showed 14-15 nm diameter range. The Raman spectroscopy showed an increase in the defects of GO when functionalized with ATA-Fe_2O_3 where the I_D/I_G decreased $0.82 \rightarrow 0.43$. The XPS measurement showed appearance of new bonds Fe−C, C−Fe, N−C and N=C. The DOS from UPS also showed the presence of $\pi - \sigma$, $2p - \sigma$ and $2p - (\pi - \sigma)$ states. XANES measurement showed a decrease in $sp^2 \quad \pi^*$ content which implies an increase in sp^3 when GO is functionalized with ATA-Fe_2O_3 nanoparticles.

An enhanced electrical conductivity and magnetization was observed. The enhancement is due to the attachment of ATA-Fe_2O_3 to the surface of GO. A superparamagnetic feature was observed for rGO-ATA-Fe_2O_3 nanocomposites at both low and room temperature whereas paramagnetic features was observed for the case of GO. The enhanced magnetization rGO-ATA-Fe_2O_3 nanocomposites may be useful for magnetic resonance imaging contrast agent application as well as electronic device applications.

Future work

The structural modification of graphene offers easy tunability of its properties. In the current study, the orientation of the composite was not considered in the experimental procedures. The anisotropic features of graphene can be harvested for different applications.

For future prospect, the orientation of the graphene sheets will be considered for enhanced optoelectronic properties. Vertically aligned graphene (VAG) has been receiving attention from researcher owing to potentials in sensors, electrochemical and battery applications [1–3]. VAG proven to be exceptional and have attracted enormous attention from the scientific community. VAG is a form of graphene nanostructure which allows systematic arrangement of the sheets in a manner where substrate influence is significantly reduced [4]. VAG involves the spatial alignment of densely packed carbon atoms into tow planar directions where they are covalently bonded to each other. The graphitic platelets can be oriented vertically with respect to the substrate. The VAG takes advantage of the large surface area to volume ratio, non-stacking appearance with prominent edges. The optical properties of VAG is expected to exhibit low reflectance which is advantageous for solar cell applications.

Recently, attempts have been made to explore the optical properties of VAG [5] where the sheets were depositd on Cu foil films. The proposed study will be focused on optimizing the performance and efficiency of optoelectric properties VAG for possible application in solar cells.

The project will focus on synthesizing graphene oxide composite and deposited on ITO substrate using plasma enhanced chemical vapor deposition technique. Different spectroscopic techniques will be employed to probe the microstructural, electronic and photoconductive properties. Based on the obtained results, recommendation will be proposed for potential application of the VAG composites.

Bibliography

[1] Shisheng Li, Yanhong Luo, Wei Lv, Wanjing Yu, Sida Wu, Pengxiang Hou, Quanhong Yang, Qingbo Meng, Chang Liu, and Hui-Ming Cheng. Vertically aligned carbon nanotubes grown on graphene paper as electrodes in lithium-ion batteries and dye-sensitized solar cells. *Advanced Energy Materials*, 1(4):486–490, 2011.

[2] H Zanin, E Saito, HJ Ceragioli, V Baranauskas, and EJ Corat. Reduced graphene oxide and vertically aligned carbon nanotubes superhydrophilic films for supercapacitors devices. *Materials Research Bulletin*, 49:487–493, 2014.

[3] Jaeseok Yi, Jung Min Lee, and Won Il Park. Vertically aligned zno nanorods and graphene hybrid architectures for high-sensitive flexible gas sensors. *Sensors and Actuators B: Chemical*, 155(1):264–269, 2011.

[4] Zhenyu Zhang, Chun-Sing Lee, and Wenjun Zhang. Vertically aligned graphene nanosheet arrays: synthesis, properties and applications in electrochemical energy conversion and storage. *Advanced Energy Materials*, 7(23):1700678–1700698, 2017.

[5] Takatoshi Yamada, Makoto Hisa, and Masataka Hasegawa. Optical properties of vertically aligned graphene sheets. *MRS Advances*, 2(2):77–82, 2017.